Spectroscopy of the $T = \frac{3}{2}$ $A = 47$ and $A = 45$ Mirror Nuclei via One- and Two Nucleon Knockout Reactions

Sivahami Uthayakumaar

Doctor of Philosophy

University of York
Physics, Engineering and Technology

September 2022

Abstract

The charge-dependent interaction between nucleons can be explored and exploited using the analogue states identified in mirror nuclei. A cascade of excited states was established for the first time in the $T_z = -\frac{3}{2}$ proton-rich nuclei, ^{47}Mn ($Z = 25, N = 22$) and ^{45}Cr ($Z = 24, N = 21$), using an in-beam γ ray spectroscopy experiment. The observed states in the proton-rich nuclei were compared to their well-studied $T_z = +\frac{3}{2}$ mirror nuclei, ^{47}Ti ($Z = 22, N = 25$) and ^{45}Sc ($Z = 21, N = 24$), respectively. Analogue one- and two-nucleon knockout reactions were exploited using the ^{48}Mn/^{48}V and ^{47}Cr/^{47}V incoming secondary beams to populate states in ^{47}Mn/^{47}Ti and ^{45}Cr/^{45}Sc, respectively. New level schemes of the proton rich ^{47}Mn and ^{45}Cr nuclei were established using mirror symmetry arguments and γ-γ coincidence analysis. The inclusive and exclusive knockout cross sections in the $A = 47$ mirror pair have been measured for the observed populated states and were compared to reaction model calculations. Large differences between the cross sections of both mirror reactions were found to result from the large binding-energy differences between both nuclei. Large-scale shell-model calculations and an in-development density-functional approach, using the no-core configuration-interaction (DFT-NCCI) method, were deployed to study the mirror energy differences (MED) between the isobaric $T = \frac{3}{2}$ states for the ^{47}Mn/^{47}Ti and ^{45}Cr/^{45}Sc mirror pairs. The inclusion of the isospin-breaking terms provides a stringent test of the model prescriptions due to the active presence of the *fp*- and *sd*-orbitals and, for the case of ^{45}Cr, the spherical and deformed states that co-exist near the ground state. Lastly, the mean lifetimes of the first excited $\frac{7}{2}^-$ yrast states in the $A = 47$ nuclei were measured using the γ-ray lineshape method. The mean lifetime of the yrast $\frac{7}{2}^-$ states in ^{47}Ti and ^{47}Mn were found to be τ=331(15) ps and τ=687(36) ps, respectively. As these two mirror transitions are almost-pure $M1$ transitions, a high-precision comparison of the mirrored $B(M1)$ strengths were performed, resulting in identical transition strengths to a precision of 10%.

Contents

List of Figures

List of Tables

Acknowledgements

Over the course of my PhD studies, I have had the pleasure of meeting and working with many people, most of whom I consider as my close friends. There are many of you to thank but there are some that should have a special recognition.

I would like to first thank Prof. Mike Bentley for his phenomenal support and guidance throughout the duration of my PhD project. Mike has encouraged me to take many opportunities throughout my PhD whether it was through conferences, summer-schools and internal group talks. His work ethic and enthusiasm throughout my PhD has played a notable role in my development and has made my time as a PhD student an unforgettable experience. Mike, it has been a pleasure to work with you. Your approach to the work done has been such an inspiration and I hope to work with you on many more projects in the near future!

A huge thank you to Dr. Ed Simpson, Prof. Wojciech Satula and Prof. Silvia Lenzi for taking their time to do their calculations for this project and for their insightful discussions that I had with them. Thank you Prof. Jeff Tostevin for your help on the cross-section analysis. I also gratefully acknowledge Dr. Mark Spieker for his discussions on the analysis.

Thank you Dr. Xesus (Suso) Pereira-Lopez, you are not only a great friend but you have helped me a lot throughout the analysis process when I was really stuck. The discussions that we had about the project has been very helpful. Another thank you to Ryan Llewellyn; this project would not have been possible if it wasn't for your help and patience while guiding me through the starting procedures of the MSU data analysis. I am indebted to both of you. Rehab Yajzey, thank you for being there while we were completing the analysis.

To the members of the nuclear physics group at York, past and present, thank you all for your support and guidance throughout my PhD. Thank you Prof. Sarah Thompson and Dr. Christian

Diget for providing me with with some insightful questions throughout the PhD.

I would also like to thank my friends and colleagues: Jenn and Matt, we had numerous board games and movie nights together. Thank you for making me step out of my comfort zone. Dan, Ruth, Gustavo, Ohoud, Irene, Harvey, James, Silvia, for being the best office mates. Ewan, Tim and Andrew, thank you for making me smile while teaching! Katie, Karen and Billy, my former flatmates turned second family in York, thank you for organising movie and board games nights, having late night discussions and for baking with me to ensure that I do not stress. Joey, Emily, Mary and Poppy for being great movie buddies. Sophie, for always trying out desserts with me and for being so supportive no matter how far away you were. To my high-school friend Sandra, your words of wisdom especially during a pandemic, have always motivated me to do the best I could.

Lastly, to my parents, Pamini and Uthayakumar, for their continued support and encouragement from the very beginning, especially the last four years. This work is dedicated to them.

Declaration

I can hereby declare that the work presented in this thesis is a presentation of original work and that I am the sole author. The work presented herein has not been submitted for any other degree or qualification at this, or any other, university prior to beginning this project. All sources of information that have been used are acknowledged as references.

All of the work presented in this thesis was completed under the supervision of Prof. M. A. Bentley. Experimental work outlined in this thesis was undertaken in collaboration with staff at the National Superconducting Cyclotron Laboratory based at Michigan State University, USA.

Some parts of this thesis have been previously published as listed below:

Publications

- S. Uthayakumaar, M. A. Bentley, E.C. Simpson *et al.*, "Spectroscopy of the $T = \frac{3}{2}$ $A = 47$ and $A = 45$ Mirror Nuclei via One- and Two- Nucleon Knockout Reactions", Physical Review C, **106**, 024327, (2022).

- S. Uthayakumaar, M. A. Bentley, E.C. Simpson *et al.*, "Analogue $B(M1)$ strengths in the $T_z = \pm\frac{3}{2}$ mirror nuclei ^{47}Mn and ^{47}Ti", in preparation for submission to EPJ A.

Chapter 1

Introduction

The fundamental concept of isospin symmetry suggests that two nuclei, where the proton and neutron numbers are interchanged (i.e. mirror nuclei), should demonstrate identical behaviour assuming that the strong nuclear force is charge-symmetric and charge-independent [1]. If this assumption is true, then isobaric analogue states will be degenerate when isospin-breaking interactions are absent, such as the Coulomb interaction [2]. In reality, in the energy spectra of mirror nuclei, there are observed shifts in the excitation energies and binding energies. The study of mirror nuclei is a useful tool that probes the symmetric nature of the strong nuclear force to understand how good isospin symmetry is.

In this thesis, isospin symmetry is probed by examining mirror energy differences (MED) in the $f_{7/2}$-shell, specifically in the $T_z = \frac{3}{2}$, $A = 47$ and $A = 45$ mirror nuclei . Another main aim was to study the analogue spectroscopic factors, through cross-section measurements, in the $A = 47$ mirror nuclei by exploiting the direct nature of the reactions. This was explored to understand the symmetry of underlying wavefunctions when one of the two nuclei is unbound or weakly-bound. A tertiary aim was to determine the lifetimes of the first-excited $\frac{7}{2}^-$ states in the ^{47}Ti and ^{47}Mn nuclei to provide an insight into the isospin-dependence of the isoscalar and isovector components of the electromagnetic transition strengths.

To address these open questions, an experiment was performed at NSCL using analogue knockout reactions, first employed by Milne *et. al* [3]. In this process, the proton (neutron)-rich nuclei are populated through a neutron (proton) knockout from their respective parent nuclei, which are also mirror nuclei themselves. A comprehensive comparison of both mirrored knockout

reactions can be made, where these analogue pairs of reactions are reflected along the $N = Z$ line. This experiment was performed to measure the MED for the $A = 47$ and $A = 45$ mirror pairs. Furthermore, for the $A = 47$ case, the resulting inclusive (σ_{incl}) and exclusive (σ_{excl}) cross sections of the populated states and the lifetime of the first-excited states were also measured.

Firstly, the comparison of the previously unreported states in the $T_z = -\frac{3}{2}$, ^{47}Mn nucleus to the corresponding mirrored states in the $T_z = +\frac{3}{2}$, ^{47}Ti nucleus allows for the MED investigations to be performed. In addition, the observed states in the $T_z = -\frac{3}{2}$, ^{45}Cr nucleus were also compared to the well-studied $T_z = +\frac{3}{2}$, ^{45}Sc analogue states to evaluate the mirror energy differences. This analysis extends the current MED studies of mirror nuclei in the $f_{7/2}$-shell. For the proton-rich ^{47}Mn nucleus, no prior information about the excited states is known. For the proton-rich ^{45}Cr nucleus, while no confirmed information on the excited states has been reported previously, the tentative location of the $J^\pi = \frac{3}{2}^+$ state was measured at an energy of 107(1) keV. This state was observed to have a lifetime >80 μs, measured via a decay-spectroscopy experiment that resulted from a fragmentation reaction of ^{58}Ni [4].

Currently, there are two experimental studies that explore the isospin-breaking effects in $T = \frac{3}{2}$ mirror pairs, described in Refs. [3] and [5]. Both studies utilised the nucleon-knockout reaction, where the latter produced the ^{53}Ni/^{53}Mn and ^{49}Fe/^{49}V mirror pairs using a three-neutron / three-proton knockout channel and through fragmentation reactions, respectively, from a radioactive ^{56}Ni secondary beam [5]. The former study, which is an extension to Ref. [5], utilised the technique of direct one-nucleon mirrored knockout reactions to populate states in ^{53}Ni/^{53}Mn from ^{54}Ni/^{54}Fe, respectively, for the first time [3].

Mirrored states of the same isospin in isobaric nuclei are approximately identical, where a few differences in the excitation energies are caused by isospin non-conserving effects (e.g. the Coulomb interaction). Examination of these mirror energy differences (MED) allows for the structure of nuclei to be explored by taking into account the Coulomb effects. To date, there have been extensive studies that investigate MED between mirror pairs in the fp-shell, as discussed in Refs. [3], [6]–[12]. Current developments to the shell-model calculations, following the work from Zuker *et. al* [13], have now incorporated multipole and monopole contributions that originate from electromagnetic effects. This work and other studies in Refs. [6] and [14] have shown that the inclusion of only Coulomb and other electromagnetic effects are inadequate to reproduce

the experimental MED in the $f_{7/2}$ region. Therefore, an additional effective isovector term of multipole origin (V_B), which has a strong J-dependence must be included within the framework to reproduce the experimental data. This effective isovector term can be probed through mirror energy differences and by observing their resulting J-dependence. The inclusion of this term has been explored in extensive studies [5], [8], [9], [12], [14]–[19], where the size of the V_B term was comparable to the contributions from the Coulomb force. Bentley *et al.* have extracted a complete set of spin-dependent effective isovector ($V_{pp} - V_{nn}$) matrix elements obtained by fitting the shell model to all measured MED from experimental data from the $f_{7/2}$ shell [20]. Matrix elements of V_B = -72(7), +32(6), +8(6), -12(4) keV for the J =0, 2, 4, 6 couplings of the $f_{\frac{7}{2}}$ orbital were extracted and implemented within the shell-model calculations. The addition of these parameters were found to improve the theoretical fit to the experimental data. With the inclusion of the effective isovector term, the structure of mirror nuclei can be well-described by the prescription of the shell-model calculations. This prescription can be tested by collecting more data from the $f_{7/2}$ shell, preferably with mirror nuclei that have larger isospin differences due to the isospin non-conserving (INC) terms being significantly dependent on the T_z value (i.e. the isospin projection along the z-axis).

The effects of weak-binding in the proton-rich nuclei on the MED is of particular interest [21]. Currently, limited data exists in the $f_{7/2}$ region that probes into the proton-rich member of the mirror nuclei pair that are either unbound or weakly bound. Hence, this is an aim of the current analysis. The application of the effective isovector contribution, and its physical origin, to the MED calculations is still under debate. However, the use of such a term provides a useful tool to probe into the residual interactions, which are missing within the shell model [20], to understand the cause for the large shifts in the MED.

Since the shell model considers excitations between the fp-shells in these two cases, excitations from deep-lying shells (i.e. *sd*-shells) are restricted. Therefore, an alternative and in-development approach to study MED can be applied, based on density-functional theory [22], known as the No-Core Configuration-Interaction (DFT-NCCI) method [23]. This new method allows for a full treatment of rotational and isospin symmetries. In this model, charge-symmetry breaking (CSB) effects, originating from Coulomb and nuclear interactions, are incorporated. This method has only been applied once, by Llewellyn *et al.* [24], to the $T_z = \pm\frac{1}{2}$, $A = 79$ mirror pairs, the heaviest

mirror pair studied to date. The DFT-NCCI method was executed as the required shell-model space hinders shell-model-based MED calculations to be performed. This method was applied in this work, for both the $T_z = \pm\frac{3}{2}$, $A = 47$ and $A = 45$ mirror pairs as the configuration space does not need to be truncated in this model. Furthermore, the configurations based on the fp- and sd-shell excitations can be included for the populated negative and positive-parity states. This is especially important for the $A = 45$ case, where a deformed rotational positive parity band is seen.

As well as exploring isospin symmetry through MED, another approach was also taken in this work by exploiting the direct nature of mirrored knockout reactions. The secondary aim of this experiment was to measure the one-nucleon knockout cross sections to the states populated in the $A = 47$ mirror nuclei. In principle, this provides information about the spectroscopic factors for the analogue states in both nuclei, which could be a sensitive test of the analogue wavefunctions. Under the definition of isospin symmetry, the wavefunctions of the analogue states in both members of the mirror nuclei should be identical. Hence, the spectroscopic factors are also expected to be identical, which should result in the measured cross sections to be identical.

The extensively studied systematics, that details the suppression of the spectroscopic strength [25]–[27], was the main motivation to examine the cross-sections measurements.From these works, the experimental cross sections for knockout reactions become suppressed for one-nucleon removal reactions on light targets, compared to the calculated theoretical cross sections. This observed suppression is dependent on the asymmetry between the separation energies of the two types of nucleons, ΔS, found by determining the difference of the separation energy of the removed nucleon from a member of the mirror pair and the separation energy of the other nucleon removed from the other member (i.e $S_n - S_p$ for neutron knockout and $S_p - S_n$ for proton knockout). Fig. 1.1 shows the ratio of the inclusive experimental and theoretical cross sections, R_s, for one-nucleon knockout reactions against ΔS [25]–[27]. The observed downward trend corresponds to the suppression of the spectroscopic strength with ΔS. By studying mirror nuclei that consist of a large difference in Z, such as the members in $A = 47$ mirror pair, results in very different values of ΔS. Hence, different measurements in cross sections are also expected, with reference to Fig. 1.1. Therefore, it is of interest to test this observation using mirrored knockout reactions.

Lastly, the isospin principles can also be tested through the measurement of mirrored life-

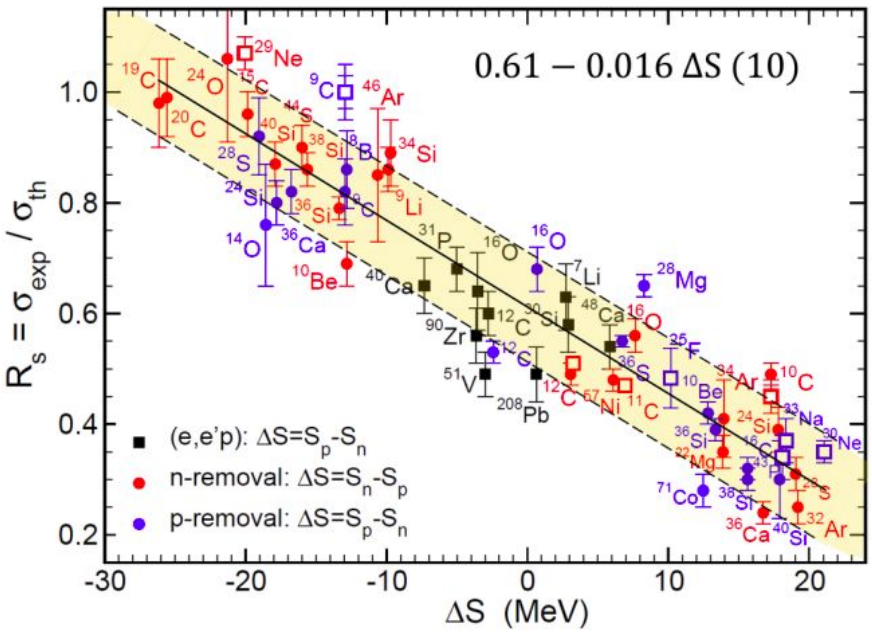

Figure 1.1: The ratio of the inclusive experimental and theoretical one-nucleon cross sections as a function of the separation energies, ΔS. The linear fit to the collected data points presented, obtained from different regions of the nuclear chart, is given as $y = 0.61 - 0.016\Delta S$ (10). Figure is taken from [27].

times of analogue states by studying the electromagnetic strengths. The isospin formalism (e.g. Ref. [28]) describes the T_z-dependence of the electromagnetic transition strengths between the analogue pairs of states within the multiplet studied. Hence, this dependence allows for the examination of isospin symmetry alongside the purity of the states that are studied. However, high statistics are required to measure lifetimes in proton-rich systems to test the T_z-dependence of the electromagnetic transition strengths. Regardless of the experimental challenges faced, the underlying wavefunctions can be explored to assess isospin symmetry as well as examining the isoscalar and isotensor components of the transition strength. This provides information on the dependence on isospin of the electromagnetic transition operators. To test isospin symmetry in mirror nuclei in terms of the electromagnetic strengths, high-precision measurements of the $J^\pi = \frac{7}{2}^-$ first-excited analogue states in the $T_z = \pm\frac{3}{2}$ mirror pair, ^{47}Mn and ^{47}Ti, were performed as part of this thesis work. In reference to the neutron-rich counterpart, ^{47}Ti, this transition is essentially a pure $M1$ transition [29]. This enables a precise comparison of analogue

$B(M1)$ measurements in the $A = 47$ mirror pair, and is the first example of such a high precision comparison of $B(M1)$ strengths in $T_z = \pm\frac{3}{2}$ mirror pairs.

In summary, this thesis aims to understand isospin symmetry by identifying new states in both of the proton-rich nuclei, ^{47}Mn and ^{45}Cr, which consequently leads to the analysis of mirror energy differences (MED). The differences between the measured excitation energies in the proton-rich nuclei are compared to their corresponding mirrored counterparts, ^{47}Ti and ^{45}Sc, respectively, to obtain experimental MED. The experimental MED are then compared to the results from the shell model and the DFT-NCCI approaches. These results were interpreted in terms of isospin non-conserving (INC) effects. Furthermore, the evaluation of the mirrored one-nucleon knockout cross sections, which consist of a large difference in the separation energy, ΔS, are discussed. The inclusive and exclusive cross sections of the $A = 47$ mirror pair were measured to explore the suppression of the spectroscopic strength. The calculation of the analogue spectroscopic factors, obtained from the shell model, and the analogue single-particle knockout cross sections, from the reaction model, were required for this analysis. Lastly, the mirrored $B(M1)$ measurements for the $J^\pi = \frac{7}{2}^-$ first-excited states in the $A = 47$ mirror pair were also analysed, where the lifetimes of these states in both ^{47}Mn and ^{47}Ti were measured with high precision.

1.1 Overview of Thesis

The overview of the analysis performed is structured as follows: Chapter 2 details the underlying concept of isospin symmetry and shell-model theory. The prescription of the shell-model calculations used to analyse the MED and the knockout calculation cross sections, obtained from reaction theory, are also discussed in this chapter. In Chapter 3, the experimental setup utilised at NSCL, MSU, is described, where all relevant components that were used are discussed. Chapter 4 details the calibrations and corrections that have been applied for the various detectors used in the experiment to enhance the particle identification spectra that are produced. Analysis techniques that were employed to produce the γ-ray spectra for nuclei of interest are also presented. The results obtained in this thesis are divided into three parts from Chapters 5-7. The results detailed in Chapters 5 and 6 have been published in Physical Review C [30], where the

key results have been highlighted and discussed. The results from Chapter 7 are to be published in EPJ A. Chapter 5 presents the experimental results and analysis of the mirrored one- and two-nucleon removal reactions. In this chapter, the deduced level schemes for the states seen in all four $T_z = \pm\frac{3}{2}$ nuclei studied in this thesis are presented with a discussion on the MED results. In Chapter 6, the results of the measured experimental cross sections for the $A = 47$ mirror pair are compared to the calculated theoretical cross sections for the states observed in this work. The impacts of these results will be discussed towards the end of this chapter. Chapter 7 will present the results of the lifetimes of the first-excited states in the $A = 47$ mirror nuclei. This will be followed by a brief discussion of the mirror $B(M1)$ electromagnetic strengths and its implications on the isoscalar and the isotensor matrix elements. Lastly, Chapter 8 will detail a summary of the key conclusions from this analysis along with future work that can be considered.

In addition to the experimental data analysis, the shell-model analysis was performed using the prescription described in Refs. [14], [20] using the ANTOINE code [31], [32]. The reaction-model calculations were produced using codes provided by Prof. J. A. Tostevin (University of Surrey) with assistance provided by Dr. E. C. Simpson (Australian National University). Except where noted, all shell-model and reaction-model calculations, alongside the lifetime simulations, have been undertaken by the author (S. Uthayakumaar). The majority of this work is also published in Ref. [30].

Chapter 2

Theory

2.1 Isospin

The role of isospin can be investigated by studying exotic isotopes in close proximity to the proton drip line, near the $N = Z$ line, as shown in Fig. 3.1 for the proton-rich nuclei of interest in this work, ^{47}Mn and ^{45}Cr. The attractive strong nuclear force that acts between protons and neutrons is generally assumed to be independent of the charge of the nucleons. This assumption forms the concept of isospin [33], which implies that the proton and neutron can be considered to be two quantum states of the same particle, the nucleon, provided that there is an absence of the electromagnetic interaction [1].

The neutron and the proton are each assigned an isospin quantum number $t = \frac{1}{2}$ with a projection t_z along the isospin quantization axis. Under this definition, in nuclear physics, the neutron is assigned a value of $t_z = +\frac{1}{2}$ and a proton having $t_z = -\frac{1}{2}$. Therefore, a nucleus comprises of a total isospin projection, T_z, given by the sum of the individual isospin projection of each nucleon[1], [7], and the total isospin quantum number, T, of each of the nucleons. Both equations for the total isospin projection and the total isospin quantum numbers are shown in Eq. 2.1 and 2.2, respectively, where N is the number of neutrons and Z is the number of protons.

$$T_z = \sum_{i=1}^{A} t_{z_i} = \frac{N - Z}{2} \tag{2.1}$$

$$\frac{|N - Z|}{2} \leq T \leq \frac{|N + Z|}{2} \tag{2.2}$$

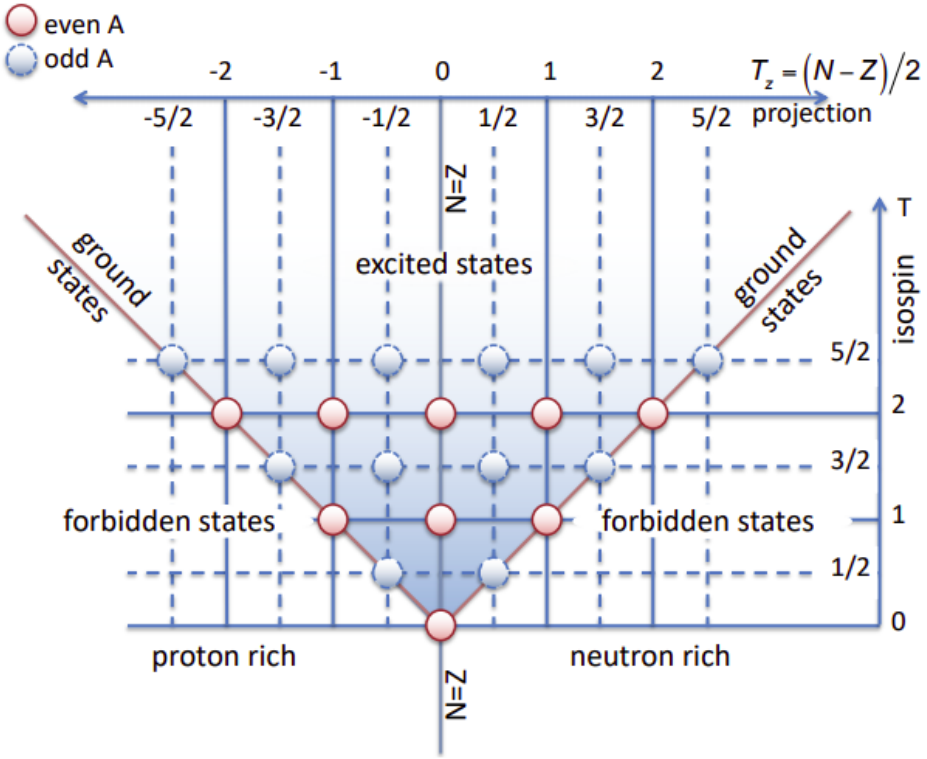

Figure 2.1: The allowed and forbidden isospin states, T, for a nucleus of interest with a total isospin projection, T_z, in relation to Eq. 2.2. The circles show the set of states of a given isospin. The dots along the red lines show the set of states that have the lowest-energy in any state studied. Dashed lines show the half-integer isospin and spin states for odd-mass nuclei, while the solid lines represent the integer isospin and spin states for even-mass nuclei. Figure taken from Ref. [34].

Different nuclei that comprise of a total isospin projection, T_z, also have corresponding T states that are forbidden, as shown by Eq. 2.2 and in Fig. 2.1, created by Prof. M. A. Bentley. Each circle represents a set of states, of a given isospin, allowed by the Pauli Principle [34]. The blue circles represent the odd-mass nuclei, A_{odd}, while the red circles correspond to the even-mass nuclei, A_{even}. For $N \neq Z$ nuclei, the yrast states (states that have the lowest excitation energy for a given spin) usually have a minimum isospin value of $T = T_z$. Nuclei with higher values of T have higher energies. The red diagonal lines in Fig. 2.1 shows that most of the odd-odd and even-even nuclei exhibit ground states of $T = |T_z|$. $T = 0$ states are only allowed in $N = Z$ nuclei, where $T_z = 0$. However, in the case of odd-odd $N = Z$ nuclei, this observation may not be completely valid as some of these nuclei were observed to have $T = 0$ ground states, while

others have $T = 1$ ground states. This has been observed in some odd-odd nuclei around the $A \sim$46, mid-fpg shell region, where the first $T = 1$ states are found to be lower in energy than the $T = 0$ states [35]. The observation of some $T = 0$ and $T = 1$ ground states in some odd-odd $N = Z$ nuclei is due to the protons and neutrons occupying orbitals of the same quantum number [36]–[38], which allows for the neutron and proton pairing (np) effects to determine the ordering of the T=0 and T=1 states.

The charge-symmetric and the charge-independent nature of the strong nuclear force are defined in Eq. 2.3 and 2.4, respectively. The charge-symmetric assumption of the strong nuclear forces accounts for the identical neutron-neutron (V_{nn}) and proton-proton (V_{pp}) interactions (see Eq. 2.3) [20]. The charge-independence of the strong nuclear force states that the strength of the nuclear force between a neutron and a proton (V_{np}) is equivalent to the average of neutron-neutron (V_{nn}) and proton-proton (V_{pp}) interactions (see Eq. 2.4).

$$V_{pp} = V_{nn} \tag{2.3}$$

$$V_{np} = \frac{V_{nn} + V_{pp}}{2} \tag{2.4}$$

When isospin non-conserving effects (INCs) are absent, degeneracy between the analogue states would be expected in nuclei consisting of the same isospin, T. This degeneracy is known as Isobaric Analog States (IASs). In reality, this degeneracy is broken and differences in the excitation energies of IASs are observed due to isospin breaking effects, mainly arising from the Coulomb interaction that acts as a long-range repulsive force felt only by the protons. To first order, the effect of the Coulomb interaction is the same for all excited states in the nucleus, including the ground state. Hence, the lifting of the degeneracy in the excitation energies between the IAS (normalised to the ground state) can be justified by INC interactions from either the electromagnetic interaction or by a small contribution from the nucleon-nucleon interaction, due to the charge-dependence or charge-asymmetry of the strong nuclear force. These interactions contribute to the Coulomb interaction[13], which results in isospin mixing. These INC interactions can be studied as two effects; the isovector effect, $V_{isovector}$, and the isotensor effect,

$V_{isotensor}$, as shown in Eq. 2.5 and 2.6, respectively.

$$V_{isovector} = V_{pp} - V_{nn} \tag{2.5}$$

$$V_{isotensor} = V_{pp} + V_{nn} - 2V_{np} \tag{2.6}$$

Isovector effects can be studied by investigating pairs of mirror nuclei through mirror energy differences (MED). In this case, the number of protons and neutrons are interchanged, hence the number of np pairs has not changed. Isotensor effects can also be studied separately by investigating the energy difference within isobaric triplets (i.e. Triplet Energy Differences, TED). This approach consists of triplets of nuclei, all having the same atomic mass number, A, centred along the N=Z line (i.e. one odd-odd nucleus along the $N = Z$ line and two neighbouring even-even nuclei consisting of $Z + 1, N - 1$ and $Z - 1, N + 1$).

2.1.1 Mirror Energy Differences

In Chapter 5, isovector effects in mirror nuclei with $T_z = \pm\frac{3}{2}$ were investigated in depth through Mirror Energy Differences (MED) using the difference in the excitation energies between the IAS of the two mirror nuclei. This is studied by using the following equation:

$$MED_J = E^*_{J,T,-T_z} - E^*_{J,T,T_z}, \tag{2.7}$$

where E^*_{J,T,T_z} is the excitation energy of a state of spin, J, total isospin, T and isospin projection along the z-axis, T_z. Since the excitation energies are measured relative to the ground state for each nucleus studied, the effects of the Mirror Displacement Energies (MDE) (i.e. the displacement energies of the ground states of the mirror nuclei), are removed. Hence, the spin-dependent contribution to the excitation energy differences is considered for the analogue states in both mirror nuclei. In order to conduct a comprehensive analysis between the deduced experimental values and theoretical results, the effects due to the Coulomb force and other isospin non-conserving effects need to be modelled to understand isospin symmetry violation. A theoretical framework is required to model these effects for the MED (see discussion in Section 2.2.1). Therefore, the state-of-the-art shell model was used to investigate all possible contributions of electromagnetic and nuclear origin to the MED in bulk nuclear systems.

Triplet energy differences (TED) probe into the isotensor effects, which are connected to the strength of the *np* interaction compared to the *pp* and *nn* interactions - i.e. the charge-dependent components of the strong nuclear force. The TED is defined as shown:

$$TED_J = E^*_{J,T,T_z=-1} + E^*_{J,T,T_z=1} - 2E^*_{J,T,T_z=0}, \tag{2.8}$$

where T represents the total isospin quantum number and T_z is the total isospin projection along the z-axis.

The dependence of the total binding energy of a set of isobaric analogue states (IAS) in a multiplet on T_z can be studied using the Isobaric Multiplet Mass Equation (IMME), first proposed by Wigner [39], where detailed descriptions of this method are described in Refs. [40], [41]. Many tests on the IMME have been conducted using high-precision mass measurements - see Ref. [42] for a full comprehensive review within the *sd*-shell. Using this formalism for the IMME equation, it is expected that the energy (and hence, the mass) of isobaric multiplet states as a function of T_z should have a quadratic dependence, and is written as:

$$\Delta BE(\alpha, T, T_z) = a + bT_z + cT_z^2, \tag{2.9}$$

where α represents all relevant quantum numbers associated with the state. The coefficient a relates to the mixing of the isoscalar component with a small contribution from the isotensor effect, while the coefficents b and c refer to the isovector and the isotensor components that define the MED and TED. The MED and TED probe into the charge-symmetric and charge-independent nature of the attractive strong nuclear force, respectively.

2.2 The Nuclear Shell Model

The shell-model approach is very effective to help understand the experimental results in atomic physics and to study the complicated nature of the atomic orbital structure. The fundamental principles of this method have been applied to develop a quantum mechanical model in 1949 known as the nuclear shell model. This model combines the work undertaken by Jensen *et al.* and Goeppert-Mayer[43], [44] leading to the Nobel Prize award in Physics in 1963 [45]. Some aspects of the atomic shell model were applied to the nuclear shell model by Goeppert-Mayer,

based on her work that explored isotopic abundances and the introduction of the strong spin-orbit interaction. The consequent result of splitting orbitals led to the understanding of "magic numbers", being 2, 8, 20, 28, 50, 82 or 126, for both the protons and/or neutrons. These magic numbers correspond to particular closed-shell structures that exhibit typically large binding energies [46].

Yet, there are some clear differences between the atomic and nuclear shell models. The atomic shell model has electrons that orbit the atomic nucleus in quantised shells, bound by a clearly defined potential caused by the attractive Coulomb field of the nucleus. However, the nuclear shell model does not have a well-defined central potential. Instead, the central mean-field potential in the nuclear shell model is produced by the motion of the nucleons themselves. Hence, the nuclear shell model is an independent-particle model where nucleons mutually move around in a mean-field that is not affected by neighbouring particles. Therefore, the shape of the nuclear central potential is determined by the distribution of the nucleons.

By considering two-body interactions, the nuclear Hamiltonian, H, can be defined as the sum of the kinetic energy, T, and the potential energy, V[47].

$$H = T + V = \sum_{i=1}^{A} \frac{\hat{p}^2}{2m_i} + \sum_{j>1}^{A} V_{i,j}(\hat{r_i})(\hat{r_(j)}). \tag{2.10}$$

The second term is approximated in the single-particle shell model, where an average potential is applied. An approach to define the central potential is by using the Harmonic Oscillator (HO) shown in red in Fig. 2.2 and given by:

$$V_{HO}(r) = \frac{1}{2} m\omega^2 \hat{r}^2, \tag{2.11}$$

where m is the mass of the nucleon, ω is the angular frequency of the oscillator and $\hat{r}^2$ is the radial distance of the nucleon. However, this potential becomes too diffuse with increasing radius. Therefore, a spherically symmetrical mean-field potential, the Woods-Saxon potential (see purple line in Fig. 2.2) [48], is typically used as shown:

$$V_0(r) = \frac{-V_0}{1 + \exp\left(\frac{r - R_0}{\alpha}\right)}, \tag{2.12}$$

where the radius of a spherical nucleus is $R_0 = 1.25A^{\frac{1}{3}}$ fm, V_0 is the potential well depth, and α is the diffuseness of the nuclear surface. Both V_0 and α are derived empirically, where the typically used values are ∼53 MeV and ∼0.65 fm, respectively [49]. For a nucleus that has neutron excess, the V_0 potential has to be corrected for both protons and neutrons. Due this excess, the protons feel a strong potential as the mean neutron-proton (np) potential is stronger than the neutron-neutron (nn) or proton-proton (pp) potentials. Hence, the following modification is made:

$$V_{0p} = V_0 + \frac{(N-Z)}{A}V_1 \text{ for protons,} \tag{2.13}$$

$$V_{0n} = V_0 - \frac{(N-Z)}{A}V_1 \text{ for neutrons,} \tag{2.14}$$

where the value for V_1 that is typically used is -30 MeV. This and other parameters can take different values depending on the mass region explored in the nuclear chart and the nucleus that is studied [49]. Due to the simplicity in solving the Schrödinger equation, the HO nuclear potential is typically chosen for many shell model applications.

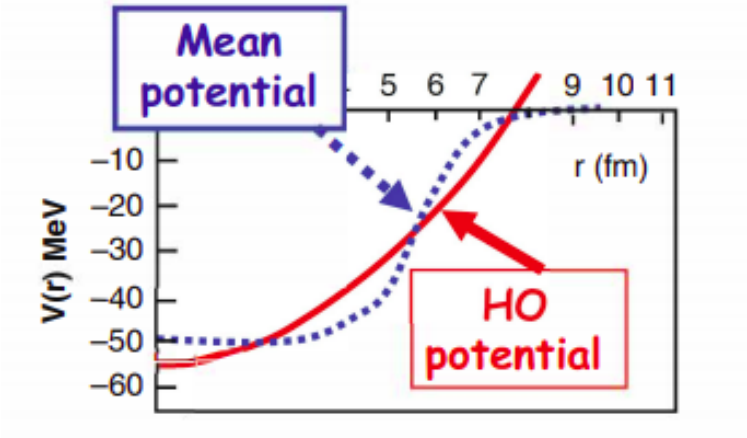

Figure 2.2: The comparison of the Harmonic Oscillator potential (red) to the Wood-Saxon potential (dashed purple line). Figure is taken from Ref. [50].

The central potential successfully reproduces magic numbers of 2, 8 and 20, but fails at magic numbers beyond 20. Therefore, two additional terms are required to be added to the central potential. The first contribution is an attractive term that is proportional to ℓ^2 ($\ell.\ell$), shown in Eq. 2.15, where V_{ll} is the strength constant of the interaction. The $\ell.\ell$ term increases the binding

energy of the nucleons that consist of larger orbital angular momentum (ℓ) values, resulting in a flatter potential well.

$$V_{\hat{\ell}\hat{\ell}} = V_{\ell\ell}\hat{\mathbf{L}} \cdot \hat{\mathbf{L}} \tag{2.15}$$

The second contribution comes from the spin-orbit interaction that is of nuclear origin, determined by the derivative of the central potential (see Eq. 2.16). The term $V_{\ell \mathrm{s}}$ is the strength of the spin-orbit interaction and is typically assigned as 22 MeV [49].

$$V_{\hat{\ell}\hat{s}} = -V_{\ell \mathrm{s}} \frac{\delta V_{HO}(\hat{\mathbf{r}})}{\delta r} \hat{\mathbf{L}} \cdot \hat{\mathbf{S}} \tag{2.16}$$

By including the spin-orbit potential, which couples ℓ and s of the nucleons to a total angular momentum ($\vec{j} = \vec{\ell} + \vec{s}$), to the central potential used splits the degeneracy of the states that have the same n and ℓ values. Different orientations of $\vec{\ell}$ and $\vec{s}$ affect the shape of the potential through the spin-orbit interaction. Parallel alignments provide a wider potential and are preferred, hence lowering the energy of the $\vec{j} = \vec{\ell} + \vec{s}$ levels. Conversely, the levels of $\vec{j} = \vec{\ell} - \vec{s}$ are raised when antiparallel couplings are present, essentially narrowing the potential.

Furthermore, a couple of additional terms are also added to the central potential along with the spin-orbit ($V_{\ell s}$) and $V_{\ell\ell}$ potentials. A centrifugal term (V_{cent}) accounts for the centrifugal force that is felt by the moving nucleons between orbitals, as shown in Eq. 2.17.

$$V_{cent}(r) = \frac{\ell(\ell+1)\hbar}{2mr^2}, \tag{2.17}$$

The terms, ℓ, represent the angular momentum of the nucleons, m is the reduced mass and r is the separation between the particles between orbitals.

The presence of protons within the nucleus introduces another potential, V_C, which results from the Coulomb potential that arises from the electric field induced by the protons. Assuming that the nucleus has a spherical shape, this potential takes the form as shown, where Z is the atomic number of the nucleus:

$$V_c = \begin{cases} \frac{Ze^2}{R_0}\left[\frac{3}{2} - \frac{r^2}{2R_0^2}\right] & \text{for r} < R_0 \\ \frac{Ze^2}{R_0} & \text{for r} > R_0 \end{cases}$$

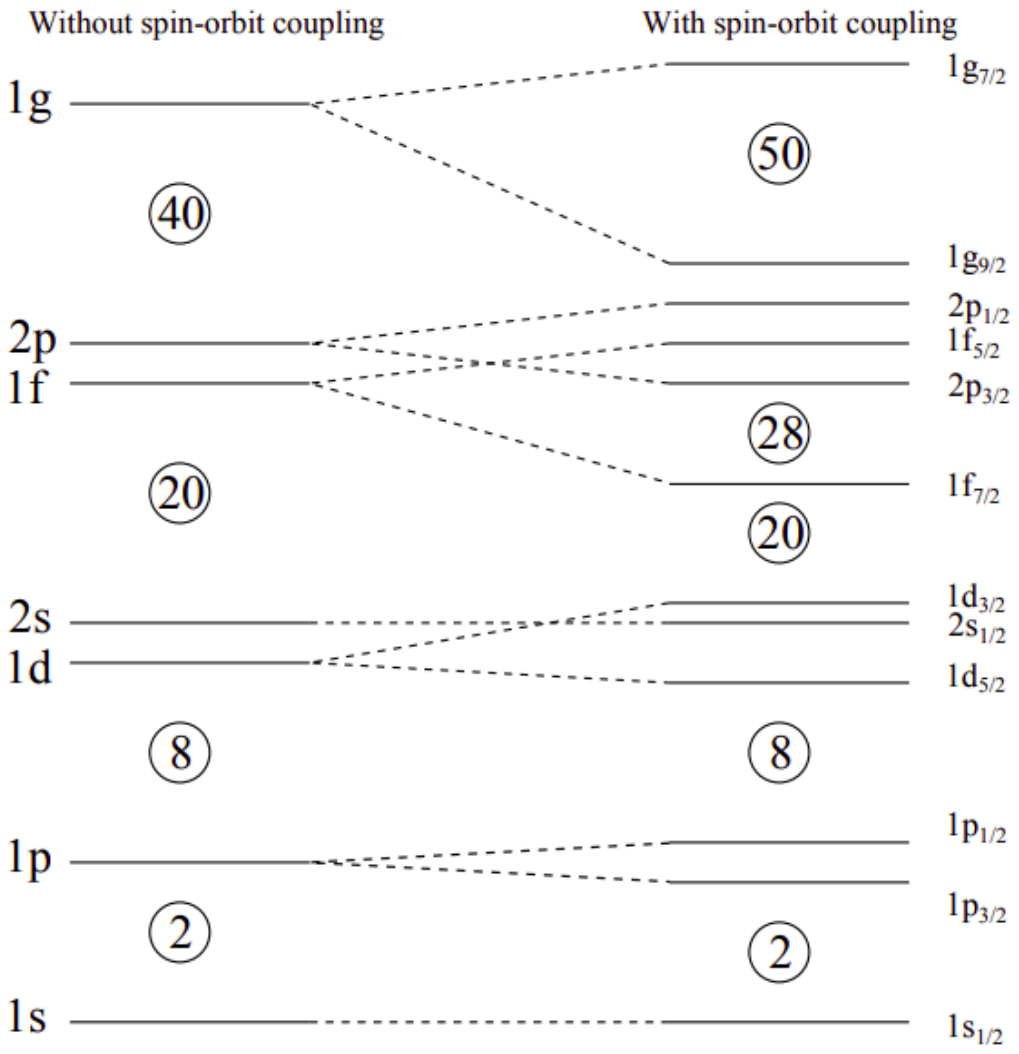

Figure 2.3: The effect of adding a strong spin-orbit component to the shell model. On the left-hand side, the levels are calculated by using a realistic potential, omitting the spin-orbit component. The right-hand levels demonstrate the effect that the strong spin-orbit component has on the levels. The additional magic numbers of 20 and 50, and the suppression of the magic number 40, were the first observations that led to spin-orbit component to be required in the shell model. Note: the level splitting in this figure is not to scale. Figure taken from Ref. [51]

By adding the central-potential term with the two $V_{\ell\ell}$ and $V_{\ell s}$ potentials, along with the centrifugal (V_{cent}) and Coulomb potentials (V_C), the total potential for the single-particle shell model can be written as:

$$V(r) = \begin{cases} V_{HO}(\hat{\mathbf{r}}) + V_{\hat{\ell}\hat{\ell}} + V_{\hat{\ell}\hat{s}}(\hat{\mathbf{r}}) + V_{cent} + V_C & \text{for protons} \\ V_{HO}(\hat{\mathbf{r}}) + V_{\hat{\ell}\hat{\ell}} + V_{\hat{\ell}\hat{s}}(\hat{\mathbf{r}}) + V_{cent} & \text{for neutrons.} \end{cases}$$

The effect of adding the spin-orbit coupling term to the central potential is shown in Fig. 2.3, where magic numbers above 20 were reproduced (i.e. 28, 50, 82 and 126). These predictions were found to be in agreement with the experimental observations.

2.2.1 Residual Interactions

Since the single-particle shell model only considers an unpaired nucleon, any other interactions that are not considered by the mean-field interaction require a residual interaction to be applied, H_{res}. Nucleon-nucleon interactions between nucleons that occupy single-particle energy levels are included in the residual interaction. The resulting Hamiltonian that accounts for the interactions between the nucleons is as follows:

$$H = H_0 + H_{res}, \tag{2.18}$$

where H_0 is the Hamiltonian used in the potential that incorporates the Coulomb, centrifugal, spin-orbit and the central potentials shown above. Two-Body Matrix Elements (TBME) are used for the residual interaction, where these matrix elements are the calculated energies of different multipole interactions between particles. Therefore, H_{res} is a small pertubative effect on H_0, where nucleon-nucleon interactions describe a potential that influences all nucleons in a system. The Two-Body Matrix Elements of a residual interaction can be determined in three ways [47]:

1. Empirical interactions: deduced using experimental data by fitting the binding energies of nuclei in the vicinity of shell-closure.

2. Schematic interactions: employing interactions such as Skyrme [52] and Gogny forces [53] that utilise the Hartree-Fock method in mean field calculations. This method was applied successfully to calculate properties such as the masses, shapes and radii of nuclei.

3. Realistic interactions: fitting effective nucleon-nucleon potentials to experimental nucleon-nucleon scattering data [54], [55].

Any effective residual interaction utilised is only reliable in the model space from where it was derived.

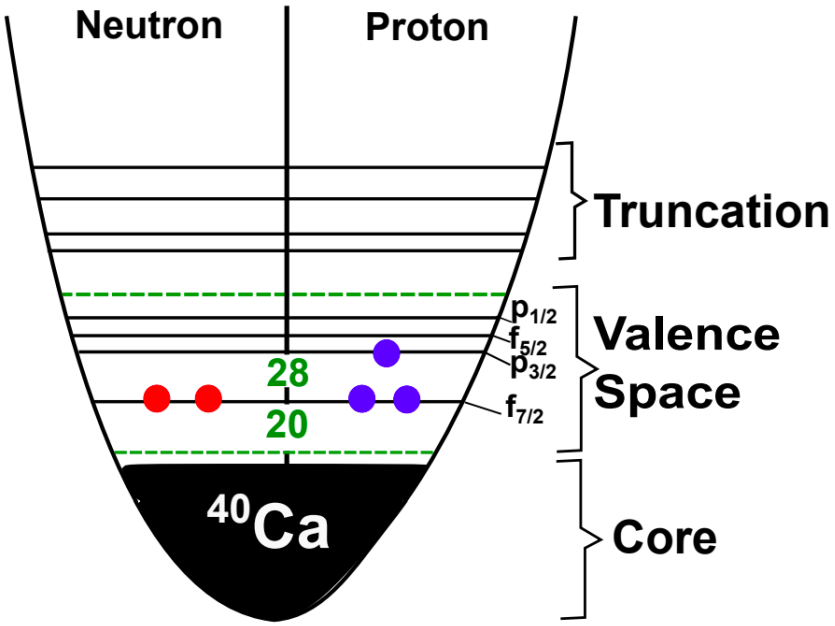

Figure 2.4: A schematic diagram showing the three main components of the shell model calculation, where the inert core is presented. In this work, an inert core of ^{40}Ca has been used within the harmonic oscillator potential, while the two fermions (protons and neutrons) are arranged in the $f_{\frac{7}{2}}$, $p_{\frac{3}{2}}$, $f_{\frac{5}{2}}$ and $p_{\frac{1}{2}}$ sub-shells. The truncated region shows some of the single-particle levels that have not been included in the shell model. Figure taken from Ref. [56].

There are three types of constraints applied to the shell model to ease the computational implementation. The first constraint restricts excitations from deep-lying states, where a closed-shell is considered as an inert core. Here, all the nucleons are paired and are tightly bound in their respective single-particle levels. Therefore, the contribution from these deep-lying states is not included in the residual interaction. In this work, a ^{40}Ca ($N = Z = 20$) inert core was utilised for the calculations performed. The second constraint is the valence space, where the nucleons can freely move and interact with each other. The valence space utilised in the shell model in this analysis is the fp region. Lastly, the shell-model space can be truncated to reduce computational power. In this work, the excitations in the full fp valence space were

not truncated. The application of these three constraints to the shell model calculations is demonstrated in Fig. 2.4.

The fp shell model region is of particular interest in this experiment. A number of residual interactions can be utilised in shell-model calculations, where a fixed ^{40}Ca core and a fp valence space can be applied. As the $A = 47$ and $A = 45$ mirror nuclei are considered in this work, either the KB3G [57] or the GXPF1 [58] interactions can be used. The KB3G interaction, being a realistic interaction, is a set of two-body matrix elements extracted from nucleon-nucleon potentials by Brown and Kuo [59], [60]. This interaction gives a good description for light nuclei in the fp shell between the 42≤A≤54 nuclei [20]. The GXPF1 interaction, an empirical interaction, uses a set of matrix elements that result from nucleon-nucleon interactions from Hjorth-Jensen *et al.*. The matrix elements and the single-particle energies were fitted to 669 energy levels from nuclei between $A = 47 - 66$ [61]. In this thesis, the KB3G interaction [57] was utilised for all shell-model calculations in the full fp space within the ANTOINE code [31].

2.2.2 MED Calculations

The nuclear shell model was utilised in this work to model the MED, which enables comprehensive comparison to the experimental MED results. Since mirror nuclei are explored in this analysis, the number of protons and neutrons are swapped, which causes the number of np pairs to be unchanged. However, the number of nn and pp pairs will be interchanged, implying that isovector effects must be considered within the shell model.

Four main isospin-breaking components are typically applied to analyse MED in the shell model calculations [14]. These components are the Coulomb multipole term (V_{CM}), the radial monopole term (V_{Cr}), the single-particle term (V_{ll} and V_{ls}) and the effective isovector INC term (V_B). In the following sections, each isospin-breaking term is discussed, where further details can be found in Refs. [13], [14], [20].

2.2.2.1 The Coulomb Multipole Term

The Coulomb multipole term (V_{CM}) accounts for the recoupling of angular momentum vectors in a pair of nucleons with increasing excitation energy. In turn, the Coulomb energy becomes affected. A pair of protons or neutrons in the middle of the $f_{\frac{7}{2}}$ shell can couple to $J = 0$, 2, 4 or

6, in accordance with the Pauli Exclusion Principle. Higher-J recouplings lead to an increase in the spatial separation between the two nucleons. Fig. 2.5 shows the calculated spatial overlap of a pair of protons coupled to $J = 0$, 2, 4 and 6 within the $f_{\frac{7}{2}}$-shell [62].

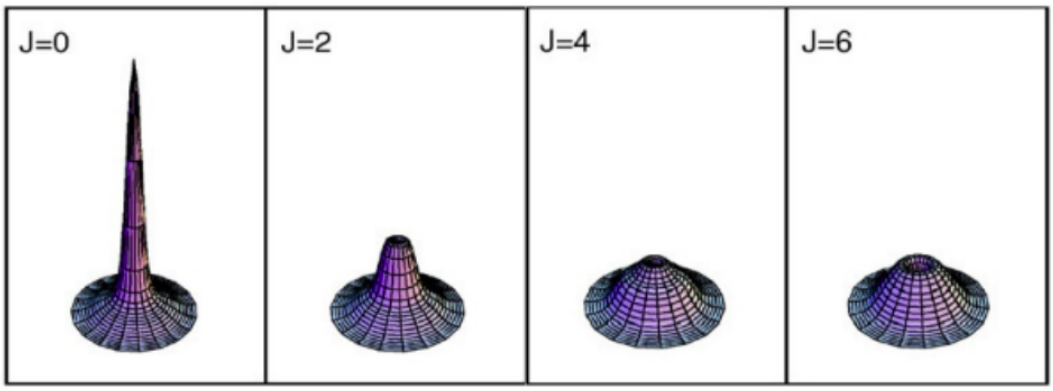

Figure 2.5: The probability distribution of the radial separation between the pair of like-nucleons in the $f_{\frac{7}{2}}$-shell coupled to J =0, 2, 4 and 6. Figure is taken from Ref. [62].

For proton-proton couplings (pp), the increase in the spatial separation between the orbits (i.e. larger J-couplings) causes a decrease in the Coulomb repulsion compared to lower J-couplings, where the Coulomb repulsion is larger. For neutron-neutron couplings (nn), the Coulomb repulsion will not be affected. To account for this effect within the shell-model framework to calculate MED, the Coulomb Matrix Elements (CME) that are calculated using the harmonic oscillator wavefunctions are added to the two-body interaction for protons in mirror nuclei.

2.2.2.2 The Radial Monopole Term

The radial term (V_{Cr}) is the Coulomb energy monopole term that is associated with changes in the mean nuclear radius and/or deformation effects as a function of spin [13]. Orbitals of low angular momentum, l, have a larger radius, and the occupation of these orbitals drives the nucleus to have a larger overall radius. Therefore, the variation in the occupation of these orbitals will contribute to energy differences as the Coulomb energy in each nucleus will be distributed differently. Admixtures from the upper fp-shell contribute significantly to the lower states in the $f_{\frac{7}{2}}$ shell, particularly around the mid-shell region, where deformation effects can be observed due to the partial occupation of the upper fp orbitals. As the total number of nucleons that

occupy the orbitals do not change in mirror nuclei, based on mirror symmetry arguments, the difference in the charge distribution between the two nuclei in the mirror pair produces the spin-dependent energy difference. The occupation of nucleons in the p-orbitals can also increase due to deformation, arising from configuration mixing. Therefore, it can also be possible that the V_{Cr} term reflects deformation changes.

For shell-model calculations performed in the $f_{\frac{7}{2}}$ region, the variation in the $p_{\frac{3}{2}}$ occupation can be tracked as a function of spin due its large mean radius. The V_{Cr} term is calculated by [14]:

$$\Delta V_{Cr}(J) = 2|T_z|\alpha_r\left(\frac{m_\pi(g.s.) + m_\nu(g.s.)}{2} - \frac{m_\pi(J) + m_\nu(J)}{2}\right), \tag{2.19}$$

where the constant $\alpha_r = 200$ keV, obtained from the single-particle relative energies in the $A = 41$ data [14], [63], m_π and m_ν are the proton and neutron occupations in the $p_{\frac{3}{2}}$ orbital of the ground state (g.s.) and the state of interest (J), respectively.

2.2.2.3 Single-Particle Monopole Term

Two effects are included in the single-particle monopole term, V_{ll} and V_{ls}, that account for the Coulomb [13] and Electromagnetic Spin-Orbit (EMSO) shifts [64] of the single-particle levels, respectively. Since the MED calculations are related to the energy, it is necessary to compute the change in energy, E_{ll} and E_{ls}, resulting from the differential of the V_{ll} and V_{ls} potentials.

Firstly, the effect due to V_{ll} considers the stored Coulomb energy in a proton single-particle orbital as a result of the overlap with the core [65]. This effect depends strongly on the square of the orbital momentum, l such that [65]:

$$E_{ll} = \frac{-4.5 Z_{cs}^{\frac{13}{12}}[2l(l+1) - n(n+3)]}{A^{\frac{1}{3}}(n+\frac{3}{2})} \text{ keV}, \tag{2.20}$$

where the Coulomb energy effect, E_{ll}, depends on Z_{cs}, the proton number of the core, and n, the principal quantum number.

Secondly, the effect of the electromagnetic spin-orbit interaction, V_{ls}, relates to the interaction between the spin moment of the nucleon and the Coulomb field of the nucleus [64], resulting in slight shifts in the single-particle levels for protons. By assuming that the Coulomb potential, V_C, is spherical with a radius, R_C, an equation estimating the energy shift of the single-particle

levels, resulting from the EMSO effect, can be derived such that [64]:

$$E_{ls} \simeq (g_s - g_l)\frac{1}{2m_N^2c^2}\left(-\frac{Ze^2}{R_C^3}\right) < \tilde{\mathbf{l}} \cdot \tilde{\mathbf{s}} >, \tag{2.21}$$

where g_s and g_l represent the spin and orbit gyromagnetic factors for protons (5.586 and 1) and for neutrons (-3.828 and 0), respectively, and m_N is the nucleon mass [14]. The spin-orbit coupling, $< \tilde{\mathbf{l}} \cdot \tilde{\mathbf{s}} >$, becomes $\frac{l}{2}$ when $j = l + s$ and $-\frac{(l+1)}{2}$ when $j = l - s$. Both the gyromagnetic factors and the spin-orbit coupling will affect the sign of the energy shift for protons and neutrons that contribute to the MED.

2.2.2.4 The Effective Isovector, V_B, Term

Although the electromagnetic effects are well understood, the inclusion of the three INC terms mentioned above in the shell model was found to be insufficient to reproduce experimental MED, especially in the $f_{\frac{7}{2}}$ region [15]. It has been previously mentioned by Zuker *et al.* that an additional isovector INC matrix element was required in the MED calculations [13]. This additional term, defined as V_B, is an isospin-breaking, empirical isovector interaction that considers the *pp* and *nn* potentials. Both of these potentials are significantly dependent on the angular-momentum coupling between nucleon pairs [20].

To produce a reasonable agreement between the experimental MED data, it was necessary to include the $J = 2$ additional isovector term to the two-body matrix elements for the $f_{\frac{7}{2}}$ protons by adding a single repulsive interaction of 100 keV [13], [14]. This additional matrix element was determined empirically by examining the MED for the $A = 42$ $T_z = \pm 1$ mirror pairs, where two nucleons were present in the $f_{\frac{7}{2}}$ shell. A sharp rise in the MED of ∼100 keV was observed for $J = 2, f_{\frac{7}{2}}$ couplings [13], [19], often referred to as the '$J = 2$ anomaly'. The origin of this term is not fully understood.

A full set of spin-dependent effective isovector $(V_{pp} - V_{nn})$ matrix elements have been studied by Bentley *et al.* in the $f_{\frac{7}{2}}$ shell. The shell model was fitted to all experimental MED data that are currently available in the $f_{\frac{7}{2}}$ region. This resulted in matrix elements of $V_B = -72, +32, +8, -12$ keV for $J = 0, 2, 4, 6$ couplings, respectively, where an ∼100 keV increase is seen between $J = 0$ and $J = 2$ couplings, in accordance with previous work [14]. The comparisons of the experimental and predicted MED for four mirror pairs that include (solid line) and exclude (dashed line) the

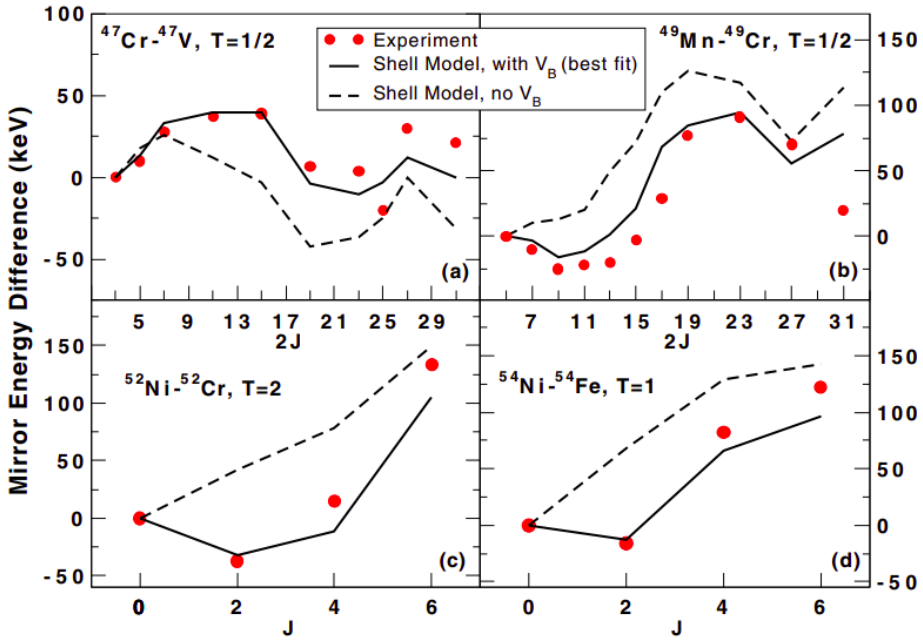

Figure 2.6: The comparison between the experimental and calculated MED for four $T_z = \frac{1}{2}$ mirror pairs in the $f_{\frac{7}{2}}$ region. The inclusion of the fitted V_B term is down by the solid black line, while the exclusion of the V_B term is shown by the dashed black line. The red dots represent the experimental MED. Figure taken from Ref. [20].

fitted V_B matrix elements are presented in Fig. 2.6. A significant improvement can be observed between the theoretical fit to the experimental data when the effective isovector $(V_{pp} - V_{nn})$ matrix elements were applied. Although the origin of this effect is currently not understood, it can be assumed that this effect arises from another type of electromagnetic contribution due to the strong J-dependence that is observed. This contribution is currently missing in the shell model [20].

Two different methods can be utilised to apply the V_B INC term in the model data. Both approaches include all four components in the shell-model calculations where either; (i) a V_B term of a single -100 keV INC matrix element for $J = 0$ is applied to all fp-subshells, or (ii) a V_B term utilising all four parameters extracted from the fit across the $f_{\frac{7}{2}}$ shell [20] is applied to all fp-subshells. In this work, method (i) was applied to the shell model, where the steps taken to calculate the MED of the $A = 47$ and $A = 45$ mirror nuclei are described in detail in Chapter 5.

2.3 Knockout Reactions and Theoretical Cross Sections

In this thesis, the population of the excited states in the exotic proton-rich $T_z = -\frac{3}{2}$ nuclei, ^{47}Mn and ^{45}Cr, and their respective mirror nuclei, ^{47}Ti and ^{45}Sc, was achieved through the use of mirrored one- and two-nucleon knockout reactions. The process of the mirrored knockout procedure and the knockout calculations performed will be described in the following sections.

2.3.1 The Projectile Fragmentation Reaction

A high intensity beam of stable nuclei is typically used for the fragmentation technique. Beams of stable nuclei are accelerated to energies of 100 MeV/nucleon to 1 GeV/nucleon [66] that impinge onto a thick target to produce fragments of radioactive nuclei. These fragments are then filtered and separated within a magnetic separator to produce secondary radioactive beams.

Many fragments are produced through particle removal from the beam or the target due to direct collisions. Consequently, many nucleons can be removed due to low-impact parameter collisions, allowing the resulting fragments to be passed through the separator. The fragmentation process of the high-energy, heavy, stable beam at a thick primary target can be described using an abrasion-ablation fragmentation model [67]. This model uses Glauber's multiple scattering theory [68], [69]. At relativistic velocities, the overlapping nucleons between the projectile and the target nuclei are essentially scraped off. This process is known as abrasion. The remaining nucleons in the projectile after this impact leave the target in an excited state, decaying through particle emission, known as ablation. The process of abrasion and ablation are shown in Fig. 2.7.

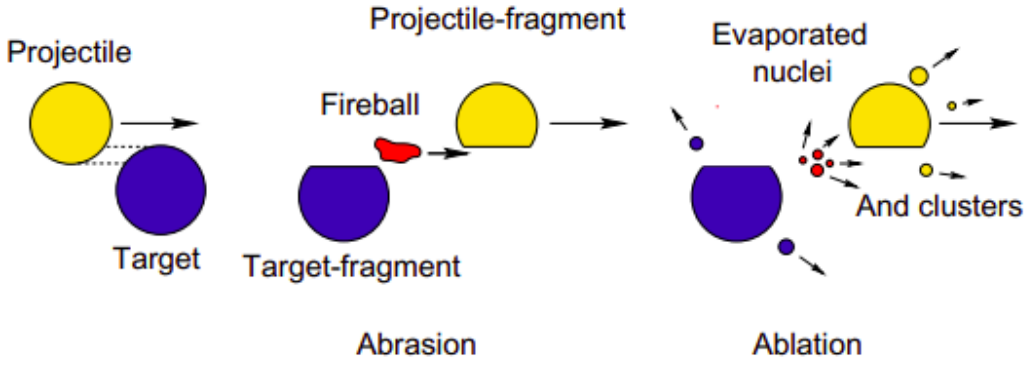

Figure 2.7: The simplified model of the fragmentation of stable beam via abrasion and ablation processes. Figure is taken from Ref. [70].

2.3.2 The Process of Knockout

Nucleon knockout reactions are direct processes that involve the removal of one or two nucleons from the secondary beam projectile following an interaction with a second target. In this process, some of the energy, angular momentum or some nucleons are transferred to or removed from the projectile. As this is a direct process, no intermediate stages take place between the initial and final products in knockout reactions. However, this is not the case for other reactions, such as fusion-evaporation or fragmentation.

Knockout reactions are performed using beams that have an energy of ∼100 MeV/nucleon impinging on light targets such as ^{9}Be or ^{12}C [71]. Since high beam energies are utilised in knockout reactions, other processes may occur depending on the impact parameter of the reaction. At low impact parameters, the fragmentation of the incoming beam can occur, causing the removal of multiple nucleons. In addition, a reaction can also occur where the target nucleus becomes broken up, known as spallation reactions.

By utilising knockout reactions as a probe to study nuclear structure, details about the underlying wavefunction of proton-rich nuclei, as well as spectroscopic information, can be provided (see Refs. [26], [72], [73] for further discussion).

2.3.3 One-nucleon Knockout Calculations

The use of mirrored one-nucleon knockout reactions was undertaken in this work to investigate the spectroscopic factors, C^2S, and to probe the underlying wavefunctions through the comparison of the experimental cross sections (σ_{exp}) and theoretical cross sections (σ_{th}). The calculation of the theoretical cross sections requires the input of two components - a single-particle knockout cross section, σ_{sp}, and a spectroscopic factor, C^2S. These inputs will be detailed in the following sections.

The knockout mechanism is comprised of two main components: stripping (absorption) and diffraction (elastic breakup). The stripping component considers the excitation of the target resulting from the absorption of the removed nucleon. The diffraction component accounts for the target nucleus in the ground state as the removed nucleon is emitted in the forward direction [74]. A third contribution is Coulomb dissociation, which accounts for the breakup of the projectile

resulting from electromagnetic interactions within the target. This process plays a minor role, especially for experiments that use a light target, and hence this contribution is neglected [75]. Fig. 2.8 shows the two main contributions of the single-nucleon knockout reactions.

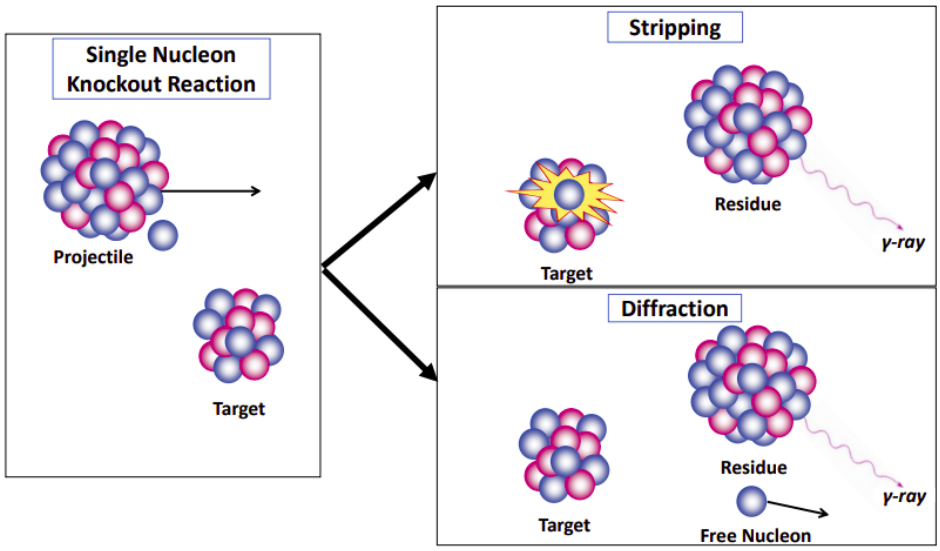

Figure 2.8: The two contributions to the single-nucleon knockout reaction, being the stripping (top right) and diffraction (bottom right) reaction processes. Figure is taken from Ref. [56].

The single-particle cross section (σ_{sp}) is comprised of the stripping and diffraction components and is given by:

$$\sigma_{sp} = \sigma_{sp}^{str} + \sigma_{sp}^{dif} \tag{2.22}$$

where σ_{sp}^{str} and σ_{sp}^{dif} are the single-particle stripping and diffraction cross sections, respectively. Each contribution largely depends on the beam energy. At high beam energies, the stripping contribution dominates. At lower energies (i.e. 50-60 MeV/nucleon), the contributions from the stripping and diffraction processes are similar [75].

In this analysis, the single-particle cross sections for each of the observed states in the $A = 47$ mirror pair were calculated using eikonal reaction dynamics by assuming a spectator-core approximation [25], [71], [73]. This method consists of a three-body reaction model that incorporates the target nucleus, projectile core and the projectile valence nucleon. The internal motion of the projectile is assumed to be adiabatic (i.e. in a frozen orientation), compared to the external motion at the centre of mass of the projectile. For high beam energies, the core and valence

system are essentially unchanged as they travel in a straight line through the target. Therefore, this three-body system can be reduced to a two-body system. The eikonal approximation is a semi-classical solution to the three-body problem shown in Fig. 2.9.

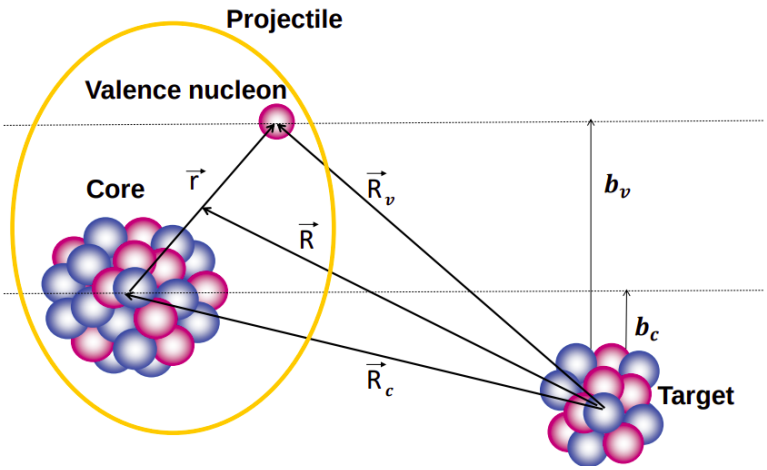

Figure 2.9: The coordinate vectors used for the core, valence nucleon and the target nuclei three-body system. Figure is taken from Ref. [56].

Both the stripping and diffraction contributions are calculated using the elastic scattering-matrices (S-matrices) of the core-target and the removed nucleon-target systems as a function of the impact parameters, as discussed in Refs. [73], [74]. Once the S-matrices are calculated, the stripping and diffraction contributions are calculated individually by integrating the centre-of-mass impact parameter, b, of the projectile using [71], [74], [76]:

$$\sigma_{sp}^{str} = \frac{1}{2J+1}\int db \sum_{M} \langle \Phi_{JM}^{c} | (1-|S_n|^2)|S_c|^2 | \Phi_{JM}^{c} \rangle, \tag{2.23}$$

$$\sigma_{sp}^{dif} = \frac{1}{2J+1}\int db \left[\sum_{M} \langle \Phi_{JM}^{c} || (1-S_c S_n)|^2 | \Phi_{JM}^{c} \rangle - \sum_{M,M'} |\langle \Phi_{J'M'}^{c} | (1-|S_c S_n|) | \Phi_{JM}^{c} \rangle|^2 \right], \tag{2.24}$$

where Φ_{JM}^{c} is the wave function of the nucleon-core relative motion, with total angular momentum J and projection M. S_c and S_n are the scattering amplitudes of the core and the valence nucleon interaction with the target, respectively [74], [77]. The $|S_c|^2$ term gives the probability of the core being elastically scattered (i.e. survives the reaction), while the $1-|S_n|^2$ term gives the probability of the valence nucleon being absorbed by the target [74], [75], [78]. It is important to note that the removal of a specific nucleon to each specific final state has a separate

single-particle cross section, σ_{sp}.

The calculated single-particle cross sections, σ_{sp} (i.e. the sum of the stripping and diffraction components), must be normalised by the spectroscopic factor, C^2S, to compare to the experimental partial cross sections. The C^2S values are calculated using the shell model, which describes the overlap of the wave functions between the initial and final state configurations. Hence, the spectroscopic factors provide information on the change in sub-orbital occupation within a nucleus. By summing the single-particle contributions for each sub-orbital, normalised by the C^2S factor, the theoretical cross section for each state populated in the daughter nucleus of J^π can be calculated as [71]:

$$\sigma_{th}(E_x, J^\pi) = \sum_{n\ell j} \left(\frac{A}{A-1}\right)^N C^2 S_{SM}(j) \sigma_{sp}(n\ell j, S_{n,p} + E_x), \tag{2.25}$$

where E_x is the excitation energy of a particular state in the residue, $S_{n,p}$ is the separation energy between the projectile ground-state to the parent ground-state depending on the type of knockout, C^2S is the spectroscopic factors deduced from the shell-model calculations, and nlj denote the quantum numbers of the orbital, angular momentum and the total spin, respectively, for the removed nucleon. The mass-dependent term, $(\frac{A}{A-1})$, is the centre-of-mass correction to the deduced spectroscopic factors from the shell model, where the harmonic oscillator number, $N = 3$, is used for the fp-shell [79]. The total theoretical cross section, σ_{th}, is summed over all allowed paths to that particular final state.

Single-nucleon removal wavefunctions were calculated using a Woods-Saxon plus spin-orbit potential. The single-particle wave functions were calculated, such that the diffuseness of $a = 0.7$ fm and a spin-orbit strength of $V_{so} = 6$ MeV were used. The geometry of the binding potential was constrained using the SkX interaction Skyrme Hartree-Fock calculations [80] to reproduce the rms radii and the binding energies of the fp orbitals. The depth of the potential well was also varied to provide states of the residue at the appropriate effective separation energy, given by $S_n + E_x$. The density folding potentials, obtained from the Hartree-Fock calculations, were used to calculate the core-target S-matrices using the $pp(r)$ and $pt(r)$ approximations (e.g. [81]).

In this work, the spectroscopic factors were obtained via the shell model using the ANTOINE code [31], [32]. The calculations were performed in the full fp-space within the KB3G interac-

tion [57] to provide information about the underlying structure of the residue.The single-particle cross sections, σ_{sp}, give details about the reaction mechanism, provided that only one-nucleon is removed from a specific state. The steps taken for these calculations using the reaction model and the shell model are detailed in Chapter 6 to calculate the theoretical cross sections for the $A = 47$ mirror nuclei.

Chapter 3

Experimental Details

3.1 Overview

The key aim of this experiment was to measure the one-nucleon knockout cross sections to the $T_z = \pm\frac{3}{2}$, ^{47}Ti/^{47}Mn mirror pair, where the spectroscopic factors for the mirrored knockout reactions in the fp-shell can be explored to better understand the symmetry of the analogue wave functions. The secondary aim was to measure the Mirror Energy Differences (MED) of the ^{47}Ti/^{47}Mn and ^{45}Sc/^{45}Cr mirror pairs, and to compare these results with DFT and state-of-the-art shell-model calculations. The former case is of particular interest to understand how MED are affected in weakly-bound nuclei. States in ^{47}Mn are unbound beyond the first excited state as the proton separation energy (S_p) is 384 keV [82]. The latter case was explored to extend our studies of how MED can be affected in nuclei that are well deformed and are in close proximity of semi-magic nuclei. Lastly, the lifetimes of the first-excited ($\frac{7}{2}^-$) state in the $A = 47$ mirror pair were determined to test the isospin principles in terms of the electromagnetic strengths.

To investigate the $T_z = -\frac{3}{2}$ proton-rich nuclei, the experiment was undertaken at the National Superconducting Cyclotron Laboratory (NSCL) facility at Michigan State University (MSU) [27] in April 2016. In the experiment, ∼120 hours of data were collected over 142 runs. A primary ^{58}Ni beam was utilised at an energy of ∼160 MeV/nucleon and was impinged onto a thick 802 mg/cm^2 ^{9}Be primary target. At this point, a cocktail of secondary radioactive beams was produced, via fragmentation, at the entrance of the A1900 separator [83]. The cocktail beam was dispersed in the separator using four dipole magnets and an aluminium degrader wedge. Contaminants in the beams were blocked by using adjustable slits. Dispersed secondary beams,

comprising of ^{49}Fe, ^{48}Mn, ^{47}Cr, ^{46}V, ^{45}Ti and ^{44}Sc, are then impinged on to the 188 mg/cm^2 ^{9}Be reaction target located at the reaction-target position of the S800 spectrograph [84] (see Fig. 3.1 and Table 3.1 for details).

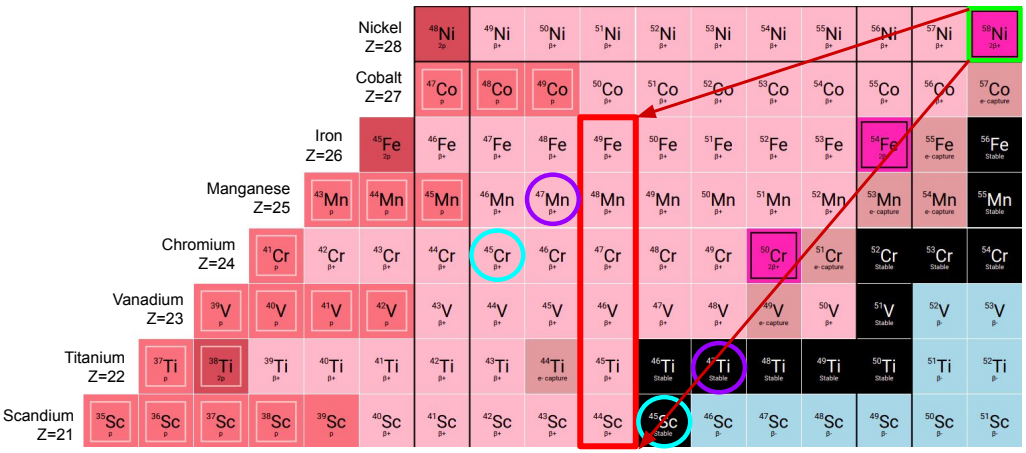

Figure 3.1: The primary ^{58}Ni beam (green) was fragmented by a ^{9}Be primary target to produce a cocktail of ^{49}Fe, ^{48}Mn, ^{47}Cr, ^{46}V, ^{45}Ti and ^{44}Sc isotones (red) at the end of the A1900 separator. The neutron-deficient nuclei, ^{47}Mn (purple circle) and ^{45}Cr (blue circle), are populated via one- and two-neutron knockout reactions from the ^{48}Mn and ^{47}Cr components of the cocktail, respectively. The respective corresponding mirror nuclei, ^{47}Ti (purple circle) and ^{45}Sc (blue circle), are populated via one- and two-proton knockout reactions from the ^{48}V and ^{47}V beams, respectively. Figure adapted from [85].

The $T_z = \pm\frac{3}{2}$ mirror nuclei of interest: ^{47}Ti/^{47}Mn and ^{45}Sc/^{45}Cr were populated via one- and two-nucleon knockout reactions from the ^{48}V/^{48}Mn and ^{47}V/^{47}Cr secondary beams respectively. Emitted γ rays due to de-excitation were detected using the High Purity Germanium (HPGe) tracking detector array GRETINA [86] that surrounds the secondary ^{9}Be reaction target. The reaction products, resulting from reactions in the target, traverse the S800 spectrograph for particle identification through energy loss and time-of-flight measurements. The S800 spectrograph also provides information on the momentum distributions of the residues produced and their velocity vectors, enabling precise Doppler corrections of γ rays on an event-by-event basis. The unknown, proton-rich ^{47}Mn and ^{45}Cr nuclei are explored to identify new excited states since little to no information about these nuclei is previously known. The inclusive and exclusive cross sections are also measured for the $A = 47$ mirror pair to specifically look for the asymmetry observed in Fig. 1.1. Furthermore, the shell-model calculations can be assessed and compared

to experimental data to observe whether nuclei of weakly-bound or unbound nature significantly affect MEDs. Furthermore, the lifetimes of the first $\frac{7}{2}^-$ excited states in the ^{47}Ti/^{47}Mn mirror pair were measured in this work.

This chapter will further detail the function of each of the constituents used for the experimental setup at NSCL. The step-by-step details of how the measurements were taken will also be discussed, starting with primary and secondary beam production, γ-ray detection using the tracking array GRETINA, and the particle identification of key residues of interest.

3.2 SuSI and the Coupled K500/K1200 Cyclotrons

To study a variety of nuclei across the nuclear chart at NSCL, a room-temperature Electron Cyclotron Resonance (ECR) ion source, known as the Superconducting Source for Ions (SuSI), is utilised to produce primary beams ranging from ^{16}O to ^{209}Bi [87], [88]. The ion source is connected to the Coupled Cyclotron Facility (CCF), comprised of the coupled K500 and K1200 cyclotrons [89] as shown in Fig. 3.2.

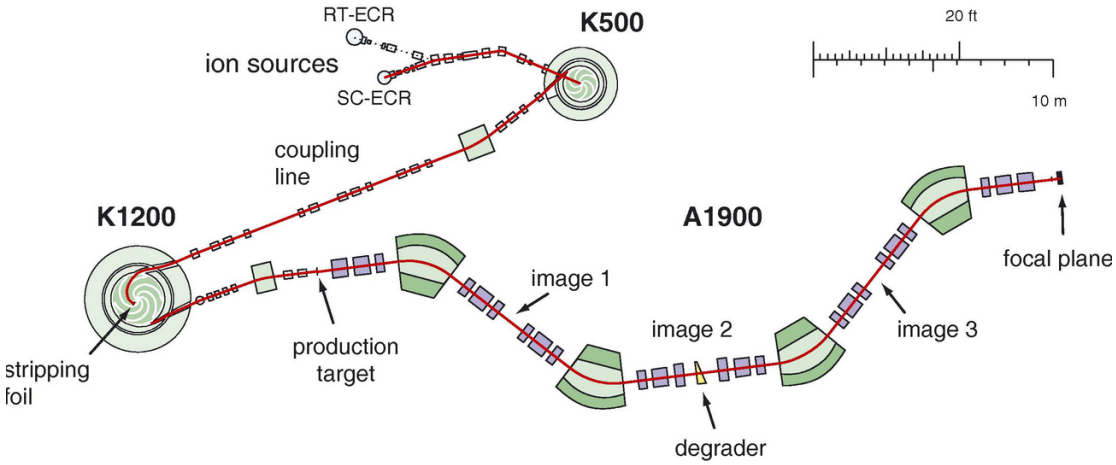

Figure 3.2: A schematic layout of SuSI, the coupled K500 and K1200 cyclotrons and the A1900 separator at NSCL taken from Ref. [83]. The primary ^{58}Ni beam is produced at SuSI (labelled as SC-ECR in diagram), which is accelerated to a final energy of ∼160 MeV/u via the coupled K500 and K1200 cyclotrons. The accelerated ^{58}Ni beam is focused by a quadrupole magnet prior to impinging the 802 mg/cm^2 ^{9}Be target, fragmenting the ^{58}Ni beam. After the fragmentation process, the secondary radioactive-beams are filtered by using a combination of quadrupole magnets, wedges and slits to focus, disperse, block the beams of less interest and to reduce the number of contaminants, respectively, prior to impinging on to the secondary ^{9}Be target, located at image 2.

The first stage of the primary beam production starts with the ECR to produce beams of positive ions, being ^{58}Ni in this experiment. The stable and intense ^{58}Ni beam is then injected into the central region of the K500 cyclotron, where the ions are accelerated to approximately 10% of the speed of light ($\sim$ 8-12 MeV/u). Subsequently, the accelerated beam is extracted from the K500 cyclotron and is injected radially into the K1200 cyclotron, where the remaining electrons are stripped off the ions by a carbon foil located near the centre of the K1200 cyclotron. Further acceleration up to energies of 140-160 MeV/u is achieved once an accelerated orbit has been established. Typically, for ions that have an equal number of neutrons and protons (N$\approx$Z), the acceleration of energies can go up to 200 MeV/u. A combination of quadrupole and sextupole magnets are used to focus the accelerated beam before impinging onto the primary 802 mg/cm^2 ^{9}Be production target, located at the start of the A1900 separator. Here, the primary ^{58}Ni beam is fragmented to produce a large number of lighter secondary radioactive beams. Secondary beams that are not of interest are removed within the A1900 separator, resulting in a cocktail beam of ^{49}Fe, ^{48}Mn, ^{47}Cr, ^{46}V, ^{45}Ti and ^{44}Sc in this experiment.

3.3 A1900 Separator

The purpose of the A1900 high acceptance projectile fragment separator [83], located directly after the production target, is to disperse and separate the vast number of secondary radioactive beams of $A < 58$ and the unreacted ^{58}Ni primary beam that result from the fragmentation reaction that occurs at the ^{9}Be production target [83], [90].

Fragments were separated by using 24 large diameter focusing quadrupole magnets and four large 45° superconducting dipole magnets [83]. The quadrupole magnets, placed in 8 cryostats in the A1900 separator, focus the beam radially when traversing through the separator. Out of the 24 quadrupole magnets used, 16 magnets account for higher-order geometrical and chromatic aberration corrections by having coaxial superconducting hexapole and octopole coils. The dipole magnets separate the secondary beams produced according to the A/Q dispersion ratio within a given plane. As a result, the beams are initially separated by setting the magnetic rigidity (Bρ) of the first two dipole magnets of the separator so that the secondary radioactive beams of interest traverse through the separator. The beam is dispersed initially in accordance with:

$$B\rho = \frac{Mc}{Ze}\beta\gamma \approx \frac{Am_u c}{Ze}\beta\gamma \tag{3.1}$$

where B represents the magnetic field strength of the dipole magnet, ρ is the bending radius of the particle trajectory, M is the mass of the particle of interest, c is the speed of light, e is the electron charge, A and Z are the mass and atomic numbers of the particle, m_u is the unified atomic mass unit and $\beta = v/c$. The equation also incorporates relativistic factors, denoted by $\gamma = \frac{1}{\sqrt{1-\beta^2}}$, as the secondary beams produced typically reach velocities of 0.4c. As the dispersion of the beam is proportional to the A/Q ratio, the Bρ of the dipole magnets can be tuned to a single value so that the maximum amount of the beam of interest, in this case ^{49}Fe, can be focused to pass through the separator. Simultaneously, the contaminants and the unreacted beam are filtered before further separation. The separated beams are then subjected to a set of slits, positioned at image 2 (see Fig. 3.2), that are varied in width to further prevent any unwanted beams or contaminants to pass through the separator after the initial dispersion. The slits also adjust the momentum acceptance of the cocktail beam, being $\pm$0.5% during this experiment.

Further improvements in the isotopic selection are made by passing nuclei through an energy-degrading, 1050 mg/cm^2-thick achromatic aluminium 'wedge' in this experiment. The wedge is constructed so that the nuclei travelling at the same magnetic rigidity, Bρ, but with different Z are produced, resulting in the particles having different momenta [83], i.e. particles with high momentum pass through the bottom of the wedge while those with low momentum pass through the top. Following this filtration procedure, the trajectories of the beams that are passed through allow for easier identification of particles due to energy loss as a result of the A/Q ratios that the nuclei have. The filtered beam is passed through the last two dipoles, which have different Bρ settings compared to the first two dipoles, and a slit to effectively separate the trajectories of the nuclei before the desired cocktail beam of interest strikes the 188 mg/cm^2-thick ^{9}Be secondary target at the S800 target position.

3.3.1 Time of Flight Scintillators

Towards the end of the A1900 separator, the nuclei impinge onto two plastic scintillators: one located at the end of the A1900 separator, the extended focal plane (XFP) scintillator, and

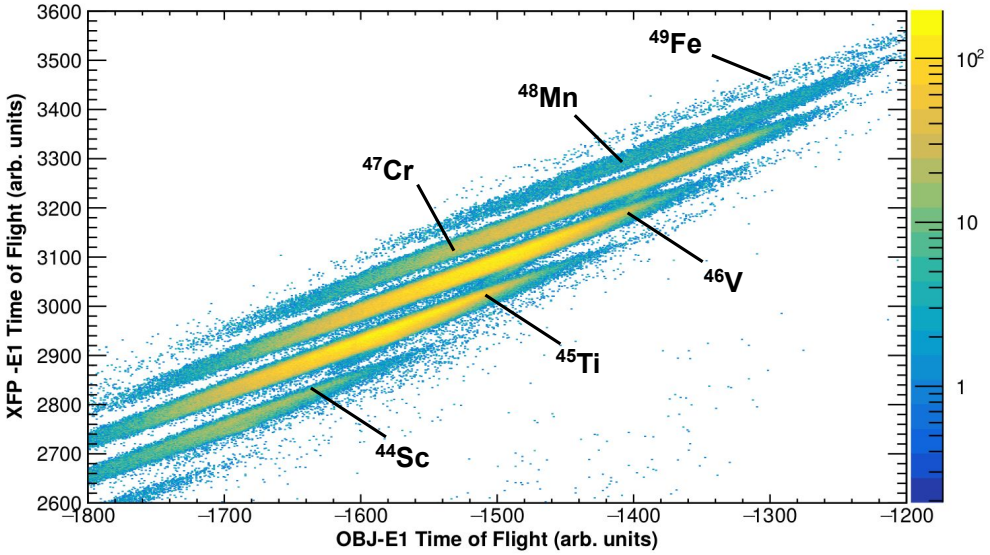

Figure 3.3: The identification of the incoming beams impinging on to the secondary 188 mg/cm^2 ^{9}Be target via the extended focal plane (XFP) and object (OBJ) scintillators relative to the E1 scintillator, located at the focal plane at the end of the S800 spectrograph. An additional γ-ray energy gating has been applied in GRETINA to eliminate contaminants or unreacted beam events. Both ToF values have arbitrary values as positional and angular corrections have been made to identify the secondary beams.

the other in the analysis line of the S800 spectrograph, the object (OBJ) scintillator. Both scintillators are separated by ∼30 m. The scintillators are located before the 188 mg/cm^2-thick secondary ^{9}Be reaction target. When a particle interacts with the XFP and OBJ scintillators, generated light pulses decay at a fast rate, providing exceptional timing resolutions. This makes the use of these scintillators ideal for time of flight (ToF) measurements.

Timing signals having a full-width half-maximum (FWHM) of the order ∼100 ps have been obtained [91], where the scintillators are capable of withstanding rates up to 1 MHz during in-beam experiments [92]. The ToF measurements from the XFP and OBJ scintillators are made with respect to the common S800 trigger provided by the E1 scintillator, located at the end of the S800 spectrograph. This allows for the identification of different incoming beams passing through the A1900 separator (see Fig. 3.3). Subsequently, by gating on a particular incoming secondary beam allows for the corresponding reaction products produced in the S800 spectrograph to be studied. Furthermore, the OBJ-E1 scintillator ToF measurement coupled with the energy-loss measurement from the ionisation chamber (see Section 3.5.3), located in the S800 spectrograph,

allows for the identification of the outgoing residues produced from a specific incoming secondary beam at the reaction target. The analysis process for both secondary beams of interest and final state product identification is detailed in Chapter 4.

Secondary Beam	Z	Fraction of Secondary Cocktail Beam (%)
^{49}**Fe**	26	0.5
^{48}**Mn**	25	5
^{47}**Cr**	24	30
^{46}**V**	23	40
^{45}**Ti**	22	23
^{44}**Sc**	21	3

Table 3.1: The proportion of the cocktail beam at the focal plane of the A1900 separator in the current work.

3.4 GRETINA

The Gamma-Ray Energy Tracking IN-beam Array (GRETINA) - see Fig. 3.4, a High-Purity Germanium (HPGe) detector array, was coupled to the S800 spectrograph to allow for analysis of the γ rays produced from a specific, tagged, outgoing residue of interest.

Figure 3.4: The positions of 7 HPGe modules applied in GRETINA from Ref. [86] being directed at the secondary 188 mg/cm^2 target that is placed within the six-inch diameter beam line. Four of these modules are centered at 58° with respect to the beam axis and the remaining three of these modules are centered around 90°.

In this experiment, GRETINA consisted of 9 detector modules (see Fig. 3.6), four of which were centred at 58^o and five at 90^o with respect to the beam axis, covering laboratory angles between 37^o-115^o. The solid angle coverage of the array is currently at 1π. It is planned to be increased to a full 4π array, named the Gamma Ray Energy Tracking Array (GRETA), to include 30 detector modules [93]. The 1π solid angle coverage is beneficial for beams having velocities of $\beta \geq 0.3$ as the γ rays are forward-focused due to the Lorentz boost [86].

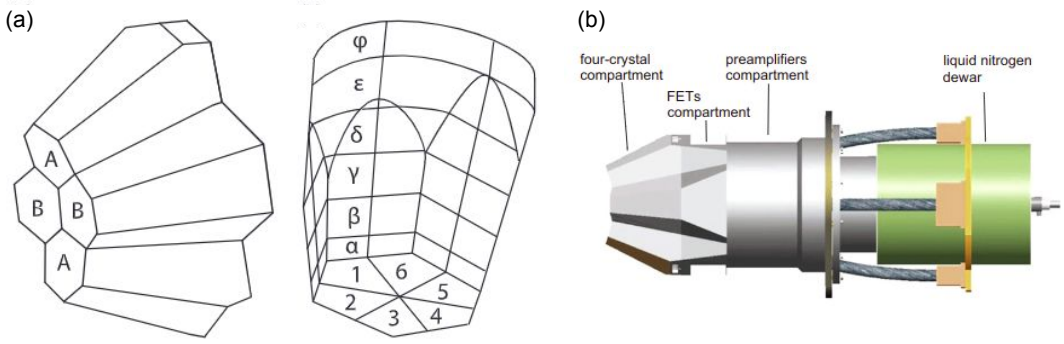

Figure 3.5: (a) Schematic drawing for a GRETINA module (left) and for a crystal (right). Each GRETINA module consists of four crystals where each crystal is equally segmented into six parts at the front tapered face and into a further six rings along the length of the crystal, each consisting of varying thicknesses, creating 36 segments in total for each crystal. (b) Side view of the GRETINA module. Each module consists of having a preamplifier to extract amplified signals from the detector when a γ ray is detected and a liquid nitrogen dewar to limit the effects of thermal excitations across the HPGe crystals. Adapted from [94].

Each detector module is composed of four HPGe crystals where one pair consists of "Type A" geometries and another pair having "Type B" geometries (see left-hand side of Fig. 3.5(a)) [94]. Each crystal is segmented into six equal slices through the depth of the crystal from the front tapered face. The slices are further segmented in the radial direction into six rings from the front to the back of the crystal, comprising of varying distances of 8, 14, 16, 18, 20 and 14 mm, giving 36-fold segments per crystal (see right-hand side of Fig. 3.5(a)). Each segment in the HPGe crystal contains a channel to record the energy deposited. Therefore, for each module consisting of four HPGe crystals, 144 channels are present for all segments. Four other channels are also present, where each channel corresponds to the core signal for each crystal, resulting in a total of 148 channels for each module [94]. Each module consists of a preamplifier and a liquid nitrogen

dewar to reduce thermal excitations in the HPGe crystals within the detector modules.

In this experiment, GRETINA was utilised to detect the emitted de-excitation γ rays from the outgoing residues produced via knockout reactions at the reaction target position. GRETINA exhibits some attractive features for this analysis, such as the position sensitivity, the ability to perform tracking, and γ-ray add-back analysis. Two types of analysis can take place with the GRETINA γ-ray tracking data:

(i) to measure the position and energy of each γ-ray interaction in the detector crystal using Pulse Shape Analysis (PSA).

(ii) using a tracking algorithm to arrange and reconstruct the full-energy γ rays as well as identifying multiple γ-ray paths from each other.

In this work, step (i) was applied in the analysis and is detailed in Section 3.4.1. Despite GRETINA having exceptional γ-ray tracking abilities, method (ii) was disabled due to its negligible benefit, as discussed further in Section 3.4.2. The tracking procedure was replaced with the cluster add-back procedure, detailed in Section 3.4.3, which is typically applied in GRETINA analysis at NSCL [86]. Using this method, the first interaction point is assumed to have the highest energy. Therefore, the combination of determining the precise position and the add-back of γ rays influences the performance of GRETINA, improving its efficiency.

3.4.1 Pulse Shape Analysis

One of the attractive features of GRETINA is the ability to measure the precise position and energy of all γ-ray interactions. A significant development in GRETINA is the signal decomposition in the DAQ firmware, which is done using the GRETINA computer farm (i.e software). The signal decomposition process has a time stamp of 10 ns [86], which allows for sub-segment position sensitivity through the use of a Pulse Shape Analysis (PSA) algorithm [95].

This is achieved by fitting the combined detector response signals against basis signals (a linear combination of simulated response signals) to determine the position of the event with sub-segment precision. The combined detector response signals consist of (a) the digitised signal pulse from each of the segments, giving the co-ordinates of the interaction position, (b) the rise time of the real charge signal, provided by the signals from each segment to obtain the

interaction position, and the whole module to provide the radial distance (r), and (c) the shape and amplitude of the image signal, which provides information on the depth (z) and polar angle (θ) by the superposition of <0.5 µs signals. The basis signals account for the charge carrier mobilities and electronic circuit effects and are simulated throughout the crystal with an average spacing of 1 mm. The closest match between the combined detector response signals and the basis signals provides the reconstructed position of interaction points (x, y, z, E), yielding position resolutions of σ <2 mm to be measured for the position of the first-point interaction of the detected γ rays.

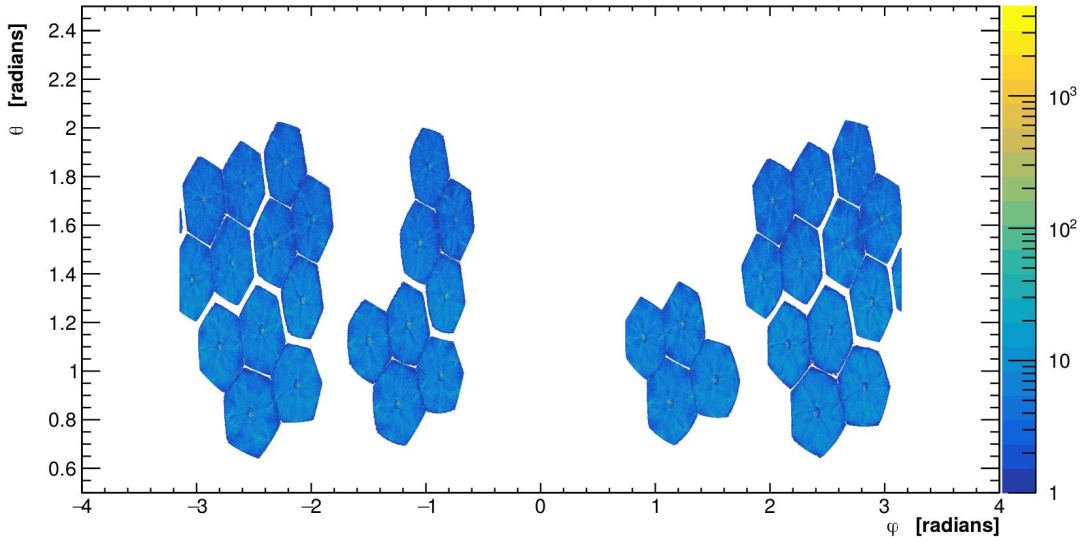

Figure 3.6: The angular coverage of GRETINA taken from the data used in this work, which consists of 36-fold segmented HPGe detectors, where 5 detectors were placed at 58° and four detectors at 90°. The detectors are directed at the reaction target position.

A unique feature of the GRETINA array is that the event-by-event angle of every γ ray emitted from the particles during the knockout reaction can be measured, as shown in Fig. 3.6. Events within the array can be examined, where multiple scattering events occur in the crystals. The spatial coordinates for each γ-ray interaction are recorded for each segment in each detector.

3.4.2 γ-ray Tracking

To reconstruct the path of the scattered photons in a given event using γ-ray tracking, the likelihood of the interaction points from a single γ ray must be defined using a tracking algorithm [96]. Using this algorithm helps to distinguish if the recorded energies of the detected γ rays originate from real Compton-scattering sequences or a single γ ray. The Compton-scattering equation is utilised for all possible Compton-scattering events within the crystals in GRETINA as shown:

$$E_{\gamma}^{'} = \frac{0.511}{1 + \frac{0.511}{E_{\gamma}} - \cos\left(\theta_{c}\right)}, \tag{3.2}$$

where $E_{\gamma}^{'}$ and E_{γ} are the energies of the scattered and unscattered γ rays in MeV, respectively, and θ_{c} represents the polar angle of scattered event. The difference between the measured angle of all of the possible Compton-scattered interaction sequences and the expected angle obtained from Eq. 3.2 can be calculated, resulting in each interaction point to be assigned a value known a Figure-of-Merit (FoM) from [86]:

$$FoM = \sum \frac{\left(\cos\left(\theta_{en}^{i}\right) - \cos\left(\theta_{vec}^{i}\right)\right)^{2}}{w_{i}}, \tag{3.3}$$

where $\cos\left(\theta_{en}\right)$ is the angle obtained through energy deposition at the interaction points using Eq. 3.2, $\cos\left(\theta_{vec}\right)$ is the geometric angle which utilises the position co-ordinates of the interaction points for a given event, w_{i} is a weighting factor that is chosen based on the number of interactions in a sequence. In theory, a good agreement between the measured scattering angles for multiple events and the expected scattering angles derived from the Compton-scattering equation will yield an FoM value $\sim$0 as the $\left(\cos\left(\theta_{en}^{i}\right) - \cos\left(\theta_{vec}^{i}\right)\right)$ term will become negligible. This is possible if events with full energy deposition and "perfect" position and energy resolutions are achieved. In reality, the reconstruction of the the energy and position measurements of the interactions will have a resolution that is non-zero and therefore, all reconstructions will have a value of FoM being $>$0. Once all possible scattering permutations have been examined, the sequence containing the lowest value of the FoM is considered the most likely scattering sequence that is compatible with the Compton-scattering process. This value is used for Doppler-shift corrections to calculate the observation angle in Eq. 4.4 by using the first interaction point of the detected γ ray. For all partial absorption events or incorrect clustering, a FoM value > 1 is obtained, and

for events where photoelectric effects are dominant, the FoM value will become 0.

For intermediate energies used at NSCL, it was found that using the highest energy deposition point for Doppler reconstruction resulted in improved peak shapes and smaller full-width half-maximum values (i.e. improved peak to background ratios) for γ-ray energies ranging from 275 keV (^{19}Ne) to 6.1 MeV (^{16}O) [86]. Therefore, the highest detected energy in each crystal in GRETINA was assumed to be the first interaction point to perform γ-ray Doppler corrections.

3.4.3 Add-back procedures of γ rays

Another key feature of GRETINA is the ability to perform add-back, which accounts for events that scatter between the neighbouring crystals to reconstruct the total energy. By assuming one γ rays per crystal, a γ ray may scatter between many neighbouring crystals, causing a distribution in the total energy. This effect can be accounted for within a detector module through add-back. The add-back process utilises algorithms that identify Compton scattered events across all the crystals. All of the γ-ray interactions across the neighbouring crystals are summed to provide the initial energy of the γ ray prior to Compton scattering. Therefore, the Compton background is significantly reduced. Three different add-back methods can be utilised in GRETINA:

- **Nearest-Neighbour**: The detected hits are added if the events occur in two neighbouring crystals that share a common boundary, regardless of whether they are neighbouring crystals within the same module or in adjacent modules.
- **Calorimeter**: All of the detected γ ray hits throughout the whole detector are summed within a given time frame.
- **Cluster**: γ-ray events are summed if they occur within neighbouring detectors in a given cone of a defined opening angle (typically 10-20°).

The neighbour and cluster add-back methods, traditionally used in GRETINA add-back analysis, have been compared to the singles spectrum for the ^{152}Eu stationary calibration source in Fig. 3.7. From Fig. 3.7, add-back effects are notable at low energies due to the vast reduction in the Compton-scattering events compared to high energy transitions. Despite that the nearest-neighbour add-back method was found to improve the peak-to-total ratios, a significant number

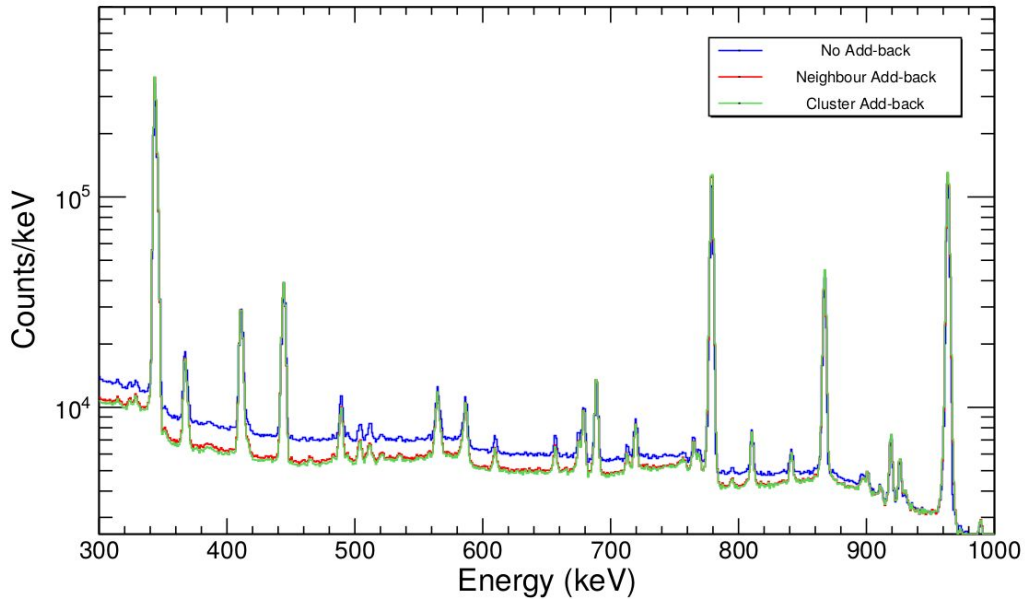

Figure 3.7: The comparison of the no add-back (blue) spectrum to the neighbour (red) and 20° cluster (green) add-back procedures for the stationary ^{152}Eu calibration source. The emitted γ rays were detected at the start of the experiment.

of γ-ray events were incorrectly summed. Therefore, the cluster add-back procedure was implemented in this work due to low statistics. In the case of ^{45}Cr, it was important to maximise the statistics to perform γ-γ coincidence analysis to construct level schemes. Hence, the cluster add-back procedure was applied using the optimum opening angles of 15° for ^{47}Ti, and 20° for ^{47}Mn, ^{45}Cr and ^{45}Sc to prevent accidental addition of γ-ray events and to maximise the number of events detected in the neighbouring crystals within the defined cone. The optimum angles were determined by systematically varying the size of the cone within the GrROOT framework.

3.4.4 Absolute Efficiency Measurements of GRETINA

The absolute efficiency of GRETINA was calculated to measure the γ-ray efficiency for each detector ring using stationary source runs of ^{152}Eu, ^{133}Ba and ^{56}Co [97]–[99], where the activities of these sources are known. The efficiency of GRETINA was calculated using two modes: the no add-back mode (i.e. the single crystal mode) and the add-back mode. When no add-back is used, the detection of two γ rays in two separate crystals are treated as two individual detectors, leading to the energy in each crystal being measured. Conversely, the add-back mode considers a signal

in each detector, where one γ ray hits a crystal and scatters into a neighbouring crystal. The signals are added together depending on the add-back method used (see Section 3.4.3). In this thesis, the absolute efficiency was measured using the no add-back mode to determine the relative intensities of the observed transitions and the exclusive cross sections of the observed states in our nuclei of interest: ^{47}Mn/^{47}Ti and ^{45}Cr/^{47}Sc. This method was chosen as the add-back mode cannot accurately determine the efficiency due to its dependence on reaction multiplicity, either from nuclei with large chains of multiple γ rays or the effect of Bremsstrahlung radiation when the beam is used.

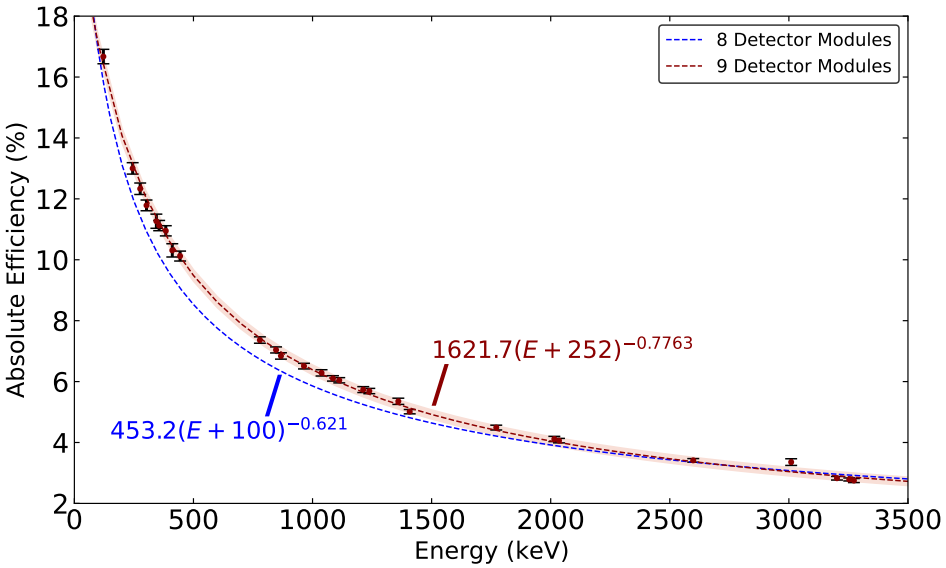

Figure 3.8: The fits of the singles absolute efficiency of GRETINA in the 8 (blue) [86] and 9 (red) module configuration without add-back.

Absolute efficiencies of 6.08(4)%, 5.49(5)%, 5.07(5)% and 4.06(3)% for γ rays of 898, 1173, 1332, and 1836 keV, respectively, have been reported using 32 crystals (i.e an eight-module configuration of GRETINA) [86]. With the nine-module configuration used in this work, an increase in the measured efficiencies was seen, especially at low energies using no add-back (see Fig. 3.8).

The absolute efficiency, ϵ_{abs}, was found by using the γ-ray singles spectra for the ^{152}Eu, ^{133}Ba

and ^{56}Co sources, which have documented relative intensities [97]–[99] by:

$$\epsilon_{abs} = \frac{N}{A \times t_{dead} \times B \times t_{run}}, \tag{3.4}$$

where N is the number of γ rays detected for a particular decay, A is the activity of the source at the time of measurement, t_{dead} is the dead time of the run (the ratio of t_{live} and t_{raw}), B is the branching ratio of the decay and t_{run} is the duration of the run. The dead time was determined by taking the recorded scaler data throughout the experiment. The activities of the sources at the time the measurements took place were calculated by using the known activities at the time of source production, A_o, the mean lifetime of the source, τ, and the time elapsed between source production and the time the measurement was taken. Each value of ϵ_{abs} for each decay has an error, derived by taking into account N, A, B and t_{run} in quadrature.

The systematic error in A was determined to be 1.4% of the measured activity in accordance with Ref. [86], and the error in the run time was assumed to be two seconds due to reaction time. The error in t_{dead} was considered to be negligible due to the accurate measurements made in the scalar data.

The absolute efficiency curves of the cluster and the no add-back methods are shown in Fig. 3.9. The error in the no add-back efficiency fit for 9 modules, highlighted by the red band in the top panel of Fig. 3.9 (also shown in Fig. 3.8), arises from the systematic error due to the activity, A, at the measured time and the residuum systematic error of an absolute error of 0.1%, shown by the red band in the bottom panel of Fig. 3.9. The latter was determined using the standard deviation of the residuals (i.e. the difference between the recorded data point at a given energy and its corresponding efficiency from the fit), assuming that the distribution is centred at 0. The residuals are shown in the bottom panel of Fig. 3.9. The systematic uncertainties in activity and the residuum were added in quadrature with the statistical errors.

When no add-back is applied, the photo-peak efficiency becomes small at higher energies. In this region, the effect of Compton scattering becomes dominant at $E_\gamma \sim 2$ MeV compared to the photoelectric effect, which becomes significant at lower energies. This results in a longer scattering path of the higher energy γ rays. The absolute efficiency was found to be enhanced at high energies following the implementation of the cluster add-back procedure, illustrated by the

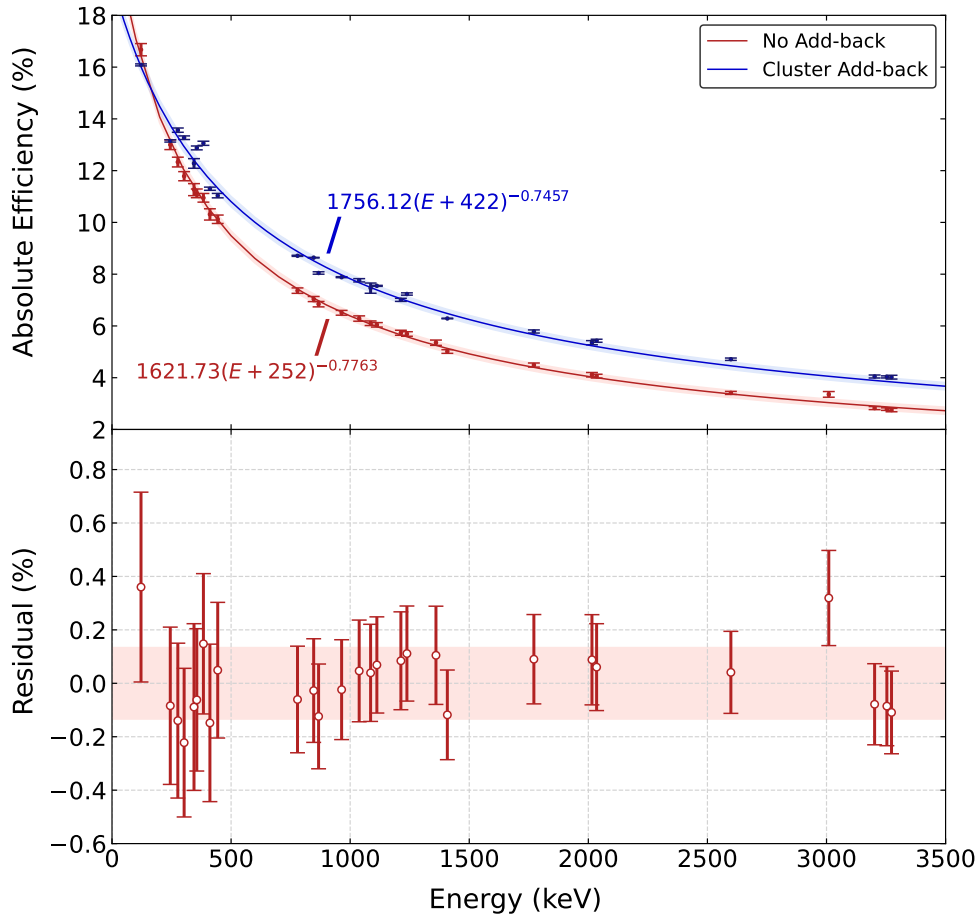

Figure 3.9: The fits of the singles absolute efficiency of GRETINA in the 9 module configuration without add-back (red) and with the cluster add-back (blue). The respective red and blue bands represent the error in the fits. The bottom panel shows the deviation between the measured absolute efficiencies and the estimation from the fitting curve when no add-back was applied to determine the residuum systematic error. The red band in the bottom panel represents the absolute error in the residuum systematic error, being 0.1%.

blue line in Fig. 3.9. It is important to note that the cluster add-back procedure was not used in this analysis.

The Lorentz boost becomes significant as relative recoil velocities of $\beta \sim 0.4$ were used in this work, which affects the measured in-beam efficiencies. At these velocities, in the frame of reference of the moving particle, the detector angles become greater in the backward direction. Therefore, the detectors in the forward direction appear to grow in size while the size of the backward detectors shrink. This effect is known as the '*headlight effect*', where the γ rays appear

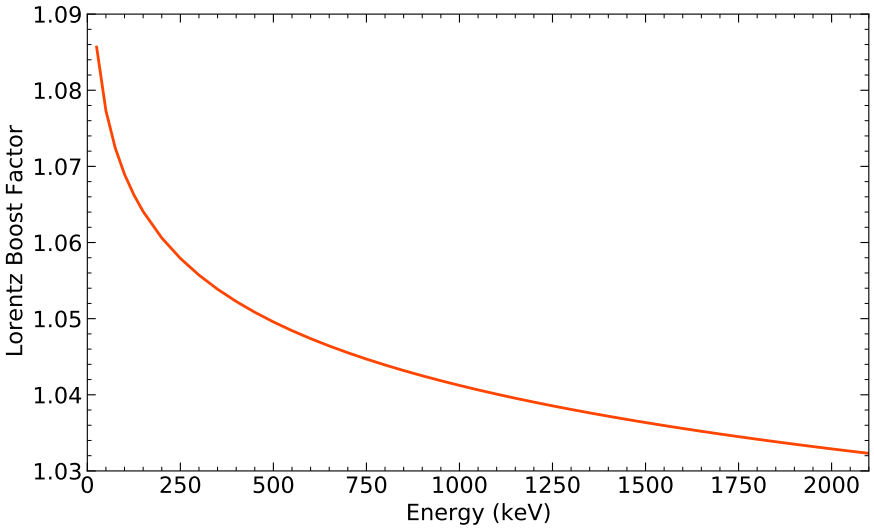

Figure 3.10: The scaling factor by which the absolute efficiency is increased by as a result of the Lorentz boost at β ~0.4 using a 9 module configuration with GRETINA. The factor was determined by comparing the simulated efficiencies at energies between 0-2 MeV for a stationary and an in-beam source.

to be focused forwards when observed in the lab. To account for the Lorentz boost, decays were simulated across an energy range of 0-2 MeV for both the stationary and in-beam γ-ray source using GRETINA within the GEANT4 simulation framework [100]. The ratio between the simulated stationary and in-beam efficiencies at β =0.4 can be obtained (see Fig. 3.10) to correct the absolute efficiencies to include the Lorentz-boost corrected factors.

3.5 S800 spectrograph

Once the secondary beam impinges on the reaction target to undergo nucleon knockout reactions, the resulting projectile-like residues traverse the S800 spectrograph. The S800 is a vertical magnetic spectrograph that has the capability of rotating in the horizontal plane between 0°-60°, covering a solid angle of 20 msr, and a momentum acceptance of 5% [84], [101]. By coupling the S800 spectrograph with the recorded information of the γ rays detected by GRETINA, at the reaction target position, allows for the unique identification of the exotic species produced.

The exotic nuclei that are produced at the reaction target traverse through the S800 analysis line, which contains two magnetic quadrupole magnets, a sextupole magnet and two 75^o-bend

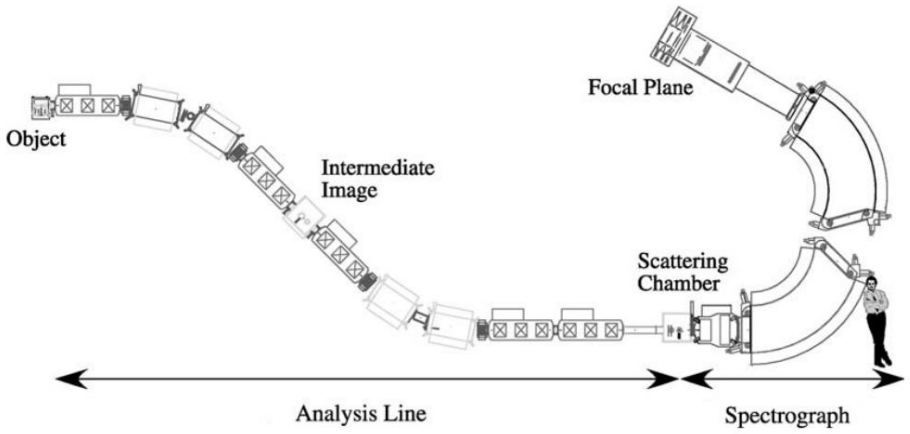

Figure 3.11: The overview of the S800 spectrograph located downstream of the A1900 separator. The secondary ^{9}Be target is located at the target position of the S800 spectrograph and is surrounded by the HPGe array, GRETINA, to detect the resulting γ rays. The OBJ (Object) scintillator is located at the start of the S800 analysis line and the XFP scintillator is located 8m upstream. Two dipole magnets are positioned upstream of the target position to focus the reaction products. The nuclei then traverse through the focal plane, consisting of the CRDCs, ionisation chamber and the E1, 2 and 3 scintillators. Image taken from [84].

superconducting dipole magnets. The maximum rigidity, Bρ, that can be reached in the dipole magnets is 4 Tm [101]. The S800 spectrograph is equipped with a range of tracking, energy loss and timing detectors that are positioned at the focal plane as seen in Figs. 3.11 and 3.12. Before entering the S800 spectrograph, the two quadrupole magnets focus the outgoing nuclei that were produced at the target. The focusing is achieved in the non-dispersive (y) plane first and then in the dispersive (x) plane to increase the acceptance of the spectrograph. Towards the end of the second quadrupole magnet, a sextupole magnet is positioned to correct any additional aberrations and to reduce the broadening of the outgoing beam at the focal plane. The two 75^{o}-bend superconducting dipole magnets are utilised to disperse the outgoing nuclei in A/Q at the focal plane [84]. Here, unreacted secondary beams are filtered out using a beam blocker to prevent the increase in the rate of the focal plane detectors. The focal plane detectors, located immediately after the magnets, consist of two position-sensitive Cathode-Readout-Drift-Chambers (CRDCs) followed by a multi-segmented ion chamber and three large plastic scintillators (see Fig. 3.12).

Beam recoil angles and positions in the dispersive (x) and non-dispersive (y) directions of the nuclei produced are provided using the CRDCs, located within the focal plane of the S800

spectrograph (see section 3.5.1 for details). The combination of energy-loss measurements from the ionisation chamber and ToF measurements, obtained from the OBJ scintillator in reference to the E1 scintillator, allow for particles to be identified. The trajectory of the nuclei can be tracked back to the target by using an inverse map (see section 3.5.2 for further details), assuming that the nuclei traverse along the central axis of target. This enables the velocity vector at the target position to be determined for the purpose of Doppler corrections. The E1 scintillator is utilised as the global and timing trigger reference in the Data Acquisition (DAQ) system.

Depending on the experiment, the S800 analysis line can operate in two modes; a 'dispersion matching mode' and a commonly used 'focus mode' [84]. The 'dispersion matching' mode uses an achromatic beam that is momentum-dispersed at the reaction target to 10 cm/%, resulting in the momentum acceptance being limited to ±0.5% and a maximum resolution of 0.02% for a 1 mm beam spot [84]. Using this mode provides the highest possible resolution at the focal plane, which is beneficial for momentum distribution measurements. The 'focus' mode also uses an achromatic beam that is focused on the target, and the focal plane displays the width of the beam folded with the momentum change that occurs within the target. This mode provides the largest momentum acceptance up to ±2%, which is comparable to the A1900 separator. Since precise momentum acceptances are not required, the energy resolution becomes limited to ∼0.1%.

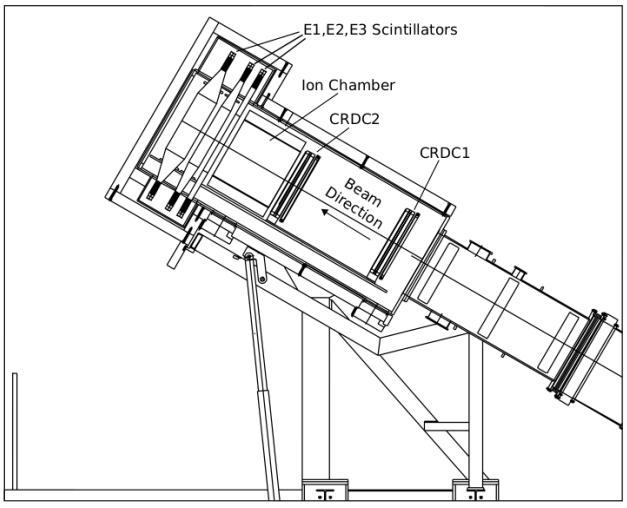

Figure 3.12: The schematic layout of the focal plane of the S800 spectrograph. The positions of the focal plane detectors; CRDCs, ionisation chamber and the E1, 2 and 3 scintillators, are shown.

As a result, this method is utilised to conduct γ-ray spectroscopy and particle identification. In this experiment, the 'focus' mode was applied to the S800 analysis line.

3.5.1 Function of the Cathode Readout Drift Chambers

The S800 spectrograph comprises of two Cathode Readout Drift Chambers (CRDCs) that determine the position and the angle of the isotopes detected in the focal plane. The two CRDCs are positioned 1.073 m apart, with an active depth of 1.5 cm and an active area of 26 cm $\times$ 56 cm in the non-dispersive (y) and dispersive (x) directions, respectively. The CRDCs are also filled with gas consisting of 80% CF_4 and 20% C_4H_{10} at 140 Torr.

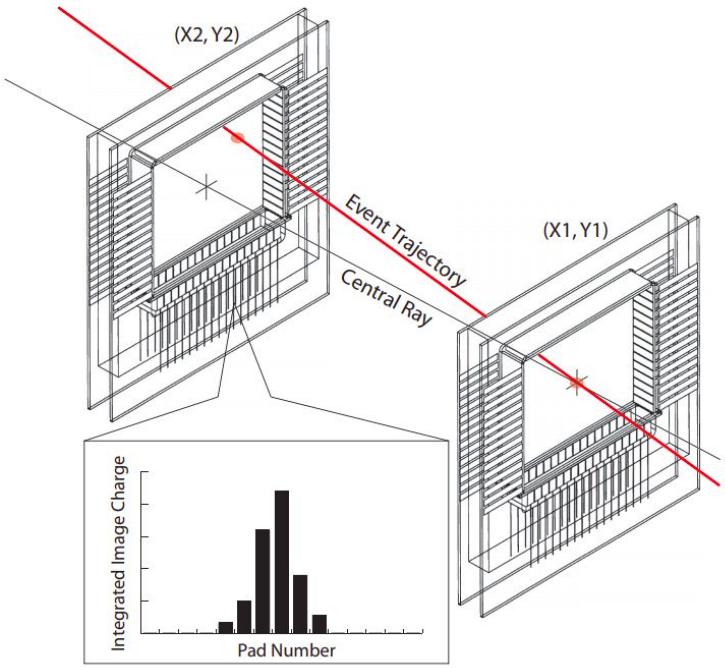

Figure 3.13: A schematic view of the CRDCs located downstream of the second dipole magnet in the S800 spectrograph. As nuclei pass through the CRDCs, gas particles become ionised, producing free electrons that drift towards the anode wire. A positive charge is consequently obtained in each of the pads where the x-position of where the charge was detected is determined by fitting a Gaussian function (see insert). The y-position is found by observing the drift time for the electrons to travel to the anode wire in relation to the E1 scintillator located at the end of the S800 focal plane. Image taken from [102].

Since the nuclei produced at the reaction target pass through the CRDCs, the nuclei ionise the mixture of gas producing electrons and ions. The free electrons are detected at an anode

wire, placed under the influence of an electric field where charge is collected. Subsequently, a positive charge is induced across the 2.54 mm wide cathode pads. The position at which the ionisation occurs, in the dispersive plane (x-position), can be determined by utilising a Gaussian fit on the charge distribution across each cathode pad (see Fig. 3.13). In the non-dispersive plane (y-position), the ionisation position is deduced by recording the drift time of the free electrons to the anode wire by utilising the trigger signal from the E1 scintillator, which is typically between 0-20 μs. Each CRDC has a spatial resolution of better than 0.5 cm and is limited to a rate of 5000 counts per second due to relatively long drift times. The rate is limited to minimise efficiency losses [92].

The x- and y-positions from the CRDCs allow for the trajectory of the nuclei of interest and the particle trajectory recoil angles to be reconstructed at the S800 focal plane in the dispersive (x) and non-dispersive (y) planes, respectively, by using an inverse map. For example, the angle in the dispersive plane (a_{fp}) in each of the CRDCs is calculated by:

$$a_{fp} = \tan^{-1}\left(\frac{x_2 - x_1}{d}\right), \tag{3.5}$$

where x_1 and x_2 are the recorded x-positions at the first and second CRDC, respectively, and d corresponds to the separation between the CRDCs being 1.073 m. This reconstruction process using the inverse map allows for precise Doppler corrections to be taken place.

3.5.2 Reconstruction of the Particle Trajectory

The S800 spectrograph is susceptible to high-order aberrations in the magnetic field due to having a large acceptance, which affects the position resolution of the spectrograph [103]. Usually, these aberrations can be partially corrected through the use of higher-order magnets. However, these corrections become challenging at larger acceptances. Therefore, high acceptances and resolutions are achieved by using additional information of a given particle to reconstruct its whole trajectory from the target position to the E1 scintillator. This additional information is obtained using the ion optics code, COSY INFINITY [104], where a transfer matrix map, **S**, is calculated [103]. The transfer matrix map is produced using the x and y positions recorded at each CRDC, the angular information recorded at the S800 focal plane and the precisely measured $B\rho$ of the two dipole magnets located at the entrance of the S800 spectrograph. The

beam properties of a particle at the target position is determined by using a tracking algorithm to invert the matrix map, **S**, prior to its application to the angular and positional coordinates measured at the focal plane on an event-by-event basis, represented as $\mathbf{S}^{-1}$:

$$\begin{pmatrix} a_{ta} \\ y_{ta} \\ b_{ta} \\ d_{ta} \end{pmatrix} = \mathbf{S}^{-1} \begin{pmatrix} x_{fp} \\ a_{fp} \\ y_{fp} \\ b_{fp} \end{pmatrix}, \tag{3.6}$$

where a and b are the dispersive and non-dispersive angles, respectively, y is the position of the particle in the non-dispersive direction, x is the position of the particle in the dispersive direction, and d ($=\delta T/T$) is the momentum spread of the beam (measured in terms of energy) at the target position, denoted by the subscript ta. The subscript fp distinguishes the a and b angles and the x and y positions at the S800 focal plane. As the energy coordinate at the target position is deduced from the inverse map, the dispersive x-position (x_{ta}) cannot be calculated and is assumed to be 0. The uncertainty of this parameter is included within the energy resolution of the S800 spectrograph.

The inverse map can be produced via the MSU map server [105] using the supplied excitation currents of the two dipole and quadrupole magnets in the spectrograph at the time of the experiment, the mass, A, and the charge, Q, of the particle of interest. In this analysis, the inverse map is incorporated into each of the runs produced in the experiment to reconstruct the recoil angles and positions on an event-by-event basis, enabling precise event-by-event Doppler corrections. The inverse map is calculated to order five, which provides the positional and angular precision to be comparable to 0.5 mm and 2 mrad, respectively [84]. A new inverse map is required for each nucleus of interest as the path traversed through the two dipole magnets is dependent on the particle's mass and charge. Furthermore, if the Bρ settings of the two dipole magnets have also changed during the experiment, a new inverse map must be generated to reconstruct the path from the target position to the E1 scintillator.

3.5.3 Ionisation Chamber

After the detection of charge in the CRDCs, the nuclei of interest will be passed through the ionisation chamber, located downstream of the S800 spectrograph and after the second CRDC (see Fig. 3.12)

The ionisation chamber identifies the fragmented beams produced at the secondary ^{9}Be target, in terms of the atomic number, Z, through energy-loss measurements. This information is utilised to plot a Particle Identification (PID) plot, shown in Chapter 4.5, where a specific outgoing nucleus can be selected, by a software gate, from a given secondary beam that has impinged with the reaction target. The ionisation chamber has an active area of 30 cm $\times$ 60 cm with a depth of 406 mm, which is filled with P10 gas, consisting of 10% methane and 90% argon at a pressure of 300 Torr [91]. The pressure within the ionisation chamber can be varied up to 600 Torr for light nuclei. The chamber is split into 16 segments, each having a narrow anode-cathode gap that is positioned orthogonal to the beam direction. An advantage of a segmented ionisation chamber allows for the electrons and the positive ions to be collected at short distances, reducing pile-up and noise reduction [102]. The isotopes, produced from the fragmented beams, ionise the P10 gas to produce free electron and positive ion pairs that drift to the closest anode and cathode, respectively. Each segment produces signals that are summed to provide the total energy loss of a particular particle passing through the chamber.

The average energy loss across the length of the ionisation chamber can be determined using the Bethe-Block equation (Eq. 3.7), which is proportional to the Z^2 of the particle:

$$-\left\langle \frac{dE}{dx} \right\rangle = \frac{4\pi n Z^2 M}{m_e c^2 E}\left(\frac{e^2}{4\pi\epsilon_0}\right)^2\left[\ln\frac{2m_e c^2\beta^2}{I(1-\beta^2)} - \beta^2\right], \tag{3.7}$$

where Z is the proton number of the nuclei of interest, m_e is the mass of the electron, c is the speed of light, $\beta = \frac{v}{c}$, e is the charge of the electron, ϵ_0 is the permittivity of a vacuum, n is the electron number density and I is the mean excitation energy of the material that the chambers are made out of, being the P10 gas.

The energy loss of a particle travelling through the ionisation chamber is dependent on the path length due to the degree of dispersion of the particles by the two dipole magnets located at the entrance of the spectrograph. Therefore, particles with different A/Q values and momenta

will also have different trajectories. Additional corrections of the energy loss within the ionisation chamber that account for the path length can be applied using the information provided from both of the Cathode Ray Drift Chambers (CRDC) (see Chapter 4.4 for further details).

3.5.4 Scintillation Detectors

Immediately downstream of the ionisation chamber, three plastic scintillators (E1, E2 and E3) are present of a thickness 5 cm, 10 cm and 20 cm, respectively [91]. The active area of the scintillators covers the same active area of the CRDC detectors. The charged particles traverse through the detector material and generate light (via scintillation) that is collected by the PhotoMultiplier Tubes (PMTs). The PMTs are connected on the top and bottom sides of the plastic scintillators that convert the light signals to electrical signals. The scintillators are coupled closely with the ionisation chamber to provide information on the timing, calculated by utilising the average time signal from each of the PMTs used. Since the charged particles are stopped within the scintillator material, energy loss and total energy loss measurements can be performed for the incoming particles.

The E1 scintillator defines the valid trigger in the S800 spectrograph, resulting in all timing signals of the scintillators and the drift times in the two CRDCs to be measured relative to the E1 scintillator signal. The E1 scintillator is used for all the ToF signals.

The maximum rate that the scintillators can withstand is 1 MHz. However, the timing resolution of these detectors can reduce at higher rates due to the different path lengths traversed by the nuclei. This effect can be corrected by tracking the event-by-event position on the scintillator using the position and angle information obtained from the CRDC detectors (see Section 3.5.2 for further details).

3.6 Data Acquisition System

The data acquisition (DAQ) of GRETINA and the S800 spectrograph is based on an event-by-event readout system. With GRETINA, events are individually converted once each digitiser channel is triggered, simultaneously assigning a time stamp of 10 ns granularity [86]. The events are then stored locally. The triggers are reported to the GRETINA Trigger Timing and Control

logic, where the locally-stored events, that satisfy a certain global trigger condition, are delivered to a global trigger through a time-stamp comparison in a process called *'event validation'*. A locally-stored event is excluded if no matching validation has been issued within a given expiration window [86]. A raw event within a detector crystal is comprised of digital signals that operate at a sampling rate of 100 MHz. The raw events from the crystals are collected by the global trigger and are transferred to the GRETINA computer farm for signal decomposition, which provides the sub-segment position and energy deposition of the γ rays detected (see Section 3.4.2).

The event readout is initiated by the master trigger signal in the S800 spectrograph, which converts all of the analogue detector signals to digital converters (ADC). The readout process takes $\sim$120-200 µs due to its dependence on the number of fired detector channels. When coupling the S800 and GRETINA DAQ systems, the time stamp counters are set to 0, allowing for coincidence correlations of S800-GRETINA events to take place through time-stamp comparison. Although the S800 focal plane detectors can withstand rates up to 6-10 kHz, the master-trigger rate is limited to $<$1.5 kHz due to deadtime. Therefore, the GRETINA-S800 coincidences are formed using the fast trigger output from the GRETINA Trigger Timing and Control logic in the S800 trigger logic, reducing the master trigger rate in the S800 DAQ system. Events measured by the S800 DAQ system are passed on the GRETINA event builder process where they are merged and stored for data analysis.

3.6.1 Trigger Types

As the GRETINA and S800 DAQ systems were combined in this experiment, two types of raw triggers that are required; (i) S800 single-particle events, where the E1 scintillator has fired but GRETINA has not, and (ii) COINC events, where a coincidence between the S800 and GRETINA is detected. These two types of triggers are generated for each event. The former is required to calculate the knockout cross sections, while the latter is needed to measure the detected γ rays. Data events for both types of trigger are written to disk. However, due to high beam rates, not all S800 events can be recorded. Therefore, a downscaler (DS) is applied to reduce the number of events recorded from the S800-only triggers. For a $DS > 1$, three types of events are written to disk:

(a) S800 only events,

(b) COINC only events,

(c) Events that contain both the S800 and COINC events.

where all three combinations (a-c) of trigger will exist, and the S800-only events become downscaled. When the downscalar is not applied to the data, then only two types of event will be observed (i.e (a) the S800 only and (c) S800 and COINC triggers).

Since both triggers, S800 and GRETINA, play a notable role in this experiment, it is necessary that both triggers need to be analysed. This is because the identification of the type of event is important to determine the mirrored knockout inclusive and exclusive cross sections in our nuclei of interest; ^{47}Ti/^{47}Mn.

Chapter 4

Calibrations and Analysis Techniques

Prior to the analysis of the data, the raw data taken at NSCL has to be unpacked and calibrated using the GROOT software package [106], which is based on the ROOT framework [107]. The raw files produced during the experiment at NSCL were converted into ROOT format objects using GROOT. The data that is originally stored as ROOT 'trees' are separated to study the correlated recorded values on an event-by-event basis.

The calibration procedures will be discussed in this chapter, where the measurements taken by the A1900 separator, GRETINA and the S800 spectrometer components are corrected for increased precision. The extracted parameters for the relevant calibration stages were applied to the experimental data using a settings file, which inputs these parameters on a run-by-run basis at the unpacking stage of the raw files.

4.1 Time-Shift Corrections

The time-of-flight (ToF) of the secondary beams traversing through the A1900 separator were measured using the object (OBJ) and extended focal place (XFP) scintillators relative to the E1 scintillator, where the latter is located at the end of the S800 spectrograph. During the experiment, a time shift of ∼40 ns was found for 14 out of the total 113 runs taken. To correct these time shifts, the data was shifted to long experimental run consisting of a high statistics (i.e. run 29). The incoming beam plot, corrected for these time shifts, is shown in Fig. 4.9.

4.2 Ion Chamber Calibrations

4.2.1 Gain Matching of Segments

Since the ionisation chamber (IC) consists of 16 segments, a gain-matching approach was employed as the first step in the calibration procedure. As mentioned in Section 3.5.3, the energy loss in the IC provides information of the atomic number, Z, of the residues produced. By combining the obtained energy loss with the information of the ToF, allows for the reaction products to be identified. For a given particle, the energy loss measured in each of the 16 segments of the IC is averaged. This gives an average energy loss, which is utilised to identify nuclei of different Z. As a result of different gains, the average energy loss in each segment will differ from one segment to the next. Therefore, it is imperative that the gains in each segment are matched so that the same energy loss signal is measured for the same event.

In order to apply the gain matching procedure, a segment within the IC was chosen as the reference segment to which the other channels will be matched to. In this case, segment 0 was chosen as the reference segment. Prior to the gain matching stage, gates were created from the PID plot for an incoming secondary beam and four outgoing recoils with high statistics to decrease statistical uncertainties. After this step, the energy loss distributions were recorded in each segment by fitting a Gaussian function for each gated outgoing recoils to determine the centroids and the amplitudes. The gains and offsets (i.e. the parameters required for the calibration) were determined by comparing the centroids and the amplitudes from the Gaussian distributions for each channel in the IC for each nuclei to the measurements obtained from the reference channel, being channel 0 in this case. The total energy loss, dE, of a particle traversing though the IC detectors is established by collecting the energy loss signals in each segment. The comparison of the 16 segments before and after the calibration parameters have been applied is shown in Fig. 4.1, where Fig. 4.1(b) shows consistent energy losses across all channels.

The PID spectra before and after the application of this calibration is demonstrated in Fig. 4.2. A sharper Z-resolution is observed.

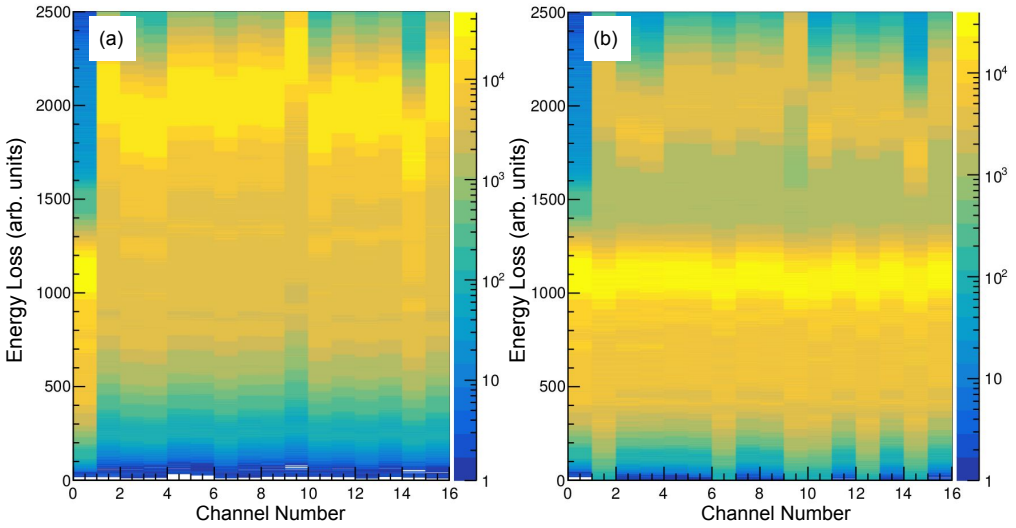

Figure 4.1: The plot of the 16 segments in the IC, gated on the incoming ^{47}Cr beam and a high statistic outgoing particle, showing (a) before and (b) after the correction parameters have been applied. Channel 0 was used as the reference channel to reduce overestimation in the gains and offsets produced.

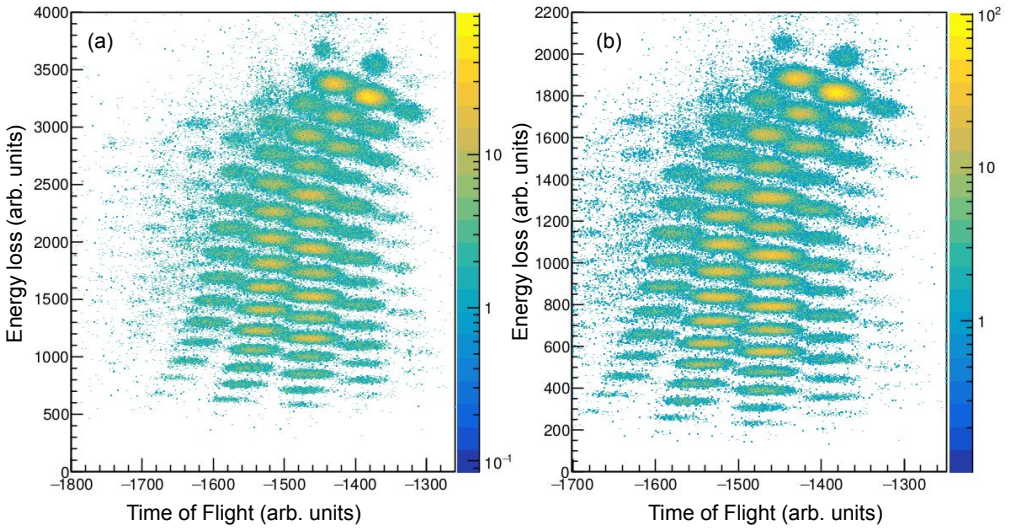

Figure 4.2: The PID plots of the energy loss in the IC as a function of the measured ToF between the OBJ and E1 scintillator, positioned at the end of the S800 spectrograph. The PID spectra were produced by looking at the incoming ^{47}Cr beam (a) before and (b) after the IC calibrations have been applied.

4.2.2 Ionisation Chamber Positional Corrections

An additional correction is required for the measurements of the energy loss within the IC. This correction accounts for the longer or shorter path lengths taken through the chamber depending on the particle trajectory, which can significantly affect the PID spectrum produced. Different positions of the beam in the IC correspond to different angles, resulting in a variety of energy loss measurements that will need to be corrected. The energy loss measured in each of the 16 segments of the ionisation chamber can be corrected by adjusting the uncorrected energy loss measurement with three additional parameters. This ensures that the dependence on the x and y positions of a particle, traversing through the CRDCs and the S800 focal plane, is removed. This correction is applied through Eq. 4.1:

$$E_{corr} = E \times A \times y_{fp} \times \exp\left[B(C - x_{fp})\right] \tag{4.1}$$

where E_{corr} is the corrected energy loss of the particle that passes through the ionisation chamber, E is the uncorrected energy loss (i.e. the detected energy loss), A and B are the correction parameters that are related to the energy loss gain in accordance to the y and x planes of the IC, respectively, y_{fp} is the detected y-position of the particle at the S800 focal plane, and C is the gain factor related to the x-position of a particle at the focal plane (x_{fp}). The x_{fp} and y_{fp} dependence can be eliminated by individually optimising the A, B and C parameters by looking at the energy loss of a reaction product. Since the x_{fp} and y_{fp} are both closely related to the angle of incidence in the ionisation chamber, the dependence can be examined through the CRDC positions. The result of this correction procedure to eliminate the first CRDC x-position dependence, once the A, B and C parameters were optimised, is shown in Fig. 4.3 gated on ^{47}Mn (populated through a neutron-knockout from the ^{48}Mn secondary beam). If this correction was not applied, then a measurement of consistent energy loss is not obtained for a particular reaction product. Therefore, this results in poor Z-resolution while identifying the particles detected as they are separated by Z through energy loss measurements.

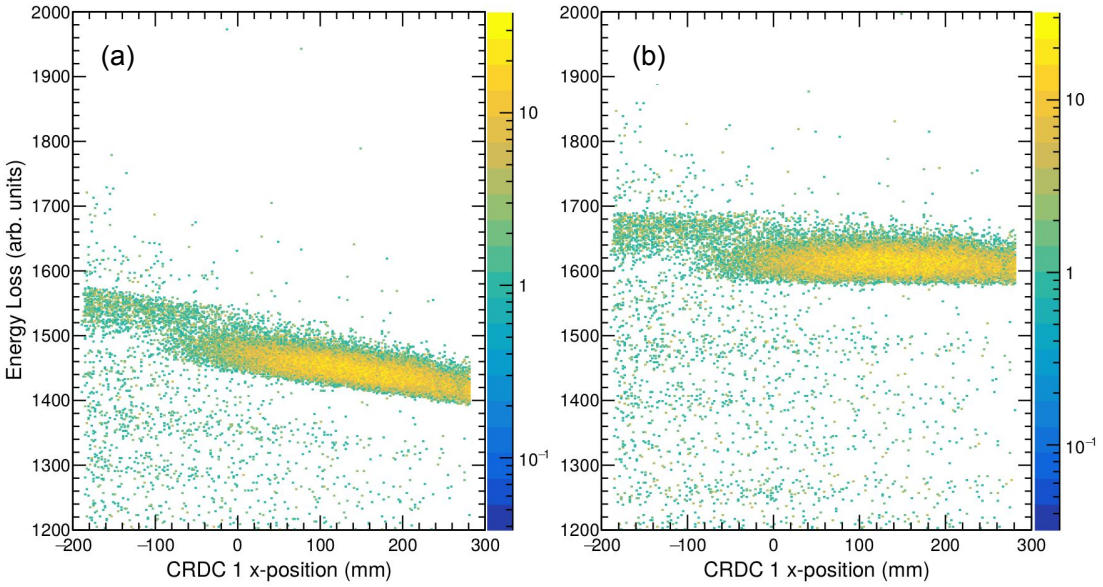

Figure 4.3: The energy loss in the ionisation chamber as a function of the recorded x-position of the first CRDC (a) before and (b) after the positional corrections have been applied. The plots were produced by gating on the ^{45}Cr residue, produced through the two-neutron knockout reaction of the ^{47}Cr secondary beam, where it can be observed that the energy loss measurements are aligned after the corrections have been applied.

4.3 CRDC Calibrations

As mentioned in Chapter 3.5.1, the x and y positions of the particles passing through the S800 spectrograph are tracked on an event-by-event basis. The charges induced from the interaction of particles with the P10 gas within the CRDC are detected. In order to provide precise Doppler corrections, it is imperative that the positional information from the CRDCs are accurately measured to provide the precise recoil angles of the residues produced. Therefore, two stages were involved in the calibration of the CRDCs to provide accurate measurements to reconstruct the trajectories of the particles traversing through the focal plane, as discussed in Chapter 3.5.2. The first step was to calibrate the CRDC pad amplitudes via gain matching to acquire the position information along the dispersive plane (x). Secondly, the mask run calibrations were performed to calibrate the position along the non-dispersive plane (y).

4.3.1 CRDC Pad Calibrations

As shown in Fig. 3.13, the x-position of a particle traversing through a CRDC is determined by fitting a Gaussian function to the detected induced charges across the 224 pads. These pads run on either side of an anode wire on both sides of the x plane in each CRDC. The recorded signals are not consistent throughout all of the pads. Therefore, it is essential that the signals are consistent with each other, hence requiring a calibration by applying an iterative gain-matching procedure. A particular incoming beam was selected, being the ^{47}Cr beam in Fig. 4.4, and four outgoing particles, consisting of high statistics, were gated on from the PID spectrum to minimise the statistical errors that can contribute to the gain-matching procedure. In this part of the calibration process, pad 70 was chosen as the reference pad due to high statistics. In a similar fashion to the IC calibration process, the pad amplitude signals measured from each pad were fitted with a Gaussian for each of the gated reaction products. By plotting the centroids of the Gaussian distributions for each reaction product against the measured centroids from pad 70, the gain and offset factors were extracted for each pad. It is important to note that for some of the

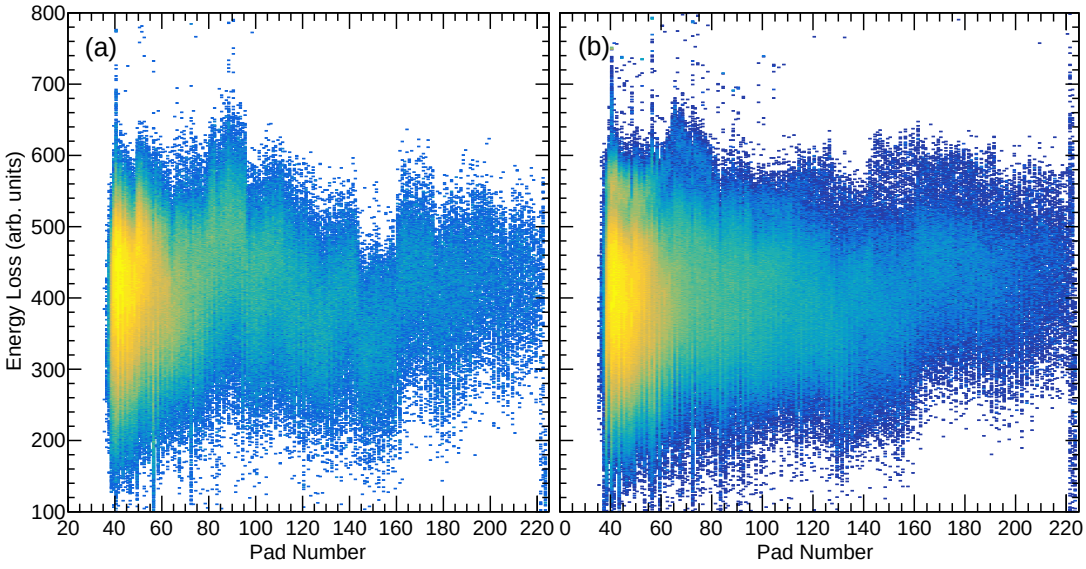

Figure 4.4: The signal amplitudes of each of the 224 pads as a function of the pad number produced by gating on the incoming ^{47}Cr beam. (a) shows the signals in each pad prior to calibration and (b) shows the consistency of the signals relative to pad 70 after the calibrations have been applied.

selected outgoing beams, consisting of low statistics, this method can be compromised where gaps may be produced for some pads as the fitting procedures could not be conducted. Therefore, the binned-likelihood fitting was applied to each pad with low statistics. By combining the gains and offsets obtained from both fitting methods, the pad amplitudes were aligned with pad 70. This process is an iterative procedure, typically requiring 2-3 iterations to obtain consistency between the pad amplitudes. Fig. 4.4 shows the effects of this calibration before and after application.

4.3.2 CRDC Mask Run Calibrations

Once the 224 pads of the each CRDC are gain-matched, the next step was to calibrate the recorded dispersive (x) and non-dispersive (y) positions of the CRDCs. This step ensures that the x and y-positions of the CRDCs are consistent throughout the experiment as the beam passes through the detectors. It is necessary that the measured x and y-positions from the CRDCs are calibrated to known values so that the arbitrarily measured positions of the particles traversing through the CRDCs correspond to their actual positions. These positions are then used to

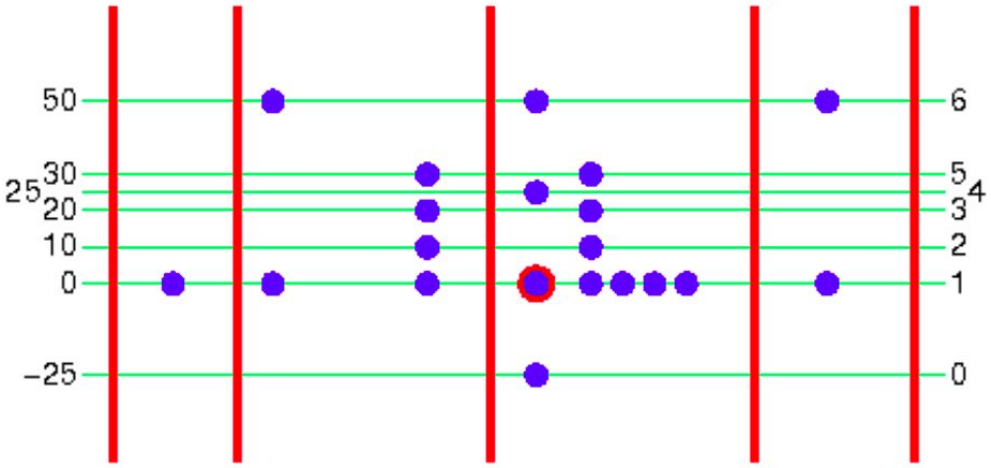

Figure 4.5: The distinct CRDC mask pattern that is utilised for the mask calibrations. The blue circles represent the holes in the masks, while the red lines represent the slits present in the mask. Particles are permitted to pass through these markings. The point outlined in red is used as a reference point located at the origin (0,0). The values on the left-hand side of represent the positions of the blue points in mm, while the values on the right-hand side represent the rows of the blue points. In this step, the points located on the 'L' shape on rows 1, 2, 3 and 4 were used as reference points.

map the trajectory of the particle (see Chapter 3.5.2). The calibration process is carried out by mapping the recorded x and y-positions of the CRDCs to the positions present in a distinct pattern (see Fig. 4.5), which has known values, to apply separate gains and offsets to the recorded x and y-positions of each CRDC.

The corrections are made by placing a mask, made out of tungsten, in front of each CRDC. The mask has holes and slits at calibrated positions, where the particles that pass through these are detected. Once the pattern has been examined after the particles were detected, the positions can be corrected to the calibrated values by determining and applying the gains and offsets to the recorded positions to translate them to the actual physical positions. For the x-plane, the gain is fixed at 2.54 mm as this corresponds to the size of the pads, and the offset is fixed at -281.94 mm. The calibration of the mask run before and after the gains and offsets have been applied is shown in Fig. 4.6.

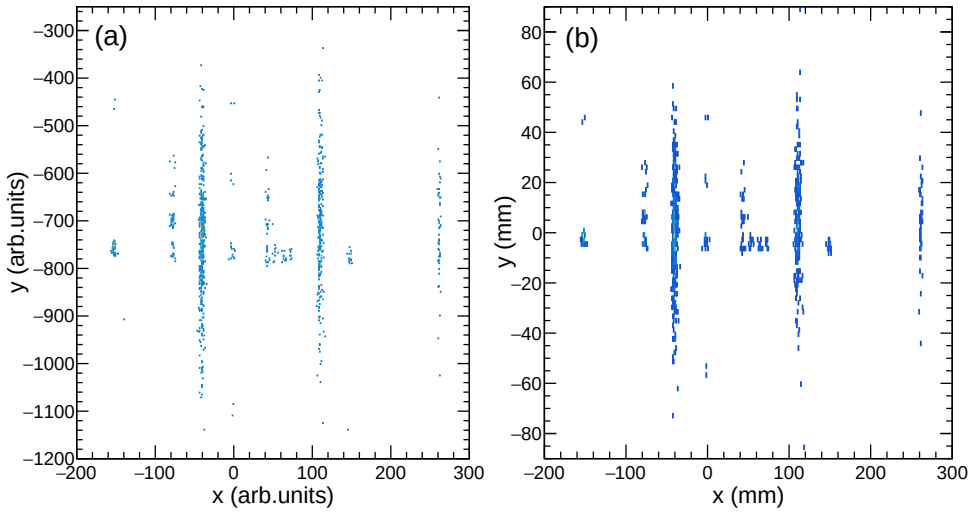

Figure 4.6: (a) shows the first mark run that was taken for the first CRDC before the gain and offset factors have been added. (b) exhibits the same mask run after the calibrations have been applied, which was found to match the recorded positions presented on the pattern in Fig. 4.5.

4.3.3 CRDC Drift Calibrations

During the experiment, there were a total of 5 separate pairs of mask runs for each CRDC. By periodically performing the CRDC mask runs, a consistent reference point throughout the

experiment is provided. Therefore, the CRDC positions can be corrected to minimise the drift in the y-positions. A total of 113 runs were divided into five approximately equal groups, where the mask run was at the centre of each group. Each group was calibrated with the corresponding gains and offsets determined using the prescription detailed above using the relevant mask run. The mask runs utilised for each run within the groups are summarised in Table 4.1.

Mask Run	**Mask Run Number (CRDC 1/CRDC 2)**	**First Run**	**Last Run**
1	21/22	19	50
2	85/86	53	101
3	114/115	102	141
4	152/153	142	166
5	178/179	167	189

Table 4.1: The procedure of the CRDC mask run applied for the calibrations of the CRDC positions for each experimental run. The experimental runs began from Run 19, where all previous runs were taken for γ-ray efficiency measurements using stationary sources and for tuning the components for the beam of interest.

Fluctuations in the temperature and pressure of the gas in each CRDC over the course of the experiment can cause the positions of the detected particle to drift. This effect can also affect the electron drift time and hence, the non-dispersive (y)-position of the particle. Since this effect is time-dependent, the drift in the CRDC y-position needs to be corrected by applying an additional correction to the gains on a run-by-run basis. The gains are adjusted such that the y-position remains centred at 0 mm between that mask runs and the whole experiment. The factors for the CRDC drift correction for each run were deduced by:

$$m = -\frac{c}{y}, \tag{4.2}$$

where c is the y-offset determined through the mask calibrations detailed above, and y is the measured CRDC y-position for a chosen residue when the offset, c, was not applied to the CRDC data. The gains attained from the mask run calibrations are multiplied by the drift correction factor, m. This new gain and the original offsets deduced from the mask run calibrations are then applied to align the y-positions of the CRDC to 0 mm for each run. The calibrated y-positions of the CRDCs, obtained from the mask run calibrations, can be tested by plotting the

drift of the y-position as a function of the run number to examine the changes before and after the corrections have been applied. The x-position of the CRDCs are unaffected by the drift and will remain constant. The changes in the y-position when accounting for the drifts is presented in Fig. 4.7. It is important to note that the CRDC drift factors were calculated on a run-by-run basis and were optimised separately for each recoiling nucleus.

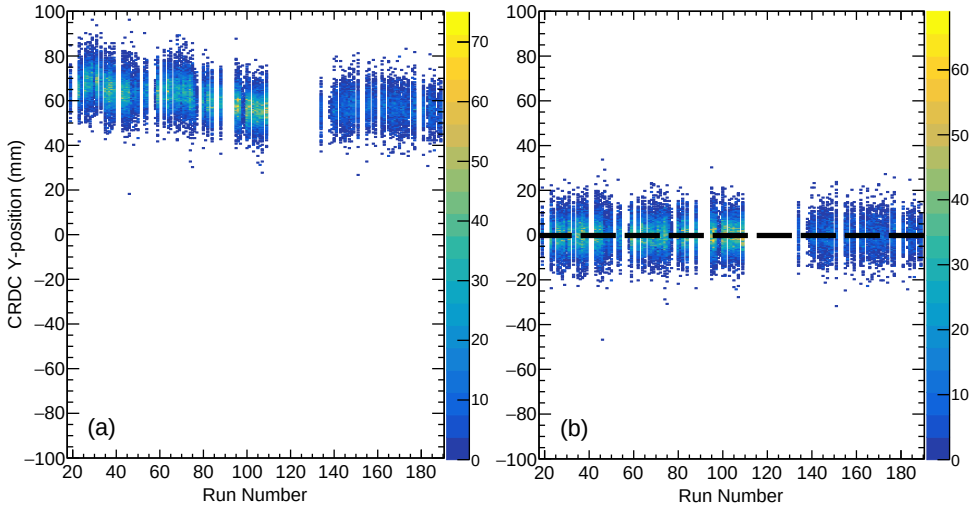

Figure 4.7: The recorded CRDC y-positions for the first CRDC while gated on ^{47}Mn, populated through the one-neutron knockout reaction of ^{48}Mn. (a) Shows the y-positions before the drift correction factors have been applied, and (b) shows the y-positions after the drift corrections have been applied to the gains obtained along with the original offset determined. The dotted black line shows the y-positions at 0 mm, being the reference point used to shift each run to.

4.4 Scintillator Corrections

The ToF of the particles traversing through the A1900 and S800 set up are measured relative to the OBJ, XFP and E1 scintillators, where this measurement help to identify recoil particles produced at the reaction target. Nuclei of the same mass and atomic numbers can traverse through the A1900 and S800 with slightly different momentum, resulting in different paths being followed. Therefore, the nuclei reach the focal plane at different angles and positions. Due to the trajectories taken by the particles in the S800 spectrograph, the ToF will vary with the angle (a_{fp}) and position (x_{fp}) of the trajectories as the particles pass through the CRDCs. It is imperative that this dependence on the ToF is removed to increase the identification resolution

of recoils in the S800 focal plane.

The corrections for the ToF data from the OBJ and XFP scintillators account for the dispersive x-position (x_{fp}) and the dispersive angle (a_{fp}). The ToF corrections were applied such that:

$$ToF_{corr} = ToF + (A \times a_{fp}) + (B \times x_{fp}), \tag{4.3}$$

where ToF_{corr} is the corrected ToF, ToF is the uncorrected time of flight measurement, and the parameters A and B are the correction factors applied to a_{fp} and x_{fp}, respectively, that act as 'skewing' parameters. The S800 a_{fp} and x_{fp} of a particle detected at the focal plane were plotted

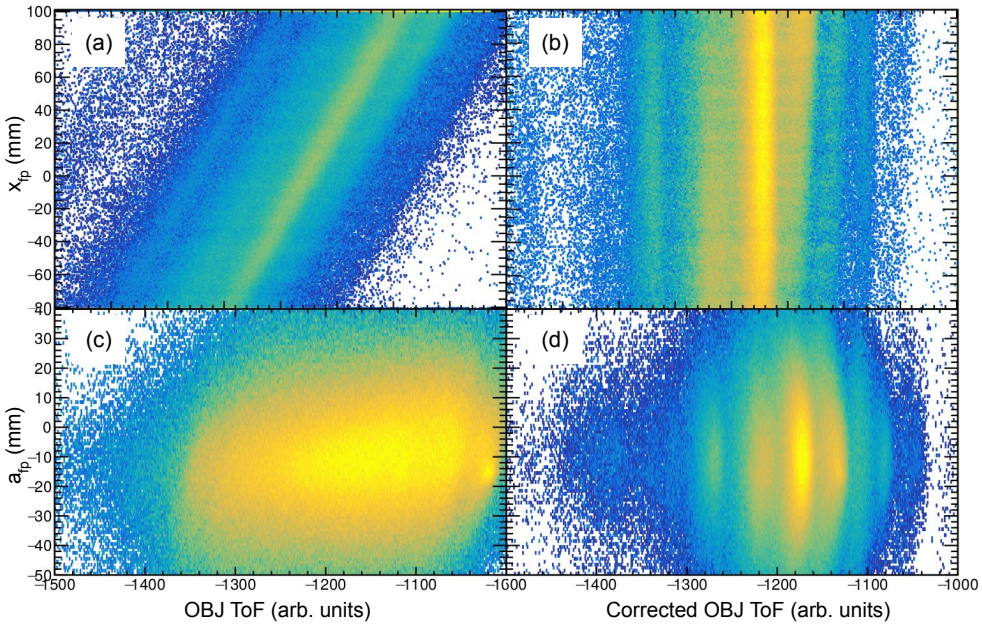

Figure 4.8: The dispersive angle (a_{fp}) and x-positions (x_{fp}) at the S800 focal plane as a function of the timing measurements relative to the OBJ-E1 scintillators (ToF). (a) and (c) show the spectra of the x_{fp} and a_{fp} plots before corrections have been applied. (b) and (d) show the effects of the blobs in the a_{fp} plot and the streaks in the x_{fp} plot after the corrections have been applied, where they were observed to be well-separated and vertical.

as a function of the OBJ scintillator, where the A and B parameters were iteratively varied to straighten the blobs in the a_{fp} plots and to straighten the streaks in the x_{fp} plots until they were vertical. The effects of this correction are shown in Fig. 4.8. These corrections, conducted visually, were found to improve the particle identification plot (PID), where the blobs appeared sharper and well separated.

4.5 Identification of Particles

As previously discussed in Chapter 3.1, the incoming radioactive secondary beams, produced through the fragmentation of a stable ^{58}Ni beam at the primary ^{9}Be target, were identified using the ToF measurements from the XFP/OBJ scintillators with respect to the E1 scintillator.

The incoming beams can be clearly identified by examining the XFP-E1 ToF as a function of the OBJ-E1 ToF, despite the presence of contaminants through the centre of the plot, as seen in Fig. 4.9(a). The cause of this contaminant streak is due to scattered beams that traverse through the target before entering the S800 spectrograph. Since these contaminants pass through the

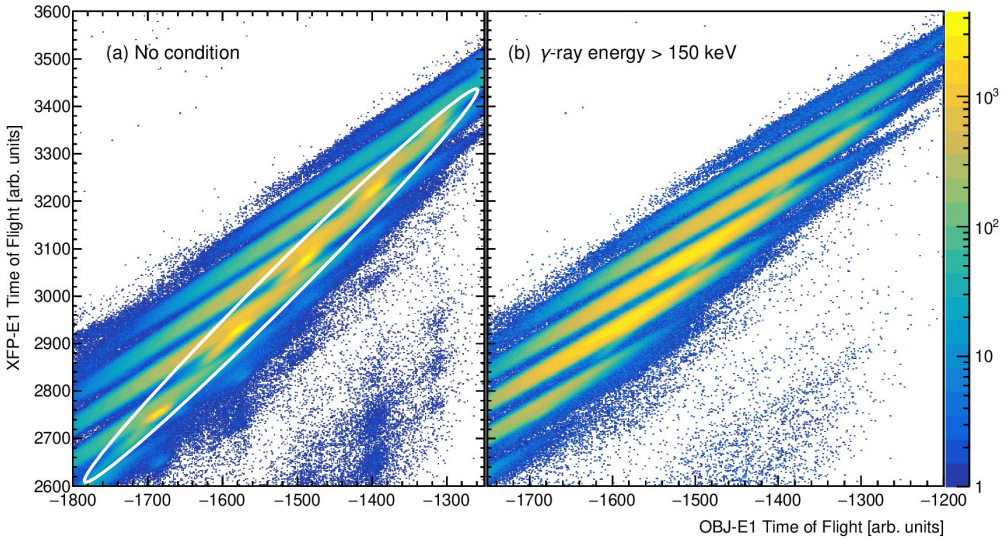

Figure 4.9: The comparison of the incoming beams obtained from the ToF information provided by the XFP-E1 and OBJ-E1 scintillators without (a) and with (b) additional γ-ray conditions, where detected γ-ray energies of >150 keV were required. This condition was found to remove scattered beam, highlighted in white in (a), which can skew the a_{ta} and b_{ta} distributions.

centre of the incoming beams of interest, it is necessary to remove these particles to prevent further contamination while identifying the outgoing reaction products produced at the ^{9}Be reaction target. Therefore, an additional condition of a particle in coincidence with a GRETINA event was applied, ensuring that the particle has reacted within the secondary target. Furthermore, a γ-ray condition of >150 keV was applied to reduce random coincidences with Bremsstrahlung radiation. The contaminant streak was significantly reduced when these two conditions were applied to the incoming beam plots, as shown in Fig. 4.9(b).

By gating on an incoming secondary beam of interest using Fig. 4.9, the corresponding reaction products produced were identified using the energy loss (δE) information given by the ionisation chamber and the corrected ToF information of the OBJ scintillator, measured relative to the E1 scintillator. The outgoing PID plots gated on the ^{48}Mn and ^{47}Cr incoming beams are shown on the left and right panels in Fig. 4.10, respectively. Fig. 4.11 shows the PID plots for the corresponding mirrored incoming beams, ^{48}V and ^{47}V, on the left and right panels, respectively. The y-axis in both plots is equivalent to the atomic number (Z) of the reaction products. The vertical dashed black lines in Fig. 4.10 represent the specific total isospin projection, T_z, of 0, corresponding to $N = Z$.

In this thesis, the nuclei of interest are ^{47}Mn, ^{47}Ti, ^{45}Cr and ^{45}Sc, that are in coincidence with the secondary beams of ^{48}Mn, ^{48}V, ^{47}Cr and ^{47}V, respectively.

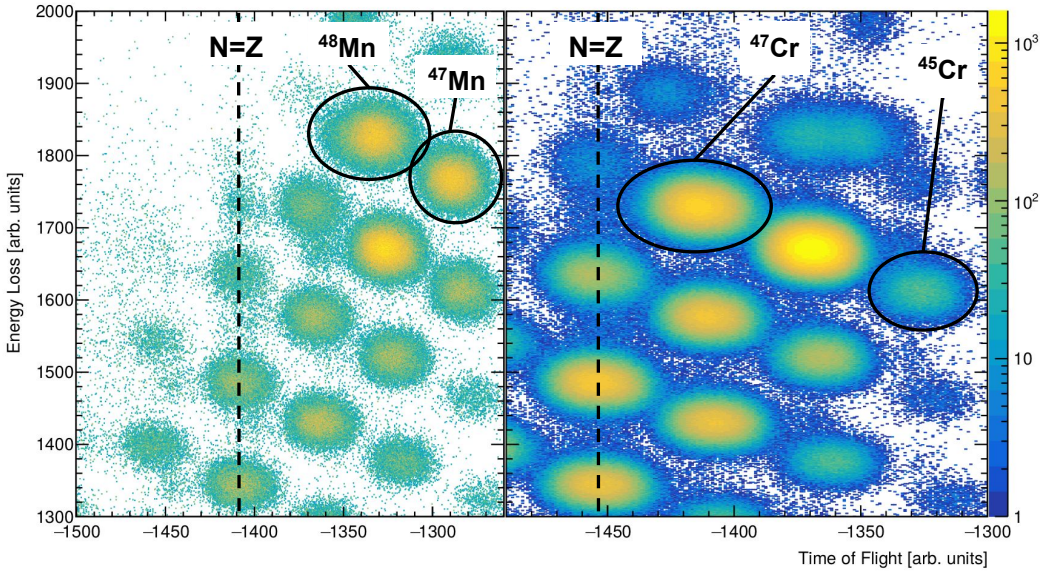

Figure 4.10: The PID spectra of the energy loss in the ionisation chamber as a function ToF measurements obtained from the corrected OBJ-E1 scintillators gated on the incoming (left) ^{48}Mn beam and (right) ^{47}Cr beam. The outgoing particles interest, ^{47}Mn and ^{45}Cr, produced through one- and two-neutron knockout reactions, respectively, are labelled. The dashed black line represent the $T_z = 0$ products, corresponding to the $N = Z$ line.

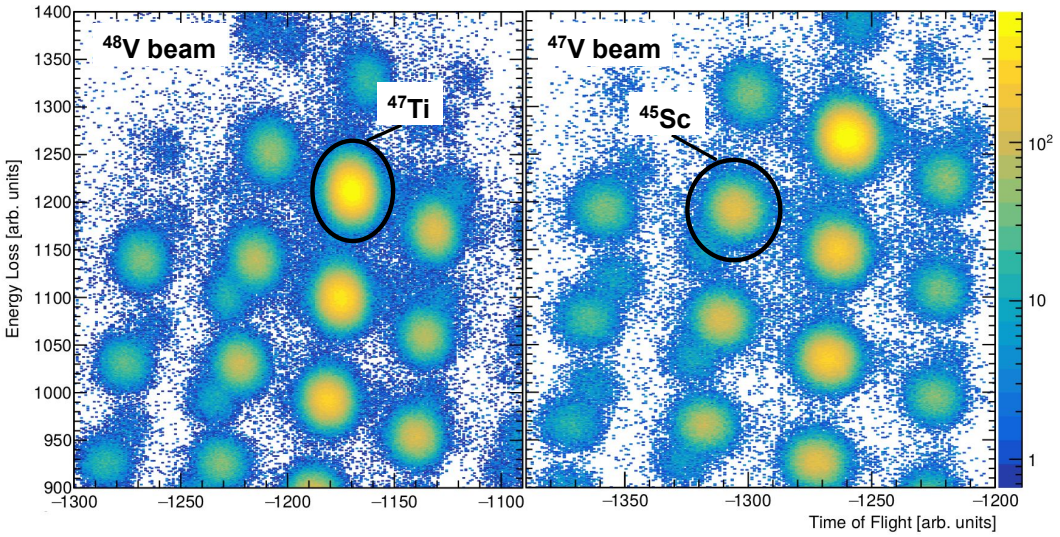

Figure 4.11: The PID spectra of the energy loss in the ionisation chamber as a function ToF measurements obtained from the corrected OBJ-E1 scintillators gated on the incoming (left) ^{48}V beam and (right) ^{47}V beam. The outgoing particles interest, ^{47}Ti and ^{45}Sc, produced through one- and two-proton knockout reactions, respectively, are labelled.

4.6 GRETINA

Once all of the calibrations were applied, gates for the different reaction channels were created using the particle identification spectrum (PID). The gating procedure provides the ability to produce γ-ray spectra in coincidence with the gated incoming and outgoing beams. Additional calibrations were conducted to produce clean γ-ray spectra when gated on the relevant beams of interest, where sharp peaks should be present at the correct energy. The energy calibrations of GRETINA were completed at the start of the experiment and were implemented in the event builder before the data was written to disk. Further energy calibrations were not performed due to the small uncertainties associated with these energies compared to the uncertainties due to Doppler reconstruction. The subsequent corrections applied to produce clean γ-ray spectra are discussed in the following sections.

4.6.1 Doppler Reconstruction of γ rays

Fast beams up to ∼160 MeV/u and velocities of ∼0.4c were used in this experiment, where Doppler shifts will contribute significantly to the γ rays detected by GRETINA, as shown [86]:

$$E_{rest} = E_{lab}\frac{1-\beta\cos\theta}{\sqrt{1-\beta^2}} \tag{4.4}$$

where E_{rest} is the γ-ray energy in the frame of reference of the nuclei moving at the direction of the relativistic velocity, $\vec{v}$, E_{lab} is the γ-ray energy in the observed frame of reference, β ($= \frac{v}{c}$) is the ratio between the velocity of the nuclei and the speed of light, c, and θ is the angle at which the γ ray was detected in the laboratory frame with respect to the beam axis. The vector of the fragment velocity, $\vec{v}$, is determined using S800 tracking detectors. The point of the first interaction of each γ ray detected in GRETINA is then coupled to the trajectory of the particles through the S800 focal plane, which is crucial to determine θ and β to perform event-by-event Doppler corrections. The detected γ rays are corrected using a sophisticated event-by-event Doppler process using a specific average value of β. Since the recoiling nucleus is assumed to decay at the centre of the target, the mid-target β value is adjusted on an event-by-event basis using the d_{ta} value calculated by the inverse map using [86]:

$$\frac{\delta\beta}{\beta} = \frac{1}{\gamma(\gamma+1)}\frac{\delta T}{T}, \tag{4.5}$$

where T is the kinetic energy of the particle, d_{ta} is the value calculated using the inverse map that corresponds to $\delta T/T$ (i.e. the momentum spread of the beam at the target), and $\gamma = 1/\sqrt{1-\beta^2}$.

An additional event-by-event shift is performed in the y-direction to the centre of the target, corresponding to the y_{ta} value calculated from the inverse map. The inverse map also calculates the dispersive (a_{ta}) and non-dispersive (b_{ta}) recoil angles at the target position that are coupled to the Doppler reconstruction process. These recoil angles slightly modify the vector of the recoiling nucleus, $\vec{v}$, from the central beam axis to the values determined from the inverse map. Consequently, this corresponds to a small but crucial event-by-event correction to the emission angle, θ, applied in the Doppler correction process.

Like the CRDC corrections, the secondary beams were also found to drift over time throughout the experiment due to beam focusing fluctuations in the A1900 separator. Therefore, the

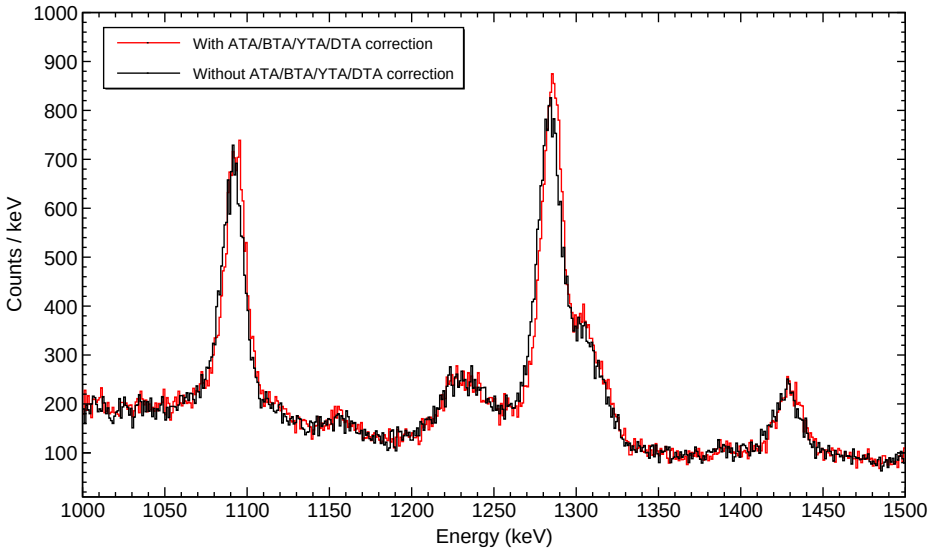

Figure 4.12: A comparison of the Doppler-corrected γ-ray spectrum for ^{47}Ti, populated from the ^{48}V secondary radioactive beam, with (red) and without (black) the inclusion of the deduced recoiling positional and angular beam parameters calculated through the inverse map (a_{ta}, b_{ta}, y_{ta}, d_{ta}) in the process of the Doppler-correction. With the inclusion of the deduced positional and angular beam correction factors, the energies of the observed transitions were found to be shifted by $\sim$2 keV.

a_{ta}, b_{ta} and y_{ta} factors were corrected on a run-by-run basis to shift the a_{ta} and b_{ta} distributions, and the non-dispersive beam position, y_{ta}, on to the secondary target. These corrections were essential in the Doppler correction process, where the outcome of these corrections is reflected in the resolution of the Doppler corrected γ-ray spectra (see Fig. 4.12). With regards to reconstruction of the recoil vector, $\vec{v}$, systematic errors contribute to the tracking of the particles from the S800. As a result, additional corrections are required to optimise the Doppler corrections to account for these systematic errors that arise. These corrections are detailed in Section 4.6.2.

4.6.2 Determination of β

As the emitted γ rays from an outgoing residue can interact with multiple segments in GRETINA via Compton scattering events, it is possible to identify which segments were hit during the γ-ray interaction and measure the amount of energy recorded in each segment. The first point of interaction in the HPGe crystals within GRETINA is identified by selecting the position of the

highest energy interaction. This defines the γ-ray emission angle.

The optimum β values used in the γ-ray Doppler correction process are determined using two recorded energies of a chosen transition, which were extracted individually from the 58° and 90° GRETINA detector rings. With reference to Eq. 4.5, if β is correct, then this results in the Doppler corrected energy being constant over all θ angles of the GRETINA array, provided that θ and $\vec{v}$ are calculated correctly. For two measured energies of E_1 and E_2 for the same transition from the Doppler corrected spectra of the forward and the back angle detectors, respectively, a given β value was used for correction. The β value that was required to correct the two spectra at the same energy, β_{new}, is given by Eq. 4.6 [108]:

$$\beta_{new} = \beta + \frac{E_1 - E_2}{-\beta^2\gamma^3(\cos\theta_1 + \cos\theta_2) + \gamma(\cos\theta_1 - \cos\theta_2)}, \tag{4.6}$$

where $\gamma = 1/\sqrt{1-\beta^2}$, and θ_1 and θ_2 are the average detector angles from the forward and backward angle detector rings (i.e. 58° and 90°), respectively. Therefore, the production of different nuclei that have different masses and charges, as well as being produced from different reaction mechanisms from the secondary beams, will have optimum β values that will vary from one nucleus to the next. Here, the optimum β value typically varies from 0.38-0.4.

The optimum β values in this work were determined by using the precisely known energies of transitions that are significantly high in intensity and consist of lifetimes on the order of a few ps. The effective lifetime of the state, where the γ ray comes from, and the feeding of other transitions into the state determine the optimum recoil velocity. Fast transitions that have timescales of <10 ps will decay within the target. This yields a higher β value as the particle has not slowed down significantly compared to a particle that has fully attenuated through whole length of the target and decayed downstream. This results in each nucleus having separate optimum β values for mid and after-target decays, denoted by β_{mid} and β_{aft}, respectively.

As a test, the previously reported ^{44}Ti nucleus [109] (produced by a -1n knockout from ^{45}Ti) was used due to its high statistics and that it has a short-lived 4^+ state of $T_{1/2}$ ~0.42 ps. The $4^+ \rightarrow 2^+$ transition, from where the 1371.2 keV transition comes from, will decay within the target. Therefore, this transition can be used to obtain an optimum β value to shift the spectra of the GRETINA rings to the correct energy. The optimum β was varied to remove any angular

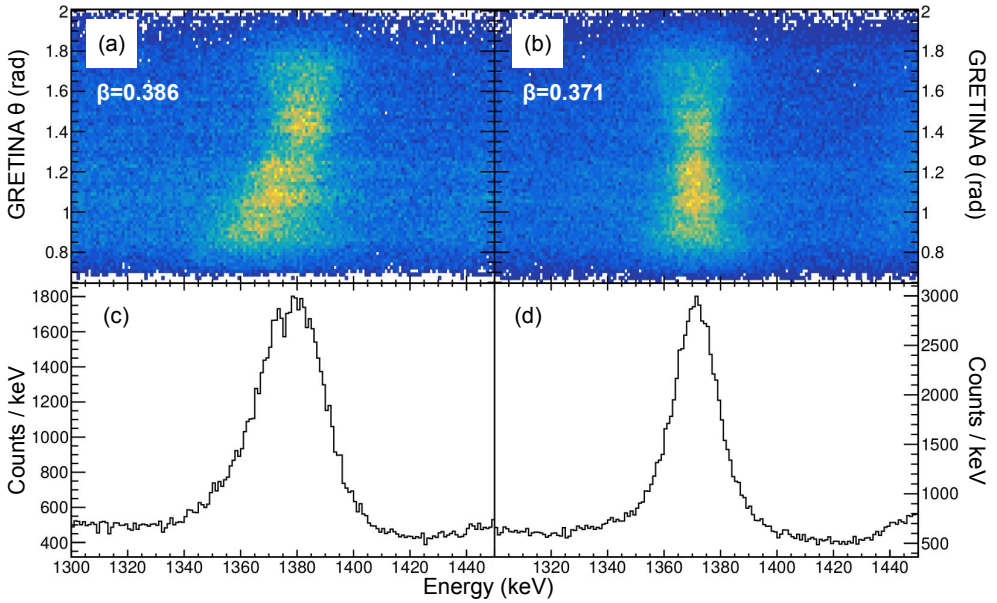

Figure 4.13: The effects of the β optimisation procedure used for the Doppler corrections for the 1371.2 keV, $4^+ \rightarrow 2^+$ transition in ^{44}Ti. Diagrams (a) and (c) show the Doppler corrected energy with the GRETINA θ angle. The corresponding γ-ray spectrum is corrected with a β value of 0.386. (b) and (d) show the same plots that are corrected using the optimum values of β=0.371, where the dependence on the GRETINA θ angle is eliminated. The FWHM resolution of the 1371 keV peak was found to be improved by ∼10 keV when the optimum value of β was applied.

dependence on the observed γ ray (i.e. 1371.2 keV transition). The effect of the β optimisation is shown in Fig. 4.13 for the 1371.2 keV transition in ^{44}Ti, where the GRETINA detector angles were plotted against the detected transition energy (Figs. 4.13(a) and (b)). The corresponding γ-ray spectra in Figs. 4.13(c) and (d) were examined to ensure that the θ dependence is removed while varying the β value. For the 1371.2 keV transition, the β value is optimised at $\beta_{mid} = 0.371$. There are systematic errors that are associated with the optimisation of β, which arises from the uncertainty in the alignment of the transition in the forward and backward detector rings.

4.6.3 Determining the Effective Target z-Position

The effective target z-position (where the beam travels along the positive z-axis) used for event-by-event Doppler corrections is subject to potential shifts. This is due to the manual position of the target at the centre of the chamber throughout the experiment. Since the target was taken out of the chamber mid-way of this experiment and put back in between main runs, the

z-position of the target will be shifted. Hence, this needs to be determined precisely for the first and second half of the data. This part of the Doppler correction process was performed to account for the offset in the z-position alongside precise reconstruction of the γ-ray events.

The z-position of the target and the β values were varied simultaneously in both halves of the data. A particular transition, that decays within the target, was aligned at the correct γ-ray energy. This was achieved by following an iterative procedure, where the z-position was adjusted until the peaks in the forward and backward detector rings matched, and by changing the value of β until the peak was at the correct energy. The value of β was varied using the procedure outlined in section 4.6.2. The z-position at the centre of the target (z_{mid}) was determined by measuring the energy of a transition from a state that has a short lifetime.

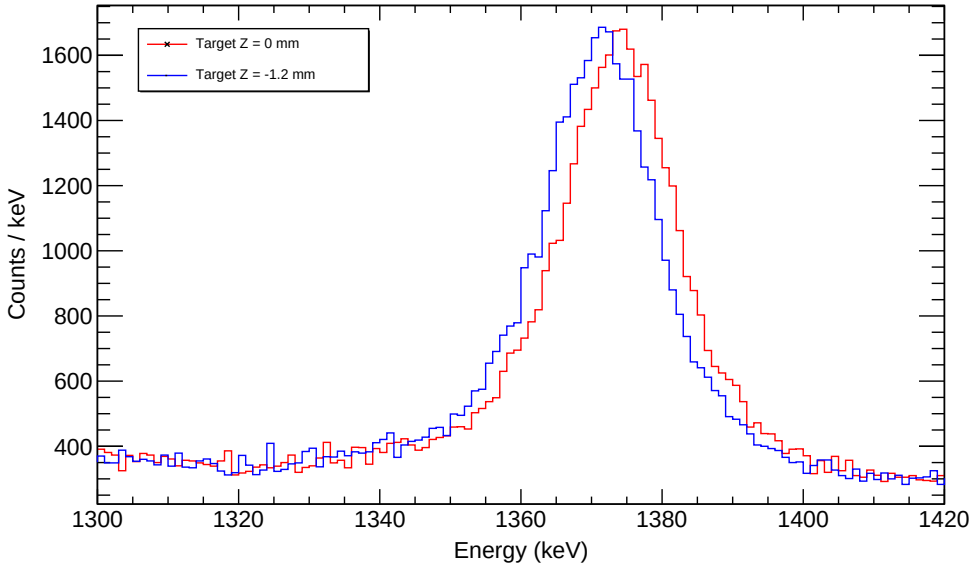

Figure 4.14: The comparison of the Doppler corrected γ-ray spectra using an optimum z-position of -1.2 mm (blue) and with no z-position offset being applied (red). It can be seen that the addition of the z-position offset effectively shifts the mean of the peak to the precise γ-ray energy of 1371.2 keV. Both spectra were produced using the same β value of 0.371.

In this case, the 4^+ state, where the 1371.2 keV transition comes from in ^{44}Ti [109], was used to optimise the z parameter. The value of z was varied after optimising the β value to shift the peak to its known energy. Since the target was removed and placed into the chamber partway through the experiment, two z_{mid} values are needed. The extracted z_{mid} values were -1.2 mm for

the first half and -0.2 mm for the second half of the experiment, relative to the central position of GRETINA. The effects of applying the determined z_{mid} values for each half of the data for the Doppler correction process is shown in Fig. 4.14, for the 1371.2 keV transition. The systematic error in the extracted values of z come from the uncertainty corresponding to how well aligned the detected energies of the transition are in the two detector rings.

The mid-target z-position remains constant for all nuclei produced within the target, provided that the lifetimes of the states are a few ps long. States that have a long lifetime (>10 ps) will decay outside the target with a lower recoil velocity. Under the Doppler reconstruction process applied for short-lived states, the correct γ-ray energies will not be produced for longer-lived states, hence, these transitions must be considered separately.

4.6.4 Determining the Effective Target x- and y-Positions

As with the effective z-position, the effective x and y-positions of the target are also subject to shifts. These positions account for any systematic inaccuracies from the inverse map calculations. This results in the modification of the beam spot position, determined from the inverse map, with respect to the centre of GRETINA. Therefore, these are adjustments to the x and y 'effective' target positions.

The effective x and y-positions were varied within the setting file used to apply the calibrations on a run-by-run basis. To determine the optimum values for these parameters, the dependence of the Doppler corrected γ-ray energy relative to the azimuthal angle of the deduced first-interaction point of GRETINA, ϕ, was explored. This dependence was probed by investigating the 58° and 90° detector rings individually, as seen in Fig. 4.15.

The Gaussian fits from each band of the forward and backward detector rings were measured until the optimum combination of the effective x and y-offsets were found. During the optimisation procedure, the spectrum of the forward detector ring was initially bowed. This effect was removed by varying the effective x-position of the target. For the 90° detector ring, the dependence on the effective x and y-positions was far less, where minimal changes were observed when adjusting the target y-position. A slight bowing effect was also observed in the 90° detector ring, which was reduced by varying the x and y-positions of the target. Although the bowing effect is still present, this could not be further improved without increasing the ϕ dependence of the 58°

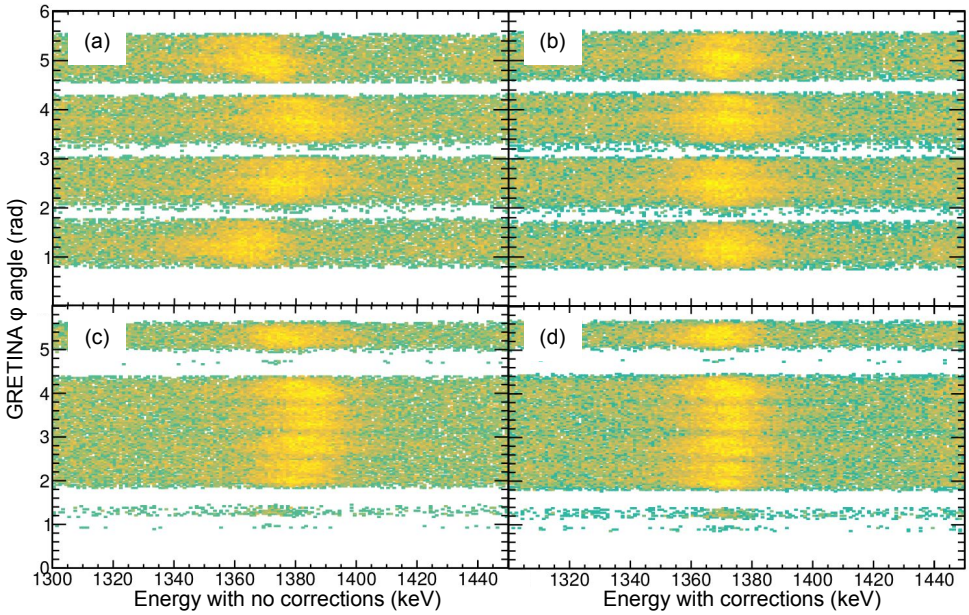

Figure 4.15: The effect of adjusting the effective target x and y-positions that is utilised in the Doppler correction process. (a) and (c) display the energies of the 1371.2 keV transitions from the forward and backward angle detector rings, respectively, before the x and y-positions were adjusted. (b) and (d) correspond to the forward and backward detector rings after the positions have been adjusted.

detector ring (see Fig. 4.15). This correction yielded effective x and y-values of -9.25 mm and -0.25 mm, respectively, for the ^{45}Ti beam and other incoming beams produced using the same A1900 separator settings.

For every secondary beam that utilises a different setting of the A1900 separator, the beam becomes shifted. Therefore, the target x, y, z and β must be corrected and applied separately for each outgoing recoil studied (e.g. the mirror nuclei runs).

4.6.5 Exploring the ϕ-Dependence on Doppler-Corrected γ-ray energies

Additional corrections to the orientation of the beam axis, with respect to GRETINA, are sometimes necessary to ensure that the Doppler corrected γ-ray energies are consistent over the beam polar angle, θ, and the azimuthal angle, ϕ, of the position of detection in GRETINA [86]. Offsets of the order of a few mrad can be applied to the θ and ϕ of the beam.

Once the optimisation of the target x, y, z-positions and β were completed, the effects of the

offset in ϕ of the beam were investigated by examining the dependence of the Doppler corrected γ-ray energies with respect to dϕ. The term, dϕ, is the difference between the azimuthal angle (ϕ) of the first point of interaction in GRETINA and the azimuthal angle of the beam. The dϕ dependence of the 1371.2 keV, $4^+ \rightarrow 2^+$ decay in ^{44}Ti is presented in Fig. 4.16. Since the dependence of dϕ was not present, no additional corrections were made to the beam polar angle, θ.

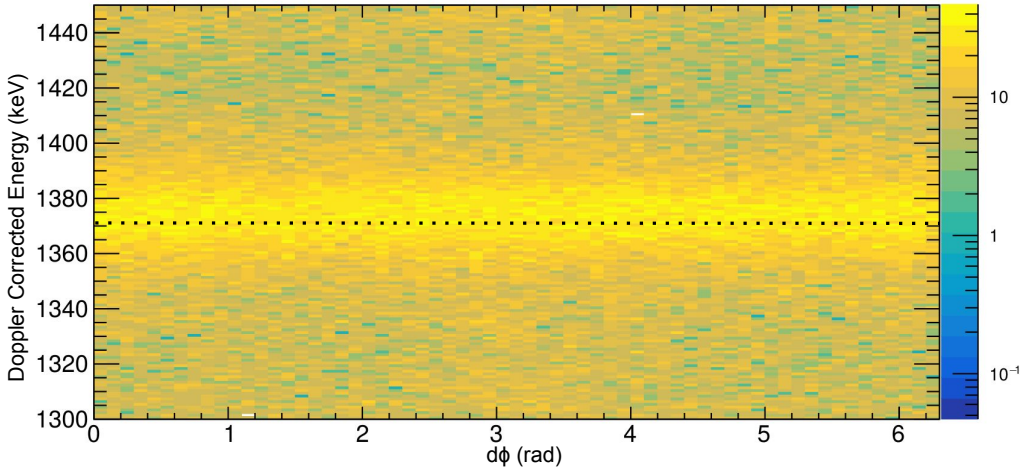

Figure 4.16: The dependence of the Doppler corrected energy of 1371.2 keV, $4^+ \rightarrow 2^+$ decay of ^{44}Ti with the difference between the azimuthal angle of the beam, ϕ, and the γ-ray detection azimuthal angle, dϕ. The spectrum was found to appear horizontal with no curving effects, signifying that there is no apparent dϕ dependence on the angle of the beam, θ.

Such dependence, if identified, can be eliminated by varying the θ value until the spectrum becomes flat, signifying that there is no dependence of θ with respect to dϕ.

4.6.6 γ-γ Coincidence Analysis

The analysis of γ-γ coincidence data is performed when a series of γ-ray decays form a given cascade, allowing for the level-scheme to be deduced for a given nucleus. A 2D γ-γ matrix can be constructed by plotting the measured γ-ray energies that consist of having a multiplicity >1, identified within the same coincidence window of the detector system. An analysis was performed to produce a symmetrical matrix along the diagonal showing all of the coincident γ-ray events using the add-back method, as shown in Fig. 4.17. Decays that occur within a single cascade

will feed into one another. To obtain γ-γ coincidence spectra for a given transition, the 2D γ-γ histogram can be projected either along the x- or y-axis. The resulting spectrum yields transitions that can occur within the same cascade or within the same coincidence.

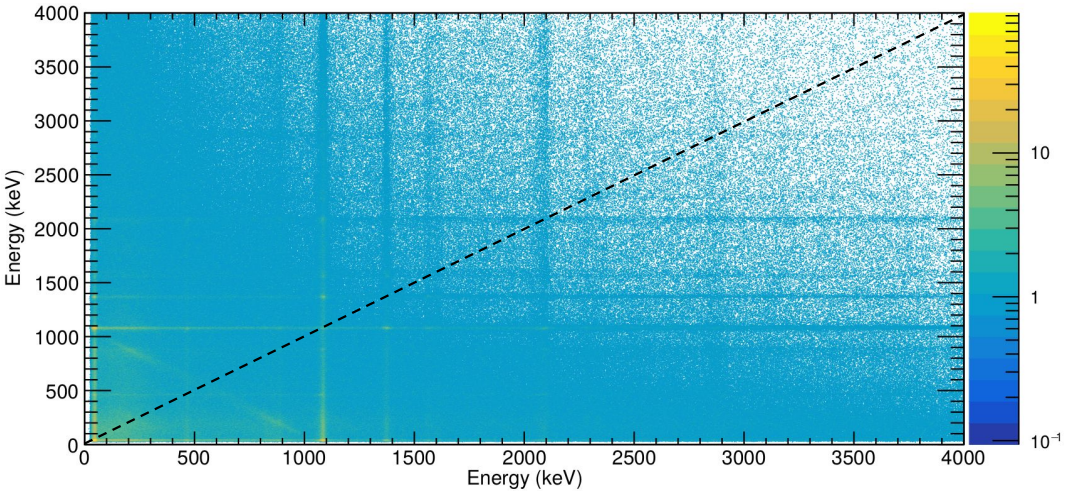

Figure 4.17: The 2D γ-γ matrix for ^{44}Ti. The diagonal dashed black line shows where the matrix has been symmetrised. The point at which the vertical and the horizontal lines intersect correlates to the two decays being in coincidence with each other. This allows for a level scheme to be deduced.

In order to remove random coincidence events and Compton background in the spectrum, a background-subtraction procedure is necessary. This was done by subtracting the average of two sample background spectra, obtained by taking gates on either side of the transition of interest, provided that each background gate are of the same width as the transition gate. The two background spectra are then scaled to match the width of the desired energy gate. This is then subtracted from the main energy gate to minimise any background events, allowing for the genuine coincidence events to be prominent.

This technique was applied to confirm the feeding of known γ-ray transitions for the ^{47}Ti and ^{45}Sc nuclei and to establish the new γ-ray transitions in the $T_z = -\frac{3}{2}$ nuclei, ^{47}Mn and ^{45}Cr, which in turn produces new level-schemes for both proton-rich nuclei.

Chapter 5

Level Schemes and Mirror Energy Differences

The ^{48}Mn and ^{47}Cr secondary beams were produced using the same A1900 and S800 magnetic rigidity settings centered on the $T_z = -2$ reaction products, where the total duration of these runs was ∼109 hours. The respective mirrored secondary beams of ^{48}V and ^{47}V were produced under two different settings where the beams were run for ∼1.5 and ∼1.25 hours, respectively. The notable time difference between the three sets of runs was due to the significantly high beam rates of the ^{48}V and ^{47}V secondary beams, being ∼10^2 and ∼10 times higher than the ^{48}Mn and ^{47}Cr beams, respectively. A cocktail of secondary beams, consisting of a wide range of isotones, were produced (i.e. ^{49}Fe, ^{48}Mn, ^{47}Cr ^{46}V, ^{45}Ti and ^{44}Sc using the ^{49}Fe setting), allowing for multiple reaction channels to be analysed. In this chapter, the analysis of the $T_z = \pm\frac{3}{2}$ mirror pairs, ^{47}Mn/ ^{47}Ti and ^{45}Cr/^{45}Sc, which were populated through one-nucleon knockout and two-nucleon removal reactions from the ^{48}Mn/^{48}V and ^{47}Cr/^{47}V secondary beams respectively, will be discussed. The work presented here is also published in Ref. [30].

The Doppler-corrected γ-ray spectra for the mirror nuclei of interest were produced by applying the calibration stages detailed in Chapter 4, where corresponding coincidence gates were applied on both the incoming and outgoing nuclei of interest (see Section 4.5). Subsequent coincidence analysis was conducted to construct level-schemes for the nuclei of interest. The MED results for the $A = 47$ and $A = 45$ mirror pairs will also be discussed, where the theoretical results from the state-of-the-art shell model and Density Functional Theory (DFT) calculations will be presented.

5.1 Population of states in the $A = 47$ mirror pair

The proton-rich ^{47}Mn ($T_z = -\frac{3}{2}$) nuclei and its well-known, stable, mirror nucleus ^{47}Ti ($T_z = +\frac{3}{2}$) were populated through mirrored one-nucleon knockout reactions from the ^{48}Mn ($T_z = -1$) and ^{48}V ($T_z = +1$) secondary beams, respectively. To understand the ordering of the observed γ rays in the unknown ^{47}Mn nucleus, a comprehensive analysis to identify which states are populated in the ^{47}Ti nucleus is required. In this section, the details on the J^π assignment of the observed γ-ray transitions and states in the unknown, exotic, proton-rich ^{47}Mn nucleus is presented. The direct and isospin symmetric nature of the mirrored one-nucleon knockout reactions is exploited to inform the construction of level schemes, along with a coincidence analysis.

5.1.1 Spectroscopy of ^{47}Ti

The Doppler corrected γ-ray spectrum for the well-known ^{47}Ti nucleus is shown in Fig. 5.1(a), where states up to an energy of 4494 keV were confidently observed. All measurements of γ-ray energies in this work were consistent with previously published values [29]. The ordering of the observed transitions was analysed via γ-γ analysis to construct a level scheme (see Fig. 5.2). Some examples of the coincidence spectra are shown in Fig. 5.1(b-c). The results are in good agreement with previous work (see Ref. [110]).

In Figs. 5.1(b) and 5.1(c), the γ-γ coincidence spectra are gated on the 1224 keV and the 1430 keV transitions, respectively. Gating on E$_\gamma$=1224 keV γ ray shows that this transition is in coincidence with the 1285 keV ($\frac{11}{2}^-_1 \rightarrow \frac{7}{2}^-_1$) and 159 keV ($\frac{7}{2}^-_1 \rightarrow \frac{5}{2}^-_{gs}$) transitions. Similarly, the gating on the E$_\gamma$=1430 keV ($\frac{11}{2}^-_2 \rightarrow \frac{9}{2}^-_1$) transition demonstrates that this transition is in coincidence with the 1093 keV ($\frac{9}{2}^-_1 \rightarrow \frac{7}{2}^-_1$) and 159 keV ($\frac{7}{2}^-_1 \rightarrow \frac{5}{2}^-_{gs}$) transitions. These cascades of transitions are presented in Fig. 5.2, based on the γ rays observed in this work for ^{47}Ti.

The majority of the observed γ rays are shown to come from the negative-parity states, particularly from the populated yrast states with $J^\pi = \frac{1}{2}^-, \frac{3}{2}^-, \frac{5}{2}^-, \frac{7}{2}^-, \frac{9}{2}^-, \frac{11}{2}^-, \frac{13}{2}^-$ and $\frac{15}{2}^-$ and from yrare states of $J^\pi = \frac{7}{2}^-, \frac{9}{2}^-, \frac{11}{2}^-, \frac{13}{2}^-$ and $\frac{15}{2}^-$, as well as the $J^\pi = \frac{3}{2}^+$ state. The negative parity states are expected to be populated directly through one-proton knockout reactions from the $f_{\frac{7}{2},\frac{5}{2}}$ and $p_{\frac{3}{2},\frac{1}{2}}$ shells from the 4^+ ground state of the ^{48}V secondary beam. The $\frac{1}{2}^-$ and $\frac{15}{2}^-$ states can only be populated through a proton knockout from the $f_{\frac{7}{2}}$ shell while the other

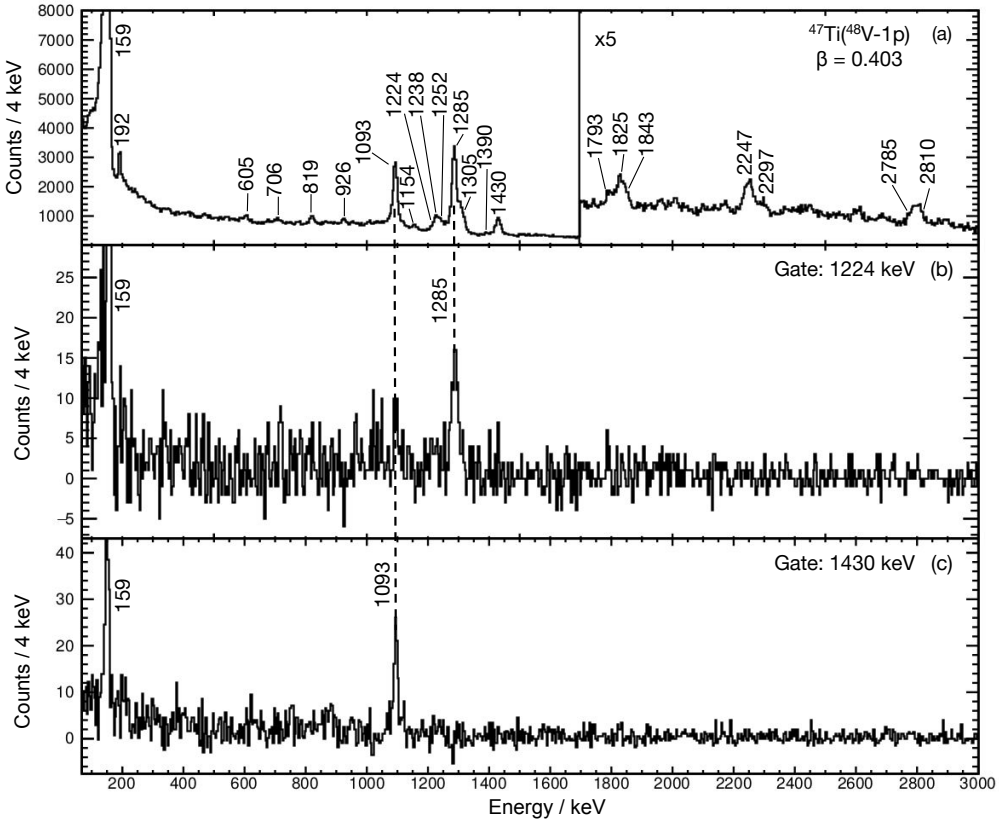

Figure 5.1: (a) The Doppler-corrected energy spectrum for the γ rays in coincidence with ^{47}Ti, which is produced from a one-proton knockout reaction from the ^{48}V secondary beam. To produce the spectrum, an average β value of 0.403(5) was applied. This was because the decay of the $\frac{11}{2}^-_1$ state occurs within the target due to its mean lifetime, τ, being 0.90(14) ps. (b-c) shows the background subtracted γ-γ coincidence analysis for γ rays that are in coincidence with (b) 1224 keV and (c) 1430 keV transitions.

states can be populated by the involvement of higher-lying fp-orbital knockout. Through this direct knockout process from the fp-orbitals, the maximum spin that can be populated is the $J = \frac{15}{2}$. However, states of higher spins are weakly populated, suggesting that this is likely due to either the feeding of unobserved γ rays from directly populated higher-lying states of lower spin (J), a weakly populated isomeric state of higher spin in the beam or by some other higher order reaction mechanism.

The 2668 keV state in ^{47}Ti, where the 1224 keV transition comes from, is assigned to have $J = \frac{9}{2}$ or $\frac{13}{2}$ in the current literature [29]. Although the results from this knockout experiment suggest that the 2668 keV state is negative parity, as this state appears to be directly populated

J_i^π	$T_{\frac{1}{2}}$	E_{J_i}	$J_i^\pi \rightarrow J_f^\pi$	E_γ	E_{J_f}	**R.I.**
$\frac{5}{2}^-_{gs}$	88.000(1) ms	0	-	0	0	-
$\frac{7}{2}^-_1$	210(6) ps	159	$\frac{7}{2}^-_1 \rightarrow \frac{5}{2}^-_1$	159	0	-
$\frac{9}{2}^-_1$	140(13) fs	1252	$\frac{9}{2}^-_1 \rightarrow \frac{7}{2}^-_1$	1093	159	70(3)
		1252	$\frac{9}{2}^-_1 \rightarrow \frac{5}{2}^-_1$	1252	0	0.9(6)
$\frac{11}{2}^{(-)}_1$	0.90(14) ps	1444	$\frac{11}{2}^{(-)}_1 \rightarrow \frac{7}{2}^-_1$	1285	159	100(5)
		1444	$\frac{11}{2}^{(-)}_1 \rightarrow \frac{9}{2}^-_1$	192	1252	9.8(9)
$\frac{3}{2}^-_1$	1.5(4) ps	1549	$\frac{3}{2}^-_1 \rightarrow \frac{7}{2}^-_1$	1390	159	4(3)
$\frac{1}{2}^-_1$	1.7^{+17}_{-6} ps	1793	$\frac{1}{2}^-_1 \rightarrow \frac{5}{2}^-_1$	1793	0	10(3)
$\frac{3}{2}^+_1$	2.1^{+19}_{-7} ps	1825	$\frac{3}{2}^+_1 \rightarrow \frac{5}{2}^-_{gs}$	1825	0	12(5)
$(\frac{7}{2}^-_2)$	<10 ps	2297	$\frac{7}{2}^-_2 \rightarrow \frac{5}{2}^-_{gs}$	2297	0	2(2)
$(\frac{9}{2}^-_2)$	23(7) fs	2406	$\frac{9}{2}^-_2 \rightarrow \frac{7}{2}^-_1$	2247	159	7(4)
		2406	$\frac{9}{2}^-_2 \rightarrow \frac{9}{2}^-_1$	1154	1252	2(1)
$(\frac{13}{2}^-_1)$	21(16) fs	2668	$(\frac{13}{2}^-_1) \rightarrow \frac{11}{2}^{(-)}_1$	1224	1444	15(4)
$\frac{11}{2}^-_2$	>2.10 ps	2682	$\frac{11}{2}^-_2 \rightarrow \frac{9}{2}^-_1$	1430	1252	29(2)
		2682	$\frac{11}{2}^-_2 \rightarrow \frac{11}{2}^{(-)}_1$	1238	1444	3(3)
$\frac{15}{2}^-_1$	1.11(21) ps	2749	$\frac{15}{2}^-_1 \rightarrow \frac{11}{2}^{(-)}_1$	1305	1444	57(5)
$\frac{13}{2}^-_2$	0.51^{+16}_{-10} ps	3288	$\frac{13}{2}^-_2 \rightarrow \frac{11}{2}^{(-)}_1$	1843	1444	11(4)
		3288	$\frac{13}{2}^-_2 \rightarrow \frac{11}{2}^-_2$	605	2682	5(1)
$\frac{17}{2}^-_1$	69(21) ps	3568	$\frac{17}{2}^-_1 \rightarrow \frac{15}{2}^-_1$	819	2749	9(1)
$\frac{15}{2}^-_2$	0.10^{+8}_{-5} ps	3994	$\frac{15}{2}^-_2 \rightarrow \frac{13}{2}^-_2$	706	3288	5(4)
$\frac{19}{2}^-_1$	0.111(28) ps	4494	$\frac{19}{2}^-_1 \rightarrow \frac{17}{2}^-_1$	926	3568	5(1)
	-	2785	$- \rightarrow \frac{5}{2}^-_{gs}$	2785	0	7(5)
	49(23) fs	2810	$- \rightarrow \frac{5}{2}^-_{gs}$	2810	0	16(5)

Table 5.1: The details of the level and γ-ray energies (in keV) observed in this work for the known ^{47}Ti nucleus where states with tentative spin and parity (J^π) values are presented in brackets. All values of energy, lifetimes and J^π values are quoted in accordance to Ref. [29]. The efficiency-corrected relative intensities (R.I.) of the decays observed are presented, relative to the 1285 keV transition, in %. It is important to note that the error of 5% in the R.I of the 1285 keV represents the absolute error intensity. The relative intensity of the first-excited state transition could not be calculated as the γ-ray efficiency is not fully understood at the low-energy region (see main text for details). The states observed in this work but are unknown in terms of J^π are also presented.

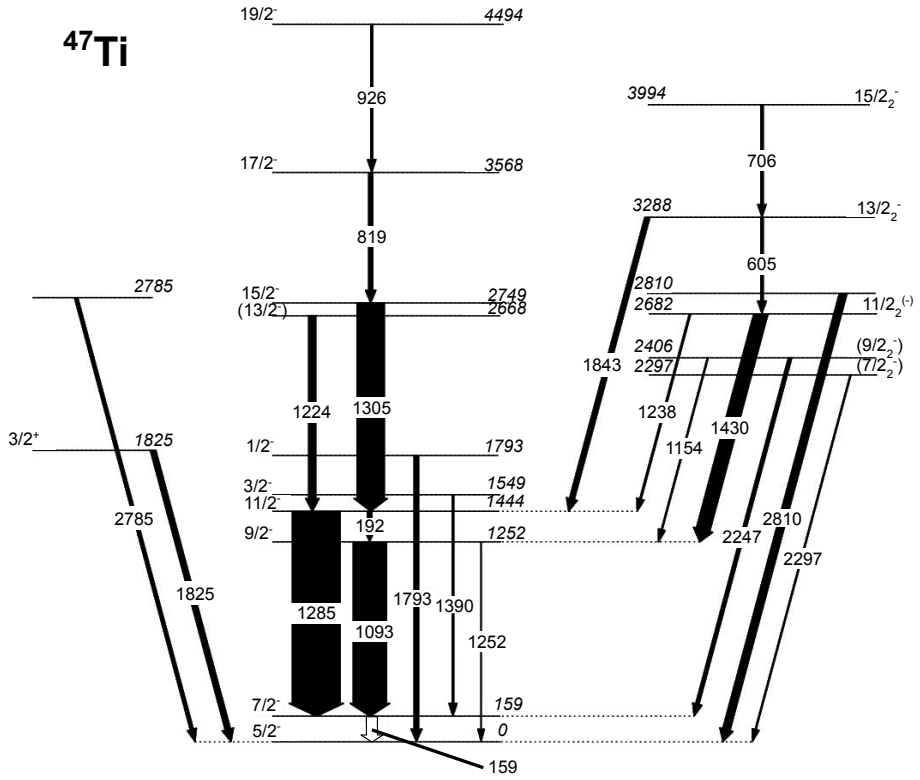

Figure 5.2: The partial level-scheme for the well-known ^{47}Ti neutron-rich nucleus observed in the current analysis. The observed γ rays were ordered by using γ-γ coincidence analysis and were found to be concordant with previous measurements in Ref. [29]. The widths of the arrows represent the relative intensity of the transitions that have been corrected for the efficiency of GRETINA and the Lorentz boost. The relative intensity of the decay from the first-excited state (hollow arrows) have not been measured (see main text for details).

in a similar fashion as the other populated negative-parity states seen in this work, it can be suggested that this state could be either the yrast $\frac{13}{2}^-$ state or the $\frac{9}{2}^-_3$ state. The non-observation of this state in some previous fusion-evaporation reactions suggests that the assignment of $J = \frac{9}{2}$ is unlikely, despite the current evaluation [29], and suggests the preferred assignment of $J = \frac{13}{2}$. Indeed, recent work conducted by Cameron *et. al* have observed an E_γ =1223 keV transition, assumed to be the same transition observed in this work, through heavy-ion fusion-evaporation reactions [110], although this transition was not ultimately placed in their scheme. Due to the nature of fusion-evaporation reactions, it can be suggested that the $\frac{9}{2}^-_3$ state is unlikely to be populated as low-lying yrast states are preferred to be strongly populated. Therefore, the 2668 keV state is tentatively assigned as a $J^\pi = \frac{13}{2}^-$ state in Fig. 5.2. This assumption was made for

the remainder of this analysis.

Only one positive parity state, $J^\pi = \frac{3}{2}^+$, was found to be populated. This is only possible through a direct knockout from the more-bound and deep-lying $d_{\frac{5}{2}}$-shell in the ^{48}V secondary beam. Furthermore, the 2785 keV and 2810 keV states were also observed to be strongly populated where current evaluation data (Ref. [29]) assigns a range of possible J^π values. Therefore, the spin and parity assignments have not been included in the partial level scheme in Fig. 5.2 for these two states.

The relative γ-ray intensities, RI, are presented in Table 5.1 for the γ rays measured in this work for ^{47}Ti. The relative intensities of each γ ray were measured using a Gaussian fitting procedure for each photopeak using the energy singles spectrum (the add-back procedure was not included). Corrections to the absolute intensities of the peaks account for the detector efficiencies, due to Lorentz boost, at the detected lab frame energies (see Chapter 3.4.4 for details). The resulting relative intensities of each measured γ ray were normalised to the 1285 keV transition. The accurate absolute intensity for the $\frac{7}{2}^-_1 \rightarrow \frac{5}{2}^-_1$ transition could not be determined as the γ-ray efficiency at the low-energy region is not fully understood. It is observed that the lineshape of the 159 keV peak extends to energies below 100 keV, as seen in Fig. 5.3, where the shape of the experimental spectra is unknown. Furthermore, with respect to lifetimes, one half-life corresponds to a γ-ray decay that occurs at large distances (>10 cm) downstream of the target, which yields a significant uncertainty in the efficiency.

As a long tailing effect was observed for the $\frac{7}{2}^-_1 \rightarrow \frac{5}{2}^-_1$ transition (see Fig. 5.3), the lifetime and the energy of the yrast $\frac{7}{2}^-$ state were determined. These measurements were made using an identical lineshape analysis described in Ref. [24] by fitting the experimental spectrum with a simulation (see Chapter 7 for details).

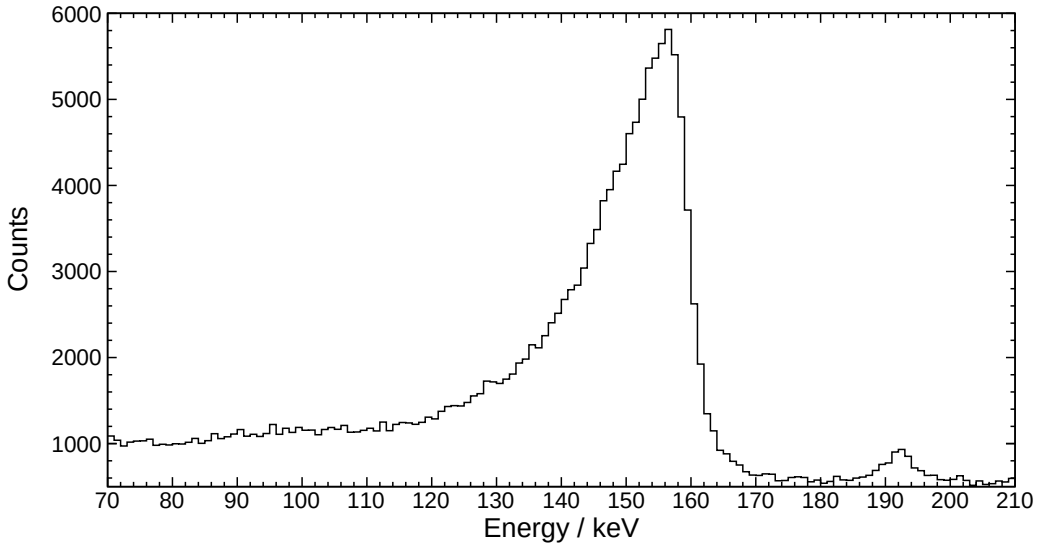

Figure 5.3: The lineshape observed for the $\frac{7}{2}^-_1 \rightarrow \frac{5}{2}^-_1$, 159 keV transition in ^{47}Ti. A long-tailing effect was observed for this transition, which extends to energies below 100 keV. Therefore, the lifetime and the energy of the $\frac{7}{2}^-_1$ state were determined using the lineshape analysis method described in Ref. [24].

5.1.2 Spectroscopy of ^{47}Mn

The Doppler corrected γ-ray spectra for the proton-rich ^{47}Mn nuclei are presented in Fig. 5.4(a), where new states up to 3568 keV are observed in this work. The errors in the measured γ ray transitions in ^{47}Mn arise from the statistical error of the Gaussian fits performed and the systematic errors due to the target position and the recoil velocity. The systematic error in the z-target position was assumed to have a 0.5 mm shift. For the recoil velocity (β), the systematic error was found to be 0.005, determined by systematically varying the β of the fast 1053 keV transition in ^{47}Mn until a straight line was clearly observed (see section 4.6.2 for details). Therefore, the total systematic error in the energy of the 1053 keV transition, taking into account the z-position of the target and β, is 0.5 keV. All γ rays identified in the spectrum are placed in a new level scheme for ^{47}Mn (see Fig. 5.5).

The placement of the strongest transitions in the unknown ^{47}Mn nucleus was initially deduced based on mirror symmetry arguments. The placement of these strong transitions in Fig. 5.4(a) have been confirmed via a γ-γ coincidence analysis and by intensity arguments. All observed

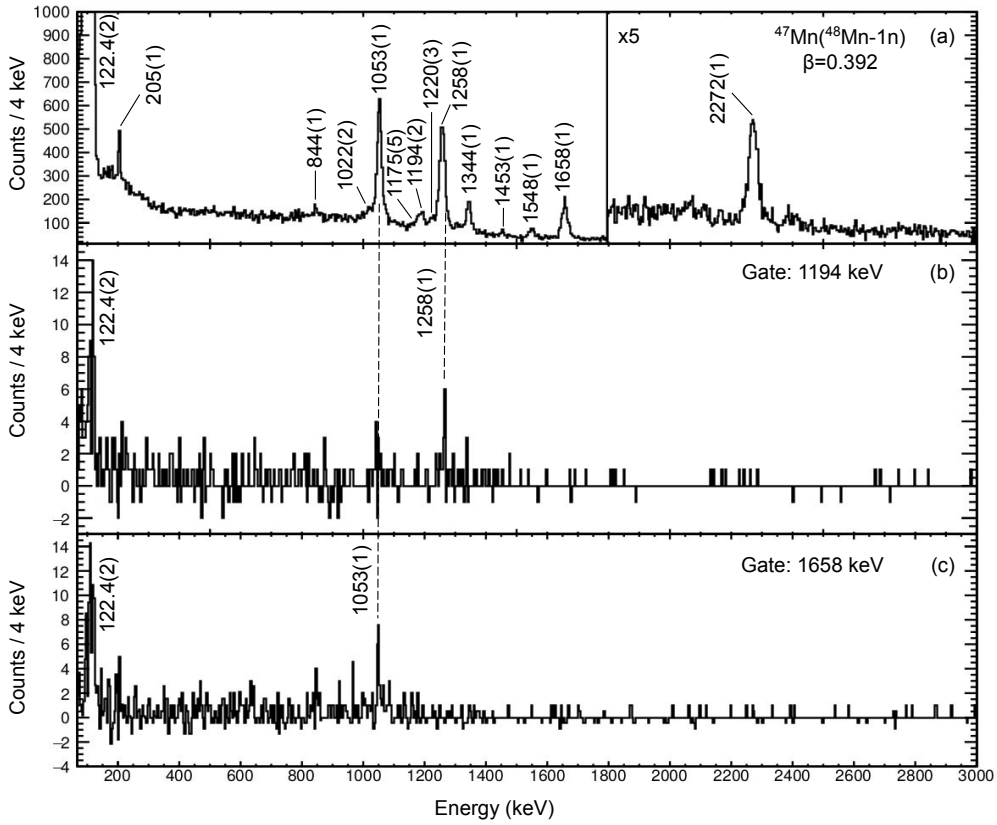

Figure 5.4: The Doppler corrected spectrum for the observed γ rays in coincidence with (a) ^{47}Mn, produced via a one-neutron knockout reaction from the ^{48}Mn secondary beam. The spectrum was obtained using the cluster add-back prescription and was optimised for the fast 1053 keV transition using a β value of 0.392(5) (based on mirror arguments). (b-c) shows the background subtracted γ-γ coincidence spectra in coincidence with (b) 1194 keV and (c) 1658 keV transitions in ^{47}Mn that the analogue transitions of the 1224 keV and 1430 keV γ rays in ^{47}Ti.

peaks in this work were analysed using $\gamma - \gamma$ coincidence analysis. Examples of coincidence spectra, gated on the 1194 keV and 1658 keV transitions, are shown in Figs. 5.4(b) and (c), respectively. These coincidence spectra are equivalent to the analogue 1224 keV and 1430 keV transitions in ^{47}Ti, respectively (see Figs. 5.1(b) and (c)). The same coincidence patterns have been observed in the analysis of both mirror nuclei.

The 122 keV transition in Fig. 5.4(a) is observed to be the analogue transition of the 159 keV transition in ^{47}Ti. As observed for the 159 keV transition, a similar peak shape is seen in ^{47}Mn, indicating that the lifetime of the yrast $\frac{7}{2}^-_1$ state is of the order of hundreds of ps. To concurrently determine the precise γ-ray energy of the transition and the lifetime of the state, an identical

lineshape analysis to that in Ref. [24] was performed, where the experimental spectrum was fitted with a simulation (see Chapter. 7 for details). Only the γ-ray energy of 122.4(2) keV was required to assign the $\frac{7}{2}^{-}_{1} \rightarrow \frac{5}{2}_{gs}$ transition in the level scheme in Fig. 5.5.

The spin and parity (J^{π}) assignments for the new states in ^{47}Mn, observed in this work, are based on mirror symmetry argumentation by comparing the measured energies of the observed states. As both the ^{47}Mn and ^{47}Ti nuclei are produced through mirrored direct knockout reactions, it can be assumed that the distribution of the population strength should be similar to each other due to isospin symmetry.

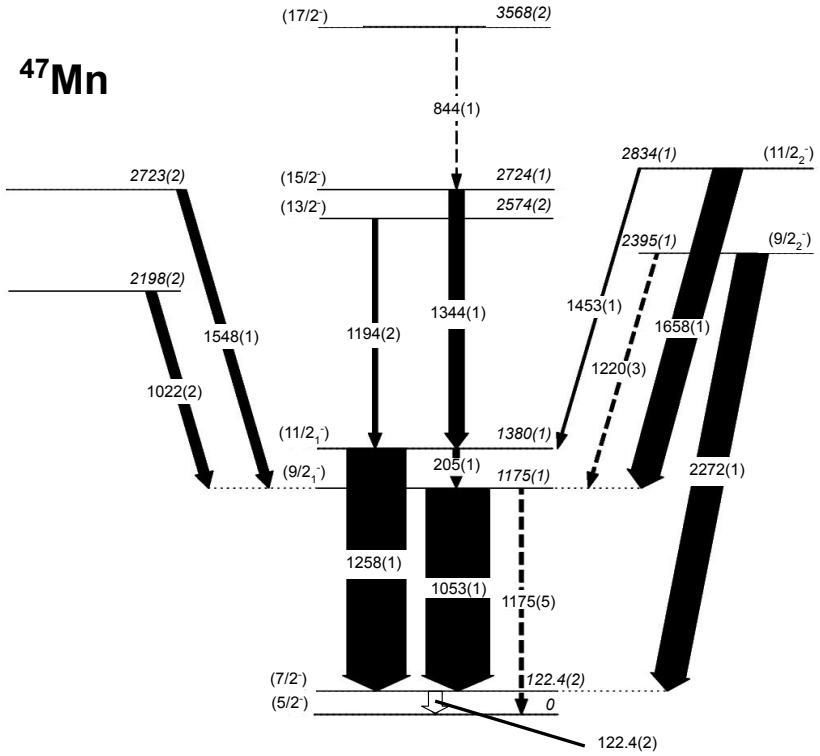

Figure 5.5: The new level-scheme for the proton-rich ^{47}Mn nucleus. The γ rays were initially ordered by using mirror symmetry arguments, where the placements of these γ rays have been confirmed via γ-γ coincidence analysis. Some observed states are not assigned a J^{π} value as the analogue transitions have not been observed in ^{47}Ti. Tentatively assigned spins and parities are assigned by parenthesis. The widths of the arrows represent the intensity of the transitions, corrected for the boosted-efficiency of GRETINA. The intensity of the decay from the first-excited state (hollow arrow) has not been measured as the efficiency of γ rays at lower energies is not fully determined. Tentative transitions are presented in dashed lines.

By comparing to ^{47}Ti, the pattern of the yrast states populated through direct fp-shell knockouts in ^{47}Mn is reasonably clear as similar energies and feeding sequences of the γ-ray transitions were observed. From $\gamma - \gamma$ coincidence analysis, it can be shown that the 844 keV transition, which decays from the 3568 keV state, feeds into the 2724 keV state (see Fig. 5.5). Therefore, the 3568 keV state is tentatively assigned as the $\frac{17}{2}^-_1$ state. The population of this state cannot occur from a direct fp-shell knockout reaction and can only be populated via indirect feeding from higher J^π states or from an unknown isomer state in the ^{48}Mn secondary beam.

The 2834 keV state in ^{47}Mn is assigned tentatively to have a spin and parity of $\frac{11}{2}^-_2$. In ^{47}Ti, the strong transition of 1430 keV from the analogue state feeds the yrast $\frac{9}{2}^-_1$ state, indicating that this state is strongly populated via the knockout reaction. By assuming mirror symmetry, a similarly strong transition is also expected to feed the 1175 keV state in ^{47}Mn. Two possible candidates, being the 1548 keV and 1658 keV transitions, were found to feed the $\frac{9}{2}^-_1$ keV state via $\gamma - \gamma$ analysis. From Fig. 5.5, the 1658 keV was found to have a significantly higher intensity of 45(4)%, which is a factor of three higher than the relative intensity of the 1548 keV transition, being 15(3)%. Therefore the 2834 keV state is tentatively assigned to have the spin and parity of $\frac{11}{2}^-_2$. This state also decays to the yrast $\frac{11}{2}^-_1$ state with a 1453 keV transition, exhibiting the same decay pattern in ^{47}Ti for the 2682 keV state, where this transition corresponds to the analogue 1238 keV transition in ^{47}Ti.

For the 2395 keV state in ^{47}Mn, a strong, high-energy 2272 keV transition decays to the first-excited state. By comparing this decay pattern to ^{47}Ti, the direct population of non-yrast $\frac{9}{2}^-_2$ state feeds into the $\frac{7}{2}^-_1$ state with a 2247 keV γ-ray transition. Therefore, the 2395 keV state in ^{47}Mn is tentatively assigned as the $\frac{9}{2}^-_2$ state. Furthermore, a weaker 1220 keV transition was also observed. Due to weak statistics, $\gamma - \gamma$ coincidence analysis did not provide further information. Therefore, based on the sum of the energies, this transition was found to add up correctly with the 1175(5) keV transition to the 2395(1) keV state. Hence, the 1220 keV transition was tentatively assigned to come from the $\frac{9}{2}^-_2$ state. Through mirror symmetry arguments, this transition would correspond to the analogue 1154 keV transition in ^{47}Ti. The 2198 keV and 2723 keV states, both observed in ^{47}Mn, do not have spin and parity assignments as the corresponding analogue states could not be identified in ^{47}Ti.

The measured γ-ray energies and the relative γ-ray intensities, RI, seen in this work are

J_i^π	E_{J_i}	$J_i^\pi \rightarrow J_f^\pi$	E_γ	E_{J_f}	**R.I.**
$(\frac{5}{2}^-_{gs})$	0	-	0	0	-
$(\frac{7}{2}^-_1)$	122.4(2)	$(\frac{7}{2}^-_1) \rightarrow (\frac{5}{2}^-_1)$	122.4(2)	0	-
$(\frac{9}{2}^-_1)$	1175(1)	$(\frac{9}{2}^-_1) \rightarrow (\frac{7}{2}^-_1)$	1053(1)	122.4(2)	100(5)
	1175(1)	$(\frac{9}{2}^-_1) \rightarrow (\frac{5}{2}^-_1)$	1175(5)	0	5(4)
$(\frac{11}{2}^-_1)$	1380(1)	$(\frac{11}{2}^-_1) \rightarrow (\frac{7}{2}^-_1)$	1258(1)	122.4(2)	93(5)
	1380(1)	$(\frac{11}{2}^-_1) \rightarrow (\frac{9}{2}^-_1)$	205(1)	1175(1)	10(2)
$(\frac{9}{2}^-_2)$	2395(1)	$(\frac{9}{2}^-_2) \rightarrow (\frac{7}{2}^-_1)$	2272(1)	122.4(2)	49(5)
	2395(1)	$(\frac{9}{2}^-_2) \rightarrow (\frac{9}{2}^-_1)$	1220(3)	1175(1)	4(3)
$(\frac{13}{2}^-_1)$	2574(2)	$(\frac{13}{2}^-_1) \rightarrow (\frac{11}{2}^-_1)$	1194(2)	1380(1)	7(4)
$(\frac{11}{2}^-_2)$	2834(1)	$(\frac{11}{2}^-_2) \rightarrow (\frac{9}{2}^-_1)$	1658(1)	1175(1)	45(4)
	2834(1)	$(\frac{11}{2}^-_2) \rightarrow (\frac{11}{2}^-_1)$	1453(1)	1380(1)	3(1)
$(\frac{15}{2}^-_1)$	2724(1)	$(\frac{15}{2}^-_1) \rightarrow (\frac{11}{2}^-_1)$	1344(1)	1380(1)	24(4)
$(\frac{17}{2}^-_1)$	3568(2)	$(\frac{17}{2}^-_1) \rightarrow (\frac{15}{2}^-_1)$	844(1)	2724(1)	1(1)
	2198(2)	$- \rightarrow (\frac{9}{2}^-_1)$	1022(2)	1175(1)	16(9)
	2723(2)	$- \rightarrow (\frac{9}{2}^-_1)$	1548(1)	1175(1)	15(3)

Table 5.2: The details of the level and γ-ray energies (in keV) observed for the previously unreported ^{47}Mn nucleus. States with tentative spin and parity (J^π) values are presented in brackets. The efficiency-corrected relative intensities (R.I.) of the decays observed are presented, relative to the 1053 keV transition, in %. The relative intensity of the first-excited state transition could not be calculated due to the lack of information about the absolute γ-ray efficiency at this low-energy region (see main text for details). The states that are unknown in terms of J^π are also presented.

presented in Table 5.2 for ^{47}Mn. The relative intensities of each γ ray were measured using the same approach detailed in Section 5.1.1, using the spectrum that does not have add-back applied. The relative intensities are normalised to the 1053 keV transition. The absolute intensity of the 122.4(2) keV transition from the first-excited state, presented as a hollow arrow in Fig.5.5, could not be accurately determined due to reasons stated in Section 5.1.1 as the γ-ray efficiency at these low energies is not fully understood.

From Fig. 5.5, the yrast $J^\pi = \frac{7}{2}^-, \frac{9}{2}^-, \frac{11}{2}^-$ and $\frac{15}{2}^-$ and yrare $J^\pi = \frac{9}{2}^-$ and $\frac{11}{2}^-$ states were populated through the knockout reaction. The population of the two yrare states were found to exhibit comparable intensities to their corresponding yrast states.

5.1.3 Comparison with Predicted Knockout Strengths

A quantitative comparison of the experimental observations to the predicted distribution of the one-nucleon knockout strength is useful to understand the population of the states seen. Theoretical knockout cross sections were calculated for the lowest three states of each J^π between $\frac{1}{2}^-$ to $\frac{15}{2}^-$. The predictions were undertaken using eikonal reaction dynamics, assuming a spectator core approximation [71], [73], Hartree-Fock constrained nucleon form factors and shell-model spectroscopic factors. The latter was obtained in the full fp-space using the KB3G interaction [111] within the ANTOINE code [31], [32]. Fig. 5.6 demonstrates the results in ^{47}Mn, where theoretical cross sections $\geq$0.1% of the total predicted cross section are presented as a function of the excitation energies obtained from the shell-model calculation. A broad agreement can be

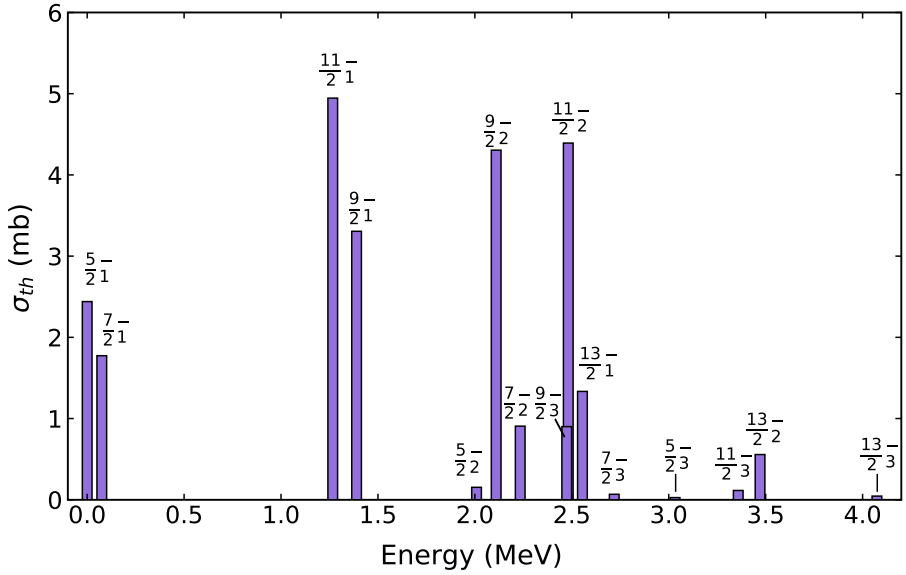

Figure 5.6: The theoretical cross sections for the lowest-three states of each J^π between $J^\pi = \frac{1}{2}^-$ to $\frac{15}{2}^-$ in ^{47}Mn. The excitation energies are obtained from the shell-model calculations. States that have theoretical cross sections $\leq$0.1% of the total predicted cross section are not included.

seen between the experimental observations and the theoretical distributions of the knockout strength, where, in both cases, the yrast $J^\pi = \frac{7}{2}^-, \frac{9}{2}^-$ and $\frac{11}{2}^-$ states and the non-yrast $\frac{9}{2}^-_2$ and $\frac{11}{2}^-_2$ states were found to be strongly populated. However, the $\frac{15}{2}^-_1$ state was found to be strongly populated in the experiment with notable intensity, despite that the theoretical cross section for this state (see Fig. 5.6) becomes insignificant. As seen for the $J^\pi = \frac{17}{2}^-$ state, it is

possible that the cause of the strong population of the $\frac{15}{2}^-_1$ yrast state in the experiment is due to unseen feeding from high-spin states. Detailed comparisons between the experimental and theoretical cross sections for the observed states in this work are shown in Chapter 6.

5.2 Population of states in the $A = 45$ mirror pair

As in the $A = 47$ mirror-nuclei, the same approach was performed to study the proton-rich ^{45}Cr ($T_z = -\frac{3}{2}$) nucleus and its well-known, stable, mirror nucleus ^{45}Sc ($T_z = +\frac{3}{2}$), populated through a two-neutron knockout and a two-proton removal reaction from the ^{47}Cr ($T_z = -1$) and ^{47}V ($T_z = +1$) secondary beams, respectively. To understand the ordering of the observed γ rays

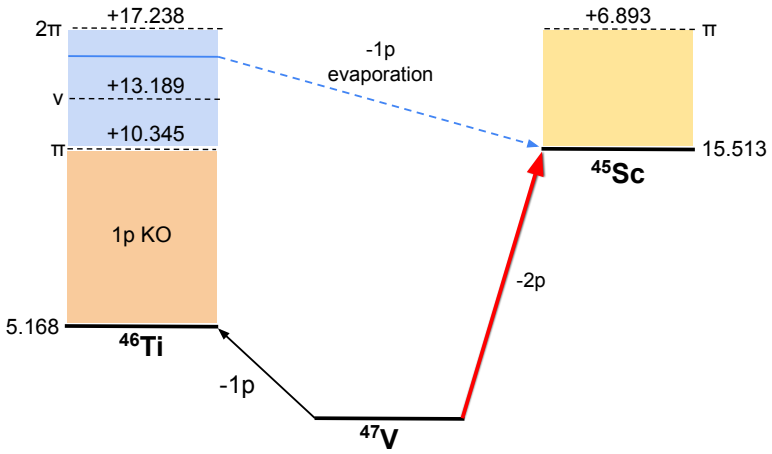

Figure 5.7: The schematic diagram comparing the two paths taken to produce ^{45}Sc, causing a mixture of direct and indirect processes. The direct two-proton process is shown by the red arrow. It can be seen that in the indirect two-proton removal reaction, proton knockout followed by proton-evaporation is possible as the one-neutron separation energy is greater than the proton-separation energy. Both of these paths are indistinguishable. Idea adapted from Ref. [112].

in ^{45}Cr, where only the $J^\pi = \frac{3}{2}^+ \rightarrow \frac{7}{2}^-$ transition is tentatively known [4], the identification of which states are populated in the known ^{45}Sc nucleus is required.

It is important to note that the ^{47}V$-2p \rightarrow^{45}$Sc reaction is likely to consist of a mixture of direct ($-2p$ knockout) and indirect reactions (i.e. a two-step process that involves a proton knockout, subsequently followed by proton-evaporation) which cannot be distinguished [112]. The indirect processes occur as energies beyond the proton-separation energy of 15.51 MeV in

^{46}Ti can be attained as a result of a proton knockout from ^{47}V, allowing for a proton to be evaporated (see Fig. 5.7). Hence, this process is energetically allowed to produce ^{45}Sc, as well as direct $-2p$ knockout.

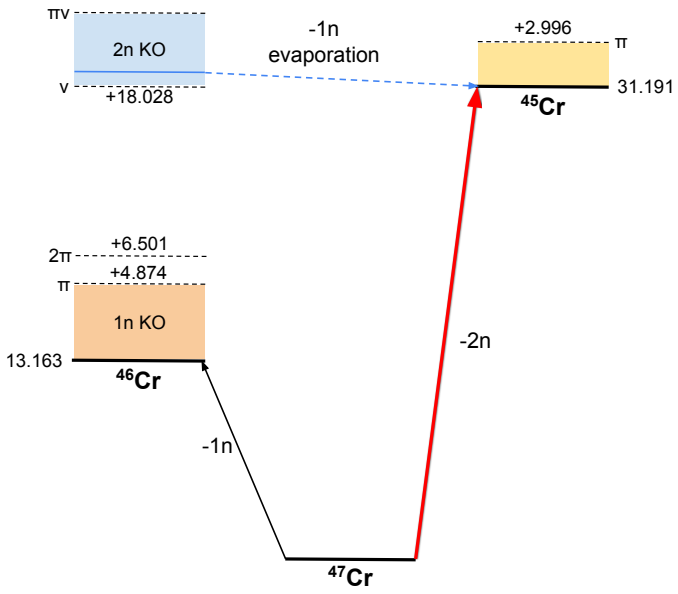

Figure 5.8: The schematic diagram comparing the possible paths that could be taken to produce ^{45}Cr. It can be seen that in the direct two-neutron knockout reaction (red), is preferred when compared to the indirect neutron-knockout followed by the neutron-evaporation reaction. This is due to the one-neutron separation energy being greater than the one- and two-proton separation energies in ^{46}Cr. Therefore, the two-neutron knockout reaction becomes energies energetically favourable to produce the ^{45}Cr nuclei. Idea adapted from Ref. [112].

In contrast, for the production of ^{45}Cr, the neutron-knockout from ^{47}V$-n \rightarrow^{46}$Cr followed by neutron-evaporation to produce ^{45}Cr is not energetically favourable as the neutron separation energy in ^{46}Cr is significantly higher than the one- and two-proton separation energies. Therefore, it is likely that protons will be evaporated in this two-step pathway rather than neutrons (see Fig. 5.8). As a result, this process becomes energetically unfavourable leading to the direct two-neutron knockout process being dominant to produce ^{45}Cr nuclei. It must be assumed that the ^{47}V$-2p \rightarrow^{45}$Sc reaction is not the analogue reaction of ^{47}V$-2n \rightarrow^{45}$Cr - see Figs. 5.7 and 5.8.

This section details how the assumption of mirror symmetry has been applied to assign the observed γ-ray transitions and states in the unknown, proton-rich ^{45}Cr nucleus.

5.2.1 Spectroscopy of ^{45}Sc

The event-by-event Doppler-corrected γ-ray spectrum in coincidence with the well-known neutron-rich and stable ^{45}Sc nucleus is shown in Fig. 5.9(a).

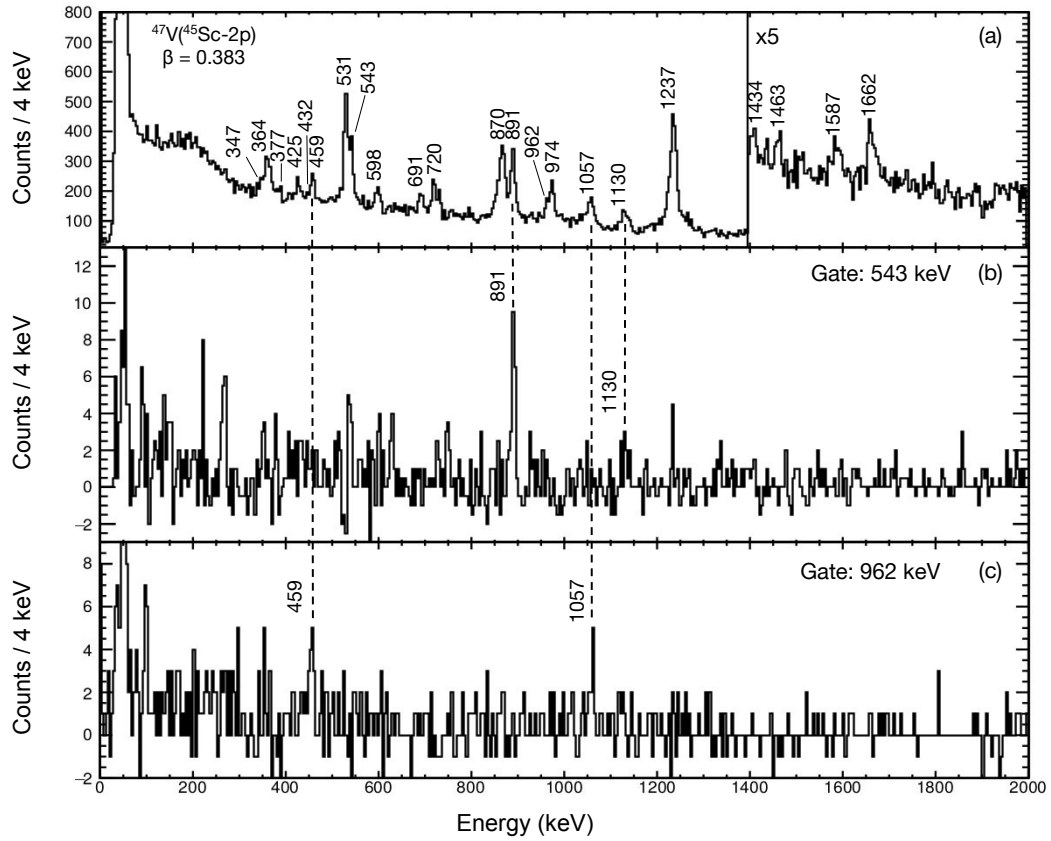

Figure 5.9: (a) The Doppler corrected spectrum for the observed γ rays in coincidence with ^{45}Sc, produced by removing two protons from the ^{47}V secondary beam. The spectrum was obtained using the cluster add-back prescription and the β was optimised for the fast 1237 keV transition, where it was 0.383(5). (b-c) shows the background subtracted γ-γ coincidence spectra in coincidence with (b) 543 keV and (c) 962 keV transitions in ^{45}Sc. The energies measured for each transition were found to be in agreement with previous measurements in Ref. [113]–[115].

To determine the optimum velocity for the Doppler-corrected γ-ray spectrum in Fig. 5.9(a), the 1237 keV transition ($\frac{11}{2}^- \rightarrow \frac{7}{2}^-_{gs}$) in ^{45}Sc was utilised as the adopted lifetime of the $\frac{11}{2}^-$ state is known to be 2.6(1) ps [113], indicating that this γ ray is produced within the 1mm-thick ^{9}Be reaction target, immediately at the point of the production for each ^{45}Sc nucleus. The resulting optimum velocity, being 0.383(5), was used to optimise the spectrum in Fig. 5.9(a).

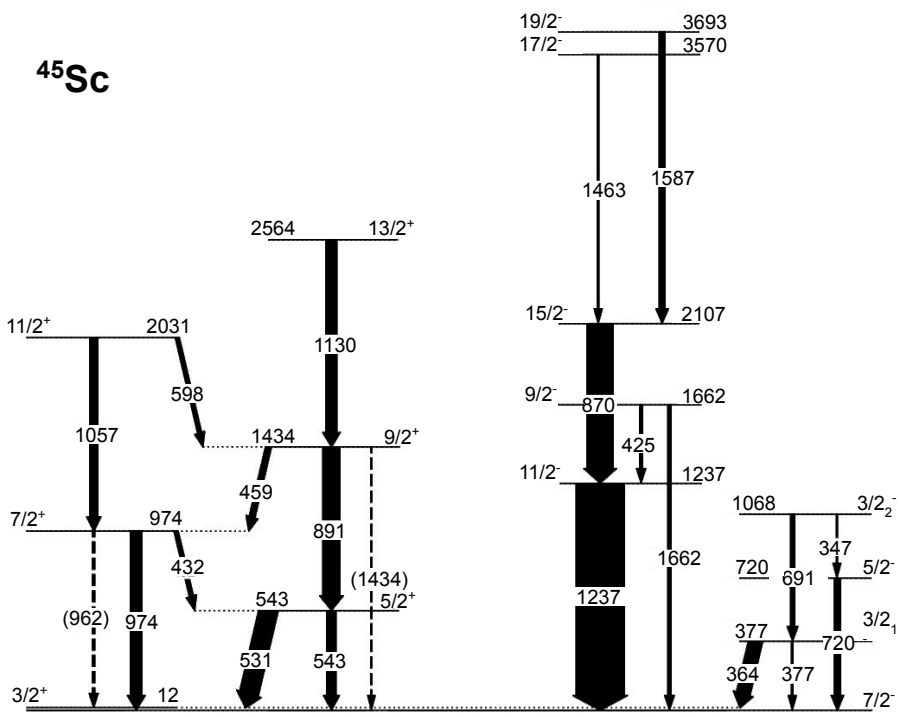

Figure 5.10: The level scheme for the stable, neutron-rich ^{45}Sc nucleus. The placement of the γ rays were made using mirror symmetry arguments and $\gamma - \gamma$ coincidence analysis. The energies and the ordering of the transitions were found to be concordant with previous measurements made in Ref. [114], [115]. Observed transitions that could not be analysed through $\gamma - \gamma$ coincidences, due to weak statistics, are labelled using dashed lines. The widths of the arrows represent the transitions that are corrected for the boosted efficiency of GRETINA. The relative γ-ray intensities for all γ rays are calculated relative to the $\frac{11}{2}^-$ to $\frac{7}{2}^-$ transition. Table 5.3 states the transitions that decay to the $\frac{3}{2}^+$ state and the $\frac{7}{2}^-$ ground state, respectively.

The decay from the long-lived, isomeric $J^\pi = \frac{3}{2}^+$, 12 keV state was not observed in this analysis due to its long lifetime of 326 ms. The observed cascade of γ-ray transitions for ^{45}Sc are presented in Fig. 5.10, where states were observed up to an energy of 3693 keV. Through the removal of two protons, both the negative and positive-parity states were populated, where the latter exhibits an interleaving structure as a result of the rotational band, built upon the low-lying $J^\pi = \frac{3}{2}^+$ state. This observation appears to exhibit a deformed nucleus as the energy spacing between the positive-parity band appears to be regular, which increases with excitation energy. This observation suggests a deformed rotor. Indeed, the population of $J^\pi = \frac{3}{2}^+$ state is likely due to the single-proton excitation from the $d_{\frac{3}{2}}$ orbital, which only comes near the Fermi level for deformed prolate shapes.

Some of the observed transitions were analysed via γ-γ coincidence analysis, as shown in Figs. 5.9(b-c) for the 543 keV and 962 keV transitions, respectively. All of the measured energies and coincidence relations in this analysis were in good agreement with previous work (see Refs. [113]–[117]). The relative γ-ray intensities, RI, are measured in reference to the 1237 keV transition, using the identical approach detailed in Section 5.1.1, for ^{45}Sc. The relative intensities are presented in Table 5.3.

Negative-parity states up to $J^\pi = \frac{15}{2}^-$ can be populated in ^{45}Sc when two protons from the $f_{\frac{7}{2}}$ and $f_{\frac{5}{2}}$-orbitals, coupled to $J_{max} = 6$, are removed from the $J^\pi = \frac{3}{2}^-$ ground state of ^{47}V. Similarly, positive-parity states up to $J^\pi = \frac{15}{2}^+$ can also be populated by removing one $d_{\frac{5}{2}}$ proton and another proton from the $f_{\frac{7}{2}}$-orbital, again when coupled to $J_{max} = 6$. States up to and beyond these predictions are weakly observed in both bands in Fig. 5.10, indicating that the indirect processes are likely to contribute significantly to the population of the higher-spin states. It is also possible that the presence of weakly-populated high-spin isomer states in the secondary beam might contribute to the population of higher-spin states in ^{45}Sc.

5.2.2 Spectroscopy of ^{45}Cr

No prior information on the structure of ^{45}Cr is known apart from the tentative location of the $J^\pi = \frac{3}{2}^+$ isomeric state [4]. A 107(1) keV γ-ray transition from this long-lived state, having a lifetime of $>80\mu s$, was observed in ^{45}Cr in a decay-spectroscopy experiment following a fragmentation reaction. Based on mirror symmetry arguments, this transition was assumed to be the analogue of the 12 keV transition from the $J^\pi = \frac{3}{2}^+$ state in ^{45}Sc. This previously known result was critical to establish the sequence of the observed γ-ray transitions in the new level scheme of ^{45}Cr.

The event-by-event Doppler-corrected γ-ray spectrum for the neutron-rich ^{45}Cr residues is shown in Fig. 5.11(a), produced through a two-neutron knockout reaction from the $T = -\frac{1}{2}$ ^{47}Cr secondary beam. An optimum velocity of 0.386 was obtained for the Doppler correction using the 1245 keV transition (i.e. the analogue transition of the 1237 keV transition in ^{45}Sc). By using a combination of mirror symmetry argumentations, $\gamma - \gamma$ coincidence analysis and γ-ray intensities, the placement of the transitions observed of Fig. 5.11(a) are tentatively assigned in a new level scheme in ^{45}Cr in Fig. 5.12. The following paragraph explains the logic of the

J_i^π	$T_{\frac{1}{2}}$	E_{J_i}	$J_i^\pi \rightarrow J_f^\pi$	E_γ	E_{J_f}	**R.I.**
$\frac{3}{2}^-_1$	43.3(23) ps	377	$\frac{3}{2}^-_1 \rightarrow \frac{7}{2}^-_{gs}$	377	0	4(2)
		377	$\frac{3}{2}^-_1 \rightarrow \frac{3}{2}^+_1$	364	12	29(4)
$\frac{5}{2}^+_1$	5.5(6) ps	543	$\frac{5}{2}^+_1 \rightarrow \frac{7}{2}^-_{gs}$	543	0	20(4)
		543	$\frac{5}{2}^+_1 \rightarrow \frac{3}{2}^+_1$	531	12	40(4)
$\frac{5}{2}^-_1$	206(16) fs	720	$\frac{5}{2}^-_1 \rightarrow \frac{7}{2}^-_{gs}$	720	0	13(5)
$\frac{7}{2}^+_1$	2.54(23) ps	974	$\frac{7}{2}^+_1 \rightarrow \frac{7}{2}^-_{gs}$	974	0	24(4)
		974	$\frac{7}{2}^+_1 \rightarrow \frac{3}{2}^+_1$	962	12	6(2)
		974	$\frac{7}{2}^+_1 \rightarrow \frac{5}{2}^+_1$	432	543	8(5)
$\frac{3}{2}^-_2$	0.28(6) ps	1068	$\frac{3}{2}^-_2 \rightarrow \frac{3}{2}^-_1$	691	377	9(3)
		1068	$\frac{3}{2}^-_2 \rightarrow \frac{5}{2}^-_1$	347	720	3(2)
$\frac{11}{2}^-_1$	1.80(10) ps	1237	$\frac{11}{2}^-_1 \rightarrow \frac{7}{2}^-_{gs}$	1237	0	100(6)
$\frac{9}{2}^+_1$	3.6(18) ps	1434	$\frac{9}{2}^+_1 \rightarrow \frac{5}{2}^+_1$	891	543	36(4)
		1434	$\frac{9}{2}^+_1 \rightarrow \frac{7}{2}^+_1$	459	974	12(3)
		1434	$\frac{9}{2}^+_1 \rightarrow \frac{7}{2}^-_{gs}$	1434	0	3(1)
$\frac{9}{2}^-_1$	98(10) ps	1662	$\frac{9}{2}^-_1 \rightarrow \frac{7}{2}^-_{gs}$	1662	0	7(2)
		1662	$\frac{9}{2}^-_1 \rightarrow \frac{11}{2}^-_1$	425	1237	6(3)
$\frac{11}{2}^+_1$	$0.76(^{+12}_{-8})$ ps	2031	$\frac{11}{2}^+_1 \rightarrow \frac{7}{2}^+_1$	1057	974	17(5)
		2031	$\frac{11}{2}^+_1 \rightarrow \frac{9}{2}^+_1$	598	1434	9(2)
$\frac{15}{2}^+_1$	>1.4 ps	2107	$\frac{15}{2}^+_1 \rightarrow \frac{11}{2}^+_1$	870	1237	55(4)
$\frac{13}{2}^+_1$	1.0(3) ps	2564	$\frac{13}{2}^+_1 \rightarrow \frac{9}{2}^-_1$	1130	1434	23(5)
$\frac{17}{2}^-_1$	<0.07 ps	3570	$\frac{17}{2}^-_1 \rightarrow \frac{15}{2}^-_1$	1463	2107	4(2)
$\frac{19}{2}^-_1$	1.39(14) ps	3693	$\frac{19}{2}^-_1 \rightarrow \frac{15}{2}^-_1$	1587	2107	13(4)

Table 5.3: The level and γ-ray energies (in keV) that have been measured in this work for the known ^{45}Sc nucleus. All values of energy and lifetimes are quoted from Ref. [113]. The efficiency-corrected relative intensities (R.I.) of the decays observed are presented in %, relative to the 1237 keV transition.

assignments and the ordering of the transitions seen.

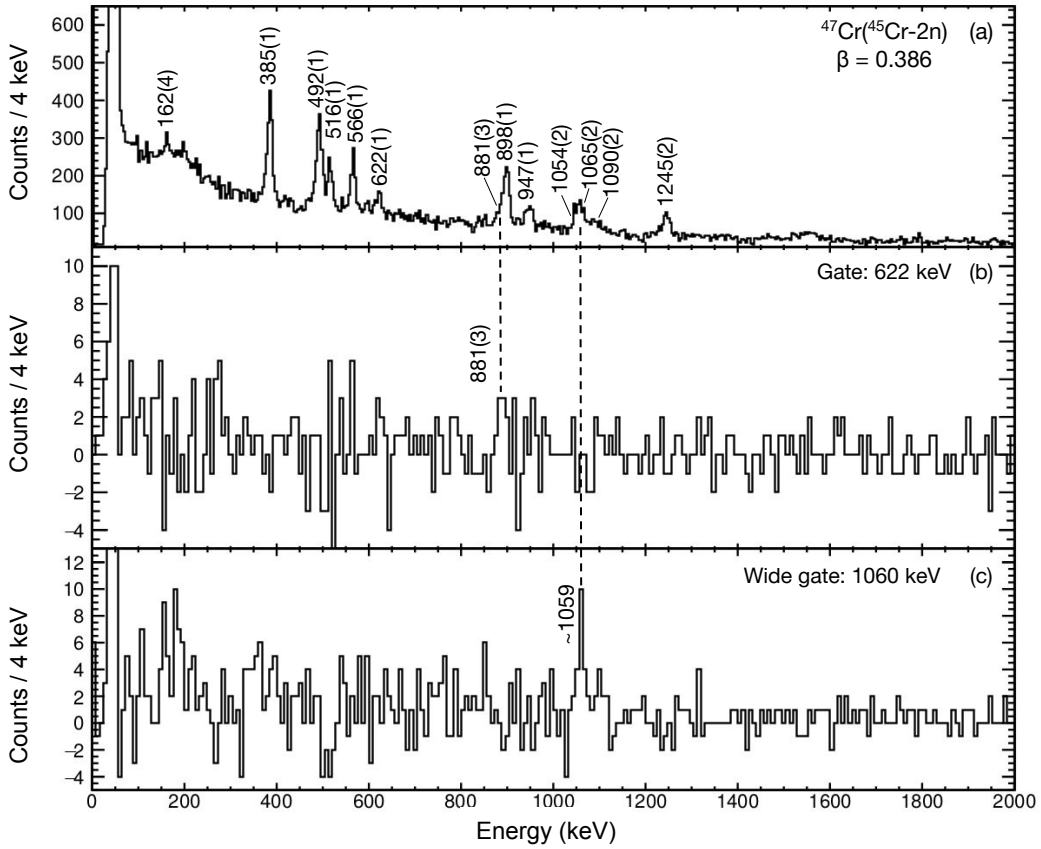

Figure 5.11: (a) The Doppler corrected spectrum for the observed γ rays in coincidence with ^{45}Cr, produced via a two-neutron knockout reaction from the ^{47}Cr secondary beam. The spectrum was obtained using the cluster add-back prescription and the β was optimised for the "fast" 1245 keV transition using a β value of 0.386(5), which is the analogue of the 1237 keV transition in ^{45}Sc based on mirror arguments. (b-c) shows the background subtracted γ-γ coincidence spectra in coincidence with (b) 622 keV and (c) 1060 keV transitions in ^{45}Cr, which are the analogue transitions of the 543 keV and 962 keV transitions in ^{45}Sc, respectively. The wide gate, of average energy of 1060 keV, was taken between 1044-1075 keV from the coincidence spectrum. This gate covers both the 1054- and the 1065 keV transitions.

From the observation of the labelled transitions in Fig. 5.11(a), three pairs of γ rays were found to be separated by 107(1) keV, which is equivalent to the energy of the decay from the $J^\pi = \frac{3}{2}^+$ isomer state in ^{45}Cr. The 947/1054, 516/622 and 385/492 keV transitions were found to exhibit this difference, and coupled with the strong intensities observed for each γ ray, these transitions were assigned to decay to the $J^\pi = \frac{3}{2}^+$ isomer and the $J^\pi = \frac{7}{2}^-$ ground state, respectively. By

comparing these transitions to the mirror nucleus, ^{45}Sc, the analogue transitions are the 962/974, 531/543 and 364/377 keV transitions, respectively. Therefore, the respective states from where these pair of transitions come from are assigned as $J^{\pi} = \frac{7}{2}^{+}, \frac{5}{2}^{+}$ and $\frac{3}{2}^{-}_{1}$ in ^{45}Cr, as shown in Fig. 5.12. Other transitions were assigned by deploying $\gamma - \gamma$ coincidence analysis to the new level scheme, despite having low statistics.

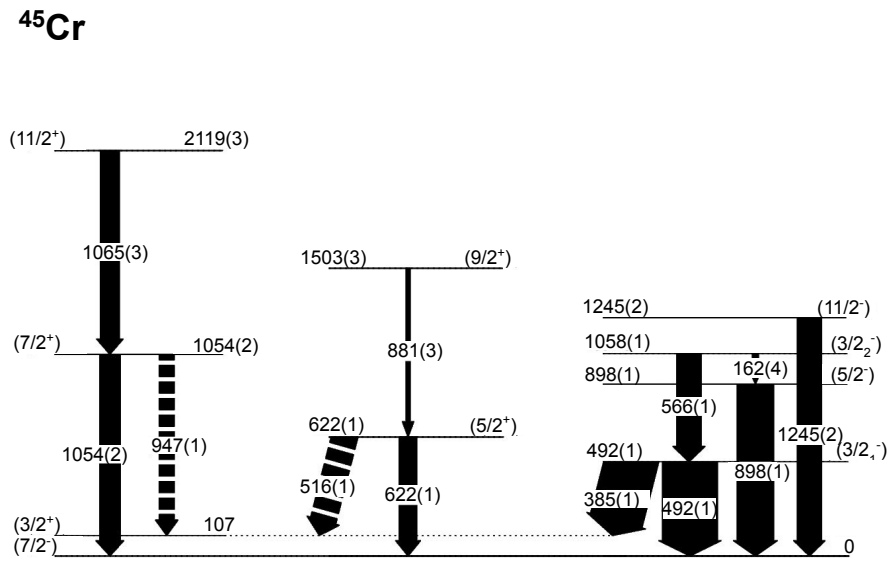

Figure 5.12: The previously unreported level scheme observed in this work for the proton-rich ^{45}Cr nucleus. The observed γ rays were ordered by using mirror symmetry arguments and γ-γ coincidence analysis. The spins and parities in the tentative level scheme of ^{45}Cr are in brackets since these assignments have been made based on mirror symmetry arguments. Tentative transitions are labelled using dashed lines. The widths of the arrows represent the relative intensities, corrected for the efficiency of GRETINA, for each measured γ ray, relative to the $\frac{3}{2}^{-}$ to $\frac{7}{2}^{-}$ transition in ^{45}Cr.

A broad peak of transitions at ∼1060 keV was observed to be in coincidence with each other in Fig. 5.11(a), suggesting that two transitions, located at this energy, form a cascade (see Fig. 5.11(c)). This peak was revealed to be too wide to be a single transition, and a double-Gaussian fit was applied by fixing the full-width half-maximum (FWHM) of the peaks. Under this procedure, two peaks with energies of 1054(2) and 1065(2) keV were observed when fixing the FWHM values to 15.8 keV and 16.0 keV, respectively – see Fig. 5.13(a). A third Gaussian was also added in the fit to show a weak 1090(2) keV transition. The resulting $\gamma - \gamma$ coincidence spectra are shown in Figs. 5.13(b) and 5.13(c) for gating on the left side (∼1054 keV) and

the right-hand side (∼1065 keV) of the peak, respectively. Both spectra exhibit the coincidence relationship, implying that the 1054 keV γ ray is in coincidence with the 1065 keV transition, and an expected slight separation between the γ-ray energies in Fig 5.13(b) and Fig. 5.13(c) was tentatively seen. The order of the 1054(2) and 1065(2) keV transitions in the level scheme can not

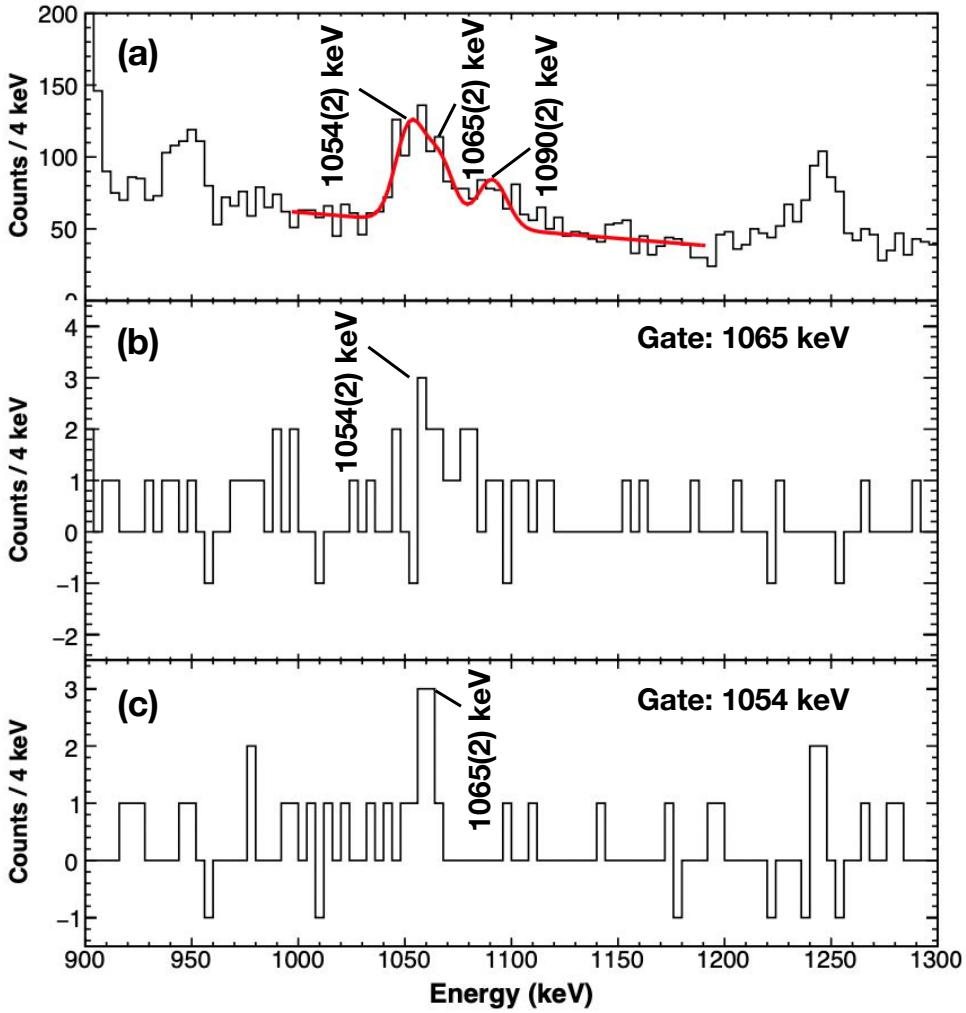

Figure 5.13: The Doppler-corrected spectra of ^{45}Cr where (a) exhibits the double-Gaussian fitting procedure of the 1054(2) and 1065(2) keV peaks. (b) and (c) shows the $\gamma - \gamma$ coincidence spectra gated on the 1065(2) and 1054(2) keV peaks, respectively.

be distinguished by using intensity arguments alone, but it can proposed that the 1054(2) keV transition could be the $\frac{7}{2}^+ \rightarrow \frac{7}{2}^-_{gs}$ transition as the 947(1) and 1054(2) keV transitions indicates

a difference of 107(1) keV. Hence, the 1065(2) keV transition feeds into the $\frac{7}{2}^+$ state. Therefore, the 2119 keV state is tentatively assigned as the $J^\pi = \frac{11}{2}^+$ state by comparing to the level scheme of ^{45}Sc. Due to low statistics, the placement of the 947(1) keV transition could not be confirmed and remains tentative based on the 107(1) keV difference between the 1054(2) keV transition. It can be suggested that the weak 1090(2) keV transition may come from the $J^\pi = \frac{13}{2}^+$ state if mirror symmetry arguments are considered. Coincidence analysis for this transition yielded no additional information to confidently place this transition in the level scheme due to low statistics.

If the tentative assignment of the 622 keV $J^\pi = \frac{5}{2}^+$ state is correct, then one obvious possibility is that the transition feeding into this state would be the 898 keV γ ray (i.e. the mirror of the 891 keV transition in ^{45}Sc), based on mirror symmetry arguments. However, intensity comparisons and coincidence analysis rules this possibility out due to the high intensity of the 898 keV transition and that the 622 keV transition is not in coincidence with the 898 keV transition, respectively. By gating on the 622 keV transition, a weak coincidence with a transition at 881(2) keV was observed, despite low statistics (see Fig. 5.11(b)). The 881 keV transition, which comes from the 1503 keV state, appears as a tail at the left-side of the 898 keV transition in Fig. 5.11(a). Therefore, the 1503 keV state is tentatively assigned as the $J^\pi = \frac{9}{2}^+$ state. The placement of the 516(1) keV transition remains tentative based on the the 107(1) keV difference compared with the 622(1) keV transition, and could not be confirmed due to insufficient statistics. Therefore, the cascade of transitions in this sequence of states is considered to be tentative.

The third pair of transitions that have a difference of 107(1) keV between them, being the 385/492 keV transitions, were both found to be in coincidence with the 566(1) keV transition, yielding a state at 1058(1) keV. Through comparison with the ^{45}Sc level scheme, this state was assigned as the $J^\pi = \frac{3}{2}^-_2$ state based on mirror symmetry arguments.

The remaining unassigned strong 898(1) keV and 1245(2) keV transitions have been investigated using $\gamma-\gamma$ coincidences. Both transitions were not in coincidence with each other, and the intensity of the 898(1) keV transition was found to be significantly higher than the 1245(2) keV transition. This rules out the possibility that the 898(1) keV transition is the analogue of the 870 keV $J^\pi = \frac{15}{2}^-_1 \rightarrow \frac{11}{2}^-_1$ transition. Since no strong coincidences have been observed for both strong transitions, it can be inferred that these are directly populated states, which feed either

into the ground state or the long-lived isomer state. The 1245(2) keV transition is assigned to be the analogue of the strongly populated 1237 keV $J^\pi = \frac{11}{2}^-_1 \rightarrow \frac{7}{2}^-_{gs}$ transition in ^{45}Sc. From a $\gamma - \gamma$ coincidence analysis for 1245(2) keV transition, there was no evidence observed for the $J^\pi = \frac{15}{2}^-_1 \rightarrow \frac{11}{2}^-_1$ transition. Therefore, a candidate for the assignment of the 898(1) keV transition is analogue of the 720 keV $J^\pi = \frac{5}{2}^-_1 \rightarrow \frac{7}{2}^-_{gs}$ transition in ^{45}Sc. If this assignment for the 898(1) keV is correct, assuming that this transition is from the $J^\pi = \frac{5}{2}^-_1$ state based on mirror symmetry arguments, then a low-energy transition from the $J^\pi = \frac{3}{2}^-_2$ state should also be observed to feed into this state. In this case, a weak 162 keV transition, having the correct energy, was observed in Fig. 5.11(a) and was placed in the level scheme.

The resulting placements of the transitions and the J^π assignments of the states observed in the ^{45}Cr scheme are tentative since these were based on mirror symmetry arguments. Furthermore, all of the observed γ-ray transitions, placed in the new level scheme of ^{45}Cr, and the states below 2 MeV in ^{45}Sc have corresponding analogue transitions that are identified in ^{45}Cr. From Fig. 5.12, the relative population intensity of the low-lying negative-parity states, $J^\pi = \frac{3}{2}^-_1, \frac{3}{2}^-_2$ and $\frac{5}{2}^-_1$, was found to be much larger compared to that of their mirror states in ^{45}Sc. It is important to note that these states were not found to be populated at all in previous fusion-evaporation reactions (i.e. in Ref. [114]), hence it can be assumed that these states are directly populated in both reactions – through a $-2n$ knockout to ^{45}Cr and $-2p$ removal from ^{45}Sc in this work. Therefore, by looking at these three low-lying negative-parity states, the relative cross sections between the $J^\pi = \frac{3}{2}^-_1, \frac{3}{2}^-_2$ and $\frac{5}{2}^-_1$ states would be expected to be similar in each member of the mirror pair, since the spectroscopic overlap for the direct reaction (indicated by the two-nucleon amplitudes) is expected to be identical based on isospin symmetry. By using the relative intensities of the transitions that feed into and out of these states (see Tables 5.3 and 5.4), the relative population of each of these states can be calculated for the direct two-nucleon removal reactions (see Ref. [118]). For the ^{47}V$-2p \rightarrow ^{45}$Sc reaction, the population intensity for the $J^\pi = \frac{3}{2}^-_1, \frac{3}{2}^-_2$ and $\frac{5}{2}^-_1$ states are found to be in the ratio of 100(21), 52(14) and 42(21). The respective states in ^{45}Cr, produced through the ^{47}Cr$-2n \rightarrow ^{45}$Cr reaction, are in the ratio of 100(9), 37(6), 37(6). These ratios were found to be within error of each other, providing further evidence that these are analogue states, and confidence in the placements and assignments of the transitions and states, respectively. It is important to note that the error in the relative

population intensity (i.e. 100(21) and 100(9) for $J^\pi = \frac{3}{2}^-_1$ states in ^{45}Sc and ^{45}Cr, respectively) represent the absolute error in the intensity.

J_i^π	E_{J_i}	$J_i^\pi \rightarrow J_f^\pi$	E_γ	E_{J_f}	**R.I.**
$(\frac{3}{2}^-_1)$	492(1)	$(\frac{3}{2}^-_1) \rightarrow (\frac{7}{2}^-_{gs})$	492(1)	0	100(8)
	492(1)	$(\frac{3}{2}^-_1) \rightarrow (\frac{3}{2}^+_1)$	385(1)	107(1)	97(8)
$(\frac{5}{2}^+_1)$	622(1)	$(\frac{5}{2}^+_1) \rightarrow (\frac{7}{2}^-_{gs})$	622(1)	0	32(10)
	622(1)	$(\frac{5}{2}^+_1) \rightarrow (\frac{3}{2}^+_1)$	516(1)	107(1)	47(7)
$(\frac{5}{2}^-_1)$	898(1)	$(\frac{5}{2}^-_1) \rightarrow (\frac{7}{2}^-_{gs})$	898(1)	0	67(6)
$(\frac{7}{2}^+_1)$	1054(2)	$(\frac{7}{2}^+_1) \rightarrow (\frac{7}{2}^-_{gs})$	1054(2)	0	40(9)
	1054(2)	$(\frac{7}{2}^+_1) \rightarrow (\frac{3}{2}^+_1)$	947(1)	107(1)	27(8)
$(\frac{3}{2}^-_2)$	1058(1)	$(\frac{3}{2}^-_2) \rightarrow (\frac{3}{2}^-_1)$	566(1)	492(1)	45(7)
	1058(1)	$(\frac{3}{2}^-_2) \rightarrow (\frac{5}{2}^-_1)$	162(4)	898(1)	11(6)
$(\frac{11}{2}^-_1)$	1245(2)	$(\frac{11}{2}^-_1) \rightarrow (\frac{7}{2}^-_{gs})$	1245(2)	0	44(7)
$(\frac{9}{2}^+_1)$	1503(3)	$(\frac{9}{2}^+_1) \rightarrow (\frac{5}{2}^+_1)$	881(3)	622(1)	7(3)
$(\frac{11}{2}^+_1)$	2119(3)	$(\frac{11}{2}^+_1) \rightarrow (\frac{7}{2}^+_1)$	1065(3)	1054(2)	41(9)

Table 5.4: The level and γ-ray energies (in keV) that have been measured in this work for the unknown ^{45}Cr nuclei. The efficiency-corrected relative intensities (R.I.) of the decays observed are presented in %, relative to the 492(1) keV transition.

5.2.3 Comparison with Predicted Knockout Strength

A similar analysis, as in the $A = 47$ mirror nuclei (see Section 5.1.2), was undertaken to predict the distribution of the knockout strength of the low-lying states in ^{45}Cr to compare to experimental observations. The theoretical two-neutron knockout cross sections for the ^{47}Cr$-2n \rightarrow^{45}$Cr reaction were calculated for all low-lying states of each J^π from $\frac{1}{2}^- \rightarrow \frac{15}{2}^-$ below the proton separation energy ($\sim$3 MeV), shown in Fig. 5.14. The two-neutron removal cross sections were calculated by J. A. Tostevin (Surrey) using the prescription provided in Refs. [71], [119], where the input of the shell-model structure is combined with eikonal reaction dynamics. It is assumed that the two neutrons are removed instantaneously from the projectile and that the residual nucleus acts as a spectator in the reaction. The two-nucleon amplitudes (TNA) were calculated by T. G. Parry (Surrey) using the KB3G interaction [57] in the full fp space through the NuSHELL@MSU interface [120]. The information about the nuclear structure input and the

amplitudes for each of the two-nucleon configurations are contained within the calculated TNA. The two-nucleon configurations with spin and parity, J^π are coupled to the final residue state J_f^π through the projectile ground-state of J_i^π. The same procedure, as shown for the single-nucleon removal calculations in the $A = 47$ instance, was applied in this case where the valence nucleon radial wave functions were calculated using the Woods-Saxon plus spin-orbit potential, constrained by using Hartree-Fock calculations.

Only negative-parity states are calculated due to the shell-model space used. The predicted cross sections for all accessible states below the proton-separation energy of 3 MeV are shown in Fig. 5.14, where the cross sections are plotted as a function of the shell-model excitation energy. Some key observed features are found to be in general agreement with experimental observations. A key observation is that the four negative-parity excited states, $J^\pi = \frac{3}{2}_1^-, \frac{3}{2}_2^-, \frac{5}{2}_1^-$ and $\frac{11}{2}_1^-$, which are directly populated in ^{45}Cr in this experiment, have the largest predicted cross sections. Furthermore, the predicted cross section of the $J^\pi = \frac{15}{2}_1^-$ state was negligible, which is consistent with the experimental non-observation of this state in ^{45}Cr.

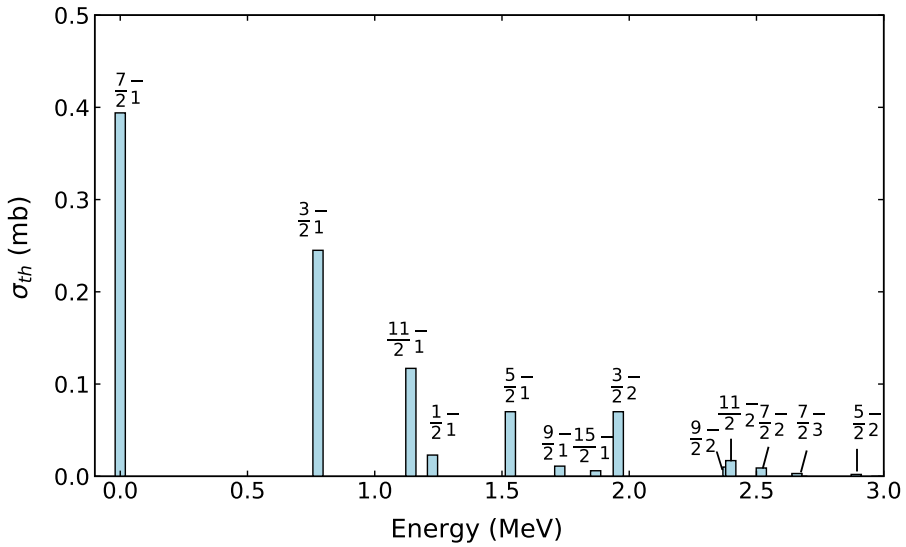

Figure 5.14: The theoretical cross sections for all low-lying states that are predicted [121] to be observed below the proton separation energy (∼3 MeV) in ^{45}Cr. Shell-model energies, obtained from the KB3G interaction in the full fp-space [122] were used in the reaction model to calculate the two-neutron knockout theoretical cross sections.

5.3 Mirror Energy Differences

Once the level schemes for the $T_z = \pm\frac{3}{2}$, $A = 47$ and $A = 45$ mirror pairs were established, the experimental mirror energy differences (MED) for the observed states can be extracted. The experimental results were compared to two theoretical approaches; large-scale shell-model calculations and a novel method based on density-functional theory (DFT).

Firstly, large-scale shell-model calculations for the $A = 47$ and $A = 45$ mirror nuclei were performed using the ANTOINE code [31], [32]. The full fp valence space was utilised within the KB3G interaction [57] where the excitations of particles between the fp-orbitals were not restricted, while using a fixed ^{40}Ca core. Only the negative-parity states could be calculated due to the shell-model space utilised by following the prescription in Refs. [14], [20]. The shell model utilises four isospin-breaking components that individually contribute to the MED calculation (see Chapter 2.2.1 for details). The four terms are:

(a) **Coulomb Multipole Term** (V_{CM}): accounts for the multipole Coulomb interaction between protons, which is included by the addition of the Coulomb matrix elements to the effective two-body interaction of protons.

(b) **Additional Isovector Term** (V_B): An additional empirical isovector interaction. This effect is strongly dependent on the total angular momentum (J) [20], where the $J = 0$ component mostly dominates. For the mirror pairs considered here, the $J = 0$ couplings for the protons were applied, being -100 keV (i.e. 100 keV more attractive for all fp-protons).

(c) **Single Particle Shifts** (V_{ll} and V_{ls}): accounts for the Coulomb single-particle shifts depending on the single-particle angular momentum, and electromagnetic spin-orbit effects, respectively [64], [123].

(d) **Radial Term** (V_{Cr}): a monopole term that considers the changes in the mean nuclear radius as a function of the angular momentum (L). The average occupation of the $p_{3/2}$-orbitals is considered and is applied using the prescription in Ref. [14].

The application of these four terms in the shell model in the fp-space extends on previous work in Refs. [3], [5], [8] for the $A = 49, 51$ and 53, $T_z = \pm\frac{3}{2}$ mirror nuclei. This approach was applied to

the $A = 47$ and $A = 45$ negative parity states in this work, where the procedure was undertaken to calculate the MED is detailed as follows:

1. An isoscalar calculation was performed, where the Coulomb interaction was not applied between the protons. This step was taken to extract the underlying wave functions, which detail the occupation of the valence particles across the fp shell. The original wavefunctions were considered to observe how they change as the isospin-breaking components were applied (i.e. using a perturbative approach).

2. After the wave functions of the particle occupation have been obtained, the Coulomb multipole term was applied to recalculate the MED.

3. Once the MED due to the Coulomb interaction has been obtained, the addition of the V_B term was applied to extract the resulting MED.

4. Following the extraction of the MED due to the Coulomb and V_B term, the effect of the single particle shifts, V_{ll} and V_{ls}, were applied to recalculate the resulting MED.

5. Once the resulting MED was obtained as a result of the addition of the V_{ll} and V_{ls} terms, the V_{Cr} term was calculated using the extracted wave functions from step 1.

Currently, there is no available interaction that can be used in the $f_{\frac{7}{2}}$ shell that can calculate both positive and negative parity states within the same valence space due to limits in computational power. Hence, the MED for the positive-parity states in the $A = 45$ mirror pair cannot be computed at the same time as the negative-parity states using the same interaction and valence space. In the ^{45}Sc/^{45}Cr mirror pair, the existence of a low-lying positive-parity structure was observed in close proximity to the ground state. The $J^{\pi} = \frac{3}{2}^{+}$ band head is thought to originate from a single particle-hole excitation from the $d_{3/2}$-orbital, signifying a well-deformed prolate shape as the $[202]\frac{3}{2}^{+}$ Nilsson level approaches the Fermi level when $N, Z = 21$. To analyse the MED of the positive-parity structures, an extended version of the shell-model calculation was performed by Professor Silvia Lenzi using the SDPF interaction [124], even though this interaction is optimised for all *sd*-shell nuclei. In the calculation performed, the *sd*-orbitals are included alongside the full fp-space, where only one particle-hole excitation is allowed from the

$d_{3/2}$-orbital (i.e. one proton (neutron) excitation in ^{45}Sc (^{45}Cr)). The multipole and monopole contributions used to calculate the MED for the negative-parity states were also applied to the positive-parity states.

The new and alternative theoretical study from Bączyk and Satuła [23] provides a new pathway to determine the MED by using multi-reference density-function theory (DFT) [22]. The No-Core Configuration-Interaction (NCCI) method was applied, allowing for the full treatment of rotational and isospin symmetries. Isospin-breaking effects originating from the Coulomb and nuclear (charge-symmetry breaking, CSB) interactions were also incorporated, where next-to-leading (NLO) contact terms were implemented to the nuclear interactions. The parameters for the NLO terms were extracted from the global fits to displacement energies [125]. The use of mean-field theory with fitted global parameters in this method, provides a unique approach from the shell model. This method was first applied by Llewellyn *et al.* [24] to the $T_z = \pm\frac{1}{2}$, $A = 79$ mirror nuclei as the shell-model framework requires a larger valence space at this region for these calculations.

In the following sections, the experimental data will be compared to the theoretically calculated MED for both the $T_z = \pm\frac{3}{2}$, $A = 47$ (^{47}Ti/^{47}Mn) and $A = 45$ (^{45}Sc/^{45}Cr) mirror pairs, from the shell-model calculations and the newly-developed density-functional theory no-core configuration-interaction method (DFT-NCCI), performed by Professor Wojciech Satula.

5.3.1 MED results for ^{47}Ti/^{47}Mn

The experimental and calculated MED, from the shell model and the DFT-NCCI method, are presented in Fig. 5.15 for the A=47 mirror pair. The contribution of each component used in the shell model to calculate the MED are shown in Fig. 5.16. The MED are calculated relative to the $\frac{5}{2}^-$ ground state for all of the observed negative-parity states.

The red points (open-circles) show a negative trend in the MED, reducing by an average of ∼75 keV before increasing to 0 keV. As a result of the Coulomb multipole effects, the MED is expected to vary up to ∼100 keV as the recoupling of the pairs of protons (in the ^{47}Ti case) can go from $J = 0 \rightarrow J_{max}$ [14], where $J_{max} = 6$ in this case. This observation where the MED goes from a negative trend to a positive trend indicates that both the protons, in ^{47}Ti, and the neutrons, in ^{47}Mn, are recoupling.

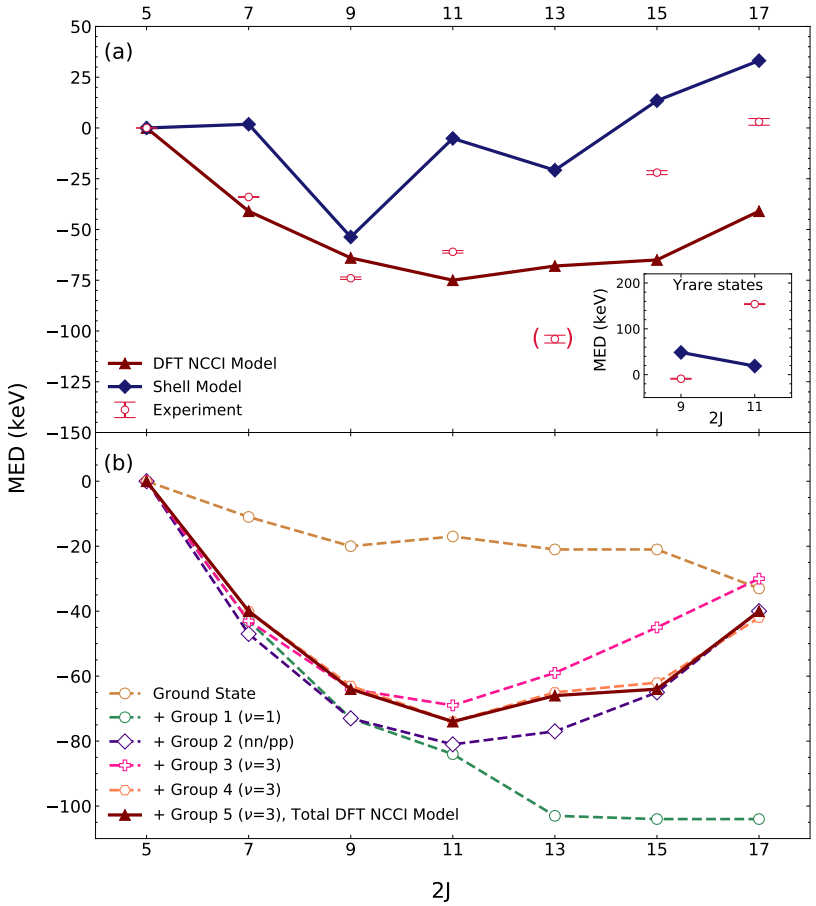

Figure 5.15: (a) The mirror energy differences presented as a function of $2J$ for the ^{47}Ti/^{47}Mn mirror nuclei. The solid blue line (diamonds) represents the MED calculated through the shell model which includes all four of the isospin-breaking components. The brown line (triangles) represents the MED obtained from the DFT-NCCI method. The red points are the experimental MED. The yrast $\frac{13}{2}^-$ state is labelled in brackets as the J^π assignment is tentative. The inset shows the MED for the yrare analogue states. (b) The DFT-NCCI calculations presented as a function of $2J$. Here, the contribution of how each of the configuration types to the final result is presented, denoted by the brown triangles in (a) and (b).

The blue line in Fig. 5.15(a) represents the MED calculations obtained from the shell model that includes all of the four isospin-breaking components, detailed in section 5.3, to produce the final result. It can be noted that a systematic shift of ∼30-40 keV can be observed between the experimental and the calculated shell-model MED for the yrast states, which seems to arise from the addition of the V_{Cr} term (see Fig. 5.16). Since the MED is normalised to the $J^\pi = \frac{5}{2}^-$ ground state, this may indicate that this state is poorly defined within the shell model. The yrast $\frac{13}{2}^-$

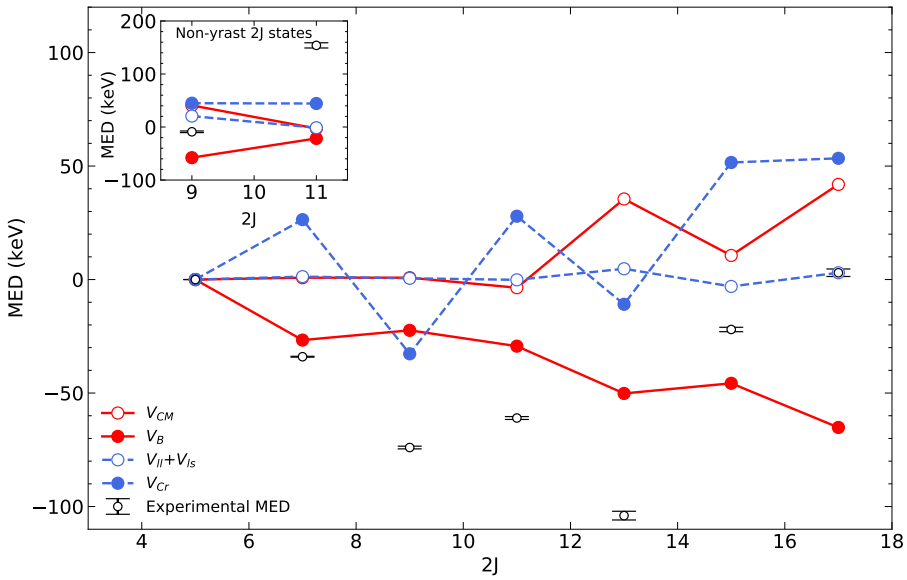

Figure 5.16: The four components applied in the shell model calculations (defined in text) for the yrast and observed yrare states (see insert). The sum of the four components produce the solid blue line in Fig. 5.15(a) for the yrast states and the yrare states, shown in the insert. The MED for the yrare states are plotted relative to the $J^\pi = \frac{5}{2}^-$ ground state.

state is presented in parenthesis due to its tentative assignment in terms of J (see Section 5.1.1), where the agreement of the experimental MED to the shell-model calculation was poor. For the yrare states, the $\frac{11}{2}^-_2$ state was also poorly reproduced by the calculations, yet a better agreement was seen for the $\frac{9}{2}^-_2$ state. The cause of the poor agreement with the shell-model calculations, compared to the experimental observations, is likely to arise from the inadequacy of the fp-space utilised, where only two protons and two neutrons are present in ^{47}Ti and ^{47}Mn, respectively. Furthermore, as a fixed ^{40}Ca core was applied in the calculations, excitations from deep lying states are restricted. Hence, it can be inferred that the two-particle two-hole excitations across the ^{40}Ca shell-closure will also contribute to this systematic shift. The comparison between the experimental and the calculated MED for the ^{47}Ti/^{47}Mn mirror pair provides a stringent and useful test for all models that incorporate the lower fp-shell and the upper sd-shell.

The MED, calculated using the DFT-NCCI approach, for the yrast states is denoted by the brown triangles in Fig. 5.15(a), which is also normalised to the $J^\pi = \frac{5}{2}^-$ ground state. The calculation was based on 23 Multi-Reference Hartree-Fock (MRHF) configurations, which were sufficient to converge the calculations shown in 5.15(b). The different lines shown represent the

cumulative contribution of the various excited configurations to the overall MED, where the five different configurations are sequentially added on top of the ground state configuration, denoted by the light brown circles. The order in which the configurations were added is as follows:

1. Group 1 (open light brown circles): seniority (ν)=1 configurations where no fully broken pairs are present. This allows for the possible locations of the odd, unpaired particle to be determined.

   +

2. Group 2 (open purple diamonds): $\nu = 1$ configurations that correspond to states built on like-particle (nn/pp) pairing excitations.

   +

3. Group 3 (open dark pink crosses): The lowest-energy $\nu = 3$ configurations that have one broken-pair in the even subsystem, in addition to an unpaired particle in the odd subsystem (being the protons in ^{47}Ti and neutrons in ^{47}Mn).

   +

4. Group 4 (open light pink hexagons): The same as Group 3, where the $\nu = 3$ configurations consist of one unpaired nucleon and one broken pair in the odd subsystem (i.e. neutrons in ^{47}Ti and protons in ^{47}Mn).

   +

5. Group 5 (closed dark brown triangles): The additional $\nu = 3$ configurations that consist of one unpaired nucleon and one broken pair in both subsystems.

The dark brown line in Fig. 5.15(b) consists of all of the configuration types that were added, which is equivalent to the dark brown line in Fig. 5.15(a). Fig. 5.17 shows the configurations applied in the DFT-NCCI calculation for the $A = 47$ mirror pair.

By including the Groups 1 and 2 configurations to the ground-state configuration, the MED obtains the observed trend as seen for the experimental MED (i.e. negative to positive trend with higher J). Therefore, this trend can be obtained through angular-momentum alignments, provided that the pairs are not broken. The addition of these $\nu = 1$ configurations seems to

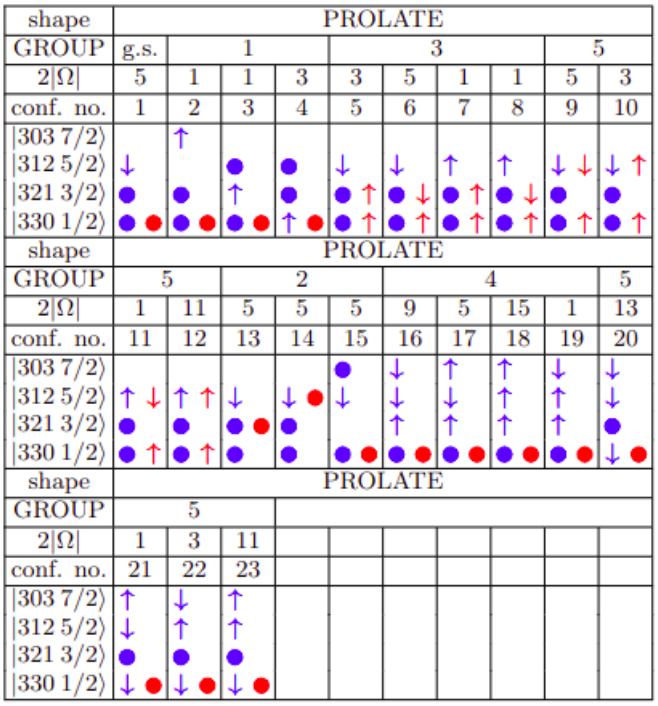

Figure 5.17: The configurations used in the DFT-NCCI calculations for the ^{47}Ti/^{47}Mn mirror pair. Filled circles represent the pair of nucleons that are paired. Arrows that are up (down) denote the single occupation of particles with positive (negative) quantum numbers, respectively. Red dots represent the even subsystem, while the blue dots denote the odd subsystem [30], [126].

account for the bulk of the MED. By adding the $\nu = 3$ configurations on top of the $\nu = 1$ configurations, the final result in the MED does not get significantly affected. The overall agreement of the results attained from the full DFT-NCCI calculation (brown line in Fig. 5.15(a)) to the experimental MED shows that the results match the trend well at lower spins, despite deviating slightly at higher-J states. Another observation is that the staggering effect seen in the experimental MED is missing in the DFT model. This suggests that some fine details are missing as one goes from state to state.

5.3.2 MED results for ^{45}Sc/^{45}Cr

The experimental and theoretical MED for the negative-parity states are shown in Fig. 5.18(a), relative to the $J^\pi = \frac{7}{2}^-$ ground state. The MED for the positive-parity states, shown in Fig. 5.18(b), are calculated relative to the $J^\pi = \frac{3}{2}^+$ band head state. The contributions from

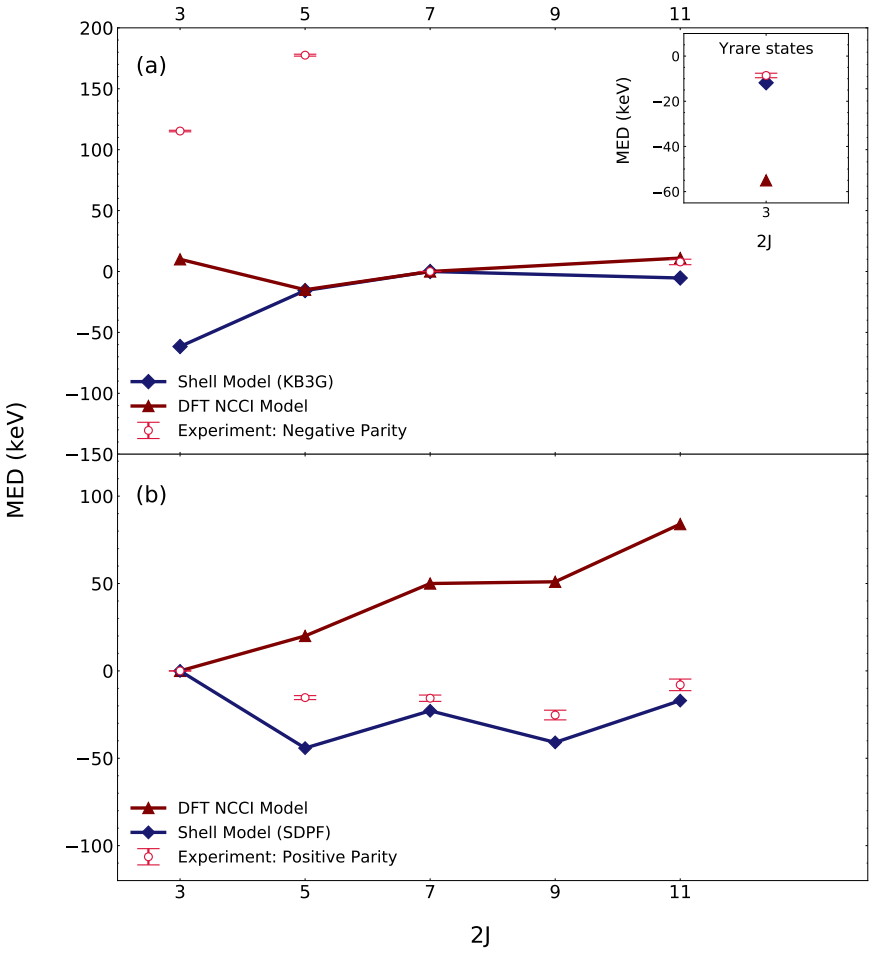

Figure 5.18: (a) MED as a function of spin $2J$ for the ^{45}Sc/^{45}Cr mirror pairs for the observed negative-parity states. The blue line (closed diamonds) denote the KB3G shell-model MED calculations that include all four isospin-breaking terms. The brown line (closed triangles) show the results from the DFT-NCCI approach and the red open circles represent the experimental MED. The inset in (a) displays the MED as the function of spin $2J$ for the observed $\frac{3}{2}^-_2$ analogue states. (b) shows the MED as a function of spin $2J$ for the positive parity states. The SDPF shell-model calculation is shown by the blue line (closed diamonds). The MED from the DFT-NCCI approach is represented by the brown line (closed triangles) and the experimental MED is shown by the red open circles.

each of the four components in the shell model calculations are shown in Fig. 5.19.

The blue line (closed diamonds) represents the KB3G shell-model calculations for the negative parity sates in Fig. 5.18(a), where a good agreement to the experimental MED is seen for the $\frac{11}{2}^-_1$ and $\frac{3}{2}^-_2$ states, despite having a poor agreement for the $\frac{3}{2}^-_1$ and $\frac{5}{2}^-_1$ states. The cause for this discrepancy is most likely due to the inadequacy of the fp-space as only one valence proton and

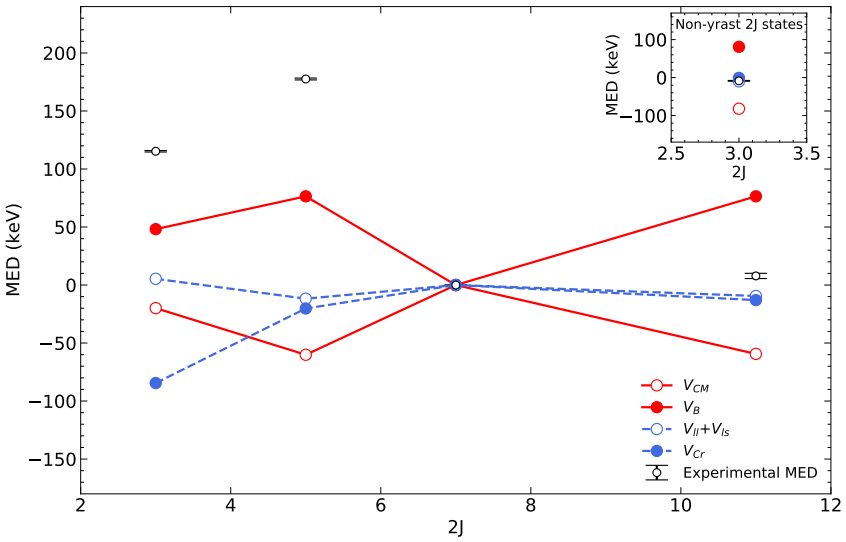

Figure 5.19: The four components applied in the shell model calculations (defined in text) for the yrast and observed yrare negative-parity states (see insert) of the $A = 45$ mirror pair. The sum of the four components produce the solid blue line in Fig. 5.18(a) for the yrast states and the solid diamond data point for the yrare states, shown in the insert. The MED for the yrare states are plotted relative to the $J^\pi = \frac{7}{2}^-$ ground state.

neutron is available in the $f_{7/2}$ shell for ^{45}Sc and ^{45}Cr, respectively. For the $\frac{3}{2}^-_1$ and $\frac{5}{2}^-_1$ states, it is possible that a single particle excitation into the $f_{5/2}$ or $p_{3/2}$ shells from the $f_{7/2}$ shell may not be well described in the fp-space, which could impact the V_{Cr} or the V_{ll} and V_{ls} calculations. Furthermore, the blue line (diamonds) in Fig. 5.18(b) show the SDPF MED calculation for the positive-parity states by exciting a single nucleon from the $d_{3/2}$-shell, conducted by Prof. Silvia Lenzi. This approach was applied to the $A = 45$ mirror pair only. A strong agreement between the SDPF interaction to the experimental MED results is observed, where small variations in the MED are seen on a state-by-state basis, suggesting that the deformed configuration remains constant throughout the rotational sequence.

The DFT-NCCI approach was also applied (by Professor Wojciech Satula) to calculate the MED for both the negative- and positive-parity states. For the latter, the configuration space was not truncated and, unlike the shell model, does include the configurations based on the sd and fp-shells. The results from the DFT-NCCI method is shown in Fig. 5.18(a) for the negative-parity states and in Fig. 5.18(b) for the positive-parity states, represented by the brown line (triangles). For the negative-parity states, 15 configurations were implemented, where three

configurations of type Group 1, three of Group 2 (i.e. excitation of pp pairs in ^{45}Cr and nn pairs in ^{45}Sc), four in Group 3 and four of Group 5 were applied. Group 4 configurations were not applied (see Section 5.3.1 for the description of each group). For the positive-parity states, 24 prolate-shape configurations were applied, where two configurations of Group 1, four of Group 2, four of Group 3, four of Group 4 and nine of Group 5 were applied.

A poor agreement between the DFT-NCCI MED calculations and the experimental results was observed for both sequences of states. This is the first case (see Ref. [22]) where the DFT-NCCI model fails to reproduce the experimental results in terms of sign and trend of the MED. Currently, this difference in the MED could not be considered, but it could be suggested that missing correlations in the DFT-NCCI model could contribute to this discrepancy. For the positive-parity states, a better energy spectrum is obtained, yet the calculated band is observed to be significantly more collective when compared to the experimental MED, based on the energy spacing. Another reason for this disagreement with the experimental data could be related to the nuclear NLO CSB interaction. This observation has prompted an investigation, conducted by Professor Wojciech Satula, to analyse the effect of the different types of charge-symmetry breaking (CSB) forces used within the DFT-NCCI framework on the resulting MEDs. It was found that the MED results have a relatively strong sensitivity to the type of CSB force (see Ref. [30] for further details).

5.4 Summary

The level schemes of the $A = 47$ and $A = 45$ mirror pairs were constructed using mirror symmetry arguments and γ-γ coincidence analysis. Level schemes for the ^{47}Mn and ^{45}Cr proton-rich nuclei are produced for the first time in this work. Comparison to the theoretical predictions shows a good agreement with the experimental data, providing confidence in the assignment and the placement of the states and transitions, respectively. Mirror energy differences (MED) have also been performed for both pairs of mirror nuclei for the first time using the shell model and the DFT-NCCI approaches. The agreement of the shell model calculations with the experimental data is generally adequate, although some deviations are present for some states, presumably due to the small number of valence particles in the shell model space. The comparison of the

DFT-NCCI calculations and the experimental MED show a reasonable agreement for the $A = 47$ case but a poor agreement for the $A = 45$ mirror pair. Further investigation is required to fully understand the discrepancy of the MED within the DFT framework, especially for the $A = 45$ case.

Chapter 6

A=47 Mirror Nuclei Cross Sections

Since the mirrored one-nucleon knockout approach was utilised in this work, first employed by Milne *et al.* [3], the 'mirrored' inclusive (for all observed states) and exclusive (for individual states) cross sections for both ^{47}Mn and ^{47}Ti can be determined.

The large difference in the binding between the two mirror pairs is of particular interest as the ratio of the experimentally determined knockout strength to the theory exhibits a strong dependence on the asymmetry of the neutron and proton separation energies, as seen in published systematics [25]–[27]. A previously detailed analysis of the analogue inclusive and exclusive cross sections, where large asymmetries in the binding were observed, have been discussed in Ref. [10].

In this chapter, the measured inclusive cross sections for the ^{47}Mn and ^{47}Ti mirror pair are discussed with reference to the published systematics, along with comments for the results obtained for ^{47}Ti. Exclusive cross sections for ^{47}Mn and ^{47}Ti will also be presented and discussed.

6.1 Experimental Inclusive Cross Sections

6.1.1 Method

The cross-section measurements from one-nucleon knockout reactions can be used to deduce spectroscopic information related to the single particle occupational strengths, which describe the extent of the overlap between the initial and final configurations. Therefore, the cross section, which gives the probability of populating a particular state in a residue from a specific initial state of the projectile, can be calculated if a direct reaction has occurred.

To extract the experimental inclusive cross sections, which provide the probability of removing

a single nucleon from the ground state of the parent nucleus to any excited state or the ground state of the residue, it was imperative that the unreacted beam runs took place to measure the rate of the incoming particles. Therefore, the unreacted and reacted outgoing particle intensities, N_U^{obs} and N_R^{obs}, respectively, can be measured. These particle intensities are required to be corrected for the deadtime, S800 acceptances and efficiency using the following equations:

$$N_{inc}^{UNR} = \frac{N_U^{obs} \cdot DS_U}{A_U \cdot \epsilon_U^{det} \cdot C_{live_U}}, \tag{6.1}$$

$$N_{out}^{R} = \frac{N_R^{obs} \cdot DS_R}{A_R \cdot \epsilon_R^{det} \cdot C_{live_R}}, \tag{6.2}$$

where 'DS' represents the downscaler factor applied in the singles event data, 'A' is the acceptance within the S800, and C_{live} is the correction in the livetime.

The measured particle intensities ($N_{U,R}^{obs}$) were determined using the S800 trigger and were corrected using the downscaler factor (DS). This factor was applied to reduce the pile-up in the DAQ system during high-rate experiments. For the ^{47}Mn and ^{47}Ti residue measurements, a downscaler factor of 1 and 3 were applied, respectively. For the unreacted beams, ^{48}Mn and ^{48}V, the downscaler factor of 1 was applied in the analysis. The second correction factor is the S800 acceptance, A, which accounts for the losses in the parallel momentum distribution (d_{ta}). These losses arise from blocking the beam to attain the outgoing beams of interest, which limits the acceptance angle in the S800 spectrograph (Fig. 6.1). The acceptance for the reacted runs was determined as the ratio of the number of particles passing through the focal plane (i.e. detected events in the histogram) to the expected number that would have been detected if the beam was not blocked (determined by a Gaussian fit).

The third correction factor is the detector efficiency, $\epsilon_{U,R}^{det}$, where the total number of detected events for a particular particle of interest within the ionisation chamber is considered by taking the energy loss range obtained from the particle identification spectrum (PID). The number of detected events in the XFP and OBJ scintillators in the S800 beam line, and the x and y directions in both CRDCs, at the focal plane, were included. The efficiency was calculated by multiplying the ratios of the detected events of each of the scintillators and CRDCs, relative to

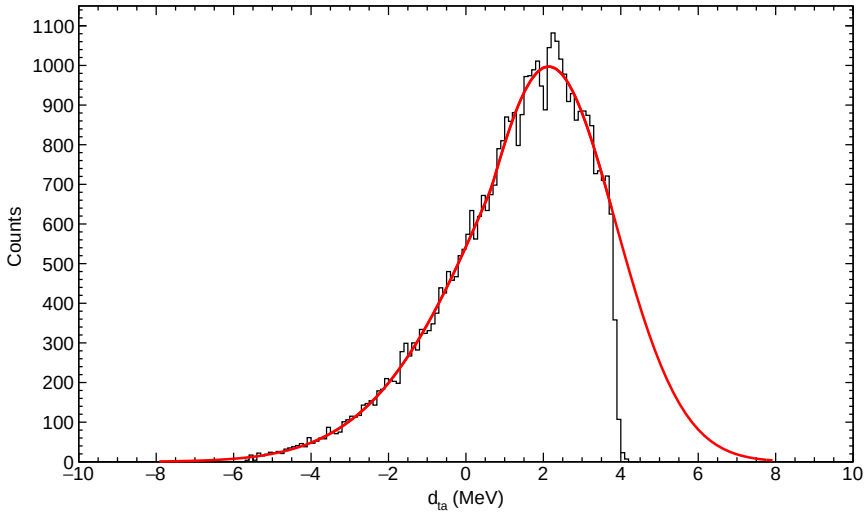

Figure 6.1: The d_{ta} spectrum showing the relative energy spread for ^{47}Mn. A sharp cut-off at the right-hand side can be observed where the beam blocker is present, effectively removing some of the events needed for the acceptance analysis. To determine the acceptance of the S800 focal plane, the number of events detected were obtained (black) and the expected number of counts, if the beam blocker was not present, was estimated (red fit).

the ionisation chamber as shown:

$$\epsilon_{tot} = \left(\frac{N_{XFP}}{N_{IC}}\right) \cdot \left(\frac{N_{OBJ}}{N_{IC}}\right) \cdot \left(\frac{N_{CRDC1_x}}{N_{IC}}\right) \cdot \left(\frac{N_{CRDC1_y}}{N_{IC}}\right) \cdot \left(\frac{N_{CRDC2_x}}{N_{IC}}\right) \cdot \left(\frac{N_{CRDC2_y}}{N_{IC}}\right). \quad (6.3)$$

The final correction factor relates to the livetime of the DAQ system. For the unreacted beams (see Eq. 6.1), the emitted γ rays were not processed as the coincidence trigger was switched off. Therefore, the S800 trigger was considered, resulting in the livetime being calculated using the ratio of the S800 live trigger to the raw trigger. For the outgoing nuclei, the ratio of the S800 triggers in the data to the triggers in the scalar data provides the livetime. The scalar data contains the reaction and transmission settings of the S800.

The number of the incoming beam particles for the reacted beam runs can be calculated by:

$$N_{inc}^{R} = N_{inc}^{UNR} \times K_{norm}, \quad (6.4)$$

$$K_{norm} = \frac{N_{norm}^{R}}{N_{norm}^{UNR}}, \quad (6.5)$$

where K_{norm} is the normalisation factor used to normalise the total secondary beam intensity

between the reacted runs (N^R_{norm}) and the unreacted beam runs (N^{UNR}_{norm}). N^R_{norm} and N^{UNR}_{norm} are the average number of the OBJ and XFP scintillator events. Subsequently, the experimental inclusive cross section for ^{47}Mn and ^{47}Ti can be calculated using:

$$\sigma_{inc} = \frac{N^R_{res}}{N_T \times N^R_{inc}}, \tag{6.6}$$

where N_T is the number of target nuclei, being $1.26{\times}10^{26}$ m^{-2} per unit area for the 188 mg/cm^2 ^{9}Be target.

The theoretical one-nucleon knockout cross sections were determined for each observed state, with spin-parity (J^π), in the $A = 47$ mirror pair using the method detailed in Section 6.3. It is customary to calculate the theoretical inclusive cross sections as the sum of the individual cross sections of the bound states. However, due to the low proton separation energy observed for ^{47}Mn in this work, the theoretical inclusive cross section was defined as the sum of the individual cross sections for all observed states.

6.1.1.1 Errors in the Inclusive Cross Section

To determine the errors in the experimental inclusive cross sections, the statistical and systematic error contributions were determined. During the main experiment, four unreacted beam runs took place for the ^{48}Mn beam. Due to fluctuations in the purity throughout the experiment, 5 runs on either side of the unreacted beam runs were considered, giving a total of 40 runs to determine the statistical and systematic error in the inclusive cross section.

The statistical error was determined by taking the squared-root of the number of observed outgoing particles, N_{obs}. The overall systematic error in the inclusive cross section accounted for the target thickness, the acceptance in the S800 focal plane, the gating of the outgoing particle of interest and the fluctuations in the purity of the beam. In this work, the target thickness was assumed to have a 1% tolerance due to surface fluctuations. The error in the acceptance of the focal plane was calculated by measuring the uncertainty in the fit, which provides information on the intensity and the parameters applied to the fit. The error in the gating of the outgoing beam was also considered as the size of the gate affects the number of observed particles from the S800 events. This was explored by drawing two types of gatings; one tight gate and one loose gate around the residue of interest. The difference between the two cuts was averaged

to determine the fractional error due to the gating, giving a percentage error of ∼0.4%. The fluctuation in the purity of the beam was found to contribute significantly to the overall error in the inclusive cross section. To determine how the purity affects the results in ^{47}Mn, the 40

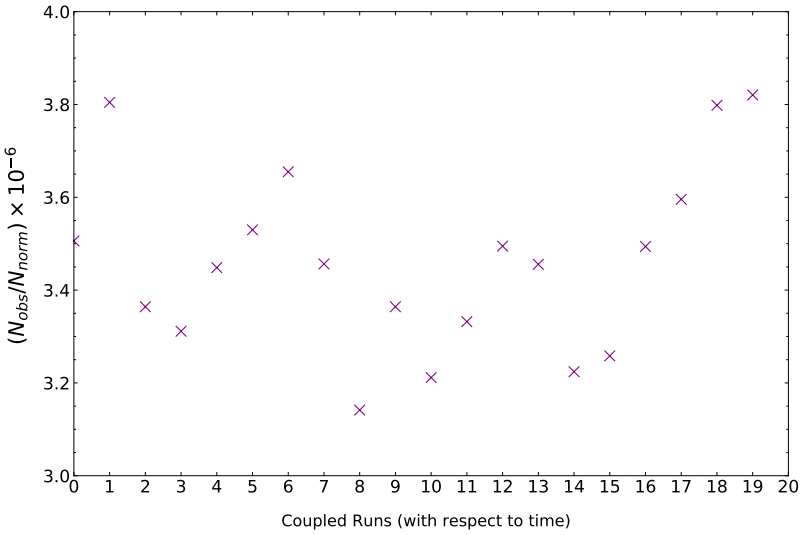

Figure 6.2: The ratio of the number of observed particles to the scalar data as a function of time for ^{47}Mn. A significant amount of drift can be observed between each pair of runs that oscillates due to purity. This approach gives a reasonable estimate of the fluctuations in the purity.

runs were paired up, giving 20 pairs of runs that were utilised for this analysis. The number of observed particles, gated on the outgoing ^{47}Mn nucleus, were measured using the S800 trigger only. The ratio between the measured events to the scalar data (N_{norm}) was determined for each pair of runs as a function of time (e.g. Fig. 6.2) to determine the standard deviation. The data in the scalars were used as the purity of the incoming ^{48}Mn beam was assumed to remain constant throughout the experiment. The standard deviation was then used to calculate the error due to the purity of the beam, which was found to contribute a percentage systematic error of ∼6% to the overall experimental inclusive cross section. For ^{47}Mn, the absolute systematic error due to the purity was calculated to be ∼0.46 mb. For the ^{47}Ti case, only one unreacted beam run and two reacted beam runs were produced. Therefore, it can be assumed that the fractional error in the purity would be the same as determined for ^{47}Mn.

The overall error in the experimental inclusive cross section adds the statistical and the four contributions of the systematic error in quadrature.

6.1.2 Experimental Inclusive Cross Section Results

By following the steps in Section 6.1.1, the experimental inclusive cross sections for the one-neutron knockout of ^{48}Mn to ^{47}Mn was measured to be 8.10 ± 0.05(stat.) ± 0.48(sys.) mb using the values in Tables 6.1 and 6.2. The fluctuations of the purity in the incoming beam were found to be the dominant source of error. The inclusive cross section of the mirrored one-proton knockout from ^{48}V to ^{47}Ti was measured to be 96.2 ± 0.3 (stat.) ± 5.6 (sys.) mb. Errors were calculated using the method detailed in section 6.1.1. This measurement of the experimental inclusive cross section was found to be ∼11 times greater than the result in ^{47}Mn.

Reacted Beam	C_{live}	ϵ^{det}	DS	N_R^{obs}	A
^{47}Mn	0.90	0.99	1	41890	0.86
^{47}Ti	0.86	0.97	3	257035	0.89

Table 6.1: The data used for the ^{47}Mn and ^{47}Ti reacted beam runs. The numbers for the correction factor due to the livetime C_{live}, the total particle efficiency ϵ^{det}, the downscaler factor DS, the number of observed residues in the focal place N_R^{obs}, and the acceptance of the focal plane for the reacted runs, A, are detailed in Section 6.1.1

Unreacted Beam	C_{live}	ϵ_i^{det}	DS	N_{obs}^R	A	N_{norm}
^{48}Mn	0.75	0.99	1	85468	1	4734
^{48}V	0.73	0.89	1	272646	1	2056

Table 6.2: The data used for the ^{48}Mn and ^{48}V unreacted secondary beam runs. The numbers for the correction factor due to the livetime C_{live}, the total particle efficiency ϵ_i^{det}, the downscaler factor DS, the number of observed residues in the focal place N_{obs}^R, and the acceptance of the focal plane for the reacted runs A are detailed in Section 6.1.1

6.2 Exclusive Cross Sections measurements

6.2.1 Method

The exclusive cross section indicates the probability of removing a single nucleon from the ground state of the incoming secondary beam to a specific state in the residue particle. The experimental exclusive cross sections for each observed state in the ^{47}Ti and ^{47}Mn recoils were determined from the efficiency-corrected γ-ray intensities. The S800 (LT_{S800}) and GRETINA (LT_γ) live times, the number of observed fragments (N_{obs}^{PID}) obtained from the S800 trigger, the downscaler factor

(DS) and the inclusive experimental cross section (σ_{inc}) need to be taken into account. The difference between the sum of the efficiency corrected absolute intensities of the γ-ray transitions emitted from a particular state and the efficiency corrected γ rays feeding into that state, N^{γ}_{obs}, was used as shown in Eq. 6.7:

$$\sigma_{excl} = \frac{N^{\gamma}_{obs} \cdot LT_{S800}}{LT_{\gamma} \cdot N^{PID}_{obs} \cdot DS} \cdot \sigma_{inc} \tag{6.7}$$

The live time of the S800 (LT_{S800}) DAQ system, the downscaler factors (DS), the number of fragments detected (N^{PID}_{obs}) and the experimental inclusive cross sections were calculated using the method detailed in section 6.1.1. The live time of the GRETINA (LT_{γ}) DAQ system was calculated by taking the ratio of the measured number of events from the coincidence trigger in the data to the average number of events detected by the coincidence trigger in the scalars. The live time of the DAQ system for the S800 and coincidence events were measured separately. The ground state does not have any γ-ray emission tag, hence the cross section of the ground state can be calculated as follows:

$$\sigma_{GS} = \sigma_{inc} - \sum_{i} \sigma_{excl(i)}, \tag{6.8}$$

where $\sigma_{excl(i)}$ is the sum of the all of the observed excited states subtracted from the overall inclusive cross section, σ_{inc}. The resulting experimental exclusive cross sections for ^{47}Mn and ^{47}Ti, produced from one-neutron/one-proton knockout from the ground states of ^{48}Mn and ^{48}V, respectively, are shown in Table 6.3.

The errors in the exclusive cross sections were determined by taking the statistical error measured for the number of events detected from the S800 trigger (N^{PID}_{obs}) and the combined error (sys. and stat.) for the experimental inclusive cross sections. The error in N^{γ}_{obs} was also included, where the error in the corresponding efficiency corrected intensities of the γ rays coming out of (N^{γ}_{out}) and into (N^{γ}_{in}) a particular state were added in quadrature.

The total error in the exclusive cross sections were determined from the errors in N^{PID}_{obs}, N^{γ}_{obs} and σ_{inc} added in quadrature. The resulting experimental cross sections for each state is shown in table 6.3 in section 6.2.2 for ^{47}Ti and ^{47}Mn.

6.2.2 Exclusive Cross Section Results

As described in section 5.1.1, the intensity of the decay from the $\frac{7}{2}^-$ first-excited state could not be measured for ^{47}Mn. Therefore, as shown in Table 6.3, the experimental exclusive cross section for this state was not determined. Instead, the combined cross section of the ground state and the $\frac{7}{2}^-$ state was calculated by taking the difference between the inclusive cross section and the sum of all measured exclusive cross sections of the other observed states. This yields a combined cross section of 3.0(6) mb for ^{47}Mn, where the average excitation energy was used in the experimental and theoretical relative cross-section measurements Fig. 6.5. This was also the case for ^{47}Ti, where the combined ground state and first-excited state cross section was 53(7) mb. The statistical and systematic errors in the experimental exclusive cross sections were added in quadrature, where the errors from the efficiency corrected γ-ray intensities and γ-ray feeding were found to dominate.

6.3 Calculations for Theoretical Cross Sections

The first step to calculate the theoretical cross sections for ^{47}Mn and ^{47}Ti is to obtain the spectroscopic factors (C^2S), which describe the nuclear wave functions. The C^2S values show the probability of a particular state being populated, where the overlap between the final state and the initial state can be assessed, provided that a hole is present in an orbital. These calculations were taken place within the *fp*-space only as the *sd*-shell contributions could not be included. The spectroscopic factors for both mirrored nucleon removal reactions (i.e the neutron removal from ^{48}Mn to ^{47}Mn and one-proton removal from ^{48}V to ^{47}Ti) are expected to be identical when using an isoscalar approach in the shell model. The 4^+ ground state wave function of the one-neutron (proton) knockout reactions from the ^{48}Mn (^{48}V) beams are presented in Table 6.4.

The spectroscopic factors for the one-neutron (proton) knockout reactions from the 4^+ ground state of ^{48}Mn (^{48}V) to ^{47}Mn (^{47}Ti) were calculated using the KB3G interaction [57] within the ANTOINE framework [31]. The interaction defines the full charge-symmetric and charge-independent nature of the nuclear force. The spectroscopic factors (C^2S) were only calculated for a subset of observed yrast and yrare states in this work from $J^\pi = \frac{1}{2}^-$ to $\frac{15}{2}^-$, where these states were populated through a knockout from the $f_{7/2}$ orbital. Through a $f_{5/2}$-orbital

$J^{\pi}_{i,^{47}Ti}$	^{47}**Ti**			^{47}**Mn**		
	E_{J_i}	σ_{exp}**(mb)**	σ_{th}**(mb)**	E_{J_i}	σ_{exp}**(mb)**	σ_{th}**(mb)**
$\frac{5}{2}^-_{gs}$	0	-[a]	2.95	0	-[b]	2.44
$\frac{7}{2}^-_1$	159	-[a]	2.07	122.4(2)	-[b]	1.77
$\frac{9}{2}^-_1$	1252	5.5(8)	4.16	1175(1)	0.4(2)	3.34
$\frac{11}{2}^-_1$	1444	4(2)	6.15	1380(1)	1.4(2)	4.93
$\frac{3}{2}^-_1$	1549	0.8(5)	0.07	-	-	-
$\frac{1}{2}^-_1$	1793	1.9(7)	0.03	-	-	-
$\frac{3}{2}^+_1$	1825	2(1)	-	-	-	-
$(\frac{7}{2}^-_2)$	2297	0.4(4)	0.95	-	-	-
$(\frac{9}{2}^-_2)$	2406	1.8(8)	4.75	2395(1)	1.1(1)	4.26
$(\frac{13}{2}^-_1)$	2668	2.9(8)	1.61	2574(2)	0.15(9)	1.34
$\frac{11}{2}^-_2$	2682	5.1(8)	5.00	2834(1)	1.0(1)	4.35
$\frac{15}{2}^-_1$	2749	9(1)	0.00	2724(1)	0.45(8)	0.00
$\frac{13}{2}^-_2$	3288	2(1)	0.59	-	-	-
$\frac{17}{2}^-_1$	3568	0.8(4)	-	3568(2)	0.03(2)	-
$\frac{15}{2}^-_2$	3994	1.0(7)	0.00	-	-	-
$\frac{19}{2}^-_1$	4494	0.9(3)	-	-	-	-
-	-	-	-	2198(2)	0.3(2)	-
-	-	-	-	2723(2)	0.29(6)	-
-	2785	1.32(98)	-	-	-	-
-	2810	3(1)	-	-	-	-
Inclusive		96(6)	-		8.1(5)	22.4

Table 6.3: The measured experimental cross sections (in mb) for all of the states that have been observed in this work for the $A = 47$ mirror nuclei. The measured energies of the states have been exploited to determine the theoretical exclusive cross sections of each state in each nuclei. The measured experimental inclusive cross sections for both pairs of nuclei are presented along with the theoretical inclusive cross section for ^{47}Mn. The theoretical inclusive cross section for the ^{47}Ti nuclei was not calculated due to the shell-model space required in the calculations.

[a] The combined cross section for the ground state and the $\frac{7}{2}^-_1$ state for ^{47}Ti is 53(7) mb – see section 6.2.2 for details

[b] The combined cross section for the ground state and the $\frac{7}{2}^-_1$ state for ^{47}Mn is 3.0(6) mb – see section 6.2.2 for details

^{48}**Mn**/^{48}**V**	**Neutron Occupation**				**Proton Occupation**			
Probability	$\mathbf{1}f_{\frac{7}{2}}$	$\mathbf{2}p_{\frac{3}{2}}$	$\mathbf{1}f_{\frac{5}{2}}$	$\mathbf{2}p_{\frac{1}{2}}$	$\mathbf{1}f_{\frac{7}{2}}$	$\mathbf{2}p_{\frac{3}{2}}$	$\mathbf{1}f_{\frac{5}{2}}$	$\mathbf{2}p_{\frac{1}{2}}$
0.430055	3	0	0	0	5	0	0	0
0.095859	3	0	0	0	4	1	0	0
0.042595	3	0	0	0	4	0	0	1
0.019203	3	0	0	0	3	2	0	0
0.016576	3	0	0	0	3	1	0	1
0.021640	3	0	0	0	3	0	0	2
0.091222	2	1	0	0	5	0	0	0
0.038413	2	1	0	0	4	1	0	0
0.010461	2	1	0	0	4	0	0	1
0.023322	2	0	0	1	5	0	0	0
0.023656	2	0	0	1	4	0	0	1
0.012906	1	2	0	0	5	0	0	0

Table 6.4: The table showing the 4^+ ground state admixture in ^{48}Mn/^{48}V, calculated using the ANTOINE code [31] that implements the KB3G interaction in the full fp-space [57].

knockout, states between $J^\pi = \frac{3}{2}^-$ to $\frac{13}{2}^-$ can be directly populated. Similarly, through a $p_{3/2}$ and $p_{1/2}$ nucleon knockout, states from $J^\pi = \frac{5}{2}^-$ to $\frac{11}{2}^-$ and $J^\pi = \frac{7}{2}^-$ to $\frac{9}{2}^-$ can be populated, respectively. It can be observed from Table 6.5, where the Coulomb and INC terms have been applied (see section 2.2.2 for further details), that the nucleon removal from the $f_{5/2}, p_{3/2}$ and $p_{1/2}$ orbitals demonstrates very small C^{2}S factors ($<< 1$). These shells are above the Fermi level, resulting in a low probability of occupation of these orbitals (see Table 6.4).

Once the spectroscopic factors have been determined for each state in the residues, the single particle cross sections (σ_{sp}) need to be calculated using eikonal reaction dynamics [71], [73], [119]. This method, coupled with the reaction model calculations, allows for the single particle cross sections (σ_{sp}) to be found for one-nucleon removal from each of the levels in the fp-shell to a specific final state. The single particle cross sections provide information about the probability of moving a nucleon from a single particle orbit, assuming that only one nucleon is in that state.

The single-particle cross section is composed of two contributions, one from the stripping cross section and another from the diffractive breakup cross section (i.e. $\sigma_{sp}^{str} + \sigma_{sp}^{dif}$). These

	^{47}Mn C^{2}S				^{47}Ti C^{2}S			
J_i^π	$\mathbf{1}f_{\frac{7}{2}}$	$\mathbf{1}f_{\frac{5}{2}}$	$\mathbf{2}p_{\frac{3}{2}}$	$\mathbf{2}p_{\frac{1}{2}}$	$\mathbf{1}f_{\frac{7}{2}}$	$\mathbf{1}f_{\frac{5}{2}}$	$\mathbf{2}p_{\frac{3}{2}}$	$\mathbf{2}p_{\frac{1}{2}}$
$\frac{5}{2}^-_1$	0.199	0.011	0.016	-	0.203	0.010	0.016	-
$\frac{7}{2}^-_1$	0.147	0.016	0.003	0.000	0.145	0.015	0.003	0.000
$\frac{9}{2}^-_1$	0.301	0.001	0.019	0.000	0.319	0.001	0.020	0.000
$\frac{9}{2}^-_2$	0.307	0.011	0.101	0.011	0.294	0.011	0.095	0.010
$\frac{11}{2}^-_1$	0.476	0.000	0.003	-	0.504	0.000	0.003	-
$\frac{11}{2}^-_2$	0.439	0.001	0.005	-	0.429	0.001	0.004	-
$\frac{13}{2}^-_1$	0.135	0.000	-	-	0.140	0.000	-	-
$\frac{15}{2}^-_1$	0.000	-	-	-	0.000	-	-	-

Table 6.5: The table of C^{2}S values for the $A = 47$ mirror nuclei using the KB3G interaction [57] in the ANTOINE code [31] where the full fp-space was used. The Coulomb, additional isovector term (V_B) and the single particle shifts (V_{ll} and V_{ls}) were applied to determine the C^2S values. Only the observed analogue states observed is presented.

two contributions were calculated separately using the residue-target and nucleon-target elastic eikonal scattering matrices [74]. By using the reaction dynamics code (J. A. Tostevin [74]), the single particle cross section for a state in the residue can be calculated at a specific energy. The total theoretical single particle cross sections for the removal of a nucleon from all allowed orbitals (j) from a projectile A to populate the final state in the residue of $A-1$ are used to calculate the theoretical cross section (σ_{th}) using Eq. 6.9 as shown below:

$$\sigma_{th}(E_x, J^\pi) = \sum_{nlj} \left(\frac{A}{A-1}\right)^N C^2S(j)\sigma_{sp}(nlj, S_n + E_x), \tag{6.9}$$

where the sum is over all the allowed paths to that state, and j is the angular momentum of the orbital from where the nucleon has been removed. The theoretical inclusive cross section, σ_{th}^{incl}, can then be calculated by taking the sum of all of the exclusive cross sections of each state that has been populated in the residue of interest (see Eq. 6.10).

$$\sigma_{th}^{incl}(E_x, J^\pi) = \sum^N \sigma_{th}^{excl}(E_x, J^\pi). \tag{6.10}$$

To calculate the theoretical single-particle cross sections for each state, σ_{sp}, a few inputs must be considered in the reaction model. These are detailed as follows:

1. Optical potentials of the residue-target and the valence nucleon-target with their corresponding scattering (S) matrices. These are utilised in the eikonal model, which affect the parameter integrals of σ_{sp}^{str} and σ_{sp}^{dif}. This results in the reaction being spatially localised.

2. The geometry of the radial wave function for the removed nucleons in the projectile ground state. The shapes and the parameters corresponding to the radial size were constrained [27] using the Hartree-Fock (HF) calculations of the neutron and proton densities for the residues and the root-mean-squared (rms) radii of orbitals in the HF mean field.

The calculation for the theoretical cross section was conducted by computing the residue and projectile density distributions using the SkX interaction Skyrme Hartree-Fock calculations, detailed in Ref [80]. The ^{9}Be target utilised in the calculations was assumed to have a Gaussian nucleon density consisting of an rms radius of 2.36 fm. This was included as an input to calculate the S matrices and the resulting radial wave function.

Assuming that the residue (i.e. the core) and the knocked out (valence) nucleon are separate entities that interact with the target, the elastic scattering S matrices for the ^{47}Mn (^{47}Ti)-^{9}Be residue-target system can be calculated. Furthermore, the S matrices for the valence nucleon-target neutron (proton)-^{9}Be system can also be calculated separately. It is required for the secondary beam energies at the centre of the target to be calculated to determine the S matrices, where the energies were found to be 84.2 MeV/u for ^{48}Mn and 89.1 MeV/u for ^{48}V using LISE++ calculations [127], [128]. These energies were calculated using the magnetic rigidity, Bρ, in the S800 spectrometer coupled with the energy loss calculations from LISE++. This part of the calculation allows the elastic and reaction cross sections to be calculated for the core-target and neutron/proton-target systems individually. The produced outputs are consequently used for the knockout process, where the probability of the knockout depends on the probability of the core being elastically scattered during the reaction and the probability of the valence nucleon being absorbed by the target.

The next stage of the calculations compute the density distributions for the projectile. This allows for the binding potential of the removed nucleon to be constrained using HF calculations. As a result, the HF radii and the binding energy for each orbital, from where the valence nucleon could come from, are produced (see Tables 6.6 and 6.7). The results in the tables show the

different HF radii and binding energies for the neutron and proton removal from ^{48}Mn and ^{48}V, respectively. The fp orbitals (highlighted in red) were used to calculate the single-nucleon cross sections for each state in the ^{47}Mn and ^{47}Ti residue nuclei. It is important to note that the calculations presented in the tables below do not account for the final state of the residue.

k	n	l	J	r(2) (fm)	Energy (MeV)
1	1	s	1/2	2.608	-41.758
2	1	p	3/2	3.187	-33.382
3	1	p	1/2	3.099	-31.118
4	1	d	5/2	3.635	-24.100
5	1	d	3/2	3.585	-19.303
6	2	s	1/2	3.560	-19.742
7	1	f	7/2	3.991	-14.098
8	1	f	5/2	4.110	-6.919
9	2	p	3/2	4.019	-9.427
10	2	p	1/2	4.185	-7.721
11	1	g	9/2	4.350	-3.315
12	1	g	7/2	4.485	-0.200
13	2	d	5/2	5.817	-0.200
14	2	d	3/2	5.852	-0.200
15	3	s	1/2	9.088	-0.200

Table 6.6: The HF neutron single-particle rms radii and energies for each orbital in the ^{48}Mn projectile. The fp orbitals were used in the single-neutron cross section calculations (in red).

Once the HF single-particle radii and energies have been determined for each orbital in the ^{48}Mn and ^{48}V projectiles, the Woods-Saxon plus spin-orbit potential is used instead of the HF potential to calculate the bound state wavefunctions for the removed particle. The following geometries are constrained: the diffuseness $a = 0.7$ fm, and the spin-orbit strength $V_{so} = 6$ MeV. Consequently, the rms radius of a particular orbital and binding energy, obtained from the HF calculations, were used to constrain the radii (r_0) of the binding potentials using the Skyrme SkX interaction [80], as shown in Table 6.8.

The last step considers the adjustment of the central potential depth, where the effective binding energies, E_x+$S_{n/p}$, of the final states are provided. At this point, the measured excitation energy (E_x) of the final state and the S_n and S_p separation energies for ^{48}Mn and ^{48}V are also required, being 14.802(3) MeV and 6.829(1) MeV, respectively, to calculate the corresponding

k	n	l	J	r(2) (fm)	Energy (MeV)
1	1	s	1/2	2.637	-33.205
2	1	p	3/2	3.219	-24.947
3	1	p	1/2	3.133	-22.627
4	1	d	5/2	3.673	-15.800
5	1	d	3/2	3.639	-10.944
6	2	s	1/2	3.629	-11.340
7	1	f	7/2	4.047	-5.972
8	1	f	5/2	4.169	-0.200
9	2	p	3/2	4.247	-1.390
10	2	p	1/2	4.468	-0.200
11	1	g	9/2	4.257	-0.200
12	1	g	7/2	4.181	-0.200
13	2	d	5/2	4.358	-0.200
14	2	d	3/2	4.404	-0.200
15	3	s	1/2	4.690	-0.200

Table 6.7: The HF proton single-particle rms radii and energies for each orbital in the ^{48}V projectile. The fp orbitals were used in the single-proton cross section calculations (in red).

	^{48}Mn(-1n)	^{48}V(-1p)
Orbital	r_0 (fm)	r_0 (fm)
$f_{\frac{7}{2}}$	1.283	1.255
$p_{\frac{3}{2}}$	1.143	1.085
$f_{\frac{5}{2}}$	1.297	1.264
$p_{\frac{1}{2}}$	1.190	1.118
$s_{\frac{1}{2}}$	-	1.265
$d_{\frac{3}{2}}$	-	1.278
$d_{\frac{5}{2}}$	-	1.290

Table 6.8: The rms radii (r_0) of the binding potentials of the nucleon removal from the fp and sd shells (used for the ^{48}V$-1p$ case). The diffuseness, a, of 0.7 fm and the spin-orbit strength, V_{so}, of 6 MeV was applied in the calculations.

single-particle cross sections. The separation energies are taken from the most recent mass evaluations in Ref. [82]. The cross sections for each state populated in the $A = 47$ mirror nuclei were calculated using the radial wavefunction between the final state of the residue and the removed nucleon using the eikonal S-matrices.

The resulting single-particle cross sections obtained from this step consist of individual strip-

ping (σ_{sp}^{str}) and diffraction (σ_{sp}^{dif}) contributions. The sum of these two contributions gives the total single-particle knockout cross sections, σ_{sp}. By taking the σ_{sp} contributions for each subshell coupled with the C^2S values obtained from the shell model calculations, the theoretical partial cross sections (j), $\sigma_{th}(E_x, J^\pi, j)$, can be calculated for a particular state in the residue nucleus (see Eq. 6.9). Different single-nucleon knockout reactions were taken place for the different fp orbitals that contribute to the total theoretical exclusive cross section of that particular state ($E_x + S_{n/p}$) using the different r_0 parameters detailed in Table 6.8. The total theoretical exclusive cross section for each state was calculated as shown in Eq. 6.9 over all possible j values.

The theoretical single particle cross sections for each observed yrast and yrare states populated in ^{47}Mn and ^{47}Ti, resulting from a neutron/proton removal from each of the fp orbitals in ^{48}Mn and ^{48}V, respectively, using the above method is shown in Tables 6.9 and 6.10. The total theoretical inclusive cross section was calculated by adding all of the exclusive cross sections of the observed states, independent of the separation energy. Therefore, the total theoretical inclusive cross section ($\sigma_{th,incl}$) of ^{47}Mn, which includes all of the fp contributions, is 22.4 mb. Predicted exclusive cross sections for each state, $\sigma_{th,excl}$, in the $A = 47$ mirror pair, using all fp contributions, and the theoretical inclusive cross section for ^{47}Mn are presented in Table 6.3. For the more bound ^{47}Ti system, the theoretical inclusive cross section was not determined using the method detailed above [25], [26] due to the high separation energies, where the calculations of all bound final states in the shell model become impossible.

Due to the restrictions in the shell model space used, the negative parity states can only be assessed. The calculated C^2S values in Table 6.5 for each member in the $A = 47$ mirror pair are observed to be similar as the same interactions (i.e the addition of $V_{CM} + V_B + V_{ll} + V_{ls}$ terms - see section 5.3 for details) were utilised in the shell model. This results in the theoretical exclusive cross sections ($\sigma_{th,excl}$) for each observed state to be similar for both ^{47}Mn and ^{47}Ti, as seen in Table 6.3.

As the *sd*-shells are not contained within the currently used shell model interactions, it was not possible to calculate the theoretical cross sections for the observed positive parity states.

Predicted Cross Sections for One-Neutron Removal from fp shells						
E_x **(MeV)**	$S_p + E_x$ **(MeV)**	J^π	j	σ_{sp} **(mb)**	C^2S	$\sigma_{th}(E_x, J^\pi, j)$ **(mb)**
0.000	14.802	$\frac{5}{2}^-$	$1f_{\frac{7}{2}}$	10.2	0.199	2.16
			$f_{\frac{5}{2}}$	8.8	0.011	0.10
			$p_{\frac{3}{2}}$	10.5	0.016	0.18
0.122	14.924	$\frac{7}{2}^-$	$1f_{\frac{7}{2}}$	10.1	0.147	1.59
			$1f_{\frac{5}{2}}$	8.8	0.016	0.15
			$2p_{\frac{3}{2}}$	10.5	0.003	0.03
			$2p_{\frac{1}{2}}$	11.0	0.000	0.00
1.175	15.977	$\frac{9}{2}^-_1$	$1f_{\frac{7}{2}}$	9.7	0.301	3.12
			$1f_{\frac{5}{2}}$	8.4	0.001	0.01
			$2p_{\frac{3}{2}}$	9.9	0.019	0.20
			$2p_{\frac{1}{2}}$	10.4	0.000	0.00
2.395	17.197	$\frac{9}{2}^-_2$	$1f_{\frac{7}{2}}$	9.3	0.307	3.05
			$1f_{\frac{5}{2}}$	8.1	0.011	0.09
			$2p_{\frac{3}{2}}$	9.3	0.101	1.01
			$2p_{\frac{1}{2}}$	9.9	0.011	0.12
1.380	16.182	$\frac{11}{2}^-_1$	$1f_{\frac{7}{2}}$	9.7	0.476	4.90
			$1f_{\frac{5}{2}}$	8.4	0.000	0.00
			$2p_{\frac{3}{2}}$	9.8	0.003	0.03
2.834	17.636	$\frac{11}{2}^-_2$	$1f_{\frac{7}{2}}$	9.2	0.439	4.29
			$1f_{\frac{5}{2}}$	8.0	0.001	0.01
			$2p_{\frac{3}{2}}$	9.1	0.005	0.05
2.574	17.376	$\frac{13}{2}^-_1$	$1f_{\frac{7}{2}}$	9.3	0.135	1.33
			$1f_{\frac{5}{2}}$	8.1	0.000	0.00
2.724	17.526	$\frac{15}{2}^-_1$	$1f_{\frac{7}{2}}$	9.2	0.000	0.00

Table 6.9: The predicted cross sections for the observed states in ^{47}Mn, produced through the ^{48}Mn$-1n$ reaction. States from $J^\pi = \frac{5}{2}^-$ to $\frac{15}{2}^-$ have been populated in this work due to the direct neutron removal from the fp orbitals in the ^{48}Mn projectile. The S_n of ^{48}Mn is 14.802(3) MeV [82] and the mass dependent term, $(A/A-1)^3$, was calculated to be 1.067. The summed single particle cross sections are calculated using the reaction model. The C^2S values were determined using the ANTOINE [31] shell model calculation, shown in Table 6.5. j represents the orbital from which the neutron was removed from the initial state of ^{48}Mn.

Predicted Cross Sections for One-Proton Removal from fp shells						
E_x **(MeV)**	$S_p + E_x$ **(MeV)**	J^π	j	σ_{sp} **(mb)**	C^2S	$\sigma_{th}(E_x, J^\pi, j)$ **(mb)**
0.000	6.829	$\frac{5}{2}^-$	$1f_{\frac{7}{2}}$	12.1	0.203	2.63
			$f_{\frac{5}{2}}$	10.3	0.010	0.11
			$p_{\frac{3}{2}}$	12.5	0.016	0.21
0.159	6.988	$\frac{7}{2}^-$	$1f_{\frac{7}{2}}$	12.1	0.145	1.86
			$1f_{\frac{5}{2}}$	10.3	0.015	0.17
			$2p_{\frac{3}{2}}$	12.4	0.003	0.04
			$2p_{\frac{1}{2}}$	12.7	0.000	0.00
1.252	8.081	$\frac{9}{2}^-_1$	$1f_{\frac{7}{2}}$	11.5	0.319	3.91
			$1f_{\frac{5}{2}}$	9.8	0.001	0.01
			$2p_{\frac{3}{2}}$	11.5	0.020	0.24
			$2p_{\frac{1}{2}}$	11.8	0.000	0.01
2.406	9.235	$\frac{9}{2}^-_2$	$1f_{\frac{7}{2}}$	10.9	0.294	3.43
			$1f_{\frac{5}{2}}$	9.4	0.011	0.11
			$2p_{\frac{3}{2}}$	10.7	0.095	1.09
			$2p_{\frac{1}{2}}$	11.0	0.010	0.12
1.444	8.273	$\frac{11}{2}^-_1$	$1f_{\frac{7}{2}}$	11.4	0.504	6.12
			$1f_{\frac{5}{2}}$	9.7	0.000	0.00
			$2p_{\frac{3}{2}}$	11.4	0.003	0.03
2.682	9.511	$\frac{11}{2}^-_2$	$1f_{\frac{7}{2}}$	10.8	0.429	4.94
			$1f_{\frac{5}{2}}$	9.3	0.001	0.01
			$2p_{\frac{3}{2}}$	10.5	0.004	0.05
2.668	9.497	$\frac{13}{2}^-_1$	$1f_{\frac{7}{2}}$	10.8	0.140	1.61
			$1f_{\frac{5}{2}}$	9.3	0.000	0.00
2.749	9.578	$\frac{15}{2}^-_1$	$1f_{\frac{7}{2}}$	10.8	0.000	0.00

Table 6.10: The predicted cross sections for the observed states in ^{47}Ti, produced through the ^{48}V$-1p$ reaction. The analogue states of the states seen in ^{47}Mn are presented here. The S_p of ^{48}V is 6.829(1) MeV [82] and the mass dependent term, $(A/A-1)^3$, was calculated to be 1.067. The summed single particle cross sections are calculated using the reaction model. The C^2S values wer determined using the ANTOINE [31] shell model calculations, shown in Table 6.5. j represents the orbital from which the neutron was removed from the initial state of ^{48}V.

6.4 Discussion of Results

6.4.1 Discussion of Inclusive Cross Sections

The experimental inclusive cross sections between the ^{47}Ti and ^{47}Mn pair exhibit a large difference by a factor of ∼11. Since states beyond the proton separation energy were directly populated, the inclusive theoretical cross section, which includes the observed states, for ^{47}Mn becomes 22.4 mb (see section 6.3 for further details). This result is ∼3 times greater than the experimental measurement. The theoretical inclusive cross section for ^{47}Ti could not be computed due to high separation energies.

The understanding of the strong suppression of the experimental cross sections compared with the theoretical cross section for knockout reactions on light targets is a key interest in recent studies [25]–[27]. From these studies, it can be established that the strong suppression observed is dependent on the (a)symmetry of the separation energies between the two mirror nuclei. A negative correlation was observed as a function of ΔS, defined as $S_n - S_p$ for neutron knockout reactions [27], as shown in the following equation:

$$\Delta S = \frac{\sum (E_x + S_n) \cdot \sigma_{th}}{\sum \sigma_{th}} - S_p, \tag{6.11}$$

where E_x is the experimental excitation energy, S_n is the neutron separation energy, σ_{th} is the theoretical cross section for each individual state and S_p is the proton separation energy.

In relation to the systematics, the current case demonstrates that the removals of a strongly bound neutron from a weakly bound system in close proximity to the proton drip line may show a strong suppression of the experimental cross section relative to the theoretical prediction. For ^{47}Mn, the suppression of the inclusive cross section was determined, where the separation energy asymmetry parameter, ΔS, was calculated to be 14.42(1) MeV using Eq. 6.11 as multiple states were populated. At this ΔS value, it can be predicted from the systematics that the $R_s = \sigma_{exp}/\sigma_{th}$ would be 0.38(10), which exhibits a good agreement with the calculated value in this work, which is 0.36(2). Turning to the results of the mirror nucleus, ^{47}Ti, the states that were observed in this work are well below the neutron and proton separation energies, being S_n = 8.88 MeV and S_p = 10.46 MeV [82], respectively, due to its strongly bound nature. Therefore, the theoretical inclusive cross section for ^{47}Ti was not determined as the shell-model

calculation would involve a significant number of bound states.

Previous examples that have used mirrored knockout reactions have also observed asymmetric inclusive cross sections but with smaller difference factors compared with the observations seen in this work. Wimmer *et al.* [129] determined a factor of ∼4 difference between the experimentally deduced inclusive cross section to the theoretical result for the $T = 1, A = 70$ mirror pair. Subsequently, Spieker *et al.* [130] found a factor of ∼3 difference for a mirrored one-nucleon knockout reaction to the $T = \frac{1}{2}, A = 55$ mirror pair from ^{56}Ni. From the work of Yajzey *et al.*, where the analysis was conducted with data taken in the same experiment as the current work, a factor of ∼9 was observed for a mirrored one-nucleon knockout reaction to the $T = 2, A = 48$ mirror pair. The above observations can be interpreted in terms of binding energy effects, where the large binding energy in the positive T_z nuclei compared to the low proton separation energy, S_p, in the negative T_z counterpart exhibits asymmetric behaviour.

As proposed by Yajzey *et al.*, essentially all *fp*- and *sd*-shell removals will likely contribute to the population of the bound states in the positive T_z nucleus. In this case, this results in the $T_z = +\frac{3}{2}$, ^{47}Ti nucleus, where $S_p = 10.46$ MeV and $S_n = 8.88$ MeV [82], to have a very large inclusive cross section. For the $T_z = -\frac{3}{2}$, ^{47}Mn proton-rich nucleus, where $S_p = 0.384$ MeV and $S_n = 18.22$ MeV [82], the excitation energy centroids of the single particle strength distribution for the *sd*-shell removal will be well above the proton separation energy, and it is therefore probable to decay via proton emission. This results in a lower inclusive cross section corresponding to only *fp*-shell removals.

If this is the case, unseen feeding is likely to be contributing to the low-lying yrast states of ^{47}Ti, which is confirmed by the very large combined cross section of 53(7) mb in Table 6.3 for the ground state and first excited state. An estimate of the maximum (sum-rule) cross section was made by taking the same approach detailed in Ref. [10], assuming that the *sd*-shells were full and that three valence protons are present in the *fp*-shell. It is further assumed that the knockout of one proton from these sub-shells populates the bound states in ^{47}Ti. As an exercise, the maximum *fp*- and *sd*-shell removal contribution to the overall theoretical cross section can be obtained using Hartree-Fock calculations. These calculations were performed using the SkX Skyrme interaction [80] (see section 6.3 for details), where it was demonstrated that the *sd*-shell orbitals in the proton-knockout of ^{48}V to ^{47}Ti are 4.97 MeV ($d_{3/2}$), 5.37 MeV ($s_{1/2}$), and 9.82

MeV ($d_{5/2}$) more bound that the protons at the $f_{7/2}$ Fermi level, as seen in Table 6.7. This gives an estimate of the location of the centroids for knockout of the *sd*-shell, see Fig. 6.3(a). Almost all of the *sd* strength in ^{47}Ti are bound except for the $d_{5/2}$ knockout. Therefore, all observed decays will go to the ground state centroid of ^{47}Ti. The same method was applied for the mirror nucleus, ^{47}Mn, where three valence neutrons were placed in the *fp*-shell. The neutron knockout from the *sd*-shells for the ^{48}Mn to ^{47}Mn reaction are found to be 5.21 MeV ($d_{3/2}$), 5.64 MeV ($s_{1/2}$), and 10.00 MeV ($d_{5/2}$) more bound than the neutrons at the Fermi level, as seen in Fig. 6.3(b). It can be observed that the states populated through *sd* removal in ^{47}Mn will not be observed as they are very high in energy. Since the proton separation energy in ^{47}Mn is just above the Fermi level ($S_p = 0.384$ MeV), proton evaporation is likely.

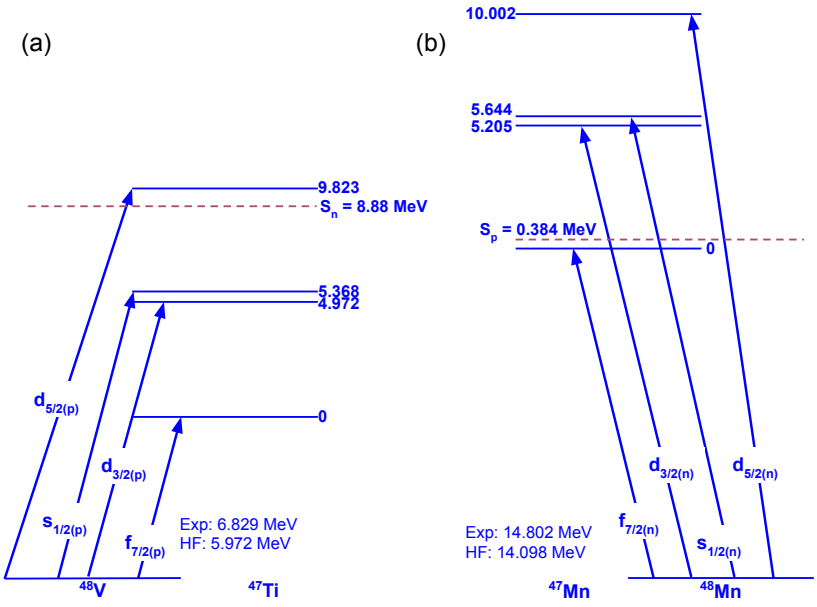

Figure 6.3: The Hartree-Fock predicted single particle centroids for (a) ^{47}Ti and (b) ^{47}Mn. Knockouts from more bound *sd*-orbitals allows for a number of states to be spread over a range of energies following a Gaussian, hence the spectroscopic strength also becomes distributed to all states. Knockouts from deeper shells (i.e. $d_{5/2}$) show a higher centroids in both (a) and (b), where the width of the centroids are on the order of a few MeV.

At this step, it is informative to estimate a maximum theoretical inclusive cross section by determining the missing *fp* strength and the addition of the *sd*-shell protons at the estimated centroid energies presented in Fig. 6.3. In this approximation, as ^{48}V has three valence protons in the *fp*-shell, the total contribution from the *fp* strength is assumed to be three throughout

all states. Therefore, the contribution of the fp strength of shell-model states up to E_x = 3.3 MeV gives a total C^2S =2.3, where the missing 0.7 units are thought to be distributed to states at higher excitation energies and are estimated to give an additional missing cross section of 5.6 mb. By determining the missing sd strength from the Hartree-Fock calculations, this yields a maximum total theoretical inclusive cross section of 138 mb when all of the spectroscopic strength from the $d_{3/2}$, $s_{1/2}$ and $d_{5/2}$ centroids (assuming C^2S =4, 2 and 6, respectively), and the missing fp contribution are included.

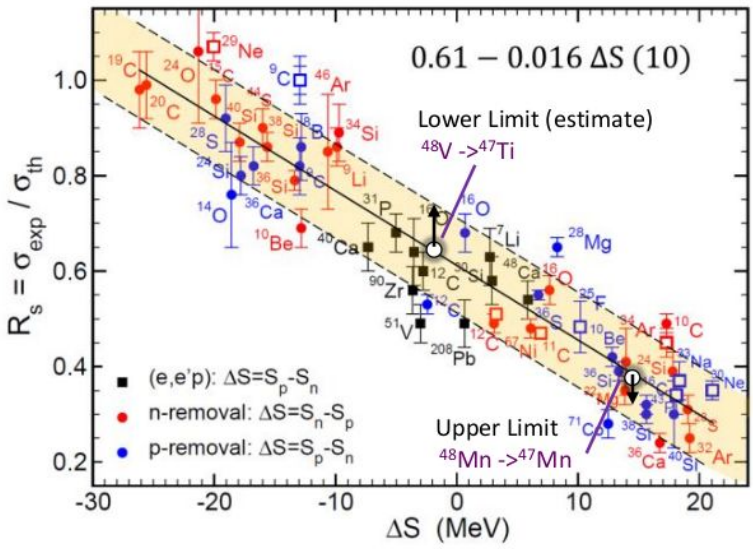

Figure 6.4: The systematics from Ref. [27], which are adapted to present the current results of the suppression of the experimental cross sections with the theory, R_s, for ^{47}Ti (lower limit) and ^{47}Mn (upper limit). Both results are presented in white dots. The ΔS values for each respective nucleus are 1.916(1) MeV and 14.42(1) MeV.

By taking the total theoretical inclusive one-nucleon knockout cross section of 138 mb, which takes into account all of the sd- plus fp-strength, the lower limit of R_s, being 0.69(4), can be calculated for the proton knockout from ^{48}V to ^{47}Ti at a ΔS value of 1.916(1) MeV, the latter calculated from using Eq. 6.11. This result conforms with the systematics presented in Ref. [27], where R_s is predicted to be 0.58(10). Conversely, for the ^{47}Mn case, only the fp-orbitals contribute significantly to the theoretical inclusive cross section. Therefore, the R_s value becomes an upper limit at a ΔS value of 14.42(1) MeV, being 0.36(2). Both R_s values for ^{47}Ti and ^{47}Mn are shown in Fig. 6.4.

6.4.2 Discussion of Exclusive Cross Sections

Once the exclusive cross sections have been determined for each observed state in the $A = 47$ nuclei, the relative cross sections can be calculated. This analysis was not done for the stable ^{47}Ti nucleus due to unseen feeding into the yrast states, which results from underlying knockout from bound *sd*-shells. Therefore, the exclusive cross sections in ^{47}Ti become artificially inflated.

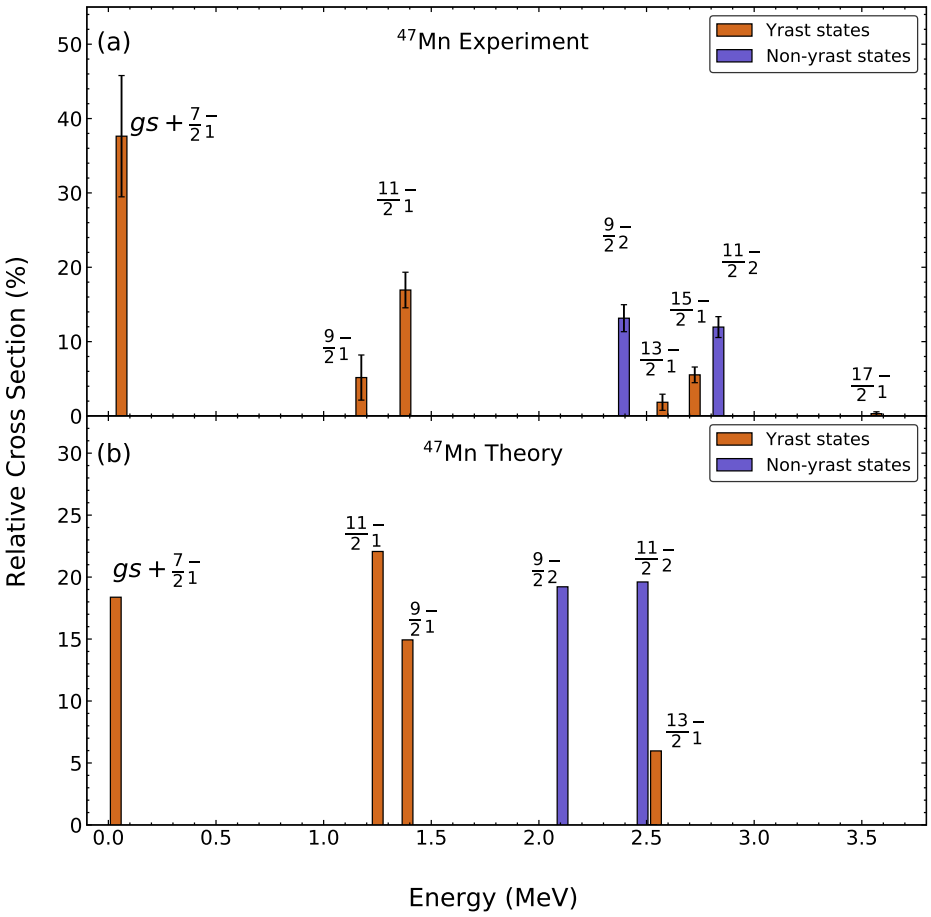

Figure 6.5: (a) Experimental and (b) theoretical relative cross sections for the observed excited states in ^{47}Mn, produced from the one-neutron knockout from the 4^+ ground state of ^{48}Mn. The calculations were obtained using spectroscopic factors, calculated from the shell model and single particle cross sections obtained from the reaction model. Panel (a) shows the measured relative cross sections for the yrast states (brown) and for the yrare states (purple). The $\frac{17}{2}^-$ state is included as it was found to be populated in the data, which can not be populated in direct knockout reactions. Panel (b) shows the predicted relative cross sections for the yrast (brown) and yrare (purple) states. The theoretical relative cross section for the $\frac{15}{2}^-$ state was found to be negligible and was therefore excluded.

Considering the proton-rich counterpart, ^{47}Mn, Figs. 6.5(a) and 6.5(b) exhibit the direct comparison between the relative experimental and theoretical cross sections, respectively, as a function of the experimentally measured excitation energies for each state seen. The relative cross section is defined as $\sigma_{excl}/\sigma_{incl}$.

Although the measured cross sections are generally found to be smaller in ^{47}Mn than the theoretical values, the comparison between the experimental and theoretical relative cross sections in ^{47}Mn exhibit some key similarities. The cross sections are dominated by the $J^\pi = \frac{5}{2}^-_1, \frac{9}{2}^-_{1,2}$ and $\frac{11}{2}^-_{1,2}$ states, where the strong direct population of the yrare $J^\pi = \frac{9}{2}^-$ and $\frac{11}{2}^-$ states are also found to be well reproduced. This result was consistent with the observation seen in section 5.1.2. Another observation is that the $J^\pi = \frac{15}{2}^-_1$ state becomes strongly populated in the data, while the theoretical prediction shows that the direct population of this state is negligible. This implies that the population of high-spin states is not a purely direct process, hence, some other indirect population process is likely to be involved. This is also the case for the $\frac{17}{2}^-$ state.

6.5 Summary of Results

Notable differences were observed between the inclusive knockout cross sections for the two members in the $A = 47$ mirror pair. It is suggested that this is due to the large difference between the nucleon separation energies and the resulting variation of the *sd*-shell strength between the two mirror pairs. Therefore, it is evident that the degree of binding-energy effects is crucial to understand the patterns in mirrored knockout reactions - a technique that has been used extensively in a number of previous works [3], [10], [129], [130].

The experimental exclusive cross sections were also compared for the observed analogue yrare states. Additional unseen feeding to the states observed is shown to contribute, especially in the strongly-bound nucleus, which, in turn affects the measured exclusive cross sections. Therefore, the ratios of the experimental and theoretical exclusive cross sections are presented as upper limits. As the two nuclei in the $A = 47$ mirror pair have significant differences in the binding, it was instructive that the exclusive cross sections are discussed in terms of the systematic suppression of the spectroscopic strength as a function of the binding energy, where a similar trend is shown as observed in published systematics (i.e. Ref. [27]).

Chapter 7

Lifetime Measurements in A=47 mirror nuclei

This chapter will present the details of extracting the lifetime and energies of the first-excited $\frac{7}{2}^-$ states in both the ^{47}Mn and ^{47}Ti nuclei. This lifetime analysis was possible through the use of a GEANT4 simulation package, where the geometrical and physical properties of GRETINA, the positional information of the target and the S800 spectrograph are considered.

The procedure of optimising the simulation parameters to replicate the experimentally observed results is presented. The measurement of lifetimes and the energies of the $\frac{7}{2}^-$ yrast states in the $A = 47$ mirror nuclei are detailed in this chapter, where the parameters within the simulation were varied systematically until the experimental spectra are reproduced. Consequently, the details of the systematic and statistical errors for the lifetime and energy measurements are also detailed in this chapter.

7.1 γ-ray Lineshapes

Since a long tailing effect was observed in both ^{47}Ti and ^{47}Mn for $\frac{7}{2}^- \rightarrow \frac{5}{2}^-_{gs}$ transition, as shown in Figs. 5.1(a) and 5.4(a), the lifetimes and energies of the respective $\frac{7}{2}^-$ states can be established using the γ-ray lineshape method [3], [131]. The states of nuclei that have a long lifetime (>100 ps), which decay downstream of the target, are considered. Typical velocities of $\sim 0.3c$ corresponds to the reaction products travelling ∼9 mm downstream of the target for every 100 ps [108]. As discussed in section 4.6.1, event-by-event Doppler corrections were performed by taking into account the angle of the γ-ray emission, θ, calculated by using the first

point of interaction within GRETINA and the beam axis (see Eq. 4.4). Using this procedure, it is assumed that the nucleus decays at the centre of the target. For nuclei that decay further downstream from the target, this results in an over correction for the Doppler shift, where a longer low-energy tailing effect and a low-energy shift of the peak centroid is seen, corresponding to an increasing lifetime (see Figs. 7.1 and 7.2). It is imperative that the γ-ray emission angle, θ, is precisely determined to perform precise Doppler corrections and to analyse γ-ray lineshapes, hence the use of GRETINA is important.

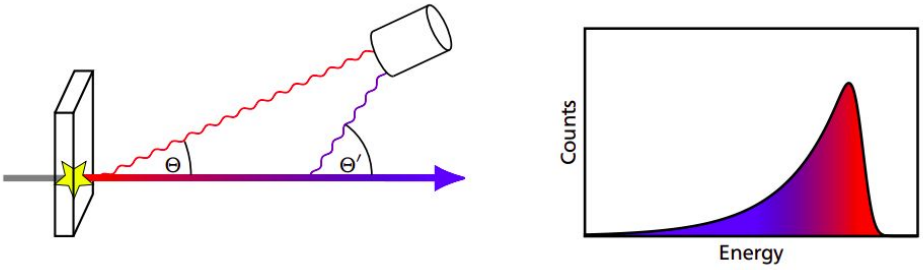

Figure 7.1: A schematic diagram from Ref. [132] showing the effect on the γ-ray lineshape of a transition from a long-lived state within the nucleus that decays downstream of the target. The longer the lifetime, the further downstream the nucleus decays. As a consequence, the magnitude of the low-energy shift becomes significant and the tailing effect of the transition becomes longer when the Doppler corrections have been applied.

7.2 G4Lifetime Package

To perform the lifetime measurement of the $\frac{7}{2}^-$ yrast state in ^{47}Ti and ^{47}Mn, a GEANT4 simulation framework was utilised [100], where the G4Lifetime package was specifically used for this analysis [133]. This package was developed by NSCL, which incorporates the geometry of GRETINA (9 detector modules), the properties of the beam line and the ^{9}Be reaction target.

GEANT4 allows for the accurate reproduction of particle and γ-ray interactions with matter. In this case, the interaction of the secondary beams with the ^{9}Be reaction target and the resulting γ rays, produced via the de-excitation of the nuclei interacting with the detector modules in GRETINA, can be modelled. The associated properties of GRETINA, such as the position resolution of the first point of interaction and the energy resolution can also be defined within the simulation package to ensure consistency with the experimental data. The simulated spectra

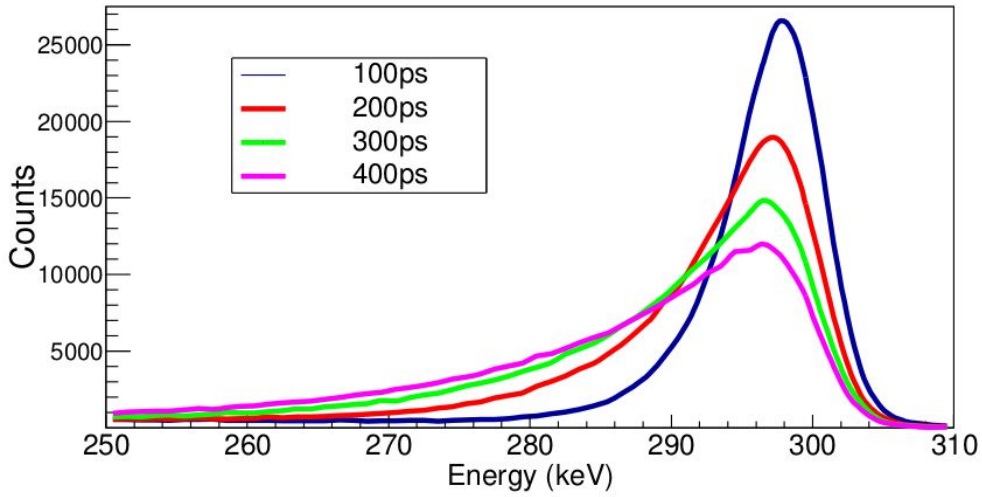

Figure 7.2: The simulated GRETINA lineshape spectra taken from Ref. [108] of the 300 keV γ ray that decays from a state. The mean lifetimes of the state were varied from 100 to 400 ps at a beam velocity of $0.3c$. With longer low-energy tails, it can also be observed that the position of the centroid becomes lower in energy as well as the value of the peak energy, hence the mean lifetime increases.

are produced in ROOT alongside the data from the experiment for comparison.

It was imperative that the properties of the incoming and outgoing beams, as well as the reaction target from the experimental spectra are replicated accurately in the simulation. This allows for the energy losses due to the knockout mechanism and the beam interactions within the target to be consistent with experimental observations. By optimising the incoming and outgoing beam energies and the properties of the secondary target, an accurate representation of the experimentally-observed outgoing beam can be provided. This is crucial due to the simulated lineshape being highly dependent on β and the momentum distribution of the decaying particles. The following experimental spectra, required to be reproduced before analysing the effect of lifetime and energy variation of a particular decaying transition, are as follows:

1. The dispersive and non-dispersive angles at the target position (a_{ta} and b_{ta}). This was corrected by changing the width and the centroid of the distribution by varying the relevant simulation parameters to replicate the experimental spectra.

2. The non-dispersive beam position on the target (y_{ta}). This was also replicated in the

simulation by varying the centroid and the width of the spectrum to be concordant with the experiment.

3. The relative energy spread, $\delta T/T$, of the outgoing fragmented residues, d_{ta}. This spectrum was reproduced in the simulation by varying the incoming and outgoing energies of the beam and the outgoing fragmented particles, respectively, as well as the momentum acceptance. Since the target was included in the simulation, the d_{ta} spectrum becomes dependent on the scale density, the thickness of the target and the reaction mechanism.

4. The recoil velocity spectrum, β (related to the d_{ta} spectrum). Once the adjustments are made to the d_{ta} spectrum to reproduce the experimental spectrum, small adjustments were made to the beam energy to obtain the experimentally measured β value. This did not substantially affect the process described in step 3, where the simulation of the d_{ta} spectrum was matched to the experimental d_{ta} spectrum.

Examples of the optimised parameters in the simulation to the experimental spectra are shown in Fig. 7.3.

By using the χ^2 minimisation procedure [134], the optimum simulation parameters can be determined through the comparison of the simulated data to the experimental data as follows:

$$\chi^2 = \sum_{i=1}^{N} \frac{(x_i - y_i)^2}{\sigma_i^2}, \tag{7.1}$$

where N is the total number of data points, x_i represents the experimental data point, y_i is the simulated data point and σ_i is the error from the experimental data point. A low value of χ^2 is favoured, which corresponds to the simulation accurately replicating the experimental data when the $(x_i - y_i)^2$ term becomes small.

7.2.1 The Simulation Procedure in this Work

The first step is to replicate the experimental d_{ta} spectrum in the simulation. Ideally, this step would be done with no reaction target in place so that the full cocktail beam is passed through the S800 spectrograph. However, in the current experiment, no runs took place when the target was not included. Therefore, the main unreacted secondary beams of interest (^{48}Mn and ^{48}V) were

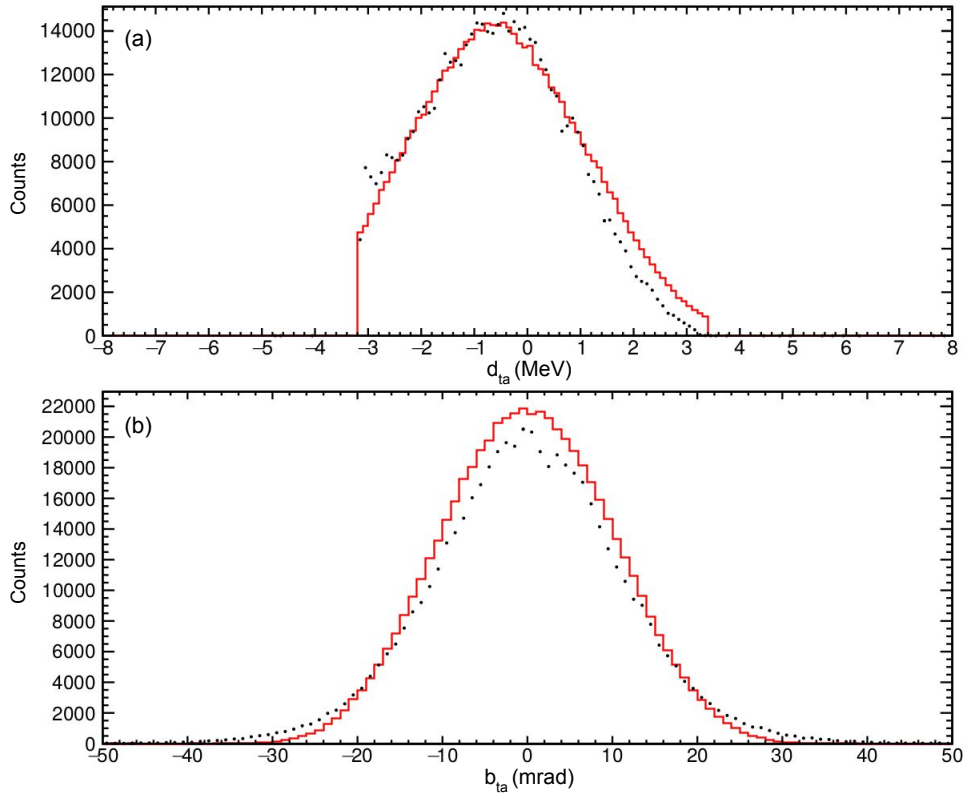

Figure 7.3: Examples of simulated spectra as seen in this work to optimise the simulation parameters to replicate the experimental data for ^{47}Ti. (a) shows the simulated d_{ta} spectrum when the reaction target has been applied (red) and the experimental data (black data points). (b) shows the comparison of the simulated b_{ta} spectrum (in red) to the experimental spectrum (black points).

considered, where the Bρ of the dipole magnets at the S800 spectrograph were set to 2.452 Tm and 2.7814 Tm, respectively. The experimental d_{ta} spectra for both incoming beams, obtained through the use of the inverse map (see Chapter 3.5.2), are replicated by simultaneously varying the incoming beam energies (KEU_{in}), momentum acceptance (dp) and the target scale density parameters in the simulation following Eq. 7.1. The target thickness was obtained from LISE++ calculations [127] and was kept constant throughout the simulation at 1.017 mm. The target scale density of the ^{9}Be target was optimised to accurately reproduce the energy loss of the secondary beam before and after the knockout reaction within the simulation. This factor, which typically lies between 0.95 and 1.05, accounts for any discrepancies between the calculations performed via LISE++ [127] and the GEANT4 stopping tables. The optimisation of the target properties

is notable since the lineshape is strongly dependent on the value of β, which is consequently related to the energy of the outgoing beams at the target position. As a result, the target scale density was varied until the obtained simulated spectrum was comparable to the experimental d_{ta} spectrum for the unreacted ^{48}Mn and ^{48}V beams, where the beams attenuate within the 188 mg/cm^2 ^{9}Be target before reaching the S800 spectrograph. Although the d_{ta} spectrum has been replicated, it is necessary to vary the outgoing beam energy (KEU_{out}) and the target scale density to obtain a similar shape in the simulation. Once the shape has been replicated, the incoming beam energy (KEU_{in}), the momentum acceptance (dp) and the target scale density were kept constant throughout the analysis for the given secondary beams.

The next step is to incorporate the one-nucleon knockout reaction within the simulation to reproduce the outgoing beam energy after the target. This was achieved by varying the dp_{frac}, dp and dp_{FWHM} parameters, which correspond to the fraction of the incoming beam momentum, the momentum spread due to the reaction and the width of the momentum shift, respectively. The dp_{frac} and dp parameters are incorporated in the simulated spectrum distribution of the outgoing particle of interest, which results from the reaction occurring within the target through [135]:

$$p_{out} = p_{in} \times dp \times dp_{frac} \times \frac{A_{out}}{A_{in}}, \tag{7.2}$$

where p_{in} and p_{out} are the momentum of the particle before and after the reaction at the target position, respectively, and A_{out}/A_{in} are the mass ratio between the outgoing residue and the incoming beam. By following the procedure above, the optimum values of dp_{frac}, dp and dp_{FWHM} of the fragmented residues (i.e. ^{47}Ti and ^{47}Mn in this case), were deduced through minimising the χ^2 factor by comparing the simulated d_{ta} spectrum to experimental spectrum of the reacted run, which includes the ^{9}Be target (see Fig. 7.3(a)). Once the optimised d_{ta} spectrum has been produced, the spectrum was compared to the simulated β spectrum to obtain the simulated recoil velocity of the outgoing particle when $d_{ta} = 0$ MeV.

Once all of the incoming and outgoing beam properties were incorporated in the simulation, the event-by-event Doppler corrected γ-ray spectrum can be produced using the optimised simulated value of β. The decay scheme of the outgoing nucleus was defined using a GEANT4 macro. The energies, lifetimes and intensities of each transition can be specified within the cur-

rent macro, where feeding from the higher-spin states can be incorporated when simulating the γ-ray spectrum of any decay sequence.

7.2.2 The Procedure of the χ^2-Minimisation

A key input parameter applied in the simulation was the effective position resolution of GRETINA. This was initially optimised within the simulation as Doppler broadening effects affect the γ-ray energy resolution. It was found that the typically used position resolution values of σ =4-5 mm [108] gave a poor agreement between the fit and the data for the particular transitions analysed in this work. Therefore, for the 159 keV transition in ^{47}Ti, the resolution was varied systematically until an optimal resolution of σ =6.7 mm was obtained. For the analogue 122.6 keV transition in ^{47}Mn, σ =7.9 mm was applied. Worsening of the position resolution for transitions of low energies may be expected (see Ref. [136]) due to the low signal height and the need for mirror charges in the neighbouring GRETINA segments to be measured for each interaction, of which the latter will improve the GRETINA position resolution. For transitions at the low energy range, the mirror charges may be subjected to significant noise, hence worsening the effective position resolution.

Following the optimisation of the simulation, the lifetimes of the yrast $\frac{7}{2}^-$ states in ^{47}Ti and ^{47}Mn were deduced by varying both the lifetime and energy simultaneously within the G4Lifetime framework. Both parameters were varied as the systematic errors in the experimental spectra could affect the measured energy and therefore, affect the extracted mean lifetime of the yrast $\frac{7}{2}^-$ state. For each combination, the optimum total χ^2 was measured compared to the experimental singles spectrum, where the simulation was produced with high statistics. The scale of the simulated spectrum, being a free parameter, was varied until the total χ^2 was minimised compared to the experimental spectrum. An exponential background contribution was also applied to each simulation in the form of $y = A\exp^{-Bx}$ to replicate the background radiation seen in the experimental spectrum, where A and B, were allowed to vary freely. A χ^2 minimisation procedure is conducted for each combination of energy and lifetime.

The reduced χ^2 (i.e. the optimum χ^2 per degree of freedom, NDF) for each simulated lifetime and energy combination is calculated following the optimisation of the scale and the exponential background function. The results can be plotted as a 2D histogram of lifetime against energy,

where the lowest χ^2 is used to extract the optimum energy and lifetime using the prescription provided in Ref. [3], [24]. The variation of the energy and the lifetime allows for the uncertainties in both measurements to be determined due to geometrical effects and the position resolution of GRETINA. A perfect match between the simulated and experimental spectra is obtained when $\chi^2/\text{NDF} \sim 1$, in accordance with the error variance detailed in Ref. [134], hence providing a reliable measurement of how well the simulation is reproducing the experimental spectrum.

7.2.3 Uncertainties

7.2.3.1 The uncertainty in the lifetime measurement

Since the χ^2/NDF distribution as a function of the lifetime at a particular energy, has a parabolic shape, the statistical error in the fit can be determined by finding the χ^2 values that have a 1σ difference from χ^2_{min} [134], i.e. χ^2 values of $\chi^2_{min} + 1$. Before performing this analysis, the χ^2 was normalised such that the χ^2/NDF has a minimum value of 1.0. The resulting error obtained through this method was scaled upwards to account for the correlation between γ-ray energy and the lifetime, τ, in the 2-dimensional χ^2/NDF histogram. In determining the scaling factor, it was assumed that the shape of the $\chi^2 + 1$ contour in this 2D surface is the same shape as the other χ^2 contours visible in the 2D histogram (see, for example, Fig.7.4).

This statistical uncertainty can be combined with the systematic uncertainties in quadrature to obtain an overall error in the measured lifetime. The systematic uncertainties arise due to:

- γ-ray anisotropy effects.
- Uncertainties due to geometrical effects.
- Uncertainty in the optimum outgoing beam velocity (β) for the transition.
- Uncertainty in the simulated position resolution of GRETINA.
- Factors associated with any contaminant peaks within the lineshape.

The uncertainties due to the γ-ray anisotropy effects and the geometrical effects are assumed to be 1.5% and 3%, respectively, taken from [137]. The systematic error associated with the uncertainty in β, utilised in the Doppler corrections, was determined by producing a Doppler corrected γ-ray spectrum that uses the mid-target β value for ^{47}Ti and ^{47}Mn (see Figs. 5.1 and

5.4), respectively. The simulation parameters within the G4Lifetime framework were updated to reflect this change in the β values of the outgoing ^{47}Ti and ^{47}Mn beams. The difference in the lifetime, deduced through the χ^2-minimisation procedure, was compared to the measured optimum lifetime values obtained from the γ-ray spectrum that uses the value of β after the target (β_{aft}) to calculate the systematic error due to β. Uncertainties due to the simulated position resolution of GRETINA were determined by changing the position resolution from σ_{opt} =6.7 mm for the 159 keV transition in ^{47}Ti and σ_{opt} =7.9 mm for the ∼122 keV transition in ^{47}Mn to 5.7 mm and 6.9 mm, respectively, and then repeating the χ^2-minimisation procedure. Effects due to feeding from higher-energy states were not considered in the final uncertainty of the lifetimes as all of the observed feeding states in ^{47}Ti have lifetimes that are < 3 ps. Therefore, it was assumed that the corresponding mirror transitions in ^{47}Mn have similar lifetimes. As the lifetimes investigated in this work are in the order of hundreds of picoseconds, it can be assumed that the addition of transitions from the higher-energy states will have a negligible effect on the deduced lifetime of the $\frac{7}{2}^-$ states.

7.2.3.2 The uncertainty in the measured energy

The uncertainty in the measured energy of the yrast $\frac{7}{2}^-$ states in ^{47}Ti and ^{47}Mn was determined in a similar fashion to determine the uncertainty in the measured lifetime.

The statistical uncertainty in the $\frac{7}{2}^- \rightarrow \frac{5}{2}^-_{gs}$ energy was determined by projecting the χ^2/NDF onto the energy axis from the 2D χ^2 histogram. As seen for the extraction of the statistical error for the deduced lifetime, the χ^2/NDF distribution as a function of the energy at a particular lifetime also has a parabolic shape. The statistical error was extracted using exactly the same procedure as described in section 7.2.3.1. The systematic errors were added in quadrature with the statistical error, producing an overall error in the optimised energy of the state. The systematic error contributions are shown below:

- Granularity effects of the 2D χ^2/NDF plot.
- The optimum outgoing recoiling beam velocity (β).
- The effective Z-position of the simulated target position applied to the Doppler corrections.
- The simulated position resolution of GRETINA.

The systematic errors due to the outgoing beam velocity and the position resolution of GRETINA were determined using the same procedure as discussed for the lifetimes. The effects of the effective Z-position of the target, used for the Doppler corrections, were taken into account by shifting the position of the target by 0.5 mm within the G4Lifetime simulation. The χ^2-minimisation procedure was repeated to determine the difference between the extracted energy due to the position shift of the target and the deduced optimum energy that uses the optimum target position. The systematic error in the energy due to the granularity comes from the projection of the 2D χ^2/NDF plot onto the energy axis at a particular lifetime. The χ^2/NDF against energy distribution was plotted to measure the energy of the $\frac{7}{2}^-$ states. Since the measured lifetime of the decay was used to project onto the energy axis, it is likely that the energy measured can be in between two bins along the lifetime axis, resulting in a slight variation in the measured energy depending on what column was projected (i.e. up through the 'valley' of the χ^2/NDF plot). Therefore, the neighbouring bin along the lifetime axis was used to project onto the energy axis to remeasure the energy. The effect of granularity was not determined for the uncertainty in the lifetime as the χ^2 measurement is less influenced by lifetime changes compared to the energy of the state as the measured energy is largely dependent on the right-edge of the γ-ray peak.

7.3 Lifetime Measurement Results

7.3.1 ^{47}Ti

The mean lifetime of the $\frac{7}{2}^-$ state in ^{47}Ti was first investigated to verify the lineshape method since the lifetime is well known to be τ =303(9) ps [29], a weighted average from Refs. [138], [139].

The recoil velocity of the ^{47}Ti particles after the target (β_{aft}) was deduced using the LISE++ [127] calculations, which implements the Bρ setting of the S800 dipole magnets, being 2.855 Tm for the reacted beam run. Using this approach, the after-target recoil velocity of β_{aft} = 0.396 was estimated for the $\frac{7}{2}^- \rightarrow \frac{5}{2}^-$ decay. Since feeding transitions in ^{47}Ti are in the order of a few ps and are thought to have an insignificant impact on the extracted lifetime for the $\frac{7}{2}^-$ state, the decay for the single state was simulated.

The 2D χ^2/NDF plot of energy against lifetime for the $J^\pi = \frac{7}{2}^-$ state in ^{47}Ti can be obtained once all the parameters have been finalised as seen in Fig. 7.4. The optimum energy and lifetime values were measured to the nearest 0.1 keV and 10 ps, respectively, from the 2D-matrix. The 2D-plot was projected onto the y- and x-axes, where a parabolic fit was performed to extract the final values of the energy and lifetime, respectively, of the $\frac{7}{2}^-$ state with their corresponding errors, where the minimised E($\frac{7}{2}^-$)= 159.35 keV and τ =331 ps were determined.

The presence of a high-energy tailing effect around 162-168 keV (see Fig. 7.7) can not come from lifetime effects. Therefore, it is assumed that this effect is associated with the γ-ray reconstruction effects for a small number of events in GRETINA, which were not accounted for within the G4Lifetime simulation. As a result, this region of 162-168 keV was excluded from the χ^2-minimisation procedure in ^{47}Ti. Further inspection of the lineshape shows that a contamination peak is present at ∼148 keV, for which the range of 144-150 keV was excluded from the fit. By repeating the χ^2-minimisation procedure to include these channels affects the lifetime result by 1.5%, which was accounted for as an additional systematic uncertainty. The effects of these systematic errors are highlighted in Table 7.1, which includes the remaining contributions of the systematic uncertainties resulting from the factors stated in section 7.2.3. Likewise, the systematic uncertainties for the measured E($\frac{7}{2}^-$) energy are also presented in Table 7.2.

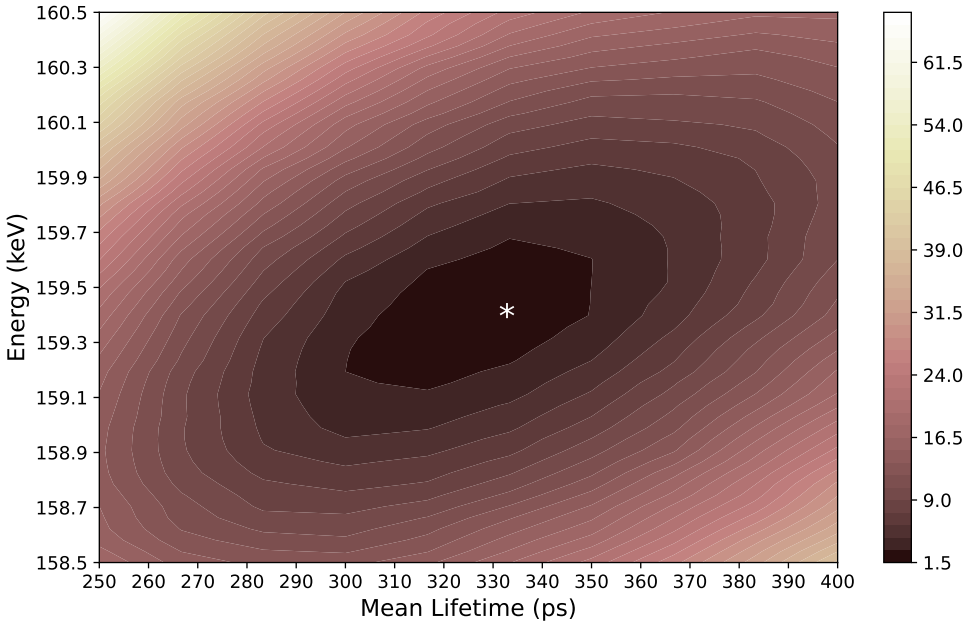

Figure 7.4: The 2D χ^2 per number of degree of freedom (NDF) histogram of the energy against the mean lifetime of the $\frac{7}{2}^-$ state in ^{47}Ti. Each data point shows the measured χ^2 of the experimental spectrum compared to the simulation for a different combination of the lifetime and energy. The white star indicates the location of the fitted minimum χ^2/NDF.

Contribution	**Lifetime (ps)**	**Sys. Error (ps)**	**Sys. Error (%)**
Optimised	331.1		
γ-ray anisotropy effects		$\pm$5.0	1.5
Geometrical uncertainties		$\pm$9.9	3.0
Variation of β (+0.007)	328.9	-2.3	0.7
Variation of position resolution (-1mm)	337.4	+6.3	1.9
Inclusion of contaminant peak	326.0	-5.1	1.6

Table 7.1: The contributions to the total systematic error for the measured lifetime of the $\frac{7}{2}^-$ state in ^{47}Ti using the χ^2-minimisation procedure.

Contribution	**E($\frac{7}{2}^-$) (keV)**	**Sys. Error (keV)**	**Sys. Error (%)**
Optimised	159.35		
2D Granularity effects	159.42	+0.07	0.04
Variation of β (+0.007)	159.45	+0.1	0.06
Variation of position resolution (-1mm)	159.38	+0.03	0.02
0.5 mm target offset	159.14	-0.21	0.13

Table 7.2: The contributions to the total systematic error for the measured energy of the $\frac{7}{2}^-$ state in ^{47}Ti using the χ^2-minimisation procedure.

The 1D projections onto the mean lifetime and energy axis of the 2D χ^2/NDF plot seen in Fig. 7.4 are displayed in Figs. 7.5 and 7.6, respectively. Statistical uncertainties in the extracted lifetime and energy were determined using the procedure outlined in section 7.2.3.1. By combining the statistical uncertainties of ±3.9 ps and ±0.06 keV for the lifetime and energy, respectively, in quadrature with the systematic uncertainties detailed in Tables 7.1 and 7.2, the overall values were determined to be τ =331 ±4 (stat.) ±14 (sys.) ps and E($\frac{7}{2}^-$)= 159.35 ±0.06 (stat.) ±0.24 (sys.) keV for the $\frac{7}{2}^-$ state. The lineshape method is very sensitive to the energy of the γ ray, therefore, the final γ-ray energy determined is dominated by the systematic errors resulting from the beam velocity and the target position. These final values with their associated errors for the lifetime and the energy are in agreement with current literature, where τ =303(9) ps and E($\frac{7}{2}^-$)=159.371(12) keV [29]. These results also validate the lineshape method used in this analysis. The experimental spectrum of ^{47}Ti, with the optimised simulated spectrum for the 159 keV transition at τ =331 ps and E($\frac{7}{2}^-$)= 159.4 keV, is presented in Fig. 7.7.

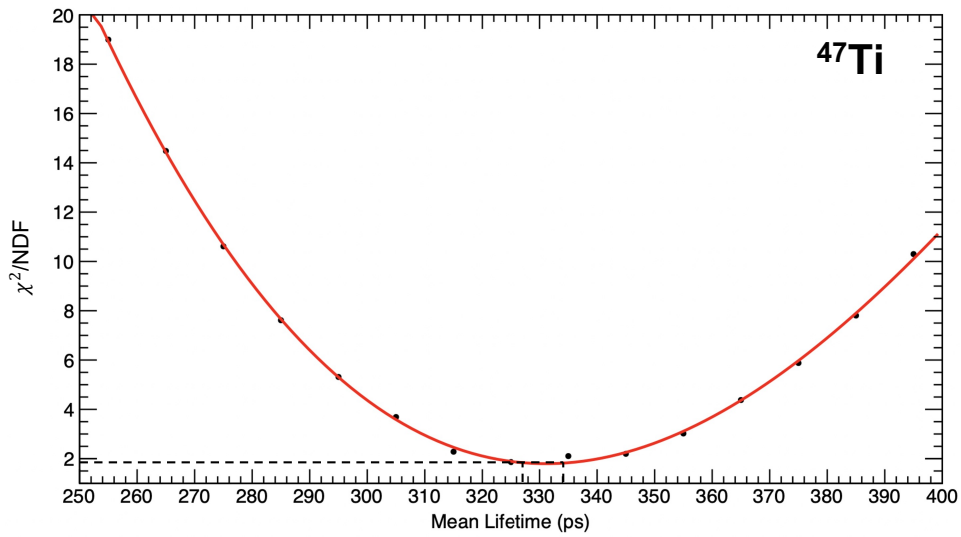

Figure 7.5: The χ^2 per degree of freedom (NDF) distribution for the simulated spectrum compared to the experimental spectrum to determine the mean lifetime of the $\frac{7}{2}^-$ state in ^{47}Ti at the optimised energy of 159.4 keV. The red line is a fit which uses the third order polynomial function to the distribution. The (χ^2_{min}+1)/NDF is shown by the dashed black line from where the statistical uncertainties ±3.4 ps were derived by projecting onto the lifetime axis.

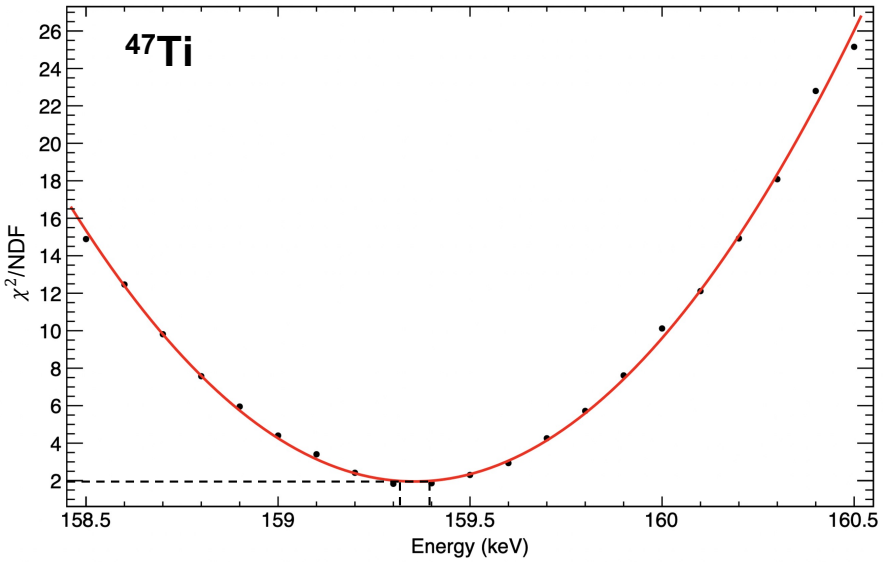

Figure 7.6: The χ^2 per degree of freedom (NDF) distribution for the energy of the $\frac{7}{2}^-$ state in ^{47}Ti at the optimised lifetime of 331 ps. The red line is a fit which uses the second order polynomial function to the distribution. The $(\chi^2_{min}+1)$/NDF is shown by the dashed black line, where the statistical uncertainties ±0.041 keV were derived by projecting onto the energy axis.

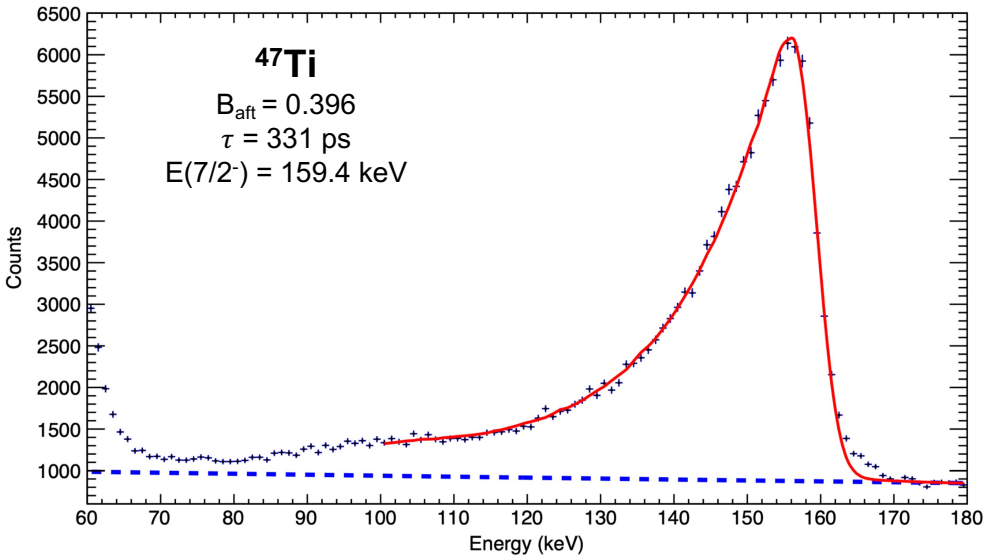

Figure 7.7: The optimised lineshape simulation (red) for the $\frac{7}{2}^-$ state in ^{47}Ti, which has τ =331 ps and E_γ=159.4 keV, compared to the experimental γ-ray spectrum. The dashed blue line shows the additional background contribution in the simulation. The observed high-energy tailing effect between 162-168 keV is due to the incorrect GRETINA event reconstruction. Furthermore, a contamination peak at ∼148 keV was also seen, which resulted in the 162-168 keV and 144-150 keV channels, respectively, to be excluded from the χ^2-minimisation procedure.

7.3.2 ^{47}Mn

To produce the simulated spectrum for ^{47}Mn, the recoil velocity after the target, β_{aft}, was determined by using the same procedure used for ^{47}Ti through LISE++ [127]. The Bρ setting of the S800 dipole magnets was set to 2.375 Tm to focus the ^{47}Mn nuclei, produced as a result of an one-neutron knockout from ^{48}Mn, through the spectrograph. Therefore, the recoil velocity after the target was found to be β =0.377 for the $\frac{7}{2}^- \rightarrow \frac{5}{2}^-$ decay. Since the other transitions in ^{47}Mn are thought to have similar lifetimes of the order of a few ps, as seen in the mirror transitions in ^{47}Ti, these transitions were not considered due to the reasons specified in section 7.3.1. Therefore, a single transition was simulated.

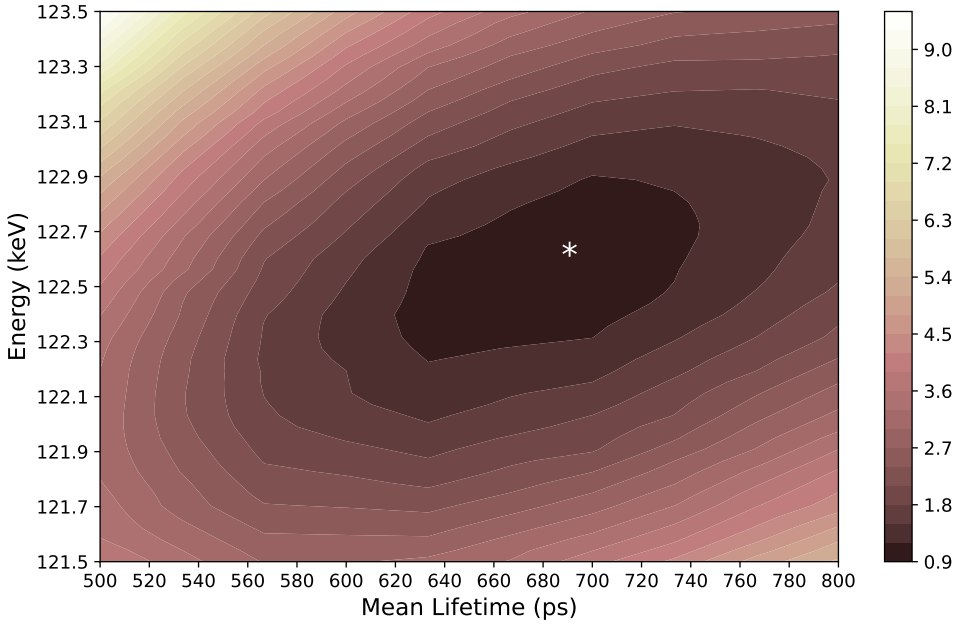

Figure 7.8: The 2D χ^2 per number of degree of freedom (NDF) plot of the energy against the mean lifetime of the $\frac{7}{2}^-$ state in ^{47}Mn. The simulated spectrum was compared to the experimental spectrum to measure the χ^2 for each combination of the lifetime and energy. The white star indicates the location of the fitted minimum χ^2/NDF.

The 2D χ^2/NDF distribution, which compares the simulated spectra to the experimental spectra, for the $\frac{7}{2}^- \rightarrow \frac{5}{2}^-_{gs}$ decay is shown in Fig. 7.8. Similar to the analysis of ^{47}Ti, the optimum energy and lifetime values were determined to the nearest 0.1 keV and 10 ps from the 2D-matrix, respectively. The 2D-plot was projected onto the y- and x-axes, respectively, to

perform a parabolic fit to deduce the final values of the energy and lifetime of the $\frac{7}{2}^-$ state, where the minimised E($\frac{7}{2}^-$)=122.6 keV and τ =687 ps. A high energy tailing effect around 125-130 keV was also observed in ^{47}Mn as in ^{47}Ti. The reasons for this high energy tailing effect are discussed above and was excluded from the χ^2-minimisation procedure. The effects of the systematic errors described in section 7.2.3 are presented in Table 7.3 for the lifetimes and in Table 7.4 for the measured energy of the $\frac{7}{2}^-$ state in ^{47}Mn.

The mean lifetime and the optimum energy of the first-excited state in ^{47}Mn were determined by taking the respective 1D projections from the 2D χ^2/NDF plot seen in Fig. 7.8. The corresponding projections are displayed in Figs. 7.9 and 7.10. Statistical uncertainties in the extracted lifetime and energy were determined using the procedure outlined in section 7.2.3.1. The overall uncertainties in the lifetime and energy are found by combining the statistical uncertainties of ±17.0 ps and ±0.09 keV for the lifetime and energy, respectively, in quadrature with the systematic uncertainties presented in Tables 7.3 and 7.4.

Contribution	**Lifetime (ps)**	**Sys. Error (ps)**	**Sys. Error (%)**
Optimised	687.4		
γ-ray anisotropy effects		±10.3	1.5
Geometrical uncertainties		±20.6	3.0
Variation of β (+0.016)	696.4	+9.0	1.3
Variation of position resolution (-1mm)	703.2	+15.8	2.3
Inclusion of contaminant peak	681.2	-6.2	0.9
Effect of varying range of fitting		±10.7	1.6

Table 7.3: The contributions to the total systematic error for the measured lifetime of the $\frac{7}{2}^-$ state in ^{47}Mn using the χ^2-minimisation procedure.

Contribution	**E($\frac{7}{2}^-$) (keV)**	**Sys. Error (keV)**	**Sys. Error (%)**
Optimised	122.57		
2D Granularity effects	122.59	+0.02	0.01
Variation of β (+0.016)	122.77	+0.20	0.2
Variation of position resolution (-1mm)	122.67	+0.10	0.1
0.5 mm target offset	122.61	-0.04	0.03

Table 7.4: The contributions to the total systematic error for the measured energy of the $\frac{7}{2}^-$ state in ^{47}Mn using the χ^2-minimisation procedure.

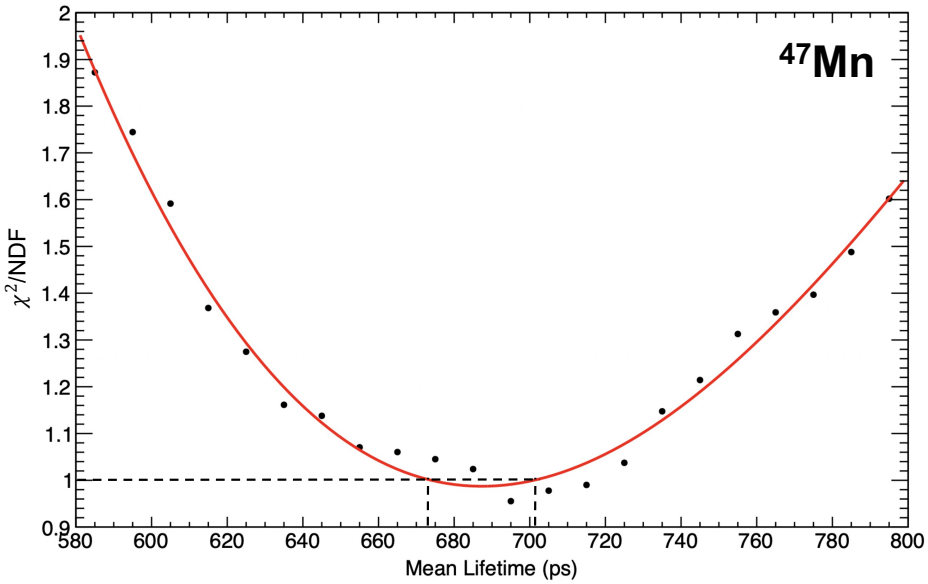

Figure 7.9: The χ^2 per degree of freedom (NDF) distribution for the simulated spectrum compared to the experimental spectrum to determine the mean lifetime of the $\frac{7}{2}^-$ state in ^{47}Mn at the optimised energy of 122.6 keV. The red line is a fit which uses the third order polynomial function to the distribution. The $(\chi^2_{min}+1)$/NDF is shown by the dashed black line from where the statistical uncertainties ±13.9 ps were derived by projecting onto the lifetime axis.

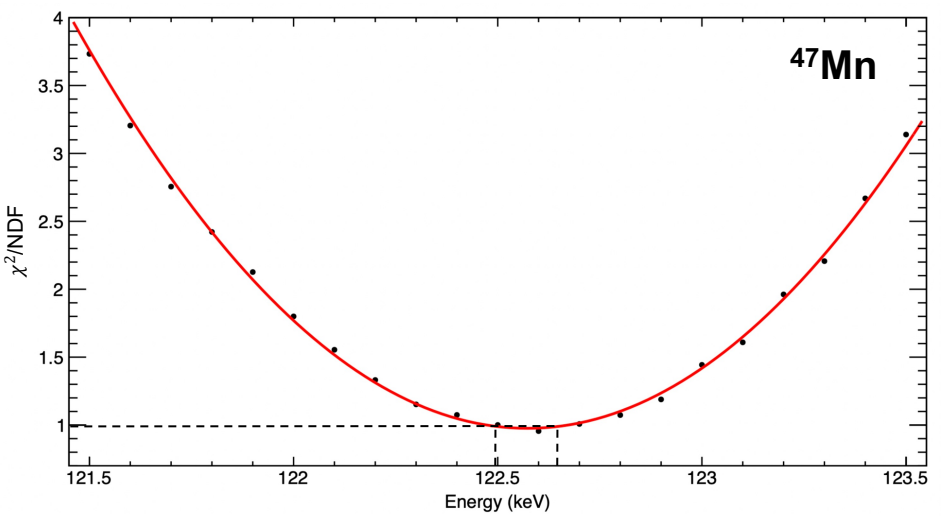

Figure 7.10: The χ^2 per degree of freedom (NDF) distribution for the energy of the $\frac{7}{2}^-$ state in ^{47}Mn at the optimised lifetime of 687 ps. The red line is a fit which uses the second order polynomial function to the distribution. The $(\chi^2_{min}+1)$/NDF is shown by the dashed black line, where the statistical uncertainties ±0.074 keV were derived by projecting onto the energy axis.

A noticeable peak can be observed below $\sim$ 70 keV in Fig. 7.11, which results from electronic noise at the low-energy edge of the spectra. This peak could potentially perturb the measurements for ^{47}Mn. Consequently, the effect of varying the lower end of the fit range was investigated, resulting in a further systematic error of $\pm$ 11 ps. These errors were all added in quadrature to obtain a final result of τ =687 $\pm$ 17 (stat.) $\pm$ 32 (sys.) ps with the measured energy for this newly-observed transition of E_γ = 122.57 $\pm$ 0.09 (stat.) $\pm$ 0.23 (sys.) keV. The experimental spectrum of ^{47}Mn with the optimised simulated spectrum is presented in Fig. 7.11.

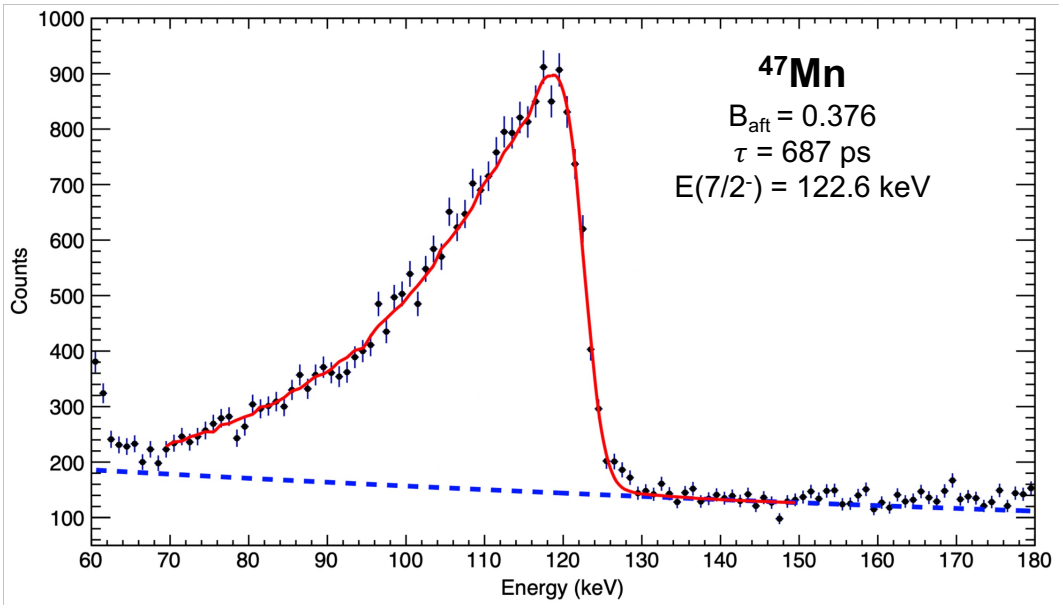

Figure 7.11: The optimised lineshape simulation (red) for the E($\frac{7}{2}^-$) =122.6(3) keV state in ^{47}Mn, which has τ =687(36) ps, compared to the experimental γ-ray spectrum. The dashed blue line shows the additional background contribution in the simulation. The observed high-energy tailing effect between 125-130 keV is due to the incorrect GRETINA event reconstruction, and was therefore excluded from the χ^2-minimisation procedure.

The deduced energy and lifetime measurements for ^{47}Mn have two purposes. The first reason is that the accurate measurement of the energy can be implemented to the level scheme of the observed transition, hence allowing for precise MED analysis. Secondly, subsequent analysis of the analogue transition strengths can be conducted. The former is a part of this thesis work while the analysis of the latter is ongoing in collaboration with Prof. M. A. Bentley [140], where the status of this analysis is presented briefly for context. The complete set of results for the lifetime and energy measurements both ^{47}Ti and ^{47}Mn are shown in Tables 7.5 and 7.6, respectively.

Nuclei	τ (ps)	Stat. Error (ps)	Sys. Error (ps)	Total Error (ps)
^{47}Ti	331	4	15	15
^{47}Mn	687	17	32	36

Table 7.5: The contributions of the statistical and systematic errors to the resulting lifetime measurement of the $\frac{7}{2}^-$ state in both ^{47}Ti and ^{47}Mn.

Nuclei	E($\frac{7}{2}^-$) (keV)	Stat. Error (keV)	Sys. Error (keV)	Total Error (keV)
^{47}Ti	159.4	0.06	0.2	0.3
^{47}Mn	122.6	0.09	0.2	0.2

Table 7.6: The contributions of the statistical and systematic errors to the deduced measurement of the energy of the $\frac{7}{2}^-$ state in both ^{47}Ti and ^{47}Mn.

7.3.3 Shell-model Results

Shell model calculations, performed by Prof. M. A. Bentley, were studied to predict the $B(M1)$ and $B(E2)$ strengths for the mirrored $\frac{7}{2}^-$ states in ^{47}Ti and ^{47}Mn. The ANTOINE code was utilised to perform these calculations [31], [32], which implements the KB3G interaction [57] within the full fp valence space.

The $B(M1)$ transition strengths were determined using the bare-nucleon g-factors while the $B(E2)$ strengths used the Dufour and Zuker effective charges [141], being $\epsilon_p = 1.31$ and $\epsilon_n = 0.46$. The measured energies of the mirrored transitions were applied in the calculations to extrapolate the lifetime of the $\frac{7}{2}^-$ states in ^{47}Ti and ^{47}Mn. The $B(E2)$ transition strengths, alongside the choice of the effective charges applied, were found to have no significant effect on the predicted lifetimes. This is due to the strong dominance of the $B(M1)$ strength ($\sim$99%) in both nuclei. From Table 7.7, it can be seen that the predicted $M1$ strengths between both nuclei are similar and are small in magnitude.

It can be further observed that the predicted $B(M1)$ and $B(E2)$ strengths in ^{47}Ti is $\sim$2 times smaller than the experimentally determined $M1$ and $E2$ strengths, respectively, yielding proportionally longer lifetimes. The cause for the large difference between the predicted and measured $B(M1)$ and $B(E2)$ strengths is likely due to the missing shell excitations between the sd and fp orbitals in the shell model interaction. The inclusion of these excitations in the

	^{47}**Ti**	^{47}**Mn**
	Experiment	
Lifetime (ps)	309(7)	687(36)
$B(M1)$ (μ_N^2)	0.0445(10)	-
$B(E2)$ (e^2fm^4)	243(43)	-
	Shell Model	
Lifetime (ps)	734	1494
$B(M1)$ (μ_N^2)	0.0187	0.0203
$B(E2)$ (e^2fm^4)	125	214

Table 7.7: Comparison of the experimental and theoretical lifetimes, $B(M1)$ and $B(E2)$ transition strengths for the $\frac{7}{2}^-_1$ to the $\frac{5}{2}^-_1$ ground state transition in the ^{47}Ti/^{47}Mn mirror pair. The quoted experimental lifetime for ^{47}Ti is the updated weighted average that includes the measured result from this work combined with previously results from Refs. [138], [139]. The mixing ratio for this transition in ^{47}Mn is unknown, therefore the $B(M1)$ and $B(E2)$ strengths have not been determined. The shell-model predictions have utilised effective charges from Dufour and Zuker [141] (ϵ_p =1.31, ϵ_n =0.46) and the bare nucleon g-factors. The experimental energies were utilised to obtain the shell-model lifetimes.

shell model will be necessary to improve the agreement. The experimental $B(M1)$ and $B(E2)$ strengths in ^{47}Mn were not determined as the mixing ratio for the 122.6(3) keV transition is unknown.

7.4 Impact of Lifetime Measurement (ongoing work)

At present, the 159.4 keV γ-ray transition in ^{47}Ti from the yrast $\frac{7}{2}^-$ state is known to be a near-pure $M1$ transition, where a small component of the $E2$ transition contributes [29]. By combining the current result of τ =331(15) ps with the two previous lifetime values in Refs. [138], [139], a new weighted average for the lifetime becomes τ =309(7) ps. The current evaluation states that the $B(E2)\downarrow$ for the 159.4 keV transition, obtained from Coulomb excitation results, is 243(43) e^{2}fm^4 [29]. Combining this result to the new lifetime measurement made for this state in ^{47}Ti yields the $B(M1)$ = 0.0445(10) μ_N^2, where $|\delta|$ becomes 0.098(9), as seen in Table 7.7. This result corresponds to an almost-pure (99%) $M1$ component to the total strength. The final values that include the measured lifetimes, $B(E2)$ and $B(M1)$ measurements for ^{47}Ti are Table 7.7.

For the 122.6(3) keV transition in ^{47}Mn, there is no current experimental information on the

mixing ratio. Therefore, the $B(M1)$ and $B(E2)$ strengths cannot be independently determined. However, the combinations of the $B(M1)$ and $B(E2)$ strengths for ^{47}Mn for a range of possible mixing ratios can be considered by following the prescription in Ref. [3]. The possible combinations of the $B(M1)$ and $B(E2)$ strengths are denoted by the solid line in Fig. 7.12, made and analysed by Prof. M. A. Bentley. An immediate observation is that the unknown $B(E2)$ value for the 122.6(3) keV transition in ^{47}Mn has very little impact on the corresponding $B(M1)$ value as the low γ-ray energy forces the transition to be dominated by the M1 component. To further extend our observations, the $B(E2)$ was varied in ^{47}Mn by a factor of 100, from 10 times smaller than the analogue value in ^{47}Ti to 10 times larger. This results in a variation in the $B(M1)$ strength from 0.044(2) to 0.042(2) μ_N^2. For analogue states in mirror nuclei, no known mechanism could cause $B(E2)$ strengths to differ to that extent. Hence, it can be assumed that the solid line in Fig. 7.12 contains all physically-reasonable combinations of $B(E2)$ and $B(M1)$ for ^{47}Mn.

Since the comparison between the analogue $B(E2)$ strengths from the mirrored yrast $\frac{7}{2}^-$ states in the $A = 47$ nuclei does not provide further information, it can be shown from Fig. 7.12 that the ratio between the $B(M1)$ strengths between both nuclei are constrained. The red lines indicated in Fig. 7.12 contain the error bounds within $\pm 1\sigma$ for the ratio between the two $B(M1)$ values. The ratio of $B(M1)_{Mn}/B(M1)_{Ti}$ can be shown to be constrained to 0.97(8), which covers the full range of values highlighted in Fig. 7.12. Therefore, the two $\frac{7}{2}^-$ transitions in both ^{47}Ti and ^{47}Mn are shown to have identical $M1$ strengths within a precision of 10%. As a result of high statistics in the measurements determined, the comparison between the $B(M1)$ strengths demonstrates a high precision compared to other lifetime measurements made in proton-rich systems near the drip line in this mass region. It is important to note that the $B(M1)$ strengths have been determined for both nuclei under identical experimental conditions, providing increased confidence in the comparisons made. Hence, the resulting observation of the experimental $B(M1)$ values being essentially identical allows for further discussion. Further work completed by Prof. M. A. Bentley in Ref. [142], explored the dependence of the transition matrix elements with T_z to determine the relative sizes of the isoscalar and isovector matrix elements. It was found that the isoscalar contribution becomes negligible [140]. This work is being prepared for publication.

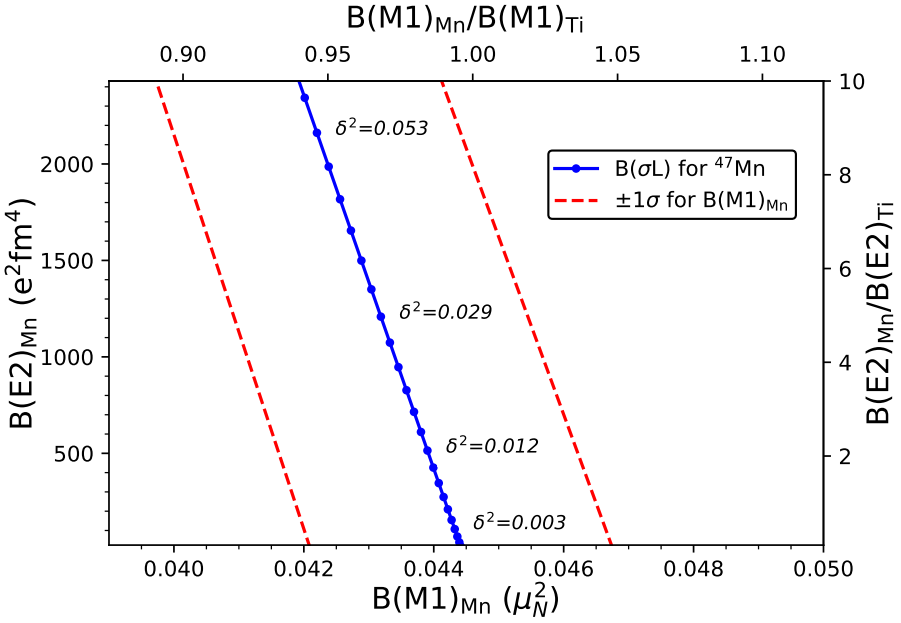

Figure 7.12: The values along the blue line, for the 122.6(3) keV transition in ^{47}Mn, provide the corresponding $B(M1)$ and $BE2$ values that are consistent with the measured lifetimes of the yrast $\frac{7}{2}^-$ state. The ratio of the analogue $B(E2)$ values is plotted as a function of the ratio of the analog $B(M1)$ values for the $A = 47$ mirror pair on the right y-axis and upper x-axis, respectively. The data points corresponding to values of $|\delta|$ =0.03 to 0.24 that go up in 0.01 intervals. The red dashed lines indicate the experimental limits on the ratio of the mirror $B(M1)$ values ($\pm 1\sigma$) that include the error from the lifetime measured and the error in the $B(M1)$ for ^{47}Ti. Figure is made and is being analysed by Prof. M. A. Bentley [142].

7.5 Summary

By using the lineshape analysis of the first-excited $J^\pi = \frac{7}{2}^-$ states in the $T_z = \pm\frac{3}{2}$, $A = 47$ mirror nuclei (^{47}Ti and ^{47}Mn), the lifetimes of these states have been determined. The lifetime of the $J^\pi = \frac{7}{2}^-$ state in ^{47}Ti was measured as $\tau = 331(15)$ ps, while for the analogue state in ^{47}Mn, the lifetime was $\tau = 687(36)$ ps. The determination of the lifetimes of the analogue $J^\pi = \frac{7}{2}^-$ state in both nuclei has allowed for the comparison of the analogue $M1$ strengths, where the two $B(M1)$ strengths were shown to be identical within 10%. Further analysis, conducted by Prof. M. A. Bentley, probes the dependence of isospin on the electromagnetic transition strengths [140], [142]. The relative absolute magnitudes of the isoscalar and isovector matrix elements were extracted, where the isovector contribution was found to be stronger than the isoscalar component by a factor of $\sim$2 even though the $B(M1)$ strength is already low.

Chapter 8

Summary and Future Work

Isospin-symmetry breaking effects were investigated for nuclei in the $f_{\frac{7}{2}}$ region, from where new results have been obtained. In this analysis, where the experiment was performed at MSU, many new γ rays have been identified in the $T_z = -\frac{3}{2}$, proton-rich ^{47}Mn and ^{45}Cr nuclei by utilising the novel technique of mirrored one- and two-nucleon knockout reactions, respectively. New level schemes have been produced for the first time through the use of a wide range of analytical tools, such as mirror symmetry arguments in relation to the energies of populated states in a mirror pair and population strengths alongside γ-γ coincidences. The states observed in the proton-rich members were compared to their mirror counterparts, ^{47}Ti and ^{45}Sc, respectively. In the $A = 47$ mirror nuclei, analogue yrast states up to $\frac{15}{2}^-$ and yrare states up to $\frac{11}{2}^-$ were found to be populated. For the $A = 45$ nuclei, negative-parity states up to $\frac{11}{2}^-$ were observed in both ^{45}Cr and ^{45}Sc, where higher-spin negative-parity states were populated up to $\frac{19}{2}^-$ in ^{45}Sc. Positive-parity states in both $A = 45$ nuclei were also populated to $\frac{11}{2}^+$, due to a nucleon removal from the deep-lying $d_{\frac{5}{2}}$-shell.

Secondly, the experimental MED between the isobaric analogue states in the $T_z = \pm\frac{3}{2}$, $A = 47$ and $A = 45$ mirror pairs were compared to large-scale shell-model calculations that incorporate isospin non-conserving effects using the KB3G model. It was evident that all sets of isospin-breaking terms should be included in the shell-model calculation to improve the agreement between the experimental data. Some deviations were present between the experimental and calculated MED for both pairs of nuclei, which is likely to result from the inadequacy of the fp valence space. In the $A = 47$ case, two protons (neutrons) were present in ^{47}Ti (^{47}Mn) in the fp

valence space, where it is possible that two-particle two-hole excitations across the $N = Z = 20$ shell closure were missing. For the $A = 45$ pair, one proton (neutron) was present in ^{45}Sc (^{45}Cr) in the fp valence space, where single-particle excitations may not be well described using just the fp-space to determine the MED between the negative-parity states. For the positive-parity states in ^{45}Sc and ^{45}Cr, the SDPF model allows for one-nucleon excitations to take place from the $d_{\frac{3}{2}}$ shell, where a reasonable agreement between the experimental and calculated MED was seen. The $A = 47$ and $A = 45$ mirror pairs allow for a stringent test of the current shell model MED prescription. However, the limited inclusion of sd-shell excitations across the ^{40}Ca shell closure in the calculations impacts the results when compared with the experimental results. Ideally, a shell model interaction that incorporates the upper sd and lower fp-shells is necessary to improve the agreement between the experimental and predicted results as well as account for the components in the sd-shell for $f_{\frac{7}{2}}$ nuclei. Further testing of the MED through a new density-functional theory (DFT) approach using the no-core configuration-interaction (NCCI) method was also performed. In this approach, the configuration space does not need to be truncated, hence excitations across the sd and fp-shells were allowed in order to determine the MED in the positive and negative-parity states, as seen in the $A = 45$ case. Although this method had a reasonable agreement with the experimental data in the $A = 47$ case, a poor agreement was observed in the $A = 45$ case. This could relate to how the NLO CSB interaction has been defined or due to missing correlations within the model. Further investigations to test the sensitivity of the various charge-symmetry breaking forces within the DFT-NCCI model will help to understand these discrepancies. Currently, the addition of triaxiality to the definition of the NLO CSB interaction is being investigated for the positive-parity bands in the $A = 45$ mirror pair by Professor W. Satula. Although the current results are tentative, a better agreement between the experimental data and the calculated MED results is observed. It can be suggested that the addition of triaxiality shows that the MED is sensitive to the shape of the nuclei studied.

Exclusive and inclusive cross sections have been measured for the ^{47}Ti/^{47}Mn mirror pair. Notable differences between the two inclusive knockout cross sections have been observed between the two members, suggesting that a large difference between the nucleon separation energies is the most probable cause. Previous studies for nuclei close to the $N = Z$ region [129], [130] have also yielded inclusive cross sections that were asymmetric by a factor of ∼3-4. In this work, a

factor of ∼11 was observed, which is similar to the result found by Yajzey *et al.* [10]. A comprehensive analysis of the experimental and theoretical exclusive cross sections was performed for the mirrored one-nucleon knockout reactions in the $A = 47$ pair. While the theoretical exclusive cross sections provided confidence in the assignment of the γ-ray transitions observed in ^{47}Mn, the experimentally determined exclusive cross sections were found to be smaller than the theoretical predictions. Yet, the distribution of the relative cross sections shows a good agreement with the experimental data, especially for the yrare states that were directly populated. Assuming isospin symmetry, it is expected that the cross sections should be identical. However, by comparing the experimental exclusive cross sections for the observed analogue states in both mirror nuclei, notable differences were observed, implying that the contribution from unseen feeding is dominant in this observed difference. As binding-energy effects between the two members of the mirror pair are evident, the mirrored cross sections were analysed such that the suppression of the spectroscopic strength (i.e. the ratio of the experimental and the theoretical inclusive cross sections), was investigated as a function of the binding energy for ^{47}Ti and ^{47}Mn. The results obtained seem to follow the trend observed in Ref. [27]. Experimentally, nuclei along the $N \sim Z$ line can be investigated using mirrored knockout reactions, especially in weakly-bound systems, to observe this asymmetrical trend, as seen in recently published systematics for inclusive cross sections [25]–[27]. The degree of suppression of the experimental cross sections of the yrare states compared to theory can also be explored to observe if a similar trend is seen (e.g. Ref. [10]). This will assist in understanding the effect of unseen feeding on the exclusive cross sections, especially for the ^{47}Ti nucleus.

Finally, the lifetimes of the long-lived first-excited ($\frac{7}{2}^-$) states in ^{47}Ti and ^{47}Mn have been extracted using the γ-ray lineshape method, yielding lifetimes of τ =331(15) ps and τ =687(36) ps, respectively. Since the corresponding transitions that come from the $\frac{7}{2}^-$ states are near-pure $M1$ transitions, the comparison of the $B(M1)$ analogue strengths was conducted. It was found that the $B(M1)$ strengths were identical within 10%. Further analysis from Professor M. A. Bentley has indicated that the isoscalar contribution of $2(13) \times 10^{-6}\mu_N^2$ is extremely small compared to the isovector component, being $4.38(18)\times10^{-2}\mu_N^2$. Further analysis will be required to understand the underlying cause of this observation. This analysis can be extended to the $A = 45$ mirror nuclei, where the $\frac{3}{2}^-$ state in ^{45}Sc has a half-life of 43.3(23) ps [113] that decays

outside the target by emitting two γ rays of 377 and 364 keV, where the former is a $B(E2)$ transition and the latter is a $B(E1)$ transition. The 492(1) and 385(1) keV transitions in ^{45}Cr can be assumed to be the respective analogue transitions. Hence, the lifetime of the $\frac{3}{2}^-$ state in ^{45}Cr can also be determined in future work.

Abbreviations

MED - Mirror Energy Differences

DFT-NCCI - Density Function Theory - No-Core Configuration-Interaction

CSB - Charge-Symmetry Breaking

INC - Isospin Non-Conserving

NSCL - National Superconducting Cyclotron Laboratory

MSU - Michigan State University

IAS - Isobaric Analogue States

TED - Triplet Energy Differences

MDE - Mirror Displacement Energies

IMME - Isobaric Multiplet Mass Equation

HO - Harmonic Oscillator

TBME - Two-Body Matrix Elements

CME - Coulomb Matrix Elements

EMSO - ElectroMagnetic Spin-Orbit

ECR - Electron Cyclotron Resonance

SuSI - Superconducting Source for Ions

CCF - Coupled Cyclotron Facility

XFP - Extended Focal Plane

OBJ - Object Scintiallator

HPGe - High-Purity Germanium

GRETINA - Gamma-Ray Energy Tracking IN-beam Array

GRETA - Gamma-Ray Energy Tracking Energy

AGATA - Advanced GAmma-ray Tracking Array

SeGA - Segmented Germanium Array

ToF - Time of Flight

FWHM - Full-Width Half-Maximum

CRDC - Cathode Readout Drift Chambers

DAQ - Data AQuisition

PID - Particle Identification

PMT - PhotoMultiplier Tubes

IC - Ionisation Chamber

DNL - Differential Non-Linearity

TNA - Two-Nucleon Amplitudes

HF - Hartree-Fock

Bibliography

[1] E. Wigner. "On the Consequences of the Symmetry of the Nuclear Hamiltonian on the Spectroscopy of Nuclei". In: *Phys. Rev.* 51 (2 Jan. 1937), pp. 106–119.

[2] N. S. Pattabiraman, D. G. Jenkins, M. A. Bentley, et al. "Analog $E1$ transitions and isospin mixing". In: *Phys. Rev. C* 78 (2 Aug. 2008), p. 024301.

[3] S. A. Milne *et. al.* "Mirrored one-nucleon knockout reactions to the $T_z=\pm\frac{3}{2}$ A=53 mirror nuclei". In: *Physical Review C* 93.2 (2016), pp. 1–10.

[4] R. Hoischen *et al.* "Isomeric mirror states as probes for effective charges in the lower pf shell". In: *Journal of Physics G: Nuclear and Particle Physics.* 38.3 (Jan. 2011), p. 035104.

[5] J. R. Brown *et. al.* "First -ray spectroscopy of Fe49 and Ni53: Isospin-breaking effects at large proton excess". In: *Physical Review C - Nuclear Physics* 80.1 (2009), pp. 1–5.

[6] M. A. Bentley, C. Chandler, M. J. Taylor, et al. "Isospin Symmetry of Odd-Odd Mirror Nuclei: Identification of Excited States in $N = Z - 2$ ^{48}Mn". In: *Phys. Rev. Lett.* 97 (13 Sept. 2006), p. 132501.

[7] J. Ekman *et. al.* "Unusual Isospin-Breaking and Isospin-Mixing Effects in the A=35 Mirror Nuclei". In: *Physical Review Letters* 92.13 (2004), pp. 1–4.

[8] P. J. Davies *et. al.* "Mirror energy differences at large isospin studied through direct two-nucleon knockout". In: *Physical Review Letters* 111.7 (2013), pp. 1–13.

[9] K. Kaneko, Y. Sun, T. Mizusaki, et al. "Variation in displacement energies due to isospin-nonconserving forces". In: *Physical Review Letters* 110.17 (2013), pp. 1–5.

[10] R. Yajzey *et al.* "Spectroscopy of the T= 2 mirror nuclei 48Fe/48Ti using mirrored knock-out reactions". In: *Physics Letters B* 823 (2021), pp. 1–8.

[11] A. Fernández, A. Jungclaus, P. Doornenbal, et al. "Mirror energy differences above the 0f7/2 shell: First -ray spectroscopy of the Tz=2 nucleus 56Zn". In: *Physics Letters B* 823 (2021), p. 136784. ISSN: 0370-2693.

[12] M.A. Bentley, C.D. O'Leary, A. Poves, et al. "Mirror and valence symmetries at the centre of the f7/2 shell". In: *Physics Letters B* 437.3 (1998), pp. 243–248. ISSN: 0370-2693.

[13] A. P. Zuker, S. M. Lenzi, G. Martı´nez-Pinedo, et al. "Isobaric Multiplet Yrast Energies and Isospin Nonconserving Forces". In: *Physical Review Letters* 89.14 (2002), pp. 1–4.

[14] S. M. Lenzi and M. A. Bentley. "Coulomb energy differences between high-spin states in isobaric multiplets". In: *Progress in Particle and Nuclear Physics* 59.2 (2007), pp. 497–561.

[15] S. J. Williams, M. A. Bentley, D. D. Warner, et al. "Anomalous Coulomb matrix elements in the $f_{7/2}$ shell". In: *Phys. Rev. C* 68 (1 July 2003), p. 011301.

[16] S. M. Lenzi, N. M ărginean, D. R. Napoli, et al. "Coulomb Energy Differences in $T = 1$ Mirror Rotational Bands in ^{50}Fe and ^{50}Cr". In: *Phys. Rev. Lett.* 87 (12 Aug. 2001), p. 122501.

[17] D. M. Debenham, M. A. Bentley, P. J. Davies, et al. "Spectroscopy of ^{70}Kr and isospin symmetry in the $T = 1fpg$ shell nuclei". In: *Phys. Rev. C* 94 (5 Nov. 2016), p. 054311.

[18] K. Kaneko, S. Tazaki, T. Mizusaki, et al. "Isospin symmetry breaking at high spins in the mirror pair ^{67}Se and ^{67}As". In: *Phys. Rev. C* 82 (6 Dec. 2010), p. 061301.

[19] A. Gadea, S. M. Lenzi, S. Lunardi, et al. "Observation of ^{54}Ni: Cross-Conjugate Symmetry in $f_{7/2}$ Mirror Energy Differences". In: *Phys. Rev. Lett.* 97 (15 Oct. 2006), p. 152501.

[20] M. Bentley, S. M. Lenzi, S. A. Simpson, et al. "Isospin-breaking interactions studied through mirror energy differences". In: *Physical Review C* 92.2 (2015), pp. 1–8.

[21] N. Michel, W. Nazarewicz, and M. Płoszajczak. "Isospin mixing and the continuum coupling in weakly bound nuclei". In: *Phys. Rev. C* 82 (4 Oct. 2010), p. 044315.

[22] P. Bączyk and W. Satuła. "Mirror energy differences in $T = 1/2$ $f_{7/2}$-shell nuclei within isospin-dependent density functional theory". In: *Phys. Rev. C.* 103 (5 May 2021), p. 054320.

[23] W. Satuła, P. Bączyk, J. Dobaczewski, et al. "No-core configuration-interaction model for the isospin- and angular-momentum-projected states". In: *Phys. Rev. C.* 94 (2 Aug. 2016), p. 024306.

[24] R.D.O. Llewellyn *et al.* "Spectroscopy of proton-rich 79Zr: Mirror energy differences in the highly-deformed fpg shell". In: *Physics Letters B.* 811 (2020), p. 135873. ISSN: 0370-2693.

[25] A. Gade *et. al.* "Reduction of spectroscopic strength: Weakly-bound and strongly-bound single-particle states studied using one-nucleon knockout reactions". In: *Physical Review C - Nuclear Physics* 77.4 (2008), pp. 1–10.

[26] J. A. Tostevin and A. Gade. "Systematics of intermediate-energy single-nucleon removal cross sections". In: *Phys. Rev. C.* 90 (5 Nov. 2014), p. 057602.

[27] J. A. Tostevin and A. Gade. "Updated systematics of intermediate-energy single-nucleon removal cross sections". In: *Phys. Rev. C.* 103 (5 May 2021), p. 054610.

[28] M. MacCormick and G. Audi. "Evaluated experimental isobaric analogue states from T=1/2 to T=3 and associated IMME coefficients". In: *Nuclear Physics A* 925 (2014), pp. 61–95. ISSN: 0375-9474.

[29] T. W. Burrows. "Nuclear data sheets for A= 47". In: *Nuclear Data Sheets* 108.5 (2007), pp. 923–1056.

[30] S. Uthayakumaar, M. A. Bentley, E. C. Simpson, et al. "Spectroscopy of the $T = \frac{3}{2}A = 47$ and $A = 45$ mirror nuclei via one- and two-nucleon knockout reactions". In: *Phys. Rev. C* 106 (2 Aug. 2022), p. 024327.

[31] E. Caurier and F. Nowacki. "Present status of shell model techniques". In: *Acta Physica Polonica B.* 30.3 (1999), p. 705.

[32] E. Caurier *et al.* "The shell model as a unified view of nuclear structure". In: *Rev. Mod. Phys.* 77 (2 June 2005), pp. 427–488.

[33] W. Heisenberg. "Über den Bau der Atomkerne. I". In: *Original Scientific Papers / Wissenschaftliche Originalarbeiten.* Ed. by Walter Blum, Hans-Peter Dürr, and Helmut Rechenberg. Berlin, Heidelberg: Springer Berlin Heidelberg, 1989, pp. 197–207. ISBN: 978-3-642-70078-1.

[34] Michael A Bentley. "Excited States in Isobaric Multipletsmdash;Experimental Advances and the Shell-Model Approach". In: *Physics* 4.3 (2022), pp. 995–1011. ISSN: 2624-8174.

[35] D. J. Dean, S. E. Koonin, K. Langanke, et al. "Rotational and pairing properties of 74Rb". In: *Physics Letters, Section B: Nuclear, Elementary Particle and High-Energy Physics* 399.1-2 (1997), pp. 1–7.

[36] S. Frauendorf and A.O. Macchiavelli. "Overview of neutron–proton pairing". In: *Progress in Particle and Nuclear Physics* 78 (2014), pp. 24–90. ISSN: 0146-6410.

[37] B. Cederwall *et. al.* "Evidence for a spin-aligned neutron-proton paired phase from the level structure of ^{92}Pd". In: *Nature* 469.7328 (2011), pp. 68–71.

[38] A. L Goodman. "Proton-neutron pairing in Z = N nuclei with A = 76-96". In: *Physical Review C* 60.1 (1999), pp. 1–17.

[39] EP Wigner. "Proceedings of the Robert A. Welch Foundation Conference on Chemical Research". In: (1957).

[40] Walter Benenson and Edwin Kashy. "Isobaric quartets in nuclei". In: *Rev. Mod. Phys.* 51 (3 July 1979), pp. 527–540.

[41] W.E. Ormand and B.A. Brown. "Empirical isospin-nonconserving hamiltonians for shell-model calculations". In: *Nuclear Physics A* 491.1 (1989), pp. 1–23. ISSN: 0375-9474.

[42] Yi Hua Lam, Nadezda A. Smirnova, and Etienne Caurier. "Isospin nonconservation in *sd*-shell nuclei". In: *Phys. Rev. C* 87 (5 May 2013), p. 054304.

[43] J. H. D. Jensen O. Haxel and H. E. Suess. "On the "magic numbers" in nuclear structure". In: *Physical Review* 75.11 (1949), p. 1766.

[44] M. G. Mayer. "Nuclear configurations in the spin-orbit coupling model. I. empirical evidence". In: *Physical Review* 78.1 (1950), pp. 16–21.

[45] *"Nobel Lecture: The Shell Model"*. `https://www.nobelprize.org/uploads/2018/06/mayer-lecture.pdf`. Accessed: 13-September-2021.

[46] Kenneth S Krane. *Introductory nuclear physics / Kenneth S. Krane.* eng. Hoboken NJ: Wiley, 1987. ISBN: 9780471805533.

[47] Hubert Grawe. "Shell Modelfrom a Practitioner's Point of View". In: *The Euroschool Lectures on Physics with Exotic Beams, Vol. I.* Springer, 2004, pp. 33–75.

[48] Roger D. Woods and David S. Saxon. "Diffuse Surface Optical Model for Nucleon-Nuclei Scattering". In: *Phys. Rev.* 95 (2 July 1954), pp. 577–578.

[49] B. A. Brown. *Lecture notes in nuclear structure physics.* 2005.

[50] S. A. Milne. "Investigation of Isospin Symmetry Breaking the in f$\frac{7}{2}$*region*, studied through one-nucleon knockout and lifetime measurements." In: *PhD Thesis, University of York* (2016).

[51] J. Henderson. "Decay tagging of neutron-deficient $^{73,74}Sr$". In: *PhD Thesis* (2014).

[52] T.H.R. Skyrme. "The effective nuclear potential". In: *Nuclear Physics* 9.4 (1958), pp. 615–634. ISSN: 0029-5582.

[53] D. Gogny. "Simple separable expansions for calculating matrix elements of two-body local interactions with harmonic oscillator functions". In: *Nuclear Physics A* 237.3 (1975), pp. 399–418. ISSN: 0375-9474.

[54] R. Machleidt. "The Meson Theory of Nuclear Forces and Nuclear Structure". In: *Advances in Nuclear Physics.* Ed. by J. W. Negele and Erich Vogt. Boston, MA: Springer US, 1989, pp. 189–376. ISBN: 978-1-4613-9907-0.

[55] M. Lacombe, B. Loiseau, J. M. Richard, et al. "Parametrization of the Paris $N - N$ potential". In: *Phys. Rev. C* 21 (3 Mar. 1980), pp. 861–873.

[56] R. Yajzey. "The Isospin Symmetry of the $A = 48$, $T = 2$ Mirror Nuclei Studied Through the Mirrored Knockout Technique". In: *PhD Thesis* (2021).

[57] A. Poves, J. Sánchez-Solano, E. Caurier, et al. "Shell model study of the isobaric chains A=50, A=51 and A=52". In: *Nuclear Physics A.* 694.1-2 (2001), pp. 157–198. ISSN: 0375-9474.

[58] M Honma, T Otsuka, BA Brown, et al. "Shell-model description of neutron-rich pf-shell nuclei with a new effective interaction GXPF 1". In: *The European Physical Journal A-Hadrons and Nuclei* 25.1 (2005), pp. 499–502.

[59] G.E. Brown and T.T.S. Kuo. "Structure of finite nuclei and the free nucleon-nucleon interaction: General discussion of the effective force". In: *Nuclear Physics A* 92.3 (1967), pp. 481–494. ISSN: 0375-9474.

[60] T.T.S. Kuo and G.E. Brown. "Reaction matrix elements for the 0f-1p shell nuclei". In: *Nuclear Physics A* 114.2 (1968), pp. 241–279. ISSN: 0375-9474.

[61] Morten Hjorth-Jensen, Thomas T.S. Kuo, and Eivind Osnes. "Realistic effective interactions for nuclear systems". In: *Physics Reports* 261.3 (1995), pp. 125–270. ISSN: 0370-1573.

[62] DD Warner, MA Bentley, and P Van Isacker. "The role of isospin symmetry in collective nuclear structure". In: *Nature Physics* 2.5 (2006), pp. 311–318.

[63] T. W. Henry. "Mirror and Triplet spectroscopy in the fp shell with SeGA and GRETINA". PhD thesis. University of York, 2015.

[64] JA Nolen Jr and JP Schiffer. "Coulomb energies". In: *Annual Review of Nuclear Science.* 19.1 (1969), pp. 471–526.

[65] J. Duflo and A. P. Zuker. "Mirror displacement energies and neutron skins". In: *Phys. Rev. C* 66 (5 Nov. 2002), p. 051304.

[66] Chun-Wang Ma, Hui-Ling Wei, Xing-Quan Liu, et al. "Nuclear fragments in projectile fragmentation reactions". In: *Progress in Particle and Nuclear Physics* 121 (2021), p. 103911. ISSN: 0146-6410.

[67] J. Hüfner, K. Schäfer, and B. Schürmann. "Abrasion-ablation in reactions between relativistic heavy ions". In: *Phys. Rev. C* 12 (6 Dec. 1975), pp. 1888–1898.

[68] RJ Glauber. "Lectures in theoretical physics, ed. WE Brittin and LG Dunham". In: *Interscience, New York* 1 (1959), p. 315.

[69] "Relativistic formulation of Glauber theory for A(e,ep) reactions". In: *Nuclear Physics A* 728.1 (2003), pp. 226–250. ISSN: 0375-9474.

[70] K Gunzert-Marx, H Iwase, D Schardt, et al. "Secondary beam fragments produced by 200 MeV usup-1/sup sup12/supC ions in water and their dose contributions in carbon ion radiotherapy". In: *New Journal of Physics* 10.7 (July 2008), p. 075003.

[71] E. C. Simpson, J. A. Tostevin, D. Bazin, et al. "Two-Nucleon Knockout Spectroscopy at the Limits of Nuclear Stability". In: *Phys. Rev. Lett.* 102 (13 Apr. 2009), p. 132502.

[72] B. A. Brown, P. G. Hansen, B. M. Sherrill, et al. "Absolute spectroscopic factors from nuclear knockout reactions". In: *Phys. Rev. C* 65 (6 May 2002), p. 061601.

[73] P. G. Hansen and J. A. Tostevin. "Direct reactions with exotic nuclei". In: *Annual Review of Nuclear and Particle Science.* 53.1 (2003), pp. 219–261.

[74] J.A. Tostevin. "Single-nucleon knockout reactions at fragmentation beam energies". In: *Nuclear Physics A* 682.1 (2001), pp. 320–331. ISSN: 0375-9474.

[75] Dolores Cortina-Gil. "Direct Reactions at Relativistic Energies: A New Insight into the Single-Particle Structure of Exotic Nuclei". In: *The Euroschool on Exotic Beams, Vol. IV.* Ed. by Christoph Scheidenberger and Marek Pfützner. Berlin, Heidelberg: Springer Berlin Heidelberg, 2014, pp. 183–232. ISBN: 978-3-642-45141-6.

[76] V. Maddalena, T. Aumann, D. Bazin, et al. "Single-neutron knockout reactions: Application to the spectroscopy of ^{16,17,19}C". In: *Phys. Rev. C* 63 (2 Jan. 2001), p. 024613.

[77] J. A. Tostevin and J. S. Al-Khalili. "Sizes of the He isotopes deduced from proton elastic scattering measurements". In: *AIP Conference Proceedings* 455.1 (1998), pp. 227–232.

[78] J A Tostevin. "Core excitation in halo nucleus break-up". In: *Journal of Physics G: Nuclear and Particle Physics* 25.4 (Jan. 1999), pp. 735–739.

[79] A. E. L. Dieperink and T. de Forest. "Center-of-mass effects in single-nucleon knock-out reactions". In: *Phys. Rev. C* 10 (2 Aug. 1974), pp. 543–549.

[80] B Alex Brown. "New Skyrme interaction for normal and exotic nuclei". In: *Physical Review C* 58.1 (1998), p. 220.

[81] J. S. Al-Khalili and J. A. Tostevin. "Matter Radii of Light Halo Nuclei". In: *Phys. Rev. Lett.* 76 (21 May 1996), pp. 3903–3906.

[82] M. Wang, W.J. Huang, F.G. Kondev, et al. "The AME 2020 atomic mass evaluation (II). Tables, graphs and references∗". In: *Chinese Physics C.* 45.3 (Mar. 2021), p. 030003.

[83] D.J. Morrissey, B.M. Sherrill, M. Steiner, et al. "Commissioning the A1900 projectile fragment separator". In: *Nuclear Instruments and Methods in Physics Research Section B: Beam Interactions with Materials and Atoms.* 204 (2003), pp. 90–96. ISSN: 0168-583X.

[84] D. Bazin, J.A. Caggiano, B.M. Sherrill, et al. "The S800 spectrograph". In: *Nuclear Instruments and Methods in Physics Research Section B: Beam Interactions with Materials and Atoms* 204 (2003), pp. 629–633. ISSN: 0168-583X.

[85] M. Goeppert Mayer. *"The Colourful Nuclide Chart"*. `https://people.physics.anu.edu.au/~ecs103/chart/`. Accessed: 13-September-2021.

[86] D. *et. al* Weisshaar. "The performance of the γ-ray tracking array GRETINA for γ-ray spectroscopy with fast beams of rare isotopes". In: *Nuclear Instruments and Methods in Physics Research, Section A: Accelerators, Spectrometers, Detectors and Associated Equipment* 847 (2017), pp. 187–198.

[87] P. A. Zavodszky, B. Arend, D. Cole, et al. "Design of SuSI – superconducting source for ions at NSCL/MSU – II. The conventional parts". In: *Nuclear Instruments and Methods in Physics Research B* 241 (2005), pp. 959–964.

[88] P. A. Zavodszky, B. Arend, D. Cole, et al. "Status report on the design and construction of the Superconducting Source for Ions at the National Superconducting Cyclotron Laboratory/Michigan State University". In: *Review of Scientific Instruments* 77.3 (2006), 03A334.

[89] D.J. Morrissey. "The coupled cyclotron project at the NSCL". In: *Nuclear Physics A* 616.1 (1997). Radioactive Nuclear Beams, pp. 45–55. ISSN: 0375-9474.

[90] D. J Morrissey. "A new high-resolution separator for high-intensity secondary beams". In: *Nuclear Instruments and Methods in Physics Research B.* 126 (1997), pp. 316–319.

[91] J. Yurkon, D. Bazin, W. Benenson, et al. "Focal plane detector for the S800 high-resolution spectrometer". In: *Nuclear Instruments and Methods in Physics Research Section A: Accelerators, Spectrometers, Detectors and Associated Equipment* 422.1 (1999), pp. 291–295. ISSN: 0168-9002.

[92] *"S800 Spectrograph Service Level Description"*. `https://nscl.msu.edu/users/s800_sld-Feb20171.pdf`. Accessed: 17-October-2021.

[93] I-Yang Lee. "Gamma-ray energy tracking array: GRETINA". In: *Journal of Physics: Conference Series* 420 (Mar. 2013), p. 012156.

[94] S. Paschalis *et. al.* "The performance of the Gamma-Ray Energy Tracking In-beam NucleArArray GRETINA". In: *Nuclear Instruments and Methods in Physics Research Section A: Accelerators, Spectrometers, Detectors and Associated Equipment* 709.44 (2013), pp. 44–55.

[95] B Bruyneel, B Birkenbach, and P Reiter. "Pulse shape analysis and position determination in segmented HPGe detectors: The AGATA detector library". In: *The European Physical Journal A* 52.3 (2016), pp. 1–11.

[96] G. J. Schmid *et al.* "A -ray tracking algorithm for the GRETA spectrometer". In: *Nuclear Instruments and Methods in Physics Research Section A: Accelerators, Spectrometers, Detectors and Associated Equipment* 430.1 (1999), pp. 69–83. ISSN: 0168-9002.

[97] Y. Yoshizawa, Y. Iwata, and Y. Iinuma. "Precision measurements of gamma-ray intensities. II. ^{152}Eu, ^{154}Eu and ^{192}Ir". In: *Nuclear Instruments and Methods* 174.1 (1980), pp. 133–139. ISSN: 0029-554X.

[98] Y. Yoshizawa *et al.* "Precision measurements of gamma-ray intensities IV. Low energy region: ^{75}Se and ^{133}Ba". In: *Nuclear Instruments and Methods in Physics Research* 212.1 (1983), pp. 249–257. ISSN: 0167-5087.

[99] Y. Yoshizawa *et al.* "Precision measurements of gamma-ray intensities I. ^{56}Co, ^{88}Y, ^{110m}Ag, ^{134}Cs and ^{207}Bi". In: *Nuclear Instruments and Methods* 174.1 (1980), pp. 109–131. ISSN: 0029-554X.

[100] S. Agostinelli *et al.* "Geant4—a simulation toolkit". In: *Nuclear Instruments and Methods in Physics Research Section A: Accelerators, Spectrometers, Detectors and Associated Equipment* 506.3 (2003), pp. 250–303. ISSN: 0168-9002.

[101] A Gade and B M Sherrill. "NSCL and FRIB at Michigan State University: Nuclear science at the limits of stability". In: *Physica Scripta* 91.5 (Apr. 2016), p. 053003.

[102] *"S800 Documentation"*. `https://wikihost.nscl.msu.edu/S800Doc/`. Accessed: 10-March-2022.

[103] M. Berz, K. Joh, J. A. Nolen, et al. "Reconstructive correction of aberrations in nuclear particle spectrographs". In: *Phys. Rev. C* 47 (2 Feb. 1993), pp. 537–544.

[104] K. Makino and M. Berz. "COSY INFINITY version 8". In: *Nuclear Instruments and Methods in Physics Research Section A: Accelerators, Spectrometers, Detectors and Associated Equipment* 427.1 (1999), pp. 338–343. ISSN: 0168-9002.

[105] *"MSU Inverse Map Server"*. `http://maps.nscl.msu.edu/~s800maps/`. Accessed: 06-June-2020.

[106] *"ROOT based analysis software for GRETINA at NSCL"*. `https://github.com/wimmer-k/GrROOT/blob/master/Documentation.txt`. Accessed: 02-August-2022.

[107] Rene Brun and Fons Rademakers. "ROOT — An object oriented data analysis framework". In: *Nuclear Instruments and Methods in Physics Research Section A: Accelerators, Spectrometers, Detectors and Associated Equipment* 389.1 (1997). New Computing Techniques in Physics Research V, pp. 81–86. ISSN: 0168-9002.

[108] R. D. O. Llewellyn. "Structure and Collectivity of Highly Deformed Nuclei along the N=Z Line". PhD thesis. University of York, 2020.

[109] J. Chen, B. Singh, and J. A. Cameron. "Nuclear Data Sheets for A = 44". In: *Nuclear Data Sheets* 112.9 (2011), pp. 2357–2495.

[110] J. A. Cameron, M. A. Bentley, A. M. Bruce, et al. "High-spin states in the mirror nuclei 49Cr and 49Mn". In: *Physics Letters B* 235.3-4 (1990), pp. 239–244.

[111] A. Poves, J. Sánchez-Solano, E. Caurier, et al. "Shell model study of the isobaric chains A=50, A=51 and A=52". In: *Nuclear Physics A.* 694.1-2 (2001), pp. 157–198. ISSN: 0375-9474.

[112] E. C. Simpson and J. A. Tostevin. "One- and two-neutron removal from the neutron-rich carbon isotopes". In: *Phys. Rev. C* 79 (2 Feb. 2009), p. 024616.

[113] T.W. Burrows. "Nuclear Data Sheets for A = 45". In: *Nuclear Data Sheets.* 109.1 (2008), pp. 171–296. ISSN: 0090-3752.

[114] P. Bednarczyk *et al.* "High spin structure study of the light Odd-A f7/2 nuclei: 45Sc, 45Ti and 43Ca". In: *The European Physical Journal A-Hadrons and Nuclei.* 2.2 (1998), pp. 157–171.

[115] P. Bednarczyk *et al.* "High Spin Spectroscopy of Light f 7/2 Nuclei Studied with EUROBALL IV and the Recoil Filter Detector: a Smooth Band Termination in 45 Sc". In: *Acta Physica Polonica B.* 32.3 (2001), pp. 747–755.

[116] D. C. Tayal, K. P. Singh, and H. S. Hans. "Low-lying levels in ^{45}Sc". In: *Phys. Rev. C.* 34 (4 Oct. 1986), pp. 1262–1269.

[117] M. Matejska-Minda *et al.* "Revised Lifetime of the $\frac{11}{2}^-$ State in ^{45}Sc via Coulomb Excitation". In: *Acta Physica Polonica B.* 51.3 (2020), p. 829.

[118] J. A. Tostevin. "Reaction spectroscopy at fragmentation beam energies – recent advances in studies of two-nucleon removal". In: *The European Physical Journal Special Topics* 150.1 (2007), pp. 67–70.

[119] J. A. Tostevin and B. A. Brown. "Diffraction dissociation contributions to two-nucleon knockout reactions and the suppression of shell-model strength". In: *Phys. Rev. C.* 74 (6 Dec. 2006), p. 064604.

[120] B. A. Brown and W. D. M. Rae. "The Shell-Model Code NuShellX@MSU". In: *Nuclear Data Sheets.* 120 (2014), pp. 115–118. ISSN: 0090-3752.

[121] J. A. Tostevin. *Private Communication.* 2021.

[122] T. G. Parry. *Private Communication.* 2021.

[123] D. R. Inglis. "Spin-Orbit Coupling in Li^7 and Be^7". In: *Phys. Rev.* 82 (2 Apr. 1951), pp. 181–189.

[124] A. Poves and J. S. Solano. "Positive-parity rotational bands in odd-A pf-shell nuclei: A shell model description". In: *Phys. Rev. C.* 58 (1 July 1998), pp. 179–183.

[125] P. Bączyk, W. Satuła, J. Dobaczewski, et al. "Isobaric multiplet mass equation within nuclear density functional theory". In: *Journal of Physics G: Nuclear and Particle Physics.* 46.3 (Jan. 2019), 03LT01.

[126] W. Satula. *Private Communication.* 2021.

[127] O.B. Tarasov and D. Bazin. "LISE++ : design your own spectrometer". In: *Nuclear Physics A* 746 (2004). Proceedings of the Sixth International Conference on Radioactive Nuclear Beams (RNB6), pp. 411–414. ISSN: 0375-9474.

[128] O.B. Tarasov and D. Bazin. "LISE++: Radioactive beam production with in-flight separators". In: *Nuclear Instruments and Methods in Physics Research Section B: Beam Interactions with Materials and Atoms* 266.19 (2008). Proceedings of the XVth International Conference on Electromagnetic Isotope Separators and Techniques Related to their Applications, pp. 4657–4664. ISSN: 0168-583X.

[129] K. Wimmer *et al.* "Shape coexistence and isospin symmetry in A= 70 nuclei: Spectroscopy of the Tz=- 1 nucleus 70Kr". In: *Physics Letters B* 785 (2018), pp. 441–446.

[130] M. Spieker *et al.* "One-proton and one-neutron knockout reactions from N= Z= 28 Ni 56 to the A= 55 mirror pair Co 55 and Ni 55". In: *Physical Review C* 99.5 (2019), p. 051304.

[131] P. Doornenbal, P. Reiter, H. Grawe, et al. "Lifetime effects for high-resolution gamma-ray spectroscopy at relativistic energies and their implications for the RISING spectrometer". In: *Nuclear Instruments and Methods in Physics Research Section A: Accelerators, Spectrometers, Detectors and Associated Equipment* 613.2 (2010), pp. 218–225. ISSN: 0168-9002.

[132] S. Heil. "Electromagnetic Properties of ^{21}O and the Self-Calibration of Compton Tracking Arrays". PhD thesis. TU Darmstadt, 2019.

[133] P. Adrich, D. Enderich, D. Miller, et al. "A simulation tool for Recoil Distance Method lifetime measurements at NSCL". In: *Nuclear Instruments and Methods in Physics Research Section A: Accelerators, Spectrometers, Detectors and Associated Equipment* 598.2 (2009), pp. 454–464. ISSN: 0168-9002.

[134] R. J. Barlow. *Statistics: a guide to the use of statistical methods in the physical sciences.* Vol. 29. John Wiley & Sons, 1993.

[135] *"NSCL Lifetime Wiki"*. `https://wikihost.nscl.msu.edu/lifetime/doku.php?id=g4lifetime:docs`. Accessed: 24-March-2022.

[136] P.-A. Söderström *et al.* "Interaction position resolution simulations and in-beam measurements of the AGATA HPGe detectors". In: *Nuclear Instruments and Methods in Physics Research Section A: Accelerators, Spectrometers, Detectors and Associated Equipment.* 638.1 (2011), pp. 96–109. ISSN: 0168-9002.

[137] A. Lemasson, H. Iwasaki, C. Morse, et al. "Observation of mutually enhanced collectivity in self-conjugate $^{\mathbf{76}}_{\mathbf{38}}\mathrm{Sr}_{\mathbf{38}}$". In: *Phys. Rev. C* 85 (4 Apr. 2012), p. 041303.

[138] M. Toulemonde, N. Schulz, J. C. Merdinger, et al. "Recoil-distance lifetime measurements of states in ^{47}V and ^{47}Ti induced by heavy-ion reactions". In: *Phys. Rev. C.* 13 (5 May 1976), pp. 1889–1892.

[139] D.C.S. White, W.J. McDonald, D.A. Hutcheon, et al. "Pulsed beam lifetime measurements in 64Cu, 59Ni, 65Zn, 45,47,49Ti and 47,49,50,51V". In: *Nuclear Physics A.* 260.2 (1976), pp. 189–212. ISSN: 0375-9474.

[140] M. A. Bentley. *Private Communication.* 2022.

[141] M. Dufour and A. P. Zuker. "Realistic collective nuclear Hamiltonian". In: *Phys. Rev. C.* 54 (4 Oct. 1996), pp. 1641–1660.

[142] S. Uthayakumaar *et al.* In: *to be published* (2023).